

AD 606393

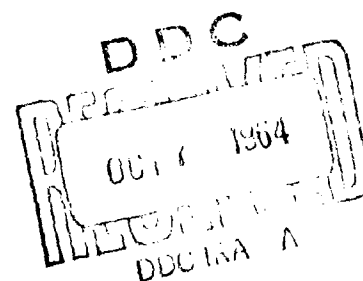
COPY	2	OF	3	Pages
HARD COPY	\$ . 7.00			
MICROFICHE	\$ . 1.50			

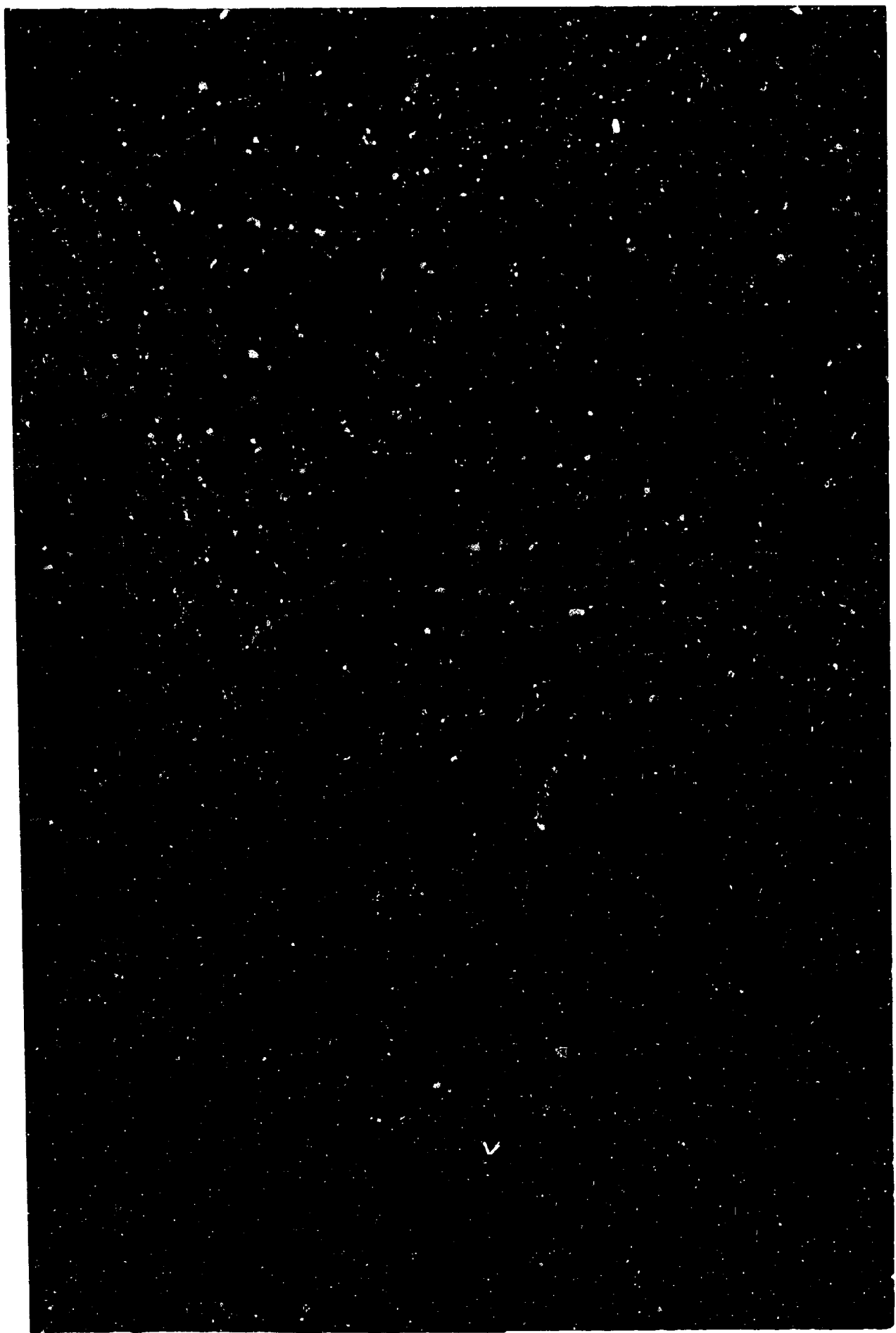
302p



**PHILCO.**

A SUBSIDIARY OF *Ford Motor Company*,  
RESEARCH LABORATORIES





**CLEARINGHOUSE FOR FEDERAL SCIENTIFIC AND TECHNICAL INFORMATION CFSTI  
DOCUMENT MANAGEMENT BRANCH 410.11**

**LIMITATIONS IN REPRODUCTION QUALITY**

**ACCESSION #**

**A 11606 393**

- ☒ 1. WE REGRET THAT LEGIBILITY OF THIS DOCUMENT IS IN PART UNSATISFACTORY. REPRODUCTION HAS BEEN MADE FROM BEST AVAILABLE COPY.
- ☒ 2. A PORTION OF THE ORIGINAL DOCUMENT CONTAINS FINE DETAIL WHICH MAY MAKE READING OF PHOTOCOPY DIFFICULT.
- ☐ 3. THE ORIGINAL DOCUMENT CONTAINS COLOR, BUT DISTRIBUTION COPIES ARE AVAILABLE IN BLACK-AND-WHITE REPRODUCTION ONLY.
- ☐ 4. THE INITIAL DISTRIBUTION COPIES CONTAIN COLOR WHICH WILL BE SHOWN IN BLACK-AND-WHITE WHEN IT IS NECESSARY TO REPRINT.
- ☐ 5. LIMITED SUPPLY ON HAND: WHEN EXHAUSTED, DOCUMENT WILL BE AVAILABLE IN MICROFICHE ONLY.
- ☐ 6. LIMITED SUPPLY ON HAND: WHEN EXHAUSTED DOCUMENT WILL NOT BE AVAILABLE.
- ☐ 7. DOCUMENT IS AVAILABLE IN MICROFICHE ONLY.
- ☐ 8. DOCUMENT AVAILABLE ON LOAN FROM CFSTI (TT DOCUMENTS ONLY).
- ☐ 9.

**NBS 9/64**

**PROCESSOR:**

**Dm**

AD 606393

**PHILCO**

A SUBSIDIARY OF *Ford Motor Company*,  
RESEARCH LABORATORIES

Publication No. U-2709  
W. O. 2104

RPL-TDR-64-140

---

FINAL TECHNICAL REPORT

---

INTERNAL ENVIRONMENT OF SOLID  
ROCKET NOZZLES

Prepared for: Rocket Research Laboratories  
Air Force Systems Command  
Edwards, California

Under Contract: AF 04(611)-9072

Prepared by: F. C. Price, Project Manager  
V. A. Marple, Modeling  
R. H. Williams, Alumina Impingement  
R. A. Dupuis, Alumina Emissivity  
H. L. Moody, Scaling Cloud Emissivity  
W. L. Smallwood, Convective Heat Transfer Analyses  
D. L. Peters, Total Heat Flux Integration  
R. A. Dobbins, Cloud Emission (Appendix)  
R. S. Briggs, Particle Sampling

Approved by: S. W. Weller  
S. W. Weller, Director  
Chemistry Laboratory

July 30, 1964



## ABSTRACT

Solid rocket motor nozzle environment was studied in cold flow modeling and in motor firings. The emphasis in the work was on the effects of the condensed phase in wall impingement and radiation. In motor firings using  $H_2 - O_2 - Al_2O_3 - H_2O$ , emissivity values for the alumina were determined. Then radiation heat flux scaling relationships were developed for application to any size motor. Particle impingement was studied in firing with a molybdenum nozzle fitted with thermocouples from which local transient heat flux data were developed. High heat flux rates due to impingement were determined. In cold flow studies particle impingement rates and static pressure values for input to corrective analysis were determined. Analyses of heat flux modes in a large motor nozzle and in a gimbaled nozzle were determined. A large part of the work involved technique development in handling micron-sized particles in firings and in cold flow. A particle sampler was developed for sampling motor exhausts.

## CONTENTS

SECTION		PAGE
1	INTRODUCTION . . . . .	1-1
2	COLD FLOW MODELING	
	2.1 Introduction . . . . .	2-1
	2.2 Cold Flow Modeling Analysis . . . . .	2-3
	2.3 Facility . . . . .	2-17
	2.4 Model Particles . . . . .	2-26
	2.5 Technique Development for Particle Impingement . . . . .	2-26
	2.6 Particle Impingement Calibration Tests . . . . .	2-29
	2.7 Particle Impingement Tests . . . . .	2-37
	2.8 Pressure Contours . . . . .	2-65
	2.9 Future Work and Applications . . . . .	2-65
	2.10 References . . . . .	2-69
3	PARTICLE IMPINGEMENT IN SIMULATOR FIRINGS	
	3.1 Introduction . . . . .	3-1
	3.2 Description of Test Apparatus and Run Procedure . . . . .	3-2
	3.3 Data Reduction and Test Results . . . . .	3-9
	3.4 Conclusions . . . . .	3-20
	3.5 References . . . . .	3-24
4	ALUMINA PARTICLE EMISSIVITY - EXPERIMENTAL	
	4.1 Introduction . . . . .	4-1
	4.2 Theory . . . . .	4-2
	4.3 Experimental Equipment . . . . .	4-9
	4.4 Results . . . . .	4-12
	4.5 Conclusions . . . . .	4-26
	4.6 References . . . . .	4-28
	Nomenclature . . . . .	4-29
5	ALUMINA CLOUD EMISSIVITY - APPLICATION TO DESIGN	
	5.1 Radiant Heat Flux From a Two Phase Mixture . . . . .	5-1
	5.2 Calculation of the Radiant Heat Flux in a Nozzle . . . . .	5-7
	5.3 Results . . . . .	5-11
	5.4 Conclusions . . . . .	5-16
	5.5 References . . . . .	5-20
	Nomenclature . . . . .	5-21

## CONTENTS (Continued)

SECTION		PAGE
6	SAMPLING OF MICRON-SIZED PARTICLES . . . . .	6-1
7	CONVECTIVE HEAT TRANSFER ANALYSES	
	7.1 Introduction . . . . .	7-1
	7.2 Method of Calculation . . . . .	7-3
	7.3 Results . . . . .	7-4
	7.4 Conclusions . . . . .	7-14
	7.5 References. . . . .	7-25
8	PREDICTION OF EROSION RATES FOR 100 FW2 AFT CLOSURE	
	8.1 Summation of Heat Fluxes. . . . .	8-1
	8.2 Establishing $Q^*$ for the Wall Material . . . . .	8-5
	8.3 Interpretation of the Analysis. . . . .	8-6
	8.4 Future Work . . . . .	8-6
	8.5 References. . . . .	8-9
9	SUMMARY AND RECOMMENDATIONS. . . . .	9-1
APPENDIX		
A	STUDIES OF TOTAL EMISSION FROM A $H_2-O_2-Al_2O_3$ PLUME USING A 1-INCH ROCKET MOTOR	
	A.1 Introduction. . . . .	A-1
	A.2 Experimental Measurement of Optical Properties of a Cloud of Scattering-Emitting Particles. . . . .	A-2
	A.3 Experiments on Small Rocket Engine . . . . .	A-4
	A.4 Integrated Radiation Measurements . . . . .	A-14
	A.5 Comparison of Total Radiation Results with Spectral Analysis Results. . . . .	A-15
	A.6 References. . . . .	A-16

# ILLUSTRATIONS

FIGURE		PAGE
2-1	Cold Flow Facility . . . . .	2-19
2-2	Spray Chamber Baffle Plate . . . . .	2-20
2-3	Spray Mixing Chamber with Particle Injection System . . . . .	2-21
2-4	Test Chamber with Nozzle and Manometer Pre-pressurizing System . . . . .	2-22
2-5	Manometer Board and Camera . . . . .	2-23
2-6	Assembly of Grain Port and Nozzle Model (with Tapes) . . . . .	2-24
2-7	Modeling Facility . . . . .	2-25
2-8	1.3 Micron Polystyrene Particles Impacted on Transfer Tape, 500 X Magnification. View Represents 0.012 Square Inches on 100-Inch Rocket Motor Wall . . . . .	2-27
2-9	Grain Port Model (Looking Upstream from Nozzle) . . . . .	2-30
2-10	Typical Particle Concentration Distribution in Grain . . . . .	2-31
2-11	Impingement Around Calibration Bar for Run 040971 . . . . .	2-32
2-12	Impingement Around Calibration Bar for Run 041574 . . . . .	2-33
2-13	Impingement Around Calibration Bar for Run 041575 . . . . .	2-34
2-14	Impingement Around Calibration Bar for Run 041576 . . . . .	2-35
2-15	Impingement Around Calibration Bar for Run 041678 . . . . .	2-36
2-16	Simulator Model . . . . .	2-40
2-17	Gimballed Nozzles and Grain Models . . . . .	2-41
2-18	Particle Impingement Tapes on Wedge and Bar for Supersonic Region of Nozzle . . . . .	2-42
2-19	Gimballed Nozzle Cold Flow Models . . . . .	2-44
2-20	Weight Percent of 1.4 $\mu$ Particles Impinging Along the Aft Closure. . . . .	2-46
2-21	Weight Percent of 2.2 $\mu$ Particles Impinging Along the Aft Closure. . . . .	2-47

# ILLUSTRATIONS (Continued)

FIGURE		PAGE
2-22	Weight Percent of $3.5\mu$ Particles Impinging Along the Aft Closure.	2-48
2-23	Reproducibility of Impingement Data . . . . .	2-49
2-24	Weight Fraction of $1.4\mu$ , $2.2\mu$ , and $3.5\mu$ , Particles Impinged at Point A vs. Percent of Burnout . . . . .	2-51
2-25	Weight Fraction of $1.4\mu$ , $2.2\mu$ , and $3.5\mu$ , Particles Impinging at Point B vs. Percent of Burnout . . . . .	2-52
2-26	Weight Fraction of $1.4\mu$ , $2.2\mu$ , and $3.5\mu$ , Particles Impinging at Point C vs. Percent of Burnout . . . . .	2-53
2-27	At Points A, B, C: Alumina Weight Fraction Impinged as a Function of Particle Size . . . . .	2-54
2-28	Particle Size Distribution of Alumina Sample Obtained from Motor Firing at 500-PSI Chamber Pressure . . . . .	2-56
2-29	Weight Fraction of Total Alumina Flow Impinged Versus Particle Size for Points A, B, and C . . . . .	2-58
2-30	Total Impingement Along Rocket Aft Closure . . . . .	2-59
2-31	100 FW2 Cold Flow Models . . . . .	2-60
2-32	Particle Impingement in 100 FW2 at 16% of Burnout . . . . .	2-62
2-33	Particle Impingement in 100 FW2 at 54% of Burnout . . . . .	2-63
2-34	Total Impingement Along 100 FW2 Aft Closure . . . . .	2-64
2-35	Photograph of Manometer Bank . . . . .	2-66
2-36	Mach Number in Gimballed Nozzle, Canted $5^\circ$ and Straight, Cold Flow Data . . . . .	2-67
2-37	Comparison of Experimental and Theoretical Mach Numbers in Straight Gimballed Nozzle . . . . .	2-68
3-1	Rocket Motor and Molybdenum Calorimetric Nozzle . . . . .	3-3
3-2	Heat Transfer Rocket Engine, Injector End . . . . .	3-4

# ILLUSTRATIONS (Continued)

FIGURE		PAGE
3-3	Molybdenum Heat Transfer Nozzle . . . . .	3-5
3-4	Surface Thermocouple Locations . . . . .	3-6
3-5	Nanmac Model P Thermocouple . . . . .	3-8
3-6	Measured Inlet Wall Temperatures During Slurry Injection . . . . .	3-11
3-7	Measured Throat Wall Temperatures During Period of Slurry Injection for Solids Loading Ratios of 0.10, 0.20, and 0.30 . . . . .	3-12
3-8	Measured Exit Cone Wall Temperature During Slurry Injection . . . . .	3-13
3-9	Experimental Inlet Film Coefficient During Period of Slurry Injection for Solids Loading Ratios of 0.0, 0.10, 0.20, and 0.30 . . . . .	3-14
3-10	Experimental Throat Film Coefficient Versus Time from Slurry Injection . . . . .	3-15
3-11	Exit Cone Film Coefficient During Slurry Injection . . . . .	3-16
3-12	Total Heat Flux at Exit Cone Location During Slurry Injection . . . . .	3-17
3-13	Transient Total Heat Flux to Simulator Nozzle . . . . .	3-18
3-14	Throat Film Coefficients for Canted Nozzle . . . . .	3-19
3-15	Film Coefficients at Peak Magnitudes of Heat Flux Versus Thermo- couple Number . . . . .	3-21
3-16	Film Coefficients at Peak Magnitudes of Heat Flux Versus Thermo- couple Number . . . . .	3-22
3-17	Total Heat Flux at Entrance and Exit Cone Locations for Aluminum Burning Propellant (18.8 Percent Aluminum) . . . . .	3-23
4-1	Chamber Temperature Versus O/F for $H_2 - O_2 - H_2O/Al_2O_3$ System . . . . .	4-5
4-2	Particle Distribution Function Versus Particle Radius . . . . .	4-7
4-3	Rocket Flame Imaging System . . . . .	4-10
4-4	Nitrogen Flushed Optical Pipe . . . . .	4-11
4-5	Engine and Spectrometer Accessories . . . . .	4-13

# ILLUSTRATIONS (Continued)

FIGURE		PAGE
4-6	Small Slurry Rocket - Rear View . . . . .	4-14
4-7	Alumina Emittance from Rocket Engine. Experiments and Mic Theory Calculations Based on Results of Burch and Gryvnak . . . . .	4-16
4-8	Alumina Absorption Coefficient Versus Wavelength - Data of Burch and Gryvnak . . . . .	4-17
4-9	Sample Spectra from Run 5B . . . . .	4-20
4-10	Sample Spectra from Run 3B . . . . .	4-22
4-11	Sample Spectra from Run 1B . . . . .	4-23
4-12	Sample Spectra from Run 10-B . . . . .	4-24
4-13	Sample Spectra from Run 12-B . . . . .	4-25
4-14	Sample Spectra from Run 11-B . . . . .	4-27
5-1	Total $Al_2O_3$ Particle Cloud Emissivity (Transparent Gas) Versus Temperature . . . . .	5-6
5-2	Predicted Radiation Heat Flux Versus Nozzle Position for Gimballed Nozzle . . . . .	5-13
5-3	Predicted Ratio of Radiation Plus Convection Heat Transfer Coefficient ( $\frac{h_r}{h_r + h_c}$ ) Versus Axial Position for Gimballed Nozzle Inlet . . . . .	5-14
5-4	Predicted Ratio of Radiation to Radiation plus Convection Heat Transfer Coefficient Versus Axial Position for Gimballed Nozzle Exit . . . . .	5-15
5-5	Predicted Ratio of Radiation to Radiation plus Convection Heat Transfer Coefficient Versus Axial Position for Molybdenum Simulator Nozzle Runs 1A and 45A . . . . .	5-17
5-6	Semi-Experimental Ratio of Radiation to Total Heat Transfer Coefficient Versus Axial Position for Molybdenum Simulator Nozzle Runs 1A and 45A . . . . .	5-18

# ILLUSTRATIONS (Continued)

FIGURE		PAGE
5-7	Path Length Required for Given Pressure and $\phi \bar{M}$ of an $Al_2O_3$ Particle Cloud to Produce Black Body Conditions . . . . .	5-19
6-1	Apparatus for Sampling Rocket Exhaust . . . . .	6-3
6-2	Sampled Alumina Particles . . . . .	6-4
6-3	Exhaust Cloud Particle Sampler . . . . .	6-5
7-1	Predicted and Experimental Convective Heat Transfer Coefficient Versus Nozzle Axial Position for Molybdenum Calorimetric Nozzle . . . . .	7-6
7-2	Predicted Convective Heat Transfer Coefficient Versus Axial Distance for 100 FW2 Aft Closure at 5 Seconds . . . . .	7-8
7-3	Predicted Convective Heat Transfer Coefficient Versus Axial Distance for 100 FW2 Aft Closure at 19.5 Seconds . . . . .	7-9
7-4	Predicted Convective Heat Transfer Coefficient Versus Axial Distance for 100 FW2 Aft Closure at 50 Seconds . . . . .	7-10
7-5	Predicted Convective Heat Transfer Coefficient Versus Axial Distance for 100 FW2 Aft Closure at 75 Seconds . . . . .	7-11
7-6	Predicted Convective Heat Transfer Coefficient Versus Axial Distance for 100 FW2 Aft Closure at 90 Seconds . . . . .	7-12
7-7	Predicted Convective Heat Transfer Coefficient Versus Axial Distance for Gimballed Nozzle Inlet at 0% Burn Time . . . . .	7-15
7-8	Predicted Convective Heat Transfer Coefficient Versus Axial Distance for Gimballed Nozzle Inlet at 23% Burn Time . . . . .	7-16
7-9	Predicted Convective Heat Transfer Coefficient Versus Axial Distance for Gimballed Nozzle Inlet at 58% Burn Time . . . . .	7-17
7-10	Comparison of Mach Numbers for one Dimensional and Model Flow for Gimballed Nozzle Inlet at 58% Burn Time . . . . .	7-19
7-11	Predicted Convective Heat Transfer Coefficient Versus Axial Distance for Gimballed Nozzle Throat - Exit Straight Configuration. . . . .	7-20
7-12	Predicted Convective Heat Transfer Coefficients Versus Axial Distance for Gimballed Nozzle Throat - Exit Straight Configuration. . . . .	7-21
7-13	Predicted Convective Heat Transfer Coefficients Versus Axial Distance for Gimballed Nozzle Throat - Exit Canted ( $5^\circ$ ) Configuration. . . . .	7-22



# ILLUSTRATIONS (Continued)

FIGURE		PAGE
8-1	Calculated Average Heat Fluxes for 100 FW2 Aft Closure . . . . .	8-4
8-2	Comparison of Measured Erosion Rate Versus Erosion Rate Predicted from Empirical $Q^*$ Versus $Q_c$ Relationship ( $T_w = 1500^\circ R$ ) . . . . .	8-7
8-3	Comparison of Erosion Rates Correlated Against Local Mach Number .	8-8
A-1	Particle Weight Fraction, $\phi$ . . . . .	A-8
A-2	Transmission Versus Volume Fraction . . . . .	A-9
A-3	Specific Turbidity Versus Volume Fraction . . . . .	A-11
A-4	Emissivity of Particles of $Al_2O_3$ plus $H_2O$ . . . . .	A-13

# TABLES

TABLE		PAGE
2.1	Modeling Test . . . . .	2-4
2.2	Tank Farm Capabilities . . . . .	2-26
2.3	Condition of Runs with Calibration Bars . . . . .	2-37
2.4	Summary of N <sub>2</sub> and SF <sub>6</sub> Properties . . . . .	2-37
2.5	Modeled Particle Sizes for Gimballed Nozzle . . . . .	2-43
2.6	Tabulation of $\frac{\delta W_1}{\delta W} \frac{D}{D}$ . . . . .	2-55
2.7	Particle Size Relationships in Modeling the 100 FW2 Nozzle . . . .	2-61
3.1	Molybdenum Calorimetric Nozzle Geometry and Thermocouple Location . . . . .	3-7
4.1	Summary of Experimental Test Data . . . . .	4-19
5.1	Sample Alumina Particle Cloud Total Emissivities for Alumina in the Liquid Phase . . . . .	5-4
5.2	Radiation Heat Fluxes in the 100 FW2 Nozzle . . . . .	5-12
7.1	Molybdenum Simulator Nozzle Geometry and Thermocouple Location . .	7-5
7.2	100FW-2 Nozzle Inlet Geometry . . . . .	7-13
7.3	Gimbal Nozzle Inlet Geometry . . . . .	7-18
7.4	Gimballed Nozzle Throat-Exit Geometry and Mach Number Distribution . . . . .	7-23
A.2	Summary of Data . . . . .	A-10

**BLANK PAGE**

## SECTION 1

### INTRODUCTION

This report summarizes the accomplishments of a 1-year study of the nozzle environment of solid rocket motors. The work was sponsored by the Rocket Research Laboratories, Edwards Air Force Base, under the technical cognizance of Mr. Leonard Slegers. Emphasis in the work was aimed toward developing new, practical understanding of the environmental effects of the condensed phase.

The work performed on this contract provides much useful information which the rocket industry can apply in (1) formulating cold flow studies of new designs, (2) determining particle sizes in engine effluents of alumina or other condensed compounds, (3) performing particle cloud radiation studies, and (4) analyzing heat fluxes in specific designs of motor nozzles.

The work focuses on the environment rather than on the complicated environment-wall interactions. However, the techniques and new understandings of this work can now be applied to studies where walls of graphite or plastics are involved which interact to modify the conditions at the environment-wall interface.

The radiation and particle impingement effects of alumina were studied. The emissivity of alumina particles was determined from the melting point up to 5200° F, using a  $H_2-O_2-H_2O-Al_2O_3$  combustion system in a 2-inch chamber without a nozzle. The emissivity data was then arranged in a form to allow calculations of radiative heat flux for specific design cases. The radiant energy emitted from a particle cloud was derived from a volume element model developed by R. A. Dobbins (see Appendix A). General expressions representing the radiant interchange between a surface and absorbing media were developed using the method devised by J. T. Bevens and R. V. Dunkle (5.4) using A. K. Oppenheim's (5.5) network method.

Particle impingement on the nozzle wall was studied both in cold flow modeling and in motor firings (1.25-inch throat). Conversion of the hot firing nozzle surface thermocouple measurements into heat flux data was done using a digital computer program presented in Jet Propulsion Laboratory Report No. 32-257 by Powell, Howell, and Irving (3.1). It is basically an analysis for radial modes of transient conduction. Thus, imposed heat fluxes from actual impingement were measured during firings and indicated impingements in large motors were determined from cold flow studies.

The cold flow studies used scale models of nozzles with tubular inserts representing certain grain burn-time instants. Nitrogen and sulfur hexafluoride gases were flowed in the models. Micron-sized polystyrene spheres were the model particles. The analysis and assumptions used to specify modeling conditions are a more thorough and sophisticated development of the work of earlier studies at Philco in cold flow modeling and gas particle flow analysis (References 2.1, 2.2, 8.1).

In the case of both radiation and particle impingement, a large part of the effort was devoted to technique development. The developments included radiancy measurement and analysis; special rocket engine and alumina-water slurry combustion operations; micron-size particles sampling, counting, and measuring; uncooled molybdenum calorimetric nozzle design; nozzle surface temperature measurement; nozzle wall transient thermal analysis to determine instantaneous local heat fluxes; cold flow modeling facility establishment; rocket nozzle model design; model particles handling, injection, impingement pickup, and counting; model wall static pressure contour measurement; time integrated particle impingement rate calculations.

A significant achievement of the work was the development of a particle sampler. This device collected by high velocity impact all the particles from a very small sample of the motor effluent directly from the plume, and displayed the particles in the complete size range distribution on one microscope slide.

Convective heat transfer analyses were performed using a computer program of the Elliott, Bartz, Silver method (7.4). These were applied to the hot firings for comparison with the total heat fluxes determined from a calorimetric nozzle. Using the cold flow modeling wall static pressure data, they were applied to infer the convective heat flux component for nozzles of large motors.

Experience in the rocket industry with the expensive and time consuming cut-and-dry approaches to nozzle design has demonstrated the need for more analytical engineering design approaches. The lack of precise design inputs creates both a high testing cost and a high burnout weight for reliability in large motors, especially where man-rated requirements exist.

Test data taking to contribute to analytical understanding has usually been very limited for two reasons: (1) It is difficult to justify instrumentation for analysis, if it imposes any jeopardy to the immediate hardware development test objectives; and (2) The severe environment of the motor often obviates meaningful measurements. Nevertheless, the rocket engineering industry is obligated to develop the same sophisticated analytical approaches used to great effectiveness in other engineering sciences.

Subjective materials screening tests and subscale motor tests have little practical meaning, if there is a lack of scaling laws or aerothermochemical detail. However, the level of effort devoted to analytical understanding has been small in the R & D programs for rocket motors, and it has been negligible in comparison with the magnitude of the major missile and booster programs. This is evident from the fact that the level of effort has never been large enough to warrant a session to present such work at a national technical meeting on solid rocket motors.

Cold flow studies conducted by contractors in support of their major hardware programs have yielded interesting results, but never quantitative data of more value than post firing inspections. The work reported here should open the way to more complete analyses and studies of current and future designs. The detailed results of such studies could be the basis for new understandings of design parameters, which could be usefully applied to advanced designs.

## SECTION 2

### COLD FLOW MODELING

#### 2.1 INTRODUCTION

There are two main objectives in the cold flow modeling of a rocket engine nozzle. The first is to determine the alumina particle impingement on the nozzle wall. This points out areas of potentially severe erosion or heat transfer and provides a quantitative figure for a detailed heat flux analysis. The second objective is the development of static pressure contours over the nozzle for input to convective heat transfer analysis. In order to accomplish this, a modeling analysis was derived to allow the setting of valid modeling conditions using certain assumptions, and a facility was designed and built to supply the required modeling flow conditions. Finally, a technique was developed for handling, injecting, picking up, and measuring the model particles.

Modeling equations were derived from an analysis of the equations of change for a compressible fluid and condensed particles in two-phase flow. The equations, written in parametric form, represent conditions within the motor and the model. For valid modeling, these parameters in the rocket and model must be equal.

From the modeling equations, it was observed that for a reasonable model size, model chamber pressure, and particles larger than submicron sizes, the particles specific gravity must be on the order of one. This restriction limited the choice of particles to a low vapor pressure liquid, atomized into small droplets, or to solid polystyrene spheres (available from Dow Chemical Company) in discrete particle sizes. The polystyrene particles were available in 0.09, 0.26, 0.36, 0.56, 0.8, 1.3, and 2.0 micron diameters.

The model chamber diameter was arbitrarily set at eleven inches. The scale factor was then set by the chamber diameter of the hot rocket being modeled. It varied from one to ten for the cases studied. The ratio of particle densities, model-to-rocket motor, was set using the polystyrene spheres. The working fluid's specific heat ratio, viscosity, molecular weight and temperature ratios, model-to-rocket, were set using unheated nitrogen or sulfur hexafluoride gas in modeling. Geometric similitude was used in all configurations. Thus, the remaining variables in experiment design were chamber pressure and particle size.

In order to develop model chamber pressures below atmospheric and to study exit cones, the facility included an air ejector which could pump the exit plane region to 1 psia with 5 lb/sec of nitrogen flowing through the chamber. All runs were fed by blowdown from a tank farm of compressed gas.

Since particle impingement on the aft-closure is dependent upon the approach velocity developed in the grain port, it was necessary to model a rocket at several different burn times and then integrate the impingement over the total firing time. At early burn times, the approach velocity to the aft-closure is higher than at later burn times when the grain port is larger but mass flow is not greatly different.

The main objective was to determine the total impingement from all particle sizes found in a rocket engine. However, it was also of interest to know where each size of particles would impinge, and how the impingement rate varied from one particle size to another. Three polystyrene particle sizes, with different discrete sizes in each batch, were used in different runs. The impingement over the entire particle size range could be obtained by integrating over the particle size distribution in a solid fuel rocket.

Two fairly important areas where the modeling was limited were the modeling of the boundary layer and the grain surface burning. Since it was impractical to have equal Reynold numbers in the model and rocket, the boundary layer could not be modeled. However, the Reynold numbers were high enough so that the flow was highly turbulent in both cases, and the stream line shapes would be essentially the same.

The flow of gases from a burning grain surface was not exactly simulated in the modeling of the grain port. However, uniform particle concentration distribution across the model grain port cross section approaching the model nozzle was an important criterion. The system geometry upstream of the model grain port was modified until an even distribution of particles was achieved.

The polystyrene particles were furnished in a latex form with 10 percent particles. By weighing a sample of the latex for a test, the exact number of particles used was known. The latex was diluted with methanol so that the atomized mixture added to the modeling gas would contain approximately one particle per drop. The diluting liquid evaporated, leaving the particles in the gas. This injection of the particles into the gas was sequenced so that the gas flow was already stabilized in the nozzle as the particles began flowing through.



Tapes that were sticky on both sides were put on the nozzle wall to act as collection receptors for the particles that impinged. After each run, the tapes were removed from the nozzle wall, placed on glass slides, and counted under a microscope. Using the same two sided tape technique, bars were placed across the grain port to check the particle concentration distribution. Duplicate runs were made to verify the reproducibility of the data.

The pressure contours were indicated on a manometer board, which was photographed when the manometers had stabilized. Since the run time for the blow down system was only about twenty seconds, a prepressurized manometer system was used to allow rapid response. Prepressurizing of the manometer tubes required the use of an auxiliary pressure supply, three-way solenoid valves, and bleed valves. Each manometer was prepressurized by the auxiliary pressure supply to approximately the height of liquid (water or mercury) which was anticipated for a given pressure measuring position in the nozzle. During the run, the three-way solenoid valves were switched to read the nozzle static pressures.

Three nozzles, which will be described in more detail later, were modeled. A gimbaled nozzle was modeled in both a straight position, and in a 5-degree canted position. A particle impingement study on the aft-closure of Aerojet-General's 100 FW2 was also made.

A total of 157 tests were made on the facility. Table 2.1 is a breakdown of the runs. Seventy-six of the runs were technique development runs, and produced modeling data.

## 2.2 COLD FLOW MODELING ANALYSIS

The modeling equations were derived by (1) considering the equations of change through the nozzle for the modeling gas and particle cloud, (2) putting the equations of change into dimensionless form, (3) setting the parameters of these equations equal in the model and rocket, and (4) applying assumptions which allow a set of modeling equations to be derived from these parameters.

Please turn to page 2-18 for foldout nomenclature sheets.

TABLE 2.1  
MODELING TEST  
TEST OBJECTIVES

	<u>Number of Tests</u>
Develop counting technique	20
Determine tape collection efficiency	17
Preliminary check out runs	8
Develop pressure reading technique	31
Check for uniform particle distribution across grain	29
<u>Straight Gimballed Nozzle</u>	
Pressure contour using N <sub>2</sub>	6
Pressure contour using SF <sub>6</sub>	2
Particle impingement using N <sub>2</sub>	23
Particle impingement using SF <sub>6</sub>	2
<u>5° Canted Gimballed Nozzle</u>	
Pressure contour using N <sub>2</sub>	10
Particle impingement using N <sub>2</sub>	3
<u>100 FW2</u>	
Particle impingement using N <sub>2</sub>	<u>6</u>
TOTAL	157

### Equations of Change Through Nozzle

The equations of change used were formulated first by Marble (1) for general gas-particle flow in polar coordinates. Marble, assuming Stokes law to be valid, defined two characteristic lengths: the "thermal range" and the "momentum range." These may be viewed physically as the distances covered by a particle in reducing its relative temperature and velocity to  $e^{-1}$  of its initial value. The equations have subsequently been reformulated for the axisymmetric case and the characteristic lengths redefined to account for deviations from Stoke's Law. These deviations were taken into account by defining  $f$  (force exerted/particle) =  $K_D f_{\text{Stokes}}$  where  $K_D = C_D/C_{D \text{ Stokes}}$  and has been determined at Philco Research Laboratories (2) to be given by

$$K_D = \frac{\left(1 + 0.15 \text{Re}_p^{0.687}\right) \left[1 + \exp\left(\frac{-0.427}{M_p^{4.63}} - \frac{3}{\text{Re}_p^{0.88}}\right)\right]}{1 + \frac{M_p}{\text{Re}_p} \left[3.82 + 1.28 \exp(-1.25 \text{Re}_p/M_p)\right]} .$$

With this correction,

$$\text{momentum range} \equiv \lambda_m = \frac{M_p a}{K_D 3\pi D_p \mu}$$

$$\text{temperature range} \equiv \lambda_t = \frac{3}{2} \text{Pr} \lambda_m .$$

In addition, a correction for heat transfer effects was introduced.

$$Nu = 2 K_H$$

where

$$K_H = \frac{2 + 0.459 Re_p^{0.55}}{2 + 6.84 \frac{M_p}{Re_p} \left( 2 + 0.459 Re_p^{0.55} \right)} .$$

The axisymmetric equations of change were then applied. The continuity equations, the momentum equations in the radial and axial directions, and the energy equations of the gas and particle cloud are presented for steady-state conditions and neglect wall-gas and wall-particle interactions.

For the gas, the continuity equation is

$$\frac{\partial}{\partial r} (\rho v r) + r \frac{\partial}{\partial x} (\rho u) = 0 , \quad (1)$$

the radial momentum equation is

$$\rho \left( v \frac{\partial v}{\partial r} + u \frac{\partial v}{\partial x} \right) = - \frac{\partial p}{\partial r} + \rho_{pc} a \left( \frac{v_p - v}{\lambda_m} \right) , \quad (2)$$

the axial momentum equation is

$$\rho \left( v \frac{\partial u}{\partial r} + u \frac{\partial u}{\partial x} \right) = - \frac{\partial p}{\partial x} + \rho_{pc} a \left( \frac{u_p - u}{\lambda_m} \right) , \quad (3)$$

and the energy equation is

$$\begin{aligned} \rho_p c_p \left( v \frac{\partial T}{\partial r} + u \frac{\partial T}{\partial x} \right) = & \rho_p c_p a \left[ \frac{(u_p - u)^2 + (v_p - v)^2}{\lambda_m} \right] \\ & + \frac{\rho_p c_p K_{11}}{K_D} \left( \frac{T_p - T}{\lambda_t} \right) \\ & + u \frac{\partial p}{\partial x} + v \frac{\partial p}{\partial r} . \end{aligned} \quad (4)$$

For the condensed phase, which will be treated as a continuum free of particle interactions, the continuity equation is

$$\frac{\partial}{\partial r} \left( \rho_{pc} v_p r \right) + r \frac{\partial}{\partial x} \left( \rho_{pc} u_p \right) = 0 , \quad (5)$$

the radial momentum equation is

$$v_p \frac{\partial v_p}{\partial r} + u_p \frac{\partial v_p}{\partial x} = - a \left( \frac{v_p - v}{\lambda_m} \right) , \quad (6)$$

the axial momentum equation is

$$v_p \frac{\partial u_p}{\partial r} + u_p \frac{\partial u_p}{\partial x} = - a \left( \frac{u_p - u}{\lambda_m} \right) , \quad (7)$$

and the energy equation is

$$c \left( v_p \frac{\partial T_p}{\partial r} + u_p \frac{\partial T_p}{\partial x} \right) = - \frac{a c_p K_H}{K_D} \frac{T_p - T}{\lambda_t} \quad (8)$$

In addition, perfect gas behavior is assumed.

$$\frac{P}{\rho} = \frac{R}{M.W.} T \quad (9)$$

#### Dimensionless Form Development

The equations of change may be put in dimensionless or parametric form by making the following substitutions:

$$\begin{aligned} u^* &= u/U & x^* &= x/D & \lambda_m^* &= \lambda_m/D \\ u_p^* &= u_p/U & T_p^* &= T_p/T_o & r^* &= r/D \\ P^* &= P/\rho U^2 & v^* &= v/U & T^* &= T/T_o \\ \lambda_t^* &= \lambda_t/D & v_p^* &= v_p/U \end{aligned}$$

The dimensionless forms of Equations (1) through (8) are then

$$\frac{\partial}{\partial r^*} (\rho v^* r^*) + r^* \frac{\partial}{\partial x^*} (\rho u^*) = 0 \quad (10)$$

$$v^* \frac{\partial v^*}{\partial r^*} + u^* \frac{\partial v^*}{\partial x^*} = - \frac{\partial P^*}{\partial r^*} + \frac{\rho_p c}{\rho} \frac{a}{U} \left( \frac{v_p^* - v^*}{\lambda_m^*} \right) \quad (11)$$

$$v^* \frac{\partial u^*}{\partial r^*} + u^* \frac{\partial u^*}{\partial x^*} = - \frac{\partial p^*}{\partial x^*} + \frac{\rho_{pc}}{\rho} \frac{a}{U} \left( \frac{u_p^* - u^*}{\lambda_m^*} \right) \quad (12)$$

$$v^* \frac{\partial T^*}{\partial r^*} + u^* \frac{\partial T^*}{\partial x^*} = \frac{\rho_{pc}}{\rho} \frac{a}{U} \frac{U^2}{c_p T_o} \left[ \frac{(u_p^* - u^*)^2 - (v_p^* - v^*)^2}{\lambda_m^*} \right] \\ + \frac{\rho_{pc}}{\rho} \frac{a}{U} \frac{K_H}{K_D} \left( \frac{T_p^* - T^*}{\lambda_t^*} \right) \quad (13)$$

$$+ \frac{U^2}{c_p T_o} \left[ u^* \frac{\partial p^*}{\partial x^*} + v^* \frac{\partial p^*}{\partial r^*} \right]$$

$$\frac{\partial}{\partial r^*} \left( \rho_{pc} v_p^* r^* \right) + r^* \frac{\partial}{\partial x^*} \left( \rho_{pc} u_p^* \right) = 0 \quad (14)$$

$$v_p^* \frac{\partial v_p^*}{\partial r^*} + u_p^* \frac{\partial v_p^*}{\partial x^*} = - \frac{a}{U} \left( \frac{v_p^* - v^*}{\lambda_m^*} \right) \quad (15)$$

$$v_p^* \frac{\partial u_p^*}{\partial r^*} + u_p^* \frac{\partial u_p^*}{\partial x^*} = - \frac{a}{U} \left( \frac{u_p^* - u^*}{\lambda_m^*} \right) \quad (16)$$

$$v_p^* \frac{\partial T_p^*}{\partial r^*} + u_p^* \frac{\partial T_p^*}{\partial x^*} = - \frac{a}{U} \frac{c_p K_H}{K_D} \left( \frac{T_p^* - T^*}{\lambda_t^*} \right) \quad (17)$$

It is apparent that the solutions of Equations (10) through (17) will be identical for two different sets of operating conditions only if certain conditions are satisfied. The solution of Equations (10) through (17) may be expressed by

$$\text{Solution} = \phi_1 \left( r^*, x^*, \frac{\rho_{pc}}{\rho}, \frac{a}{U}, \frac{\rho_{pc} a}{\rho U c_p T_o}, \frac{\rho_{pc} a K_H}{\rho U K_D}, \frac{U^2}{c_p T_o}, \right. \\ \left. \frac{a}{U}, \frac{a c_p K_H}{U c K_D}, \lambda_m^*, \lambda_t^* \right). \quad (18)$$

But, since certain of the similarity groups on the right hand side of Equation (18) are related, it is possible to write

$$\text{Solution} = \phi_2 \left( r^*, x^*, \frac{\rho_{pc}}{\rho}, \frac{a}{U}, \frac{U^2}{c_p T_o}, \frac{K_H}{K_D}, \frac{c_p}{c}, \lambda_m^*, \lambda_t^* \right). \quad (19)$$

#### Equated Modeling Parameters

Thus, if the parameters are individually equal in two different systems, the solutions in terms of the dimensionless variables are equal. In order to simulate rocket performance in a model, it is necessary that

$$r_M^* = r_R^*$$

$$(K_H/K_D)_M = (K_H/K_D)_R$$

$$x_M^* = x_R^*$$

$$(c_p/c)_M = (c_p/c)_R$$



$$(\rho_{pc}/\rho)_M = (\rho_{pc}/\rho)_R \quad \left( \lambda_m^* \right)_M = \left( \lambda_m^* \right)_R$$

$$(a/U)_M = (a/U)_R \quad \left( \lambda_t^* \right)_M = \left( \lambda_t^* \right)_R$$

$$(U^2/c_p T_o)_M = (U^2/c_p T_o)_R$$

Four of these similarity groups may be further simplified. Making use of the ideal gas relationships and the appropriate defining relationships, it is possible to demonstrate

$$U^2/c_p T_o = \frac{U^2}{a^2} (\gamma - 1)$$

and, since  $\frac{U}{a}$  is already constrained, we may state that  $\gamma_M = \gamma_R$  is a necessary condition;  $a$  is also a function of  $\gamma$ .

$$K_H/K_D = f(Re_p, M_p)$$

and thus,

$$(K_H/K_D)_M = (K_H/K_D)_R \text{ if}$$

$$(Re_p)_M = (Re_p)_R \text{ and } (M_p)_M = (M_p)_R$$

$$c_p = \frac{R\gamma}{M.W. (\gamma - 1)} ;$$

therefore,

$$\text{if } \gamma_M = \gamma_R ,$$

$$\left( \frac{c_p}{c} \right)_M = \left( \frac{c_p}{c} \right)_R \text{ may be replaced by}$$

$$(M.W.)_M c_M = (M.W.)_R c_R .$$

Since  $\lambda_{in}^*$  is constrained,  $\left( \lambda_t^* \right)_M = \left( \lambda_t^* \right)_R$  may be replaced by

$$(Pr)_M = (Pr)_R$$

The similarity criteria may be rearranged and presented in the following form

$$\frac{r_M}{D_M} = \frac{r_R}{D_R} \quad (20)$$

$$\frac{x_M}{D_M} = \frac{x_R}{D_R} \quad (21)$$

$$\frac{(\rho c)_M}{(\rho c)_R} = \frac{P_M}{P_R} \cdot \frac{T_R}{T_M} \cdot \frac{M.W._M}{M.W._R} \quad (22)$$

$$\frac{U_M}{U_R} = \left( \frac{\gamma_M}{\gamma_R} \cdot \frac{T_M}{T_R} \cdot \frac{M.W._R}{M.W._M} \right)^{1/2} \quad (23)$$

$$\gamma_M = \gamma_R \quad (24)$$

from  $(Re_p)_M = (Re_p)_R$ :

$$\frac{\bar{u}_{S_M}}{\bar{u}_{S_R}} = \frac{D_{P_R}}{D_{P_M}} \cdot \frac{P_R}{P_M} \cdot \frac{M.W._R}{M.W._M} \cdot \frac{T_M}{T_R} \cdot \frac{M}{R} \quad (25)$$

from  $(M_P)_M = (M_P)_R$ :

$$\frac{\bar{u}_{S_M}}{\bar{u}_{S_R}} = \left( \frac{\gamma_M}{\gamma_R} \cdot \frac{T_M}{T_R} \cdot \frac{M.W._R}{M.W._M} \right)^{1/2} \quad (26)$$

$$\frac{c_M}{c_R} = \frac{c_{P_M}}{c_{P_R}} = \left( \frac{M.W._R}{M.W._M} \right) \quad (27)$$

$$\frac{D_M}{D_R} = \left( \frac{D_{P_M}^2}{D_{P_R}^2} \cdot \frac{\rho_{P_M}}{\rho_{P_R}} \cdot \frac{a_M}{a_R} \cdot \frac{\mu_R}{\mu_M} \right) \quad (28)$$

from  $\lambda_m^* M = \lambda_m^* R$  with  $(Re_p)_M = (Re_p)_R$  and  $(M_P)_M = (M_P)_R$ :

$$(Pr)_M = (Pr)_R \quad (29)$$

### Assumptions

It is apparent from these conditions, which should be satisfied at all corresponding points in model and rocket, that to achieve an exact modeling condition, the modeling fluid, modeling particulate phase, and model geometry must satisfy rigid

conditions. To satisfy these conditions exactly may be impossible, but an attempt was made to satisfy those which appear to be most critical for effective modeling.

Similarity condition, Equation (24), must be satisfied in order to model fluid flow conditions. If  $\gamma_M = \gamma_R$ , model and rocket area ratios, pressure ratios and temperature ratios are easily related when simple geometrical scaling is used. In addition, taking

$$Pr = \frac{4\gamma}{9\gamma-5}$$

the Prandtl number will be equal in systems of equal  $\gamma$ . Thus, satisfying Equation (24), satisfies Equation (29), and makes possible direct geometric scaling. Thus, conditions, Equations (20) and (21), are easily met.

The specific heat ratios encountered in hot rocket firings are low ( $\gamma = 1.18$  for gas alone,  $\gamma_{\text{effective}} = 1.1$  for gas and condensed phases) as is the molecular weight of the hot products. Unfortunately, at the relatively low temperatures (ambient or slightly higher) desired for cold-flow modeling, only high molecular weight, polyatomic molecules (e.g.,  $CCl_2F_2$  and  $SF_6$ ) have specific heat ratios of the necessary value. These high molecular weights will make it difficult to satisfy conditions, Equations (22) and (27), since high-particle cloud density and extreme low-particle specific heat will be required. High-particle cloud

density requires the use of a large number of particles which is an undesirable modeling condition, since it complicates analysis. A modeling particle with low specific heat (as compared to that of  $\text{Al}_2\text{O}_3$  in rocket firings) will be difficult to find, since it appears that the necessary molecular weight ratio ( $\text{M.W.}_R/\text{M.W.}_M$ ) will be on the order of 1/6 in order to satisfy Equation (24). The effect of failing to satisfy the conditions imposed by Equations (22) and (27) appears to be less severe than if the equal  $\gamma$  condition, Equation (24), were neglected. While  $\gamma$  determines the fluid flow field, particle cloud density and specific heat serve to modify the field. In addition, if it may be assumed that individual particles behave independently of surrounding particles, neglect of the particle cloud density as a parameter is reasonable.

The final governing modeling relationships can now be stated from Equations (20) to (29) considering the limitations of not being able to satisfy Equations (22) and (27).

From Equations (20) and (21),

$$\text{Scale Factor} = \frac{D_R}{D_M} = \frac{X_R}{X_M} = \frac{r_R}{r_M} \quad (30)$$

That is, there is geometric similarity in all directions.

By equating Equations (25) and (26), the model pressure can be expressed as

$$P_M = \frac{D_{P_R}}{D_{P_M}} \frac{\mu_M}{\mu_R} \left[ \frac{T_M}{T_R} \frac{M.W._R}{M.W._M} \frac{\gamma_R}{\gamma_M} \right]^{1/2} P_R, \quad (31)$$

and Equation (28) can be arranged to give

$$\frac{D_{P_M}}{D_{P_R}} = \left[ \frac{D_M}{D_R} \frac{\rho_{P_R}}{\rho_{P_M}} \frac{a_{*R}}{a_{*M}} \frac{\mu_M}{\mu_R} \right]^{1/2} \quad (32)$$

which is the particle scale factor.

### 2.3 FACILITY

To accomplish the modeling, a facility had to be designed and built which would satisfy the previously mentioned requirements. Figure 2-1 shows a schematic of the modeling facility. The particles were mixed with 35 cubic centimeters of methanol and fed from two tanks during a run. The indicated valves were opened for the modeling gas with the pressure regulator controlling the flow to maintain the desired model chamber pressure. After the flow was stabilized, the valves on the bottom of the alcohol-particle tanks were opened and the mixture was atomized into the mixing chamber. The particle atomizing system consisted of two sets of pneumatic atomizing spray nozzles, one set of six on each side of the "T" shaped spray mixing chamber.

As can be seen in Figure 2-1, there were baffle plates over the two primary gas inlets located with the atomizing nozzles. These baffles, shown in greater detail in Figure 2-2, directed the primary modeling gas to envelop each spray and keep the spray from wetting the walls.

Figure 2-3 is a view of the part of the facility just described and also shown is the ejector gas valve which regulates the flow of pumping air to the air ejector.

In the spray mixing chamber, the methanol was evaporated leaving the polystyrene spheres entrained in the modeling gas. The particle laden gas then flowed on to the propellant grain port and nozzle. The test chamber and a nozzle model are shown in Figure 2-4. Figure 2-4 also shows the manometer prepressurizing system, while Figure 2-5 shows the manometer board and camera used to record the data. If care were taken in prepressurizing the manometers, the time for the manometers to adjust was approximately two seconds. A typical run length was twenty seconds.

Prior to a run, the sticky tapes for collecting impinging particles were placed on the nozzle wall and the propellant grain port put in place. A rubber seal was used around the tubular grain port to ensure a leakproof intersection between the grain port and model. The grain port was attached to the model nozzle by a system of springs and the assembly was then inserted into the test chamber. Figure 2-6 shows a grain port and nozzle being assembled; four particle collection tapes can also be seen. The air ejector, used to pull a vacuum on the exit cone, is shown in Figure 2-7 along with the other components of the cold flow modeling facility.

All modeling was accomplished by using the blowdown method. Air, sulfur hexafluoride, and nitrogen were used for the modeling gas. Table 2.2 shows the tank farm gas storage capacities.

# NOMENCLATURE

A	Area	$T_p$	Particle temperature
a	Local sonic velocity	U	Characteristic velocity
c	Particle specific heat	u	Axial component of fluid velocity
$c_p$	Gas specific heat	$u_p$	Axial component of particle velocity
$C_D$	Particle drag coefficient	$\bar{u}_s$	Particle slip velocity
$C_{DStokes}$	Particle drag coefficient predicted by Stokes law	v	Radial component of fluid velocity
D	Characteristic dimension	$v_p$	Radial component of particle velocity
$D_p$	Particle diameter	W	Mass flow rate
f	Force exerted on a particle	x	Local axial dimension
$f_{Stokes}$	Force exerted on a particle as predicted by Stokes law		
$\Delta H_{subl}$	Heat of sublimation	<u>Greek Letters</u>	
$K_D$	As given	$\gamma$	Specific heat ratio
$K_H$	As given	$\lambda_m$	Momentum range
M	Fluid Mach number	$\lambda_t$	Thermal range
$M_p$	Particle Mach number $\equiv \bar{u}_s/a$	$\mu$	Fluid viscosity
M.W.	Molecular weight	$\rho$	Fluid density
Nu	Nusselt number	$\rho_p$	Particle density
P	Pressure	$\rho_{pc}$	Density of particle cloud (mass of solid/gas volume)
Pr	Prandtl number	<u>Subscripts</u>	
R	Gas constant	c	Condition in chamber
Re	Fluid Reynolds number	e	Condition at exit plane
$Re_p$	Particle Reynolds number $\equiv D_p \bar{u}_s \rho / \mu$	M	Model condition
r	Local radial dimension	R	Rocket condition
T	Local static temperature	*	Condition at nozzle throat
$T_o$	Stagnation temperature $\equiv T_c$ , chamber temperature		



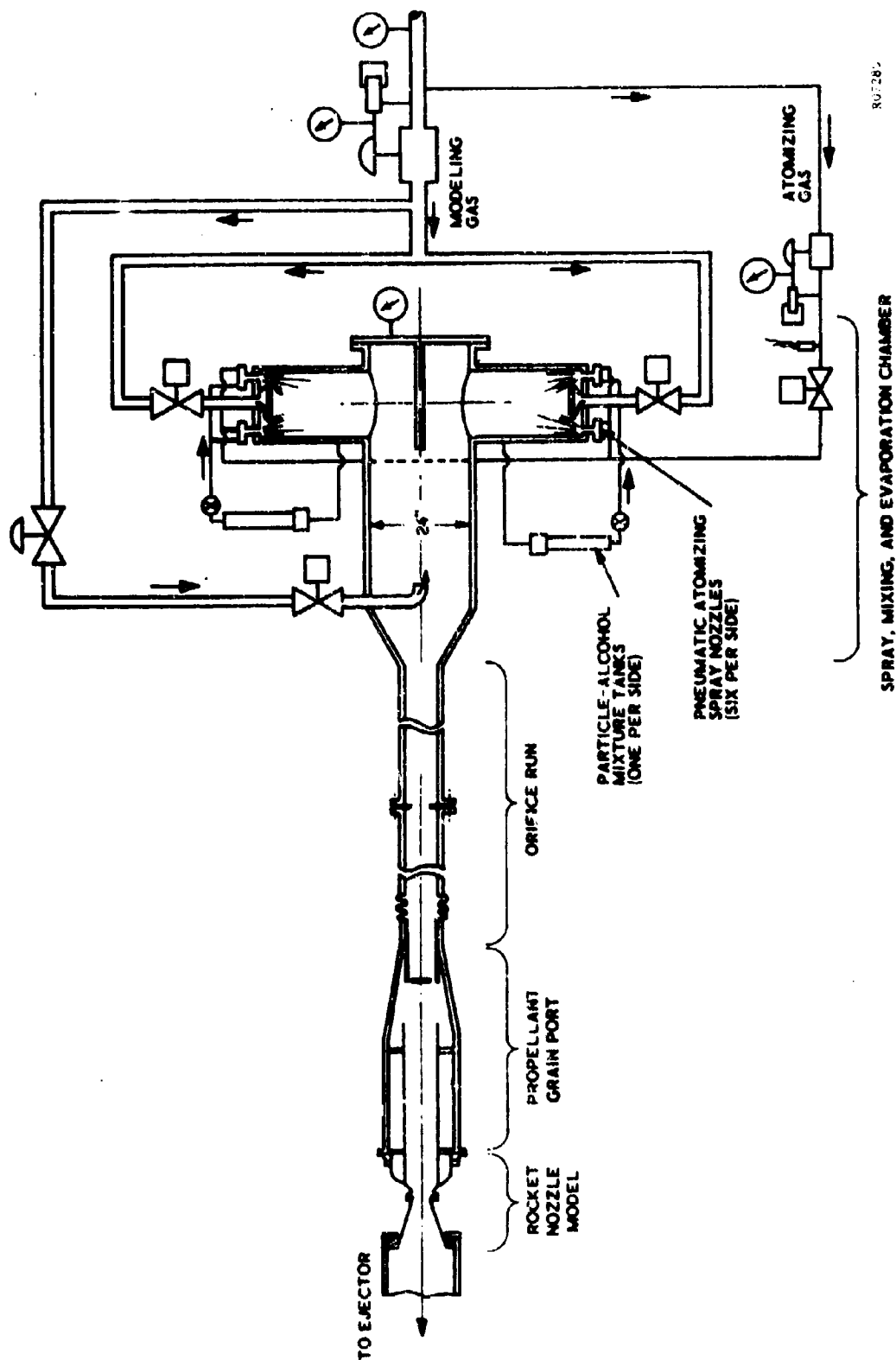


FIGURE 2-1. COLD FLOW FACILITY

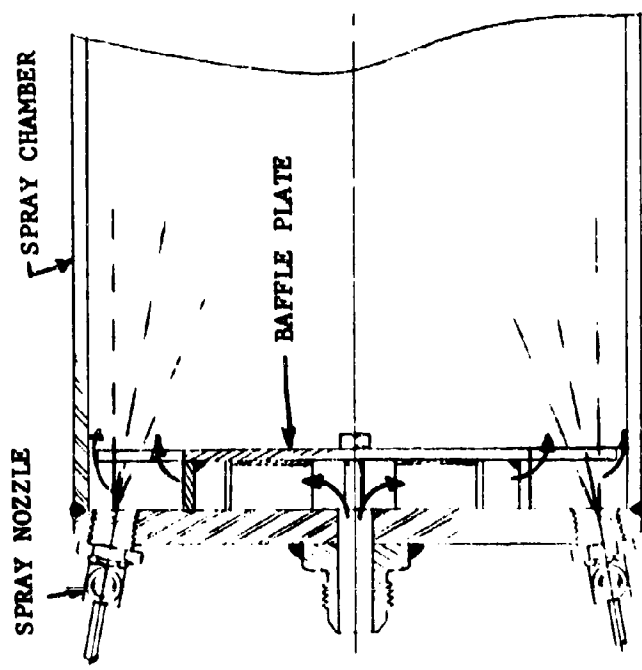
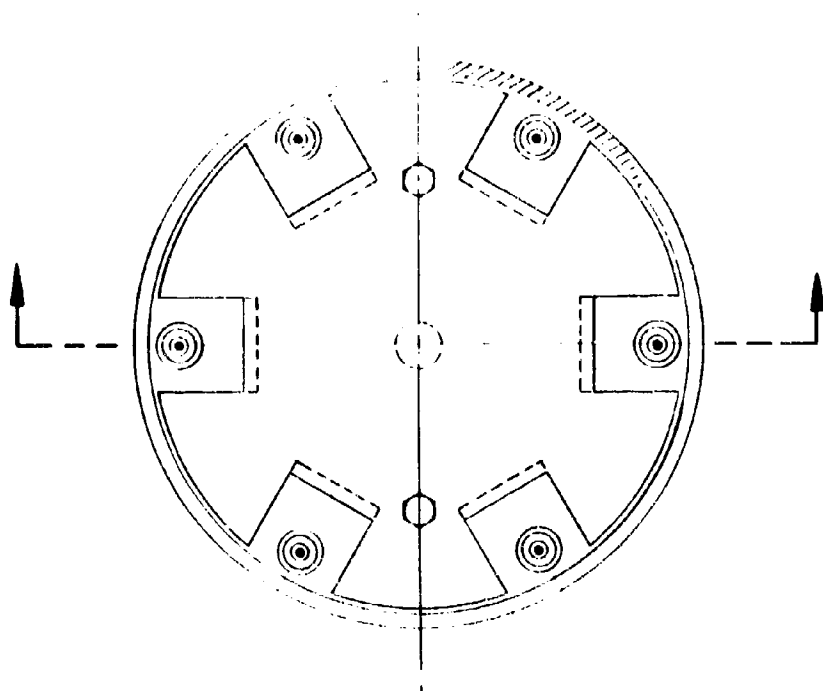


FIGURE 2-2. SPRAY CHAMBER BAFFLE PLATE



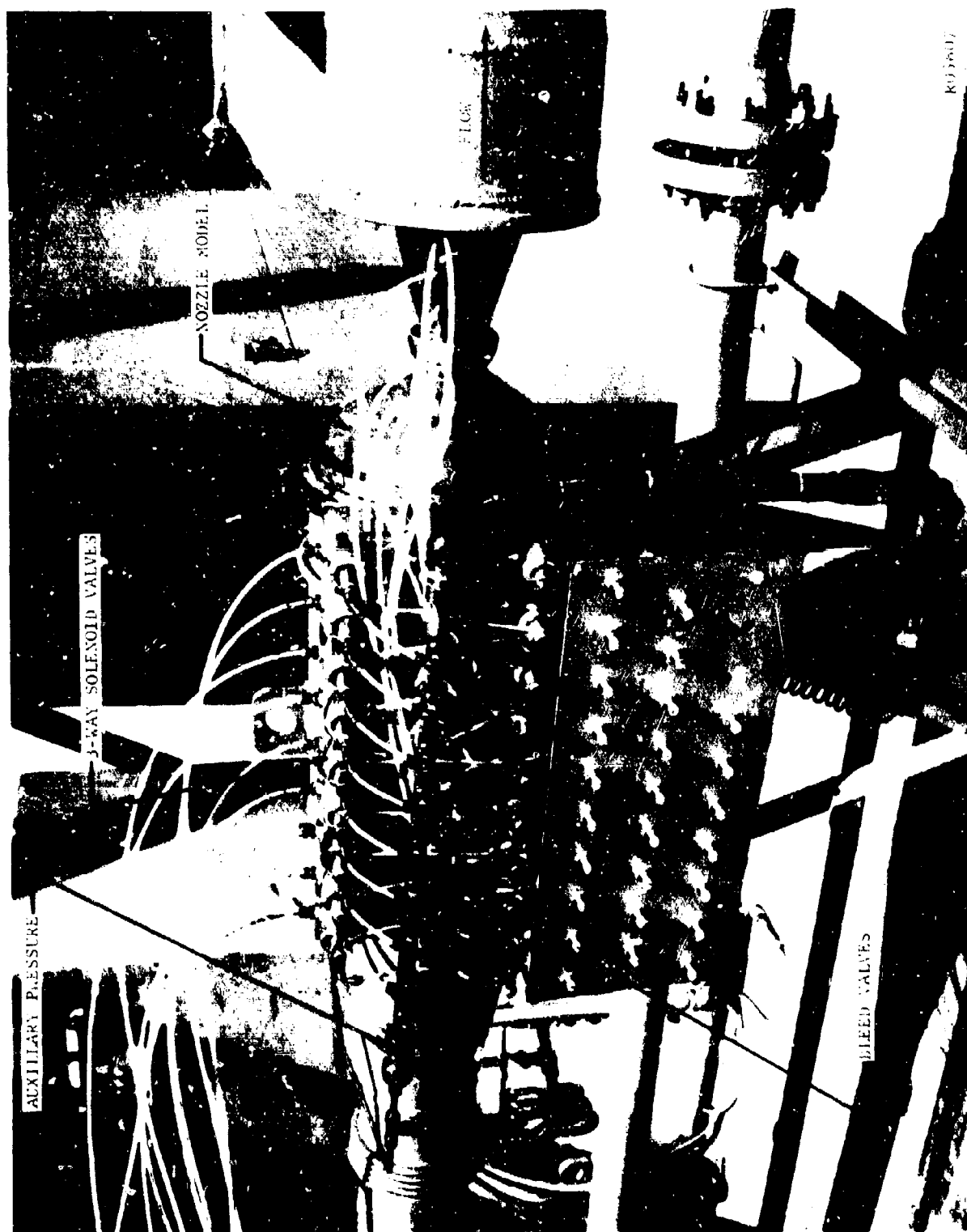


FIGURE 2-4. TEST CHAMBER WITH NOZZLE AND MANOMETER PRE-PRESSURIZING SYSTEM

FIGURE 2-5. MANOMETER BOARD AND CAMERA





FIGURE 2-6. ASSEMBLY OF GRAIN PORT AND NOZZLE MODEL (WITH TAPES)



K05610

TABLE 2.2  
TANK FARM CAPABILITIES

<u>Gas</u>	<u>Max. Pressure (psi)</u>	<u>No. of 25 ft.<sup>3</sup> Cylinders</u>	<u>Total Volume (ft.<sup>3</sup>)</u>
Air	1500	21	525
Nitrogen	2200	18	450
SF <sub>6</sub>	300	3	75

#### 2.4 MODEL PARTICLES

At the outset of the program, both dyed atomized liquid droplets and polystyrene spheres were considered for model particles. The liquid droplets could be picked up on blotters placed along the nozzle model surface. Particle size sampling and analysis would have been required. A demister would have been used to remove over-sized droplets.

The polystyrene spheres were selected because their size was predetermined no sampling, measuring, or counting were required to establish this. Sticky tape was found to be very effective in picking up the impinging polystyrene spheres for counting.

All counting of the polystyrene particles was accomplished with the use of a microscope at 430X. An attempt was made to dye the particles for easier counting. However, it was not possible to get the particles to absorb enough dye.

Figure 2-8 is a photograph of the 1.3 micron particles at 500X; These particles had been impinged on tape.

#### 2.5 TECHNIQUE DEVELOPMENT FOR PARTICLE IMPRINGEMENT

Before meaningful data could be obtained from the modeling facility, considerable technique development was required. The five main areas of technique development were (1) dispersing of polystyrene particles in the modeling gas, (2) establishing the correct number of particles in each run, (3) developing an even particle distribution across the grain port, (4) obtaining a leak-free precision, grain port-nozzle intersection, and (5) counting the particles.

As mentioned earlier, the polystyrene particles were mixed in a liquid and sprayed into the spray chamber where the liquid evaporated leaving the particles in the gas. The two problems in accomplishing this were (1) spraying small enough liquid droplets to preclude settling out before evaporation and (2) obtaining unagglomerated single particles in the gas. To get a fine spray into the spray



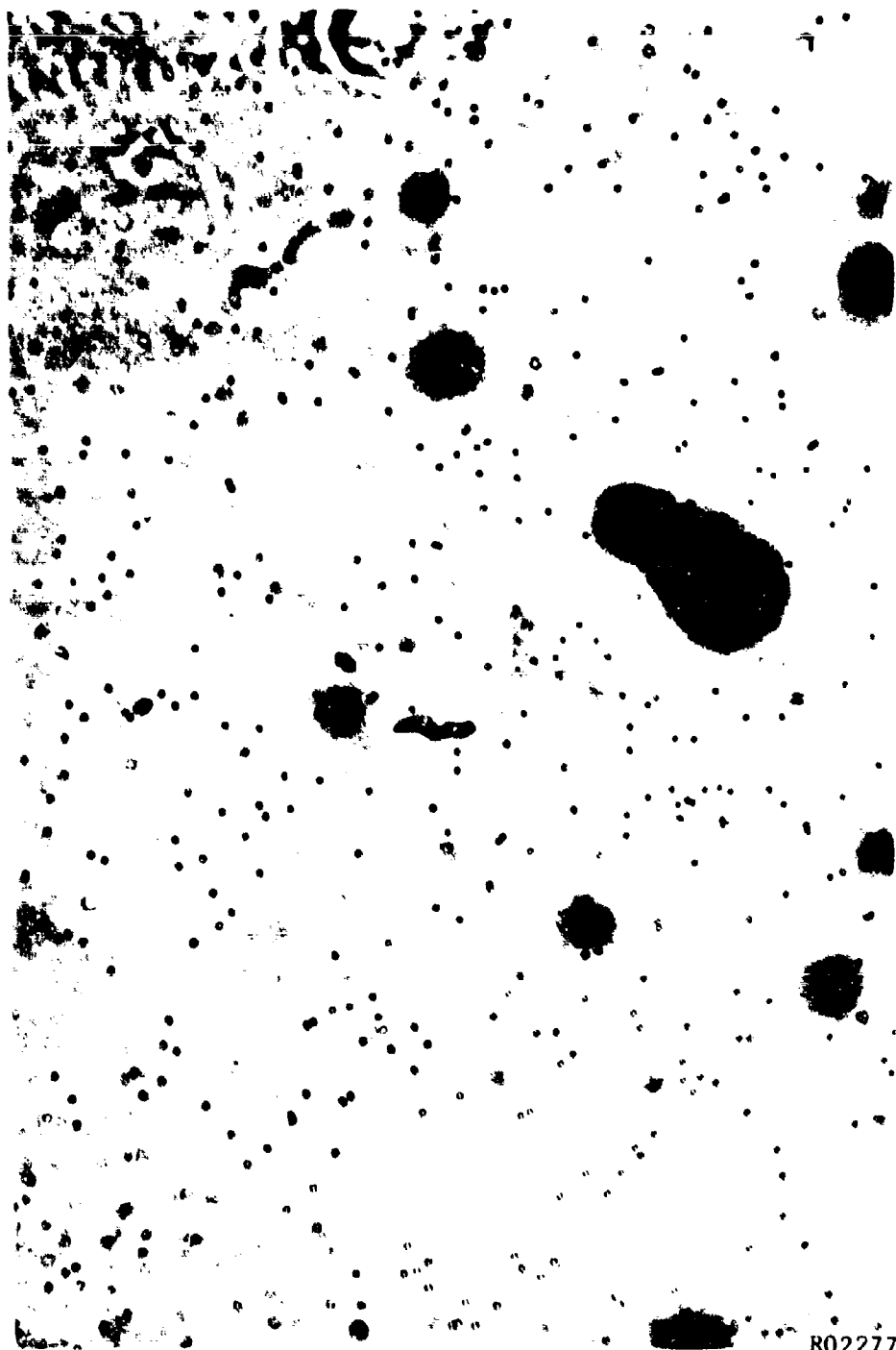


FIGURE 2-8. 1.3 MICRON POLYSTYRENE PARTICLES IMPACTED ON TRANSFER TAPE, 500 X MAGNIFICATION. VIEW REPRESENTS 0.012 SQUARE INCHES ON 100-INCH ROCKET MOTOR WALL

chamber, twelve Spraying Systems Company No. 1A pneumatic atomizing nozzles were used. In the beginning, the particles were mixed with water, but inspection of the collection tapes indicated that not all of the water was evaporating. This problem was solved by using methyl alcohol instead of water for the mixing fluid in order to increase the evaporation rate.

To indicate whether or not the spray nozzles were spraying excessively large drops, or were wetting the chamber walls, a run was made using dye in the alcohol. Blotters were attached to the inside of the spray chamber. No large dye drops were found, indicating the spray was very fine, and no appreciable wall splashing was indicated. It was interesting to note that the dye gave a good visual picture of particle impingement on the nozzle aft closure and indicated clearly the point of separation in the exit cone.

In order to have no particle agglomerates in the gas, it was first necessary to assure that no agglomerates existed in the alcohol-particle mixture. It was found that by placing the alcohol-particle mixture in an ultra-sonic vibrator directly before each run, the particles in the mixture would be deagglomerated. The mixture of alcohol and latex was proportioned so that there would be only one particle per drop of atomized liquid assuming an average drop size of twenty microns. Examination of the tapes then indicated no appreciable agglomeration.

At first, the number of particles in each run was determined by weighing the particle latex for that one run and then mixing it with the alcohol. It became apparent that small errors in the weight of the sample could cause rather large errors in the number of particles. Therefore, it was necessary to mix a large quantity of particle latex with the alcohol and then divide the alcohol-particle mixture into smaller samples. In this manner, small errors in measurement made negligible errors in the number of particles.

Obtaining an even particle distribution in the grain port required that the particles be thoroughly mixed in the modeling gas and then having a flow path which would not cause particle-gas separation ahead of the grain port model.

At first, the particle concentration was very high near the grain port wall. Three changes were then made in the test facility to correct this. The first change was to put baffle plates (Figure 2-2) over the two gas inlets near the pneumatic spray nozzles. The baffle plate divided the main gas inlet stream into six streams, one surrounding each spray nozzle. The second improvement was to turn the center gas inlet toward the rear as shown in Figure 2-1. When the inlet was toward the test nozzle, it frequently produced a core of particle-free gas. The third improvement was to put a baffled, tubular insert into the entrance to the modeling chamber, also shown in Figure 2-1. This device was designed to break up any boundary layer particle concentrations developed in the 6-inch pipe approaching the test section. These three improvements resulted in a very even particle concentration across the grain port flow.

Two grain port wall configurations were tried before the above improvements were made. One was a solid wall tube and the other was a perforated wall which was intended to simulate more closely the flow from a burning grain. After an even concentration distribution was found in the solid wall grain port, it was chosen for testing. Furthermore, it was much easier to check the distribution across this type of grain.

For the first tests little attention was paid to the grain port nozzle intersection. It soon became apparent that this intersection had to be a leak-free precision fit to avoid secondary flow disturbances which would upset particle impingement. A leak-free seal was obtained by placing the grain in the nozzle and then pouring in a polymerizing liquid rubber behind the grain port.

Various attempts were made to ease the job of counting the particles. Initially, the particles were photographed by use of a microscope, and the particles counted on the photograph. However, this left too much room for error since a particle slightly out of focus would look like a blotch on the tape. Also, a speck of dirt out of focus would look like a particle. For accurate counting, the plane of focus had to be changed while counting which meant the particles had to be counted by eye directly with a microscope. The microscope used had a 43X objective with 10X eye pieces. A grid in one eye piece was used to give a constant known counting area.

## 2.6 PARTICLE IMPINGEMENT CALIBRATION TESTS

To monitor particle flow through the grain port for uniformity, impingement samples were obtained along 1/4-inch diameter bars placed perpendicular to the flow, Figure 2-9. This data also lent itself to a comparison of particle size and velocity effects on impingement.

Figure 2-10 shows data obtained from the vertical and short horizontal bars in the largest diameter grain port used (7.8 inches), which gives the most severe test for a uniform particle concentration across the port.

Table 2.3 shows conditions for five of the runs which used the calibration bars. The actual data taken from these bars are shown in Figures 2-11 through 2-15. For all five runs, the total number of particles in each run was 10 billion. Therefore, when Runs 041575 and 041576 are compared to the other three runs, the difference in particle flux due to different grain ports must be considered.

By comparing Run 040971 to 041678 and Run 041575 to 041576, the effect of particle size can be seen on impingement at the stagnation point on the bar at the same velocity. This shows that impingement is proportional to the third power of the particle diameter. The velocity effects on impingement can be seen by comparing runs at different velocity with the particle size constant. By comparing Run 041574 to 041678 and Run 041574 to 041575, it will be seen that impingement is approximately proportional to the first power of the velocity.



FIGURE 2-9. GRAIN PORT MODEL (LOOKING UPSTREAM FROM NOZZLE)

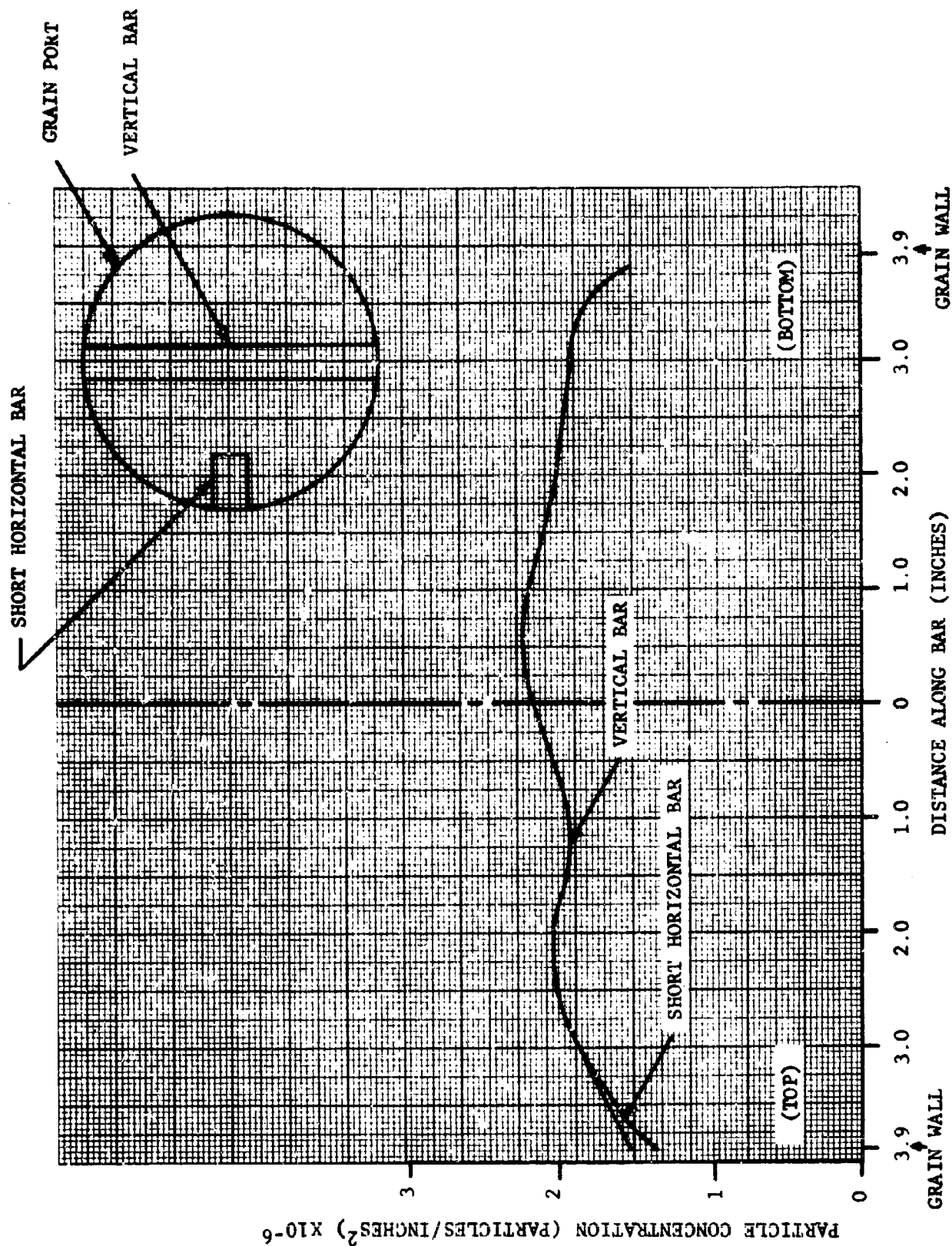


FIGURE 2-10. TYPICAL PARTICLE CONCENTRATION DISTRIBUTION IN GRAIN

R07277

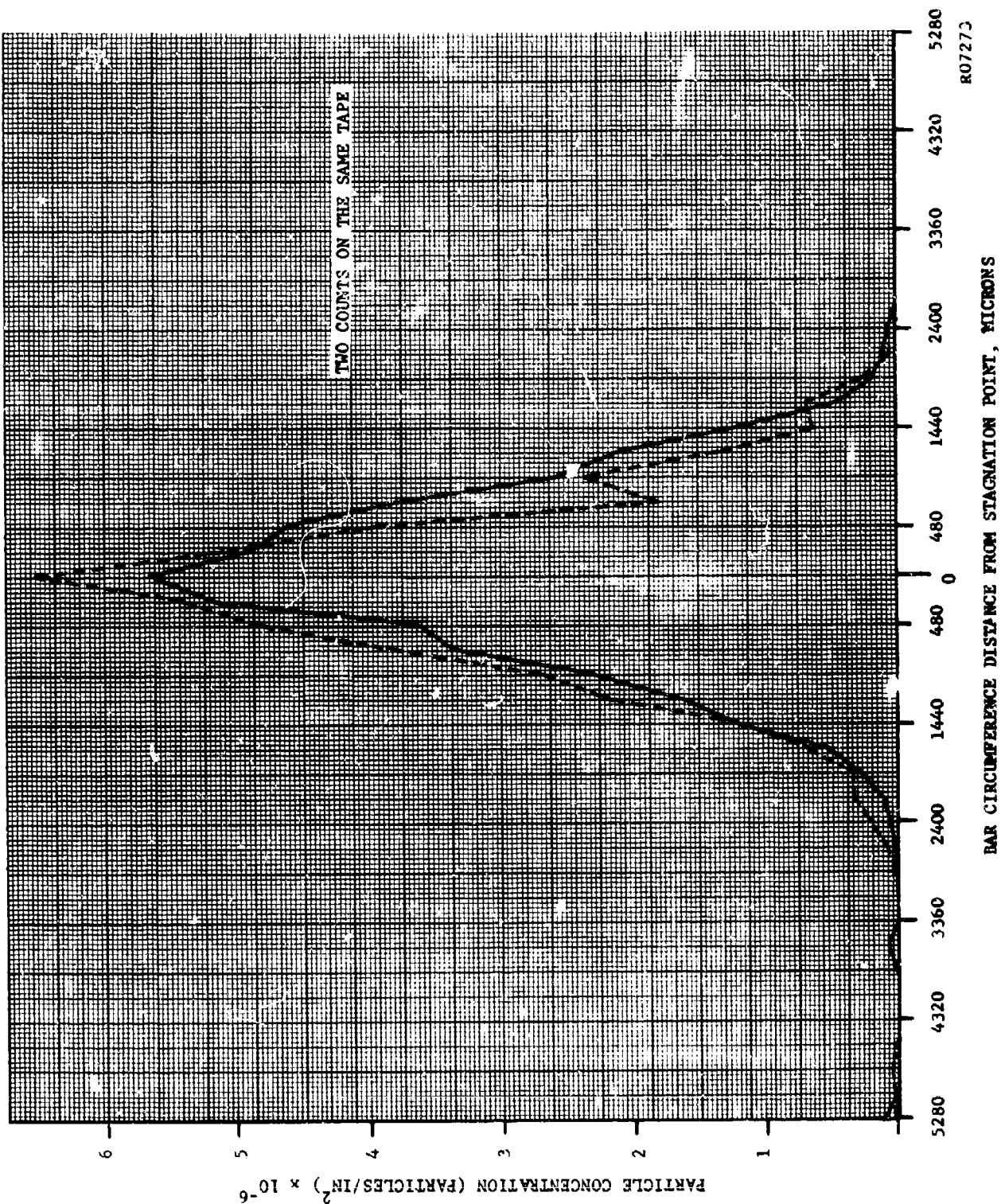


FIGURE 2-11. IMPINGEMENT AROUND CALIBRATION BAR FOR RUN 040971

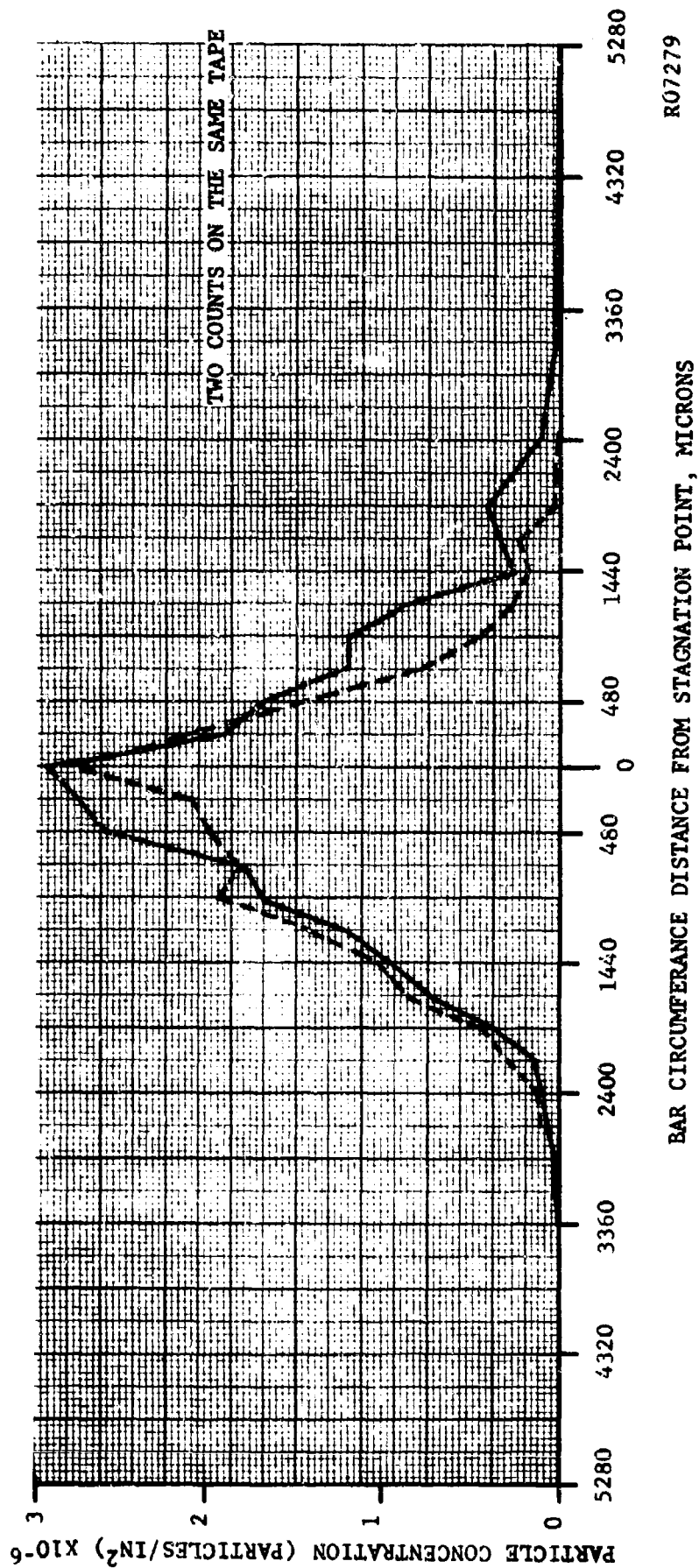


FIGURE 2-12. IMPINGEMENT AROUND CALIBRATION BAR FOR RUN 041574

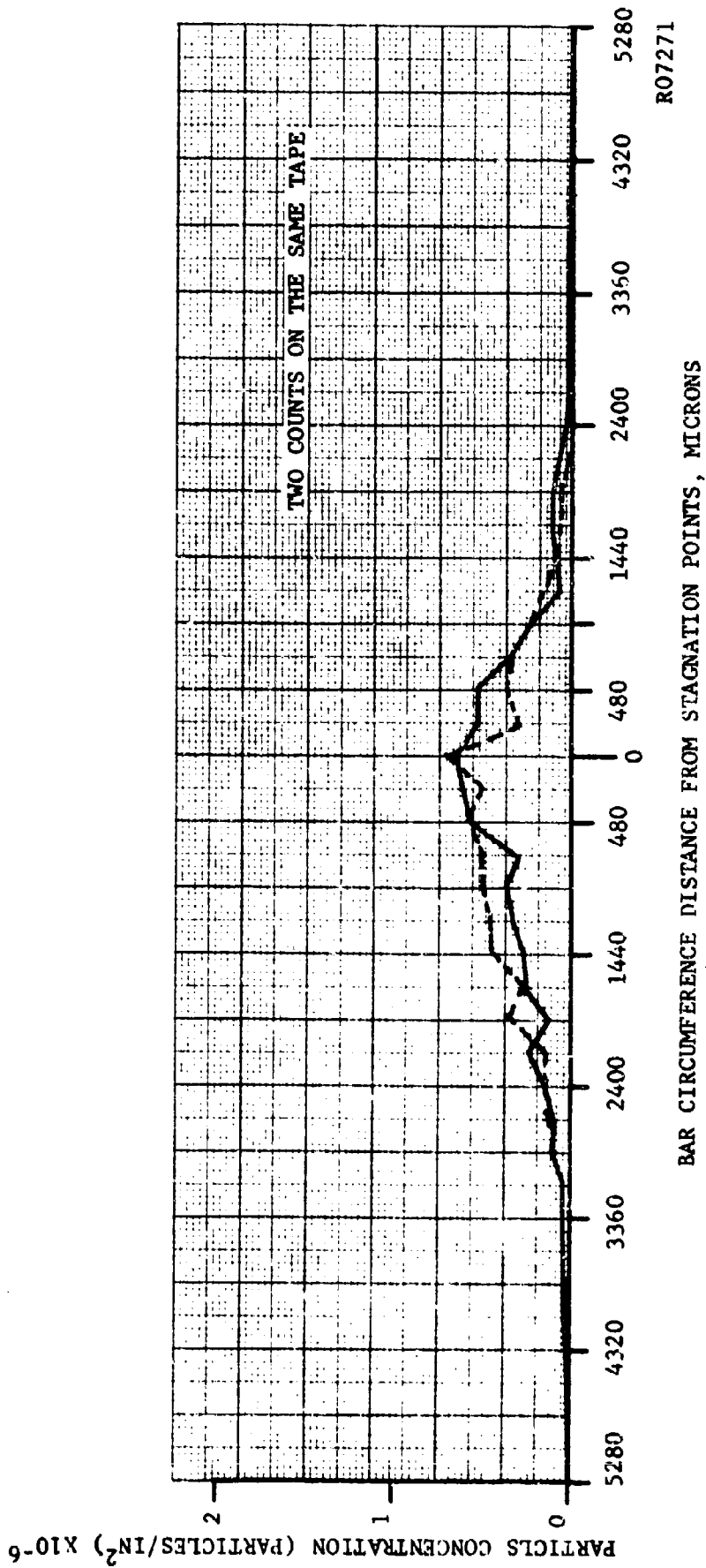


FIGURE 2-13. IMPINGEMENT AROUND CALIBRATION BAR FOR RUN 041575



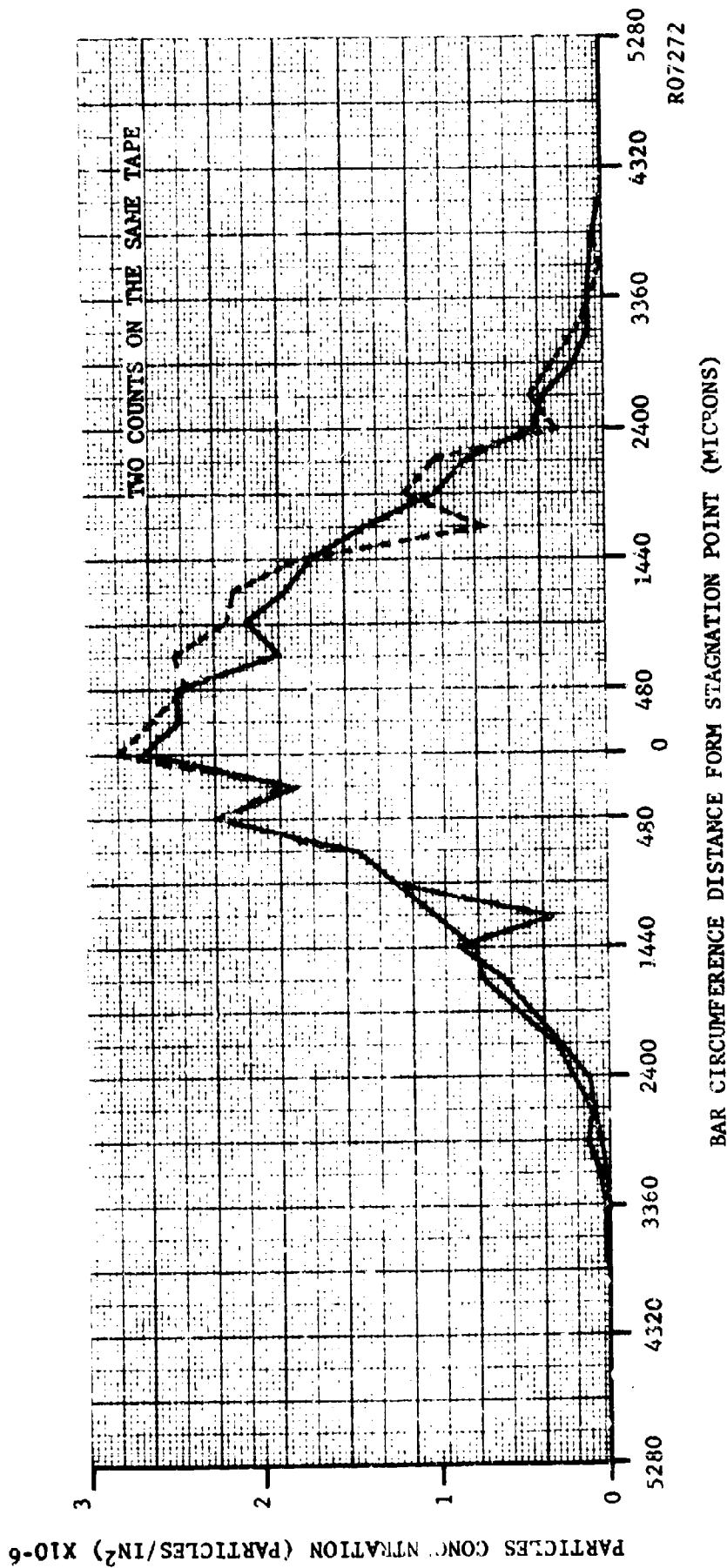


FIGURE 2-14. IMPINGEMENT AROUND CALIBRATION BAR FOR RUN 041576

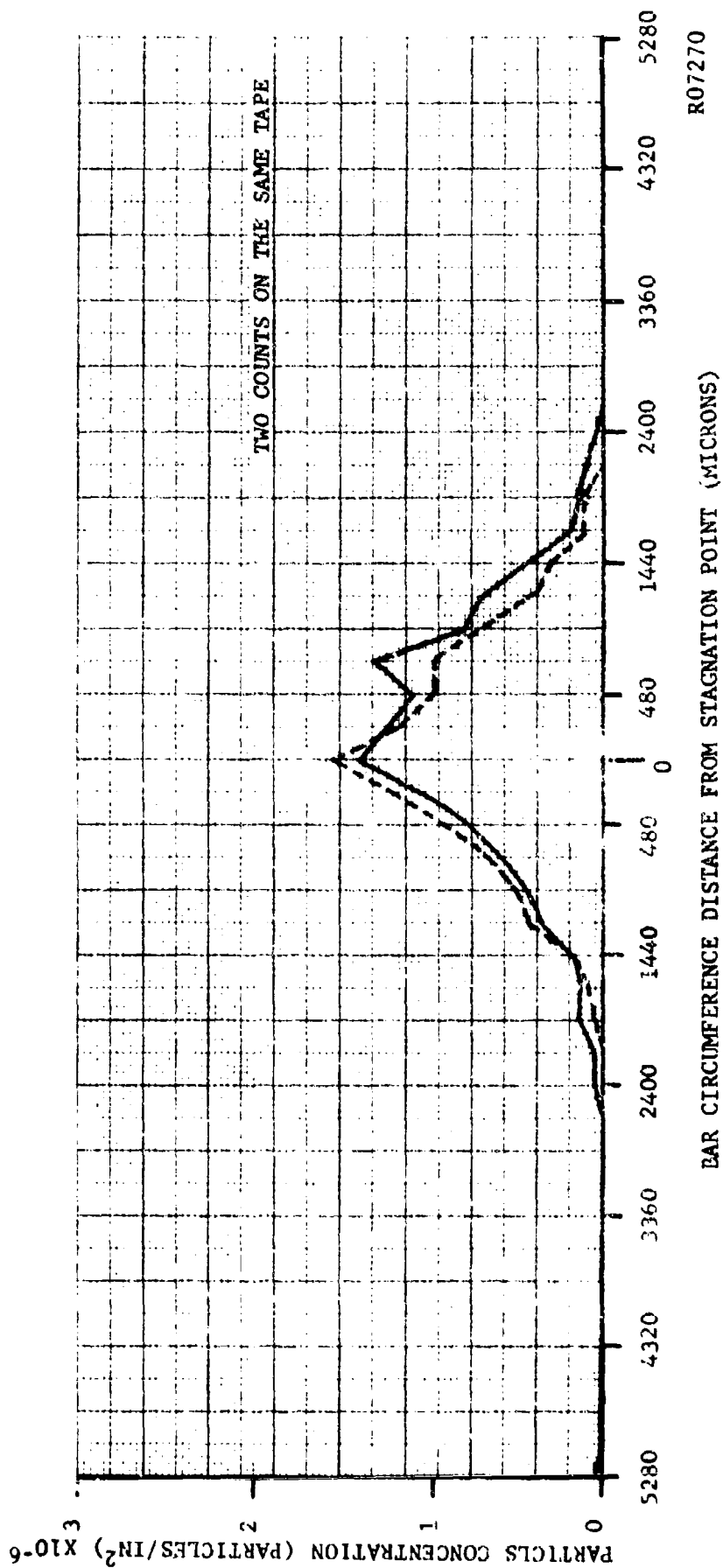


FIGURE 2-15. IMPINGEMENT AROUND CALIBRATION EAR FOR RUN 041678

TABLE 2.3

## CONDITION OF RUNS WITH CALIBRATION BARS

<u>Run No.</u>	<u>Polystyrene Particle Size</u>	<u>Grain Port Size Dia., in.</u>	<u>Grain Port Velocity, ft/sec.</u>	<u>Impingement at Stagnation Point</u>
040971	2.05 $\mu$	5.2	165	160
041574	1.3 $\mu$	5.2	258	75
041575	1.3 $\mu$	7.8	113	18
041576	2.05 $\mu$	7.8	113	75
041678	1.3 $\mu$	5.2	165	40

## 2.7 PARTICLE IMPINGEMENT TESTS

Particle impingement studies were made on four nozzles: (1) a model of the nozzle used in hot firing studies of particle impingement, (2) a gimballed nozzle (straight), (3) a gimballed nozzle (canted 5 degrees) and (4) a model of the aft closure of the Aerojet-General 100 FW2 engine.

As mentioned earlier, both nitrogen and sulfur hexafluoride ( $\text{SF}_6$ ) were used as the modeling gas. A summary of  $\text{N}_2$  and  $\text{SF}_6$  properties is shown in Table 2.4.

TABLE 2.4

SUMMARY OF  $\text{N}_2$  AND  $\text{SF}_6$  PROPERTIES

<u>Gas</u>	<u><math>\text{N}_2</math></u>	<u><math>\text{SF}_6</math></u>
Temperature ( $T_M$ ) <sup>o</sup> R	480	500
$\gamma$	1.4	1.1
Molecular Weight	28	146
Viscosity ( $\mu_M$ ) lb/ft sec	$1.2 \times 10^{-5}$	$1.01 \times 10^{-5}$

### 2.7.1 SIMULATOR NOZZLE

The simulator nozzle (Figure 2-16) was a full scale model of the nozzle used in the hot firing part of this program. All impingement found on this nozzle was negligible when  $3\ \mu$  particles were modeled. This indicated that large agglomerated particles must have been produced in the hot firing to produce the impingement indicated in those tests.

### 2.7.2 GIMBALLED NOZZLE

In the gimballed nozzle (Figure 2-17), there was no impingement in the gimbaling section of the nozzle in either the straight or canted 5 degree position. Therefore, a full impingement study was made only on the entrance section of the straight nozzle.

It was questioned whether or not the absence of impingement in the gimbaling section was due to no particles impinging on the tapes or the velocity was too high and the particles bounced off the tape. A 90 degree wedge and a bar were placed in the exit cone (Figure 2-18) of the gimballed nozzle to check whether or not any particles could be picked up in the supersonic region. Two runs were made, one with sulfur hexafluoride and one with nitrogen as the modeling gas. A high concentration of particles were found on the wedge and bar for the sulfur hexafluoride run, but none was found for the nitrogen run. Since the molecular weight of sulfur hexafluoride is larger than nitrogen, the sonic velocity would have been lower and thus the velocity at the wedge smaller. This indicates that the higher velocity particles in the nitrogen flow may not have been picked up. On the other hand, impingement was also negligible on the gimbaling part when sulfur hexafluoride was used. (One explanation of the difference in impingement on the shapes in the exit cone with the two gases is that the differences are a function of the differences in shock lines produced and their effect on the particles.)

The gimballed nozzle which was modeled had a 63-inch diameter chamber with a 15-inch gimballed throat. It was assumed that the rocket had a total burn time of 90 seconds, a burn rate of 500 lb/sec., and an alumina loading of 32 percent. Since for subsonic flow the impingement is nearly the same when nitrogen and sulfur hexafluoride is the modeling gas, nitrogen was used for the study.

From the modeling equations (Equations 2.31 and 2.32), the particle diameter ratio and model pressure can be determined for the case of nitrogen as the modeling gas and Dow polystyrene spheres as the particles. Since the model chamber is 11 inches in diameter, a scale factor of  $D_R/D_M = 5.73$  is dictated. The other values needed to solve Equations (2.31) and (2.32) are:

$$\rho_{P_R} = 2.28\ \text{gm/cm}^3$$

$$T_R = 6360^\circ\text{R}$$

$$\rho_{P_M} = 1.05\ \text{gm/cm}^3$$

$$T_M = 480^\circ\text{R}$$

$$a_R^* = 4100 \text{ fps}$$

$$MW_R = 20.4$$

$$a_M^* = 992 \text{ fps}$$

$$MW_M = 28$$

$$\mu_R = 6.7 \times 10^{-5} \text{ lb/ft sec.}$$

$$\gamma_R = 1.18$$

$$\mu_M = 1.06 \times 10^{-5} \text{ lb/ft sec.}$$

$$\gamma_M = 1.4$$

$$P_R = 613 \text{ psia}$$

Therefore, from the modeling equations, the particle diameter ratio and the model chamber pressure are

$$\frac{D_{P_M}}{D_{P_R}} = \left[ \frac{1}{5.73} \times \frac{2.28}{1.05} \times \frac{4100}{992} \times \frac{1.06 \times 10^{-5}}{6.7 \times 10^{-5}} \right]^{1/2} = 0.496 \quad (2.33)$$

and

$$P_M = \frac{1}{0.496} \times \frac{1.06 \times 10^{-5}}{6.7 \times 10^{-5}} \times \left[ \frac{480}{6360} \times \frac{20.4}{28} \times \frac{1.18}{1.4} \right]^{1/2} \times 613 \text{ psia} = 42 \text{ psia} \quad (2.34)$$

In Equation (2.32),  $\rho_{P_R}$  and  $D_{P_R}$  correspond to the conditions in the rocket at 6360°R, and when a certain particle diameter is being modeled, it refers to the diameter of the particle at room temperature (530°R). For example, if a 2μ diameter particle is being modeled, the diameter of the particle in the model must be determined with the knowledge that the hot particle in the rocket is actually larger than 2μ. The hot diameter can be determined by conserving mass.

Mass of hot particles = mass of cold particle

$$\left( \frac{4}{3} \pi \frac{D_P^3}{8} \rho_P \right)_{\text{hot}} = \left( \frac{4}{3} \pi \frac{D_P^3}{8} \rho_P \right)_{\text{cold}} \quad (2.35)$$

or

$$\left( D_P^3 \right)_{\text{hot}} (2.28) = (2)^3 (3.7) \quad \left( D_P \right)_{\text{hot}} = 2.35\mu$$



FIGURE 2-16. SIMULATOR MODEL

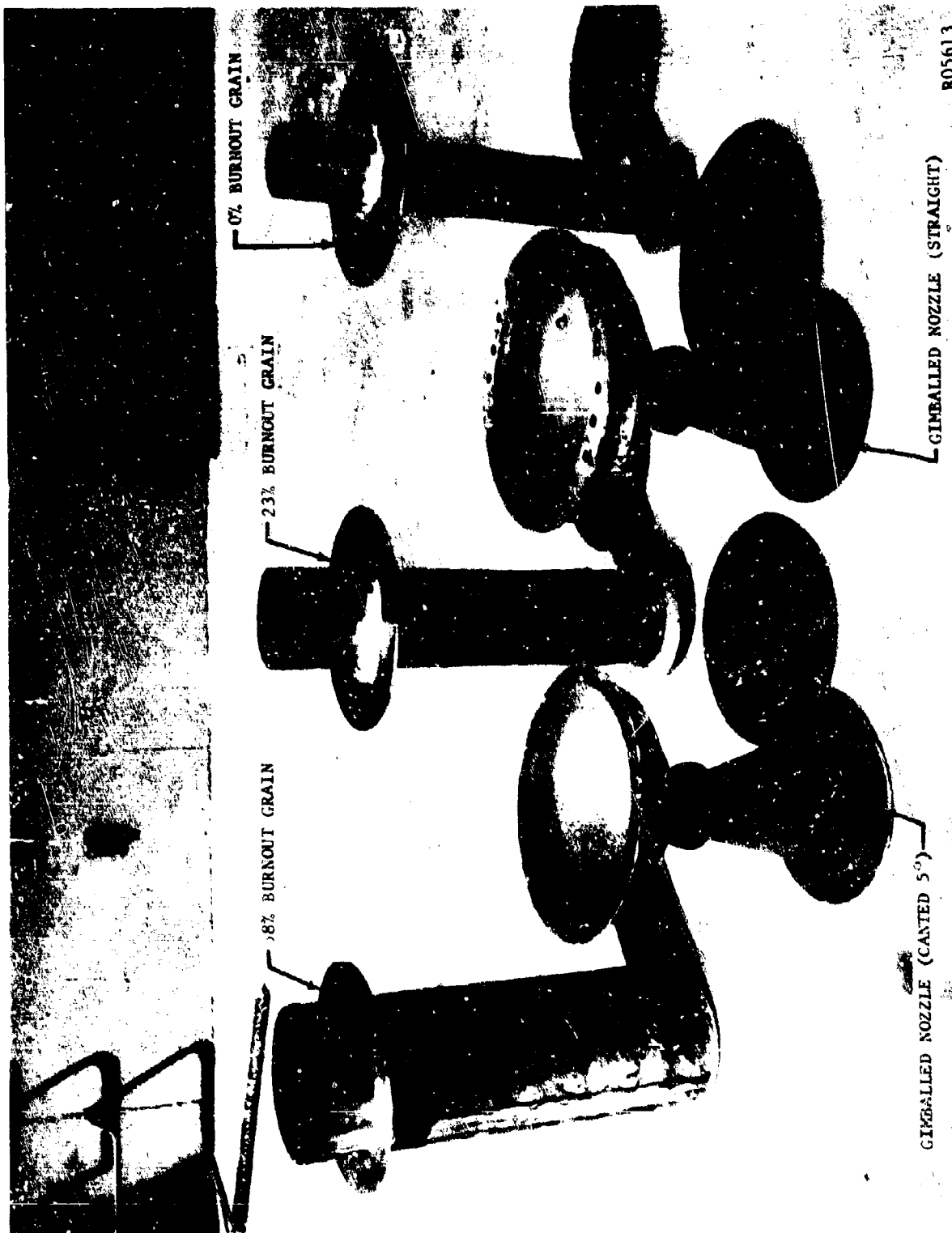


FIGURE 2-17. GIMBALED NOZZLES AND GRAIN MODELS

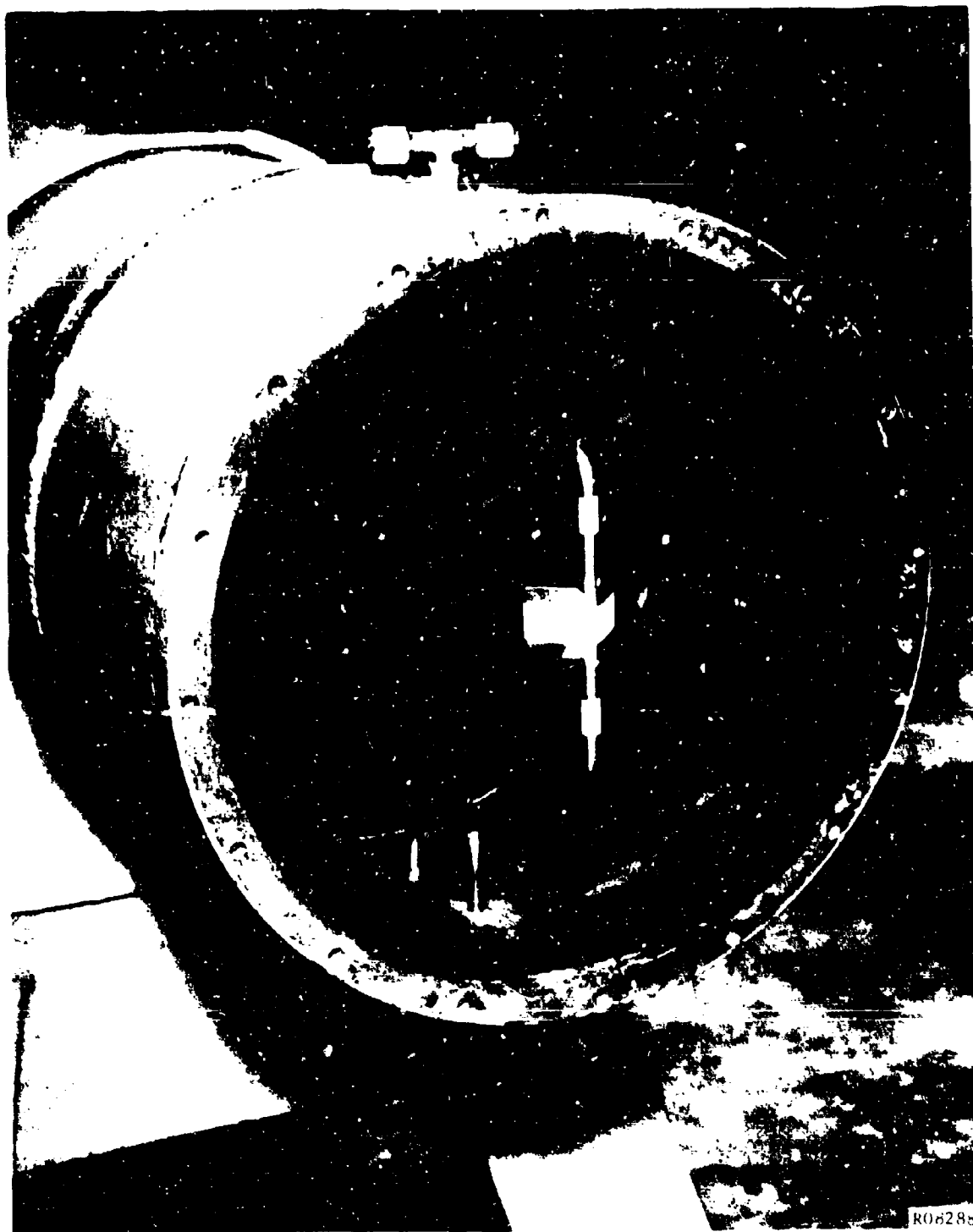


FIGURE 2-18. PARTICLE IMPINGEMENT TAPES ON WEDGE AND BAR FOR SUPERSONIC REGION OF NOZZLE



Therefore, to model a cold  $2\mu$  diameter particle with a density of  $3.7 \text{ gm/cm}^3$ ,  $\rho_{P_R}$  and  $D_{P_R}$  must be  $2.28 \text{ gm/cm}^3$  and  $2.35\mu$ , respectively.

The density for aluminum oxide at  $6360^\circ\text{R}$  was taken by extrapolating the data of Kirshenbaum and Cahill.<sup>2,3</sup>

For the three sizes of polystyrene particles used, Table 2.5 shows the sizes of aluminum oxide particles being modeled.

TABLE 2.5

MODELED PARTICLE SIZES FOR GIMBALLED NOZZLE

<u>Polystyrene Particle Dia.</u>	<u>Hot Aluminum Oxide Particle Dia. in Rocket</u>	<u>Cold Aluminum Oxide Particle Dia. from Rocket</u>
0.8 $\mu$	1.6 $\mu$	1.4 $\mu$
1.3 $\mu$	2.6 $\mu$	2.2 $\mu$
2.05 $\mu$	4.1 $\mu$	3.5 $\mu$

As shown in Figure 2-19, three grain port sizes representing three different instants in burn-time (0, 23, and 58 percent of burn-out) were needed to show the variation of impingement with time. Since three grains and three particle sizes were used, nine runs were made to develop the overall impingement picture.

Figures 2-20, 2-21, and 2-22, present the impingement data of the  $1.4\mu$ ,  $2.2\mu$ , and  $3.5\mu$  particles, respectively. The ordinate is expressed as the weight percent of that particular particle size, at that particular instant of time, impinging on the aft closure. Each data point represents the average of from 6 to 12 counts of impinged particle density in the region of the particular position along the aft closure.

An example is given to illustrate how the particles which are impinged on the tape of the model can be converted to weight percent impinged on the aft closure of the rocket. Assume counting by use of a microscope gives  $N$  particles/sq. in. on the tape at some point along the aft closure. Also, it is known that  $10^{10}$  particles were originally injected into the gas and the scale factor from the model to the rocket is 5.75. Then the weight percent impinged is

$$\frac{N}{10^{10}} \times \frac{1}{(5.75)^2} \times 100.$$

It is also interesting to note how reproducible the data are by comparing one person's particle count with another's and by comparing two tapes from the same run or from duplicate runs. These comparisons, shown in Figure 2-23 indicate reproducibility of the data.

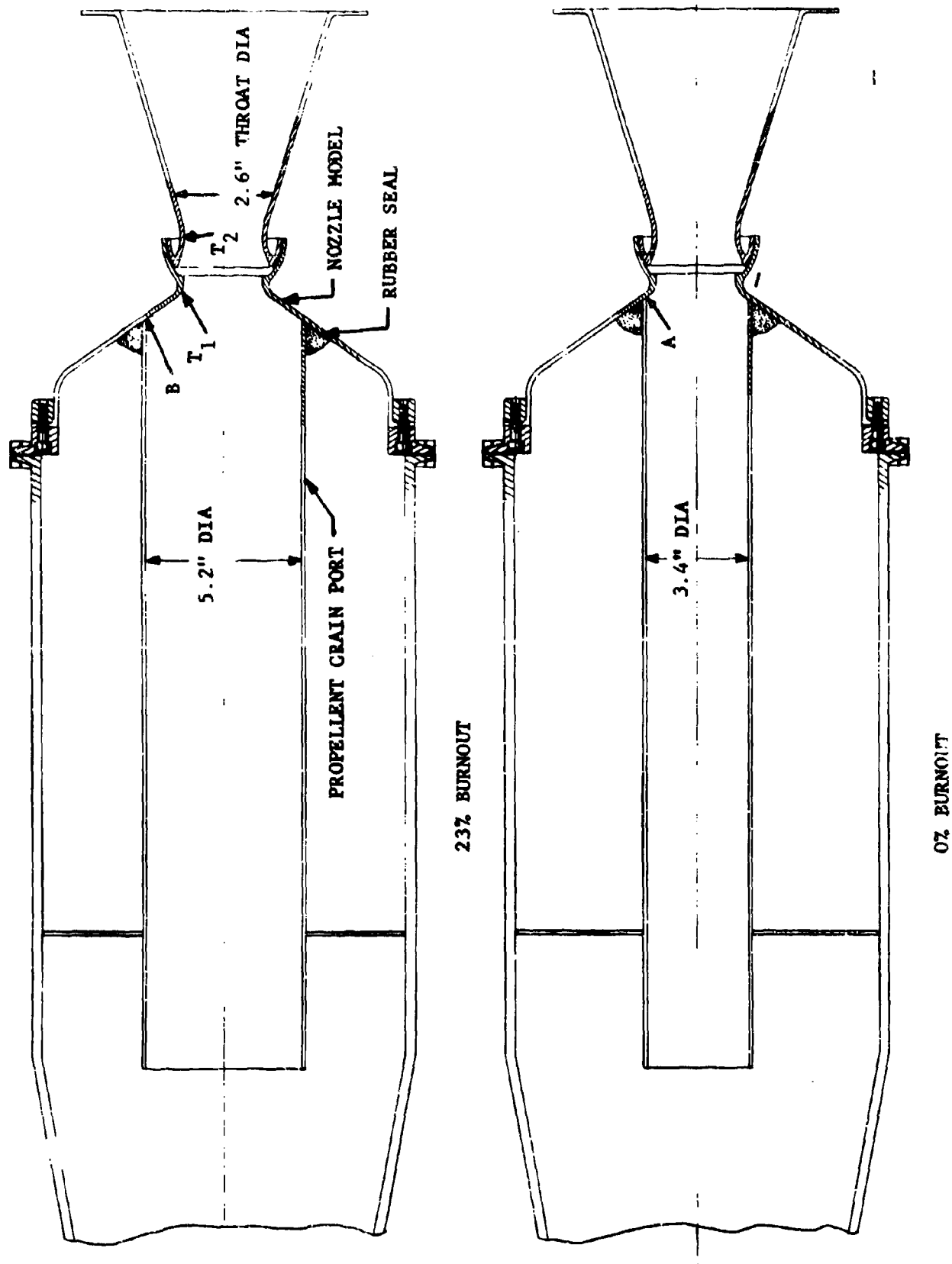
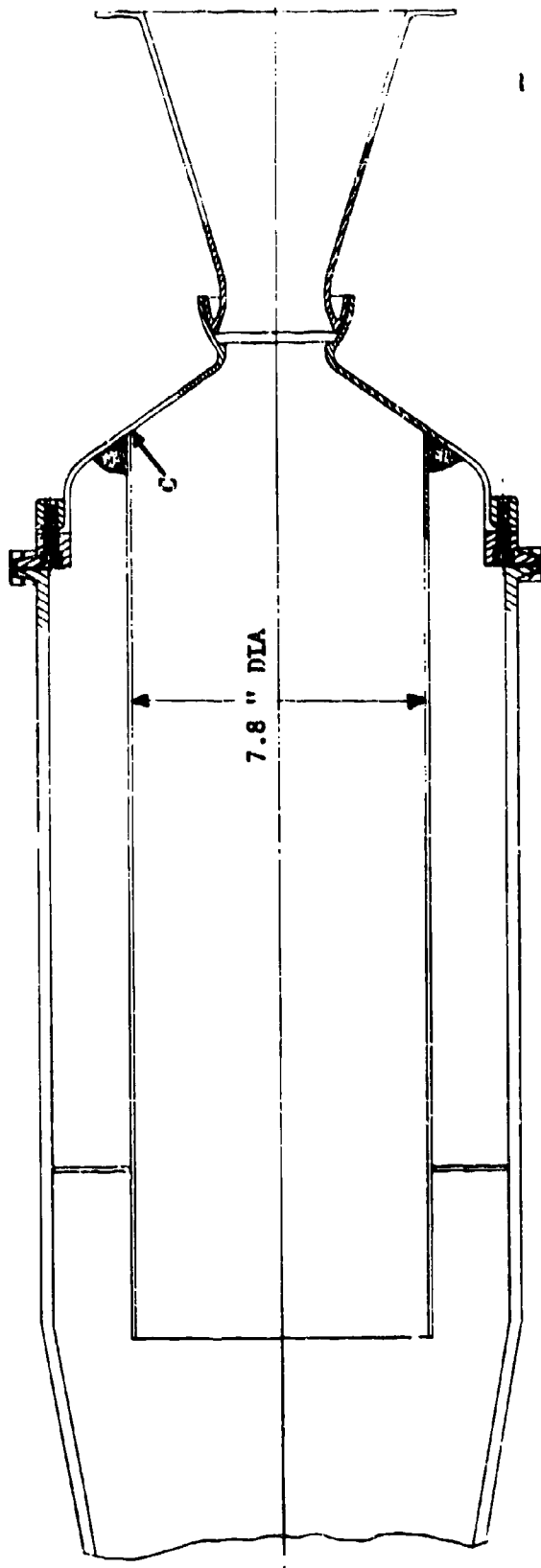


FIGURE 2-19. GIMBALLED NOZZLE COLD FLOW MODELS



58% BURNOUT

FIGURE 2-19. (CONTINUED)

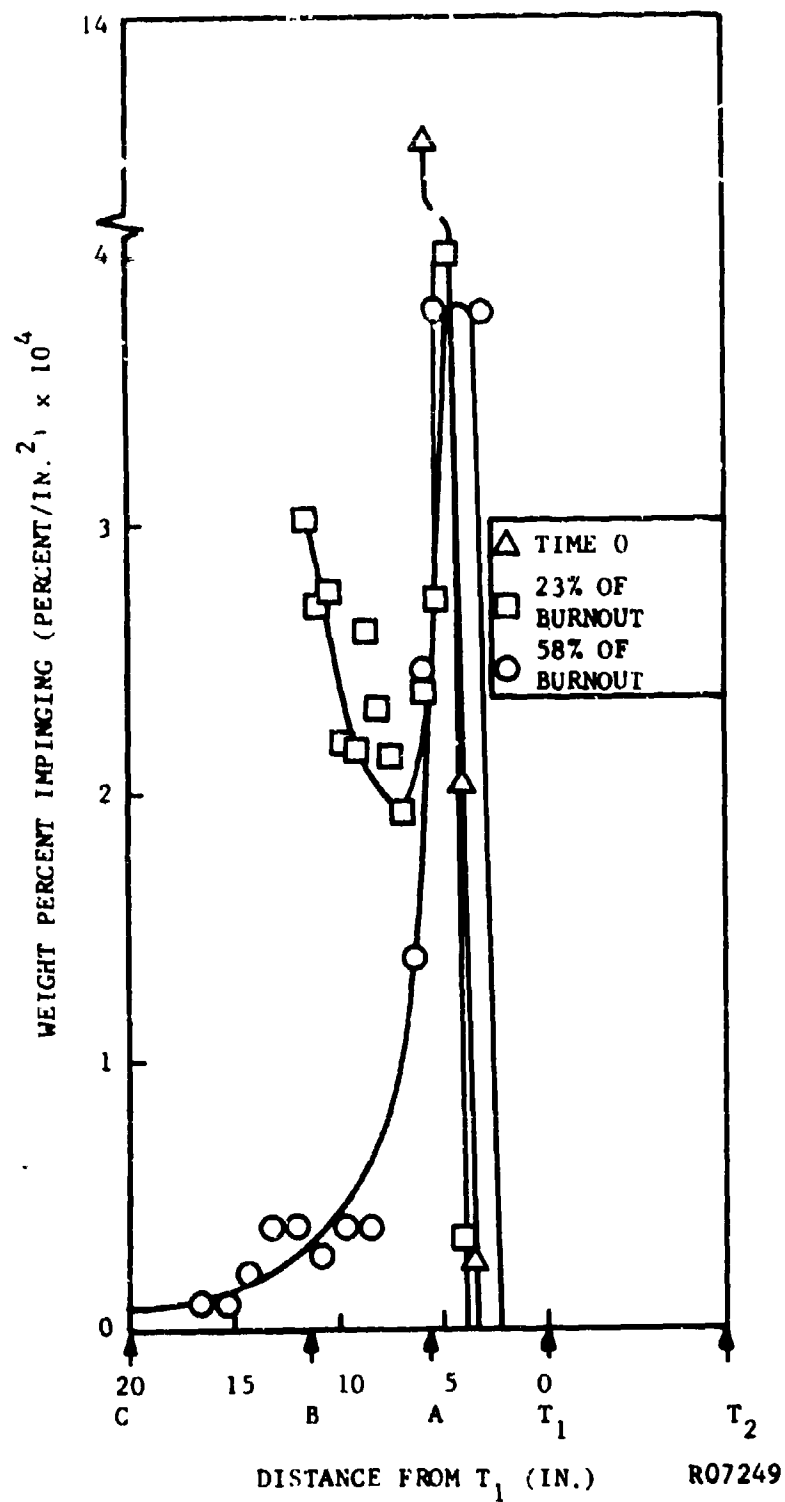


FIGURE 2-20. WEIGHT PERCENT OF 1.4μ PARTICLES IMPINGING ALONG THE AFT CLOSURE

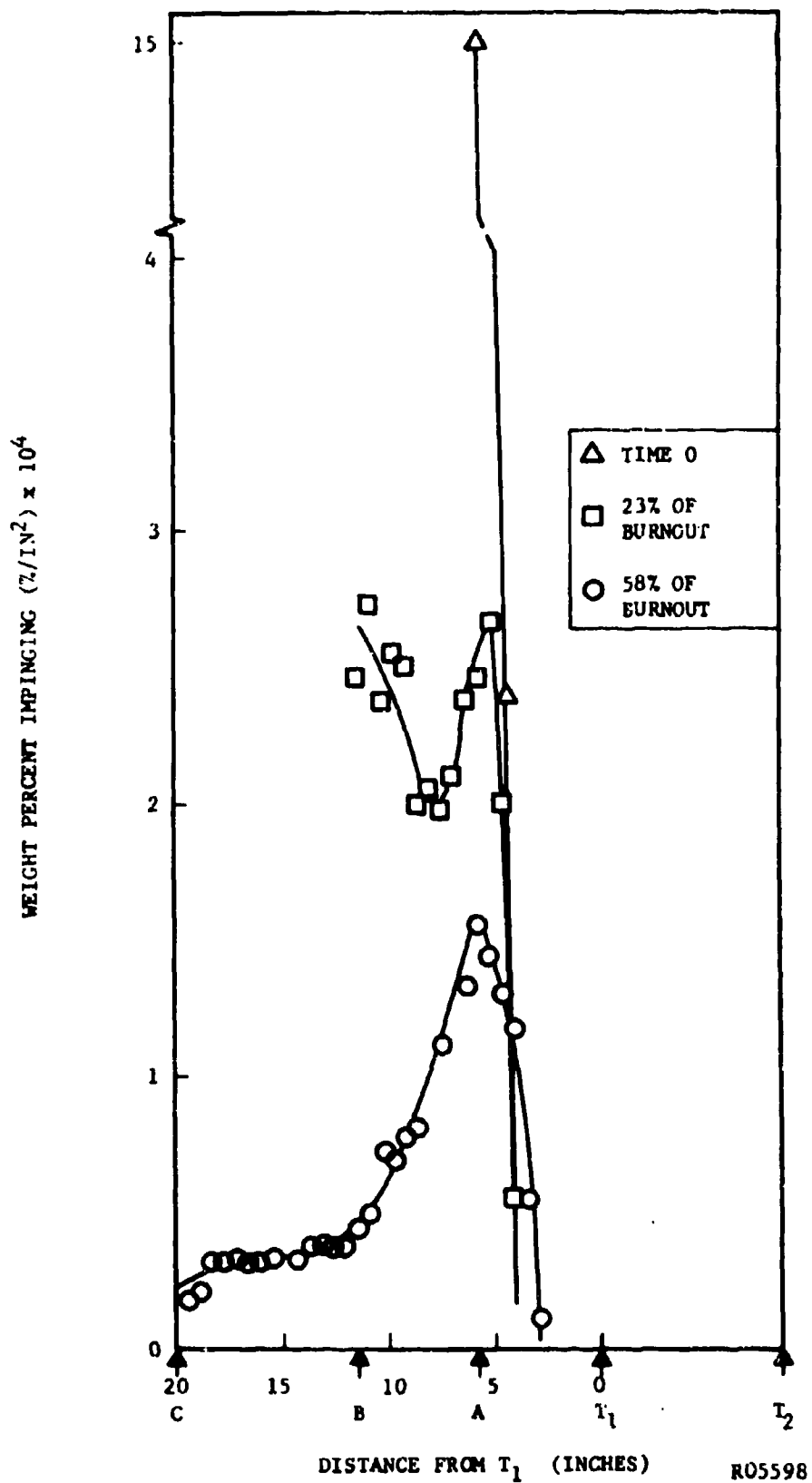


FIGURE 2-21. WEIGHT PERCENT OF  $2.2\mu$  PARTICLES IMPINGING ALONG THE AFT CLOSURE

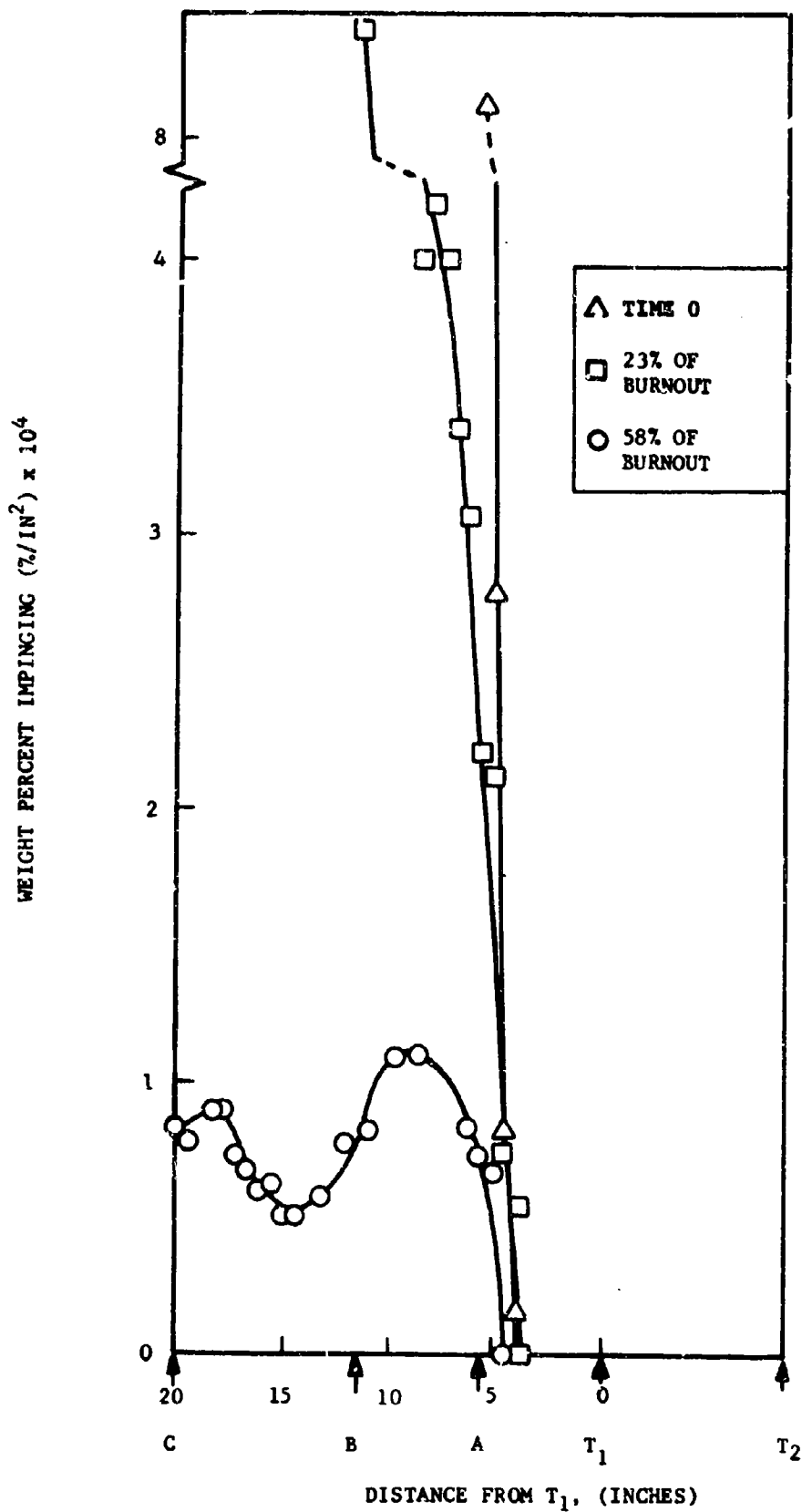


FIGURE 2-22. WEIGHT PERCENT OF  $3.5\mu$  PARTICLES IMPINGING ALONG THE AFT CLOSURE

2-48

R05597

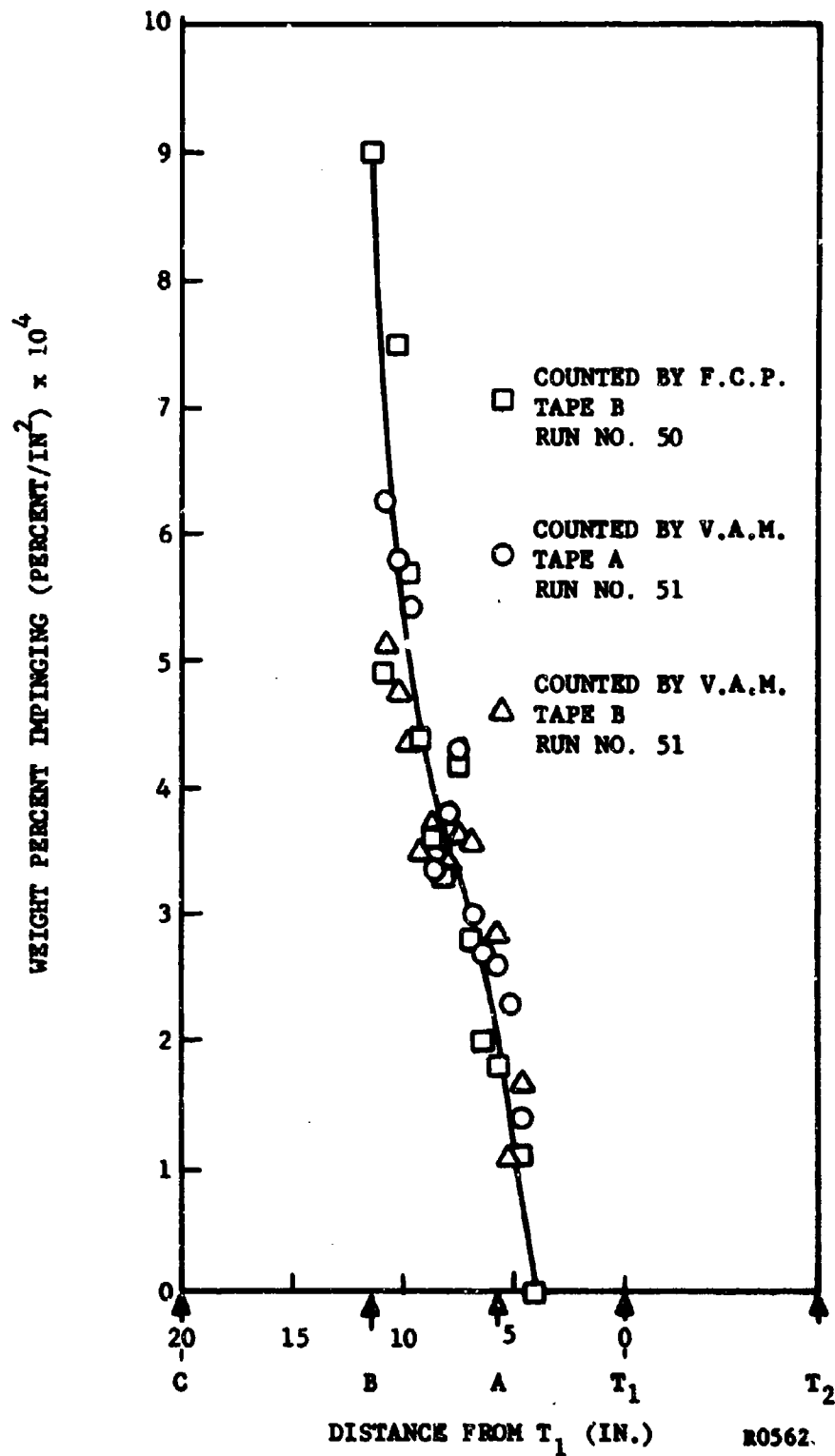


FIGURE 2-23. REPRODUCIBILITY OF IMPINGEMENT DATA

From Figures 2-20, 2-21, and 2-22, it is now possible to develop a curve of impingement versus grain burn-time for each particle size at any point along the aft closure. Figures 2-24, 2-25, and 2-26 present such curves for points A, B, and C, of Figure 2-19, respectively. The ordinates of these curves have been changed to weight fraction impinging per square inch instead of weight percent impinging per square inch as in Figures 2-20, 2-21, and 2-22.

From the curves in Figures 2-24 through 2-26, an average weight fraction impinged can be found from each particle size at points A, B, and C by noting:

$$(100 - t_b) \frac{\delta w_i \{D\}}{\delta w \{D\}} = \int_{t_b}^{100} \frac{\delta w_i \{D\}}{\delta w \{D\}} \{t\} dt \quad (2.36)$$

where D is a particular particle size

$$\frac{\delta w_i \{D\}}{\delta w \{D\}} = \text{average weight fraction impinged per sq. in. for this particle size}$$

$$\frac{\delta w_i \{D\}}{\delta w \{D\}} \{t\} = \text{weight fraction impinged per sq. in. for the same particle size as a function of time}$$

$$t_b = \text{time, percent of burnout when the point on the aft closure is first exposed to particle impingement}$$

$$\text{The integral } \int_{t_b}^{100} \frac{\delta w_i \{D\}}{\delta w \{D\}} \{t\} dt \text{ is the area under the curves of}$$

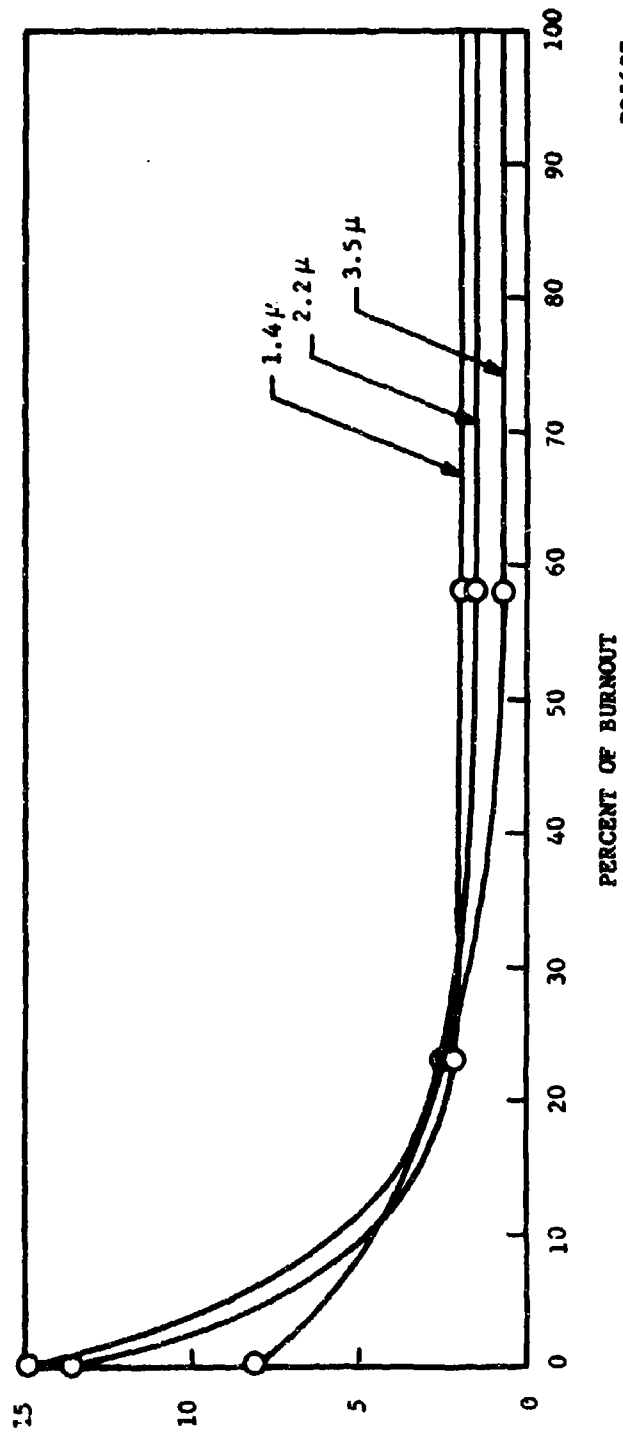
Figures 2-24, 2-25, and 2-26. Table 2.6 is a tabulation of  $\frac{\delta w_i \{D\}}{\delta w \{D\}}$ .

From Table 2.5, it is possible to obtain  $\frac{\delta w_i \{D\}}{\delta w \{D\}}$  as a function of par-

ticle size for points A, B, and C. These curves are shown in Figure 2-27. As will be explained later, the particle size range of interest is from  $0.5\mu$  to  $5.5\mu$ .



WEIGHT FRACTION IMPINGING,  $\frac{\delta w_1 \{D\}}{\delta w_1 \{D\} \{c\} (1/IN^2) 10^6}$



RD 5627

FIGURE 2-24. WEIGHT FRACTION OF 1.4 μ, 2.2 μ, AND 3.5 μ, PARTICLES IMPINGED AT POINT A VS. PERCENT OF BURNOUT

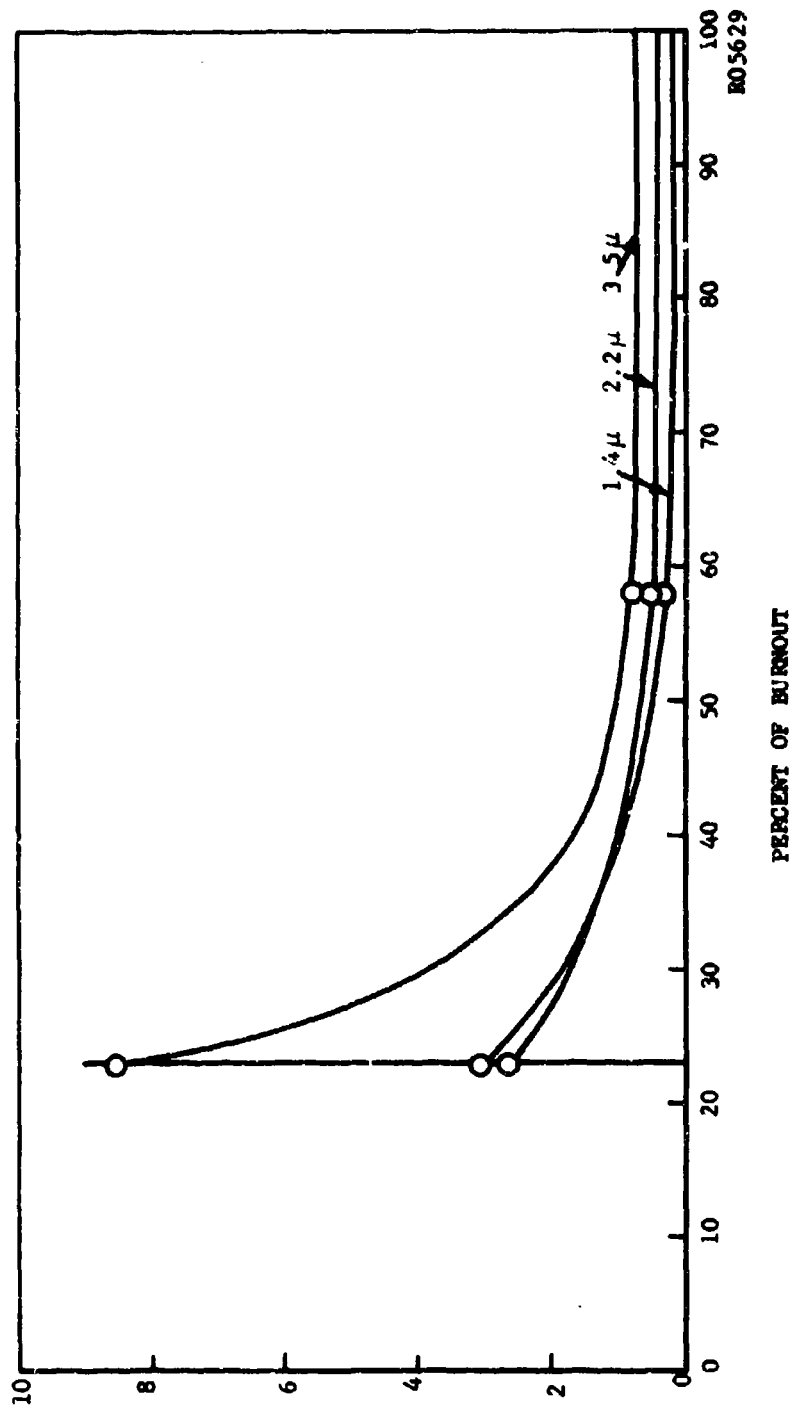


FIGURE 2-25. WEIGHT FRACTION OF 1.4μ, 2.2μ, AND 3.5μ PARTICLES IMPINGING AT POINT B VS. PERCENT OF BURNOUT

805629

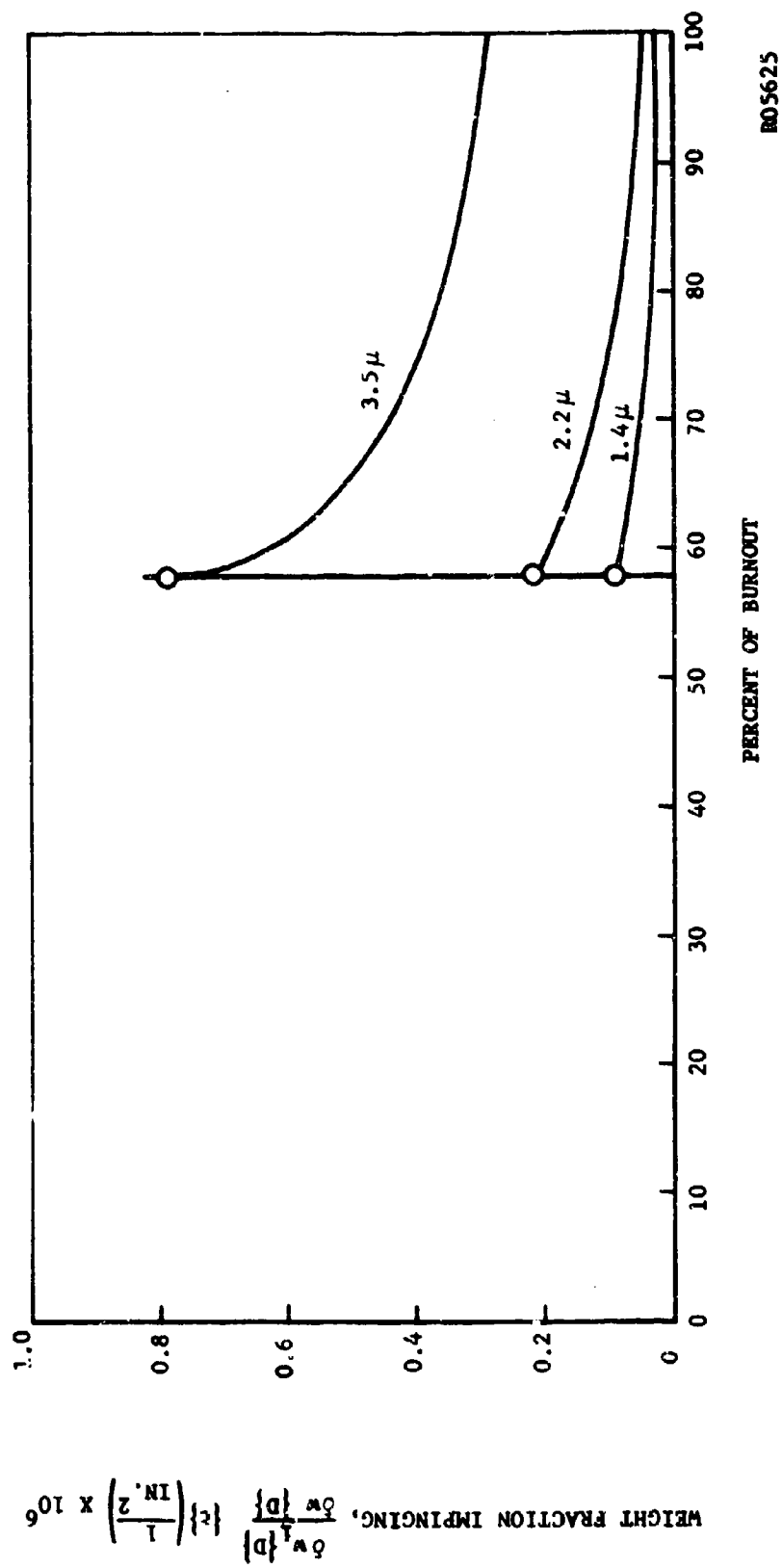


FIGURE 2-26. WEIGHT FRACTION OF 1.4μ, 2.2μ, AND 3.4μ PARTICLES IMPINGING AT POINT C VS. PERCENT OF BURNOUT

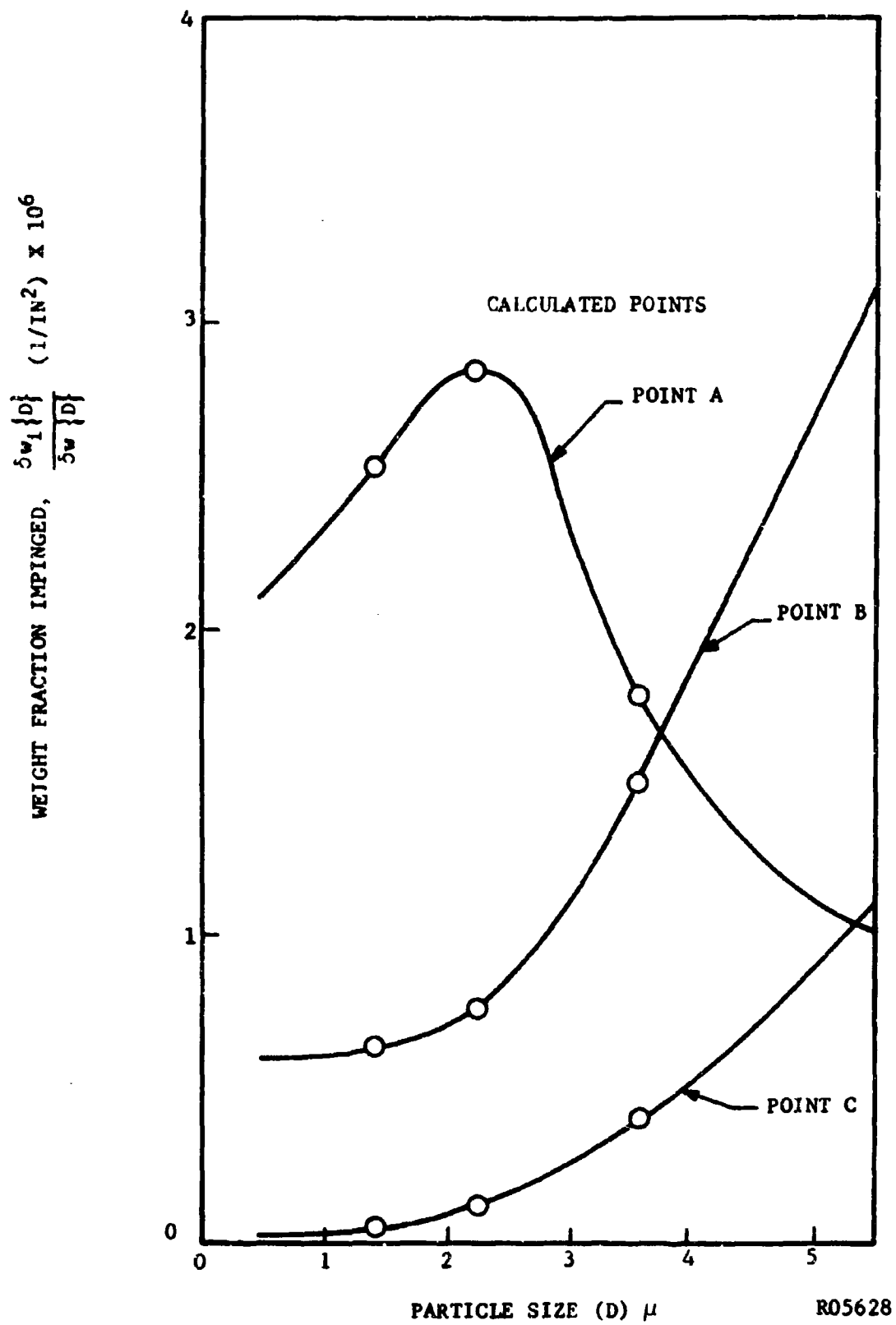


FIGURE 2-27.. AT POINTS A, B, C: ALUMINA WEIGHT FRACTION IMPINGED AS A FUNCTION OF PARTICLE SIZE

TABLE 2.6

TABULATION OF  $\frac{\delta W_1 \langle D \rangle}{\delta W \langle D \rangle}$

Point	$t_b$ (% of Burnout)	D ( $\mu$ )	$\int_{t_b}^{100} \frac{\delta W_1 \langle D \rangle}{\delta W \langle D \rangle} \langle t \rangle dt$ (% of Burnout) $\ln^2$	$\frac{\delta W_1 \langle D \rangle}{\delta W \langle D \rangle} \left( \frac{1}{\ln^2} \right)$
A	0	1.4	254	2.54
A	0	2.2	285	2.85
A	0	3.5	168	1.68
B	23	1.4	49.6	0.65
B	23	2.2	59	0.77
B	23	3.5	115.4	1.5
C	58	1.4	2.1	0.05
C	58	2.2	4.6	0.115
C	58	3.5	16	0.4

The next step is to integrate impingement over the size range of particles found in a rocket. However, to do this the weight fraction of particles as a function of particle size must be known. This function can be obtained by differentiating a curve of Sehgal's<sup>2.4</sup> data for a 500 psi chamber pressure. The differential of his percent total volume below curve is shown in Figure 2-28 with units of the ordinate as  $1/\mu$  since

$$\frac{\delta W \langle D \rangle}{W_T} = \frac{d}{dD} \left( \frac{W \langle D \rangle}{W_T} \right)$$

where  $W_T$  is the total weight of all the alumina particles.

By multiplying the ordinate of the curves in Figure 2-27 with the ordinate of the curve in Figure 2-28 at each particle size and plotting as a function of

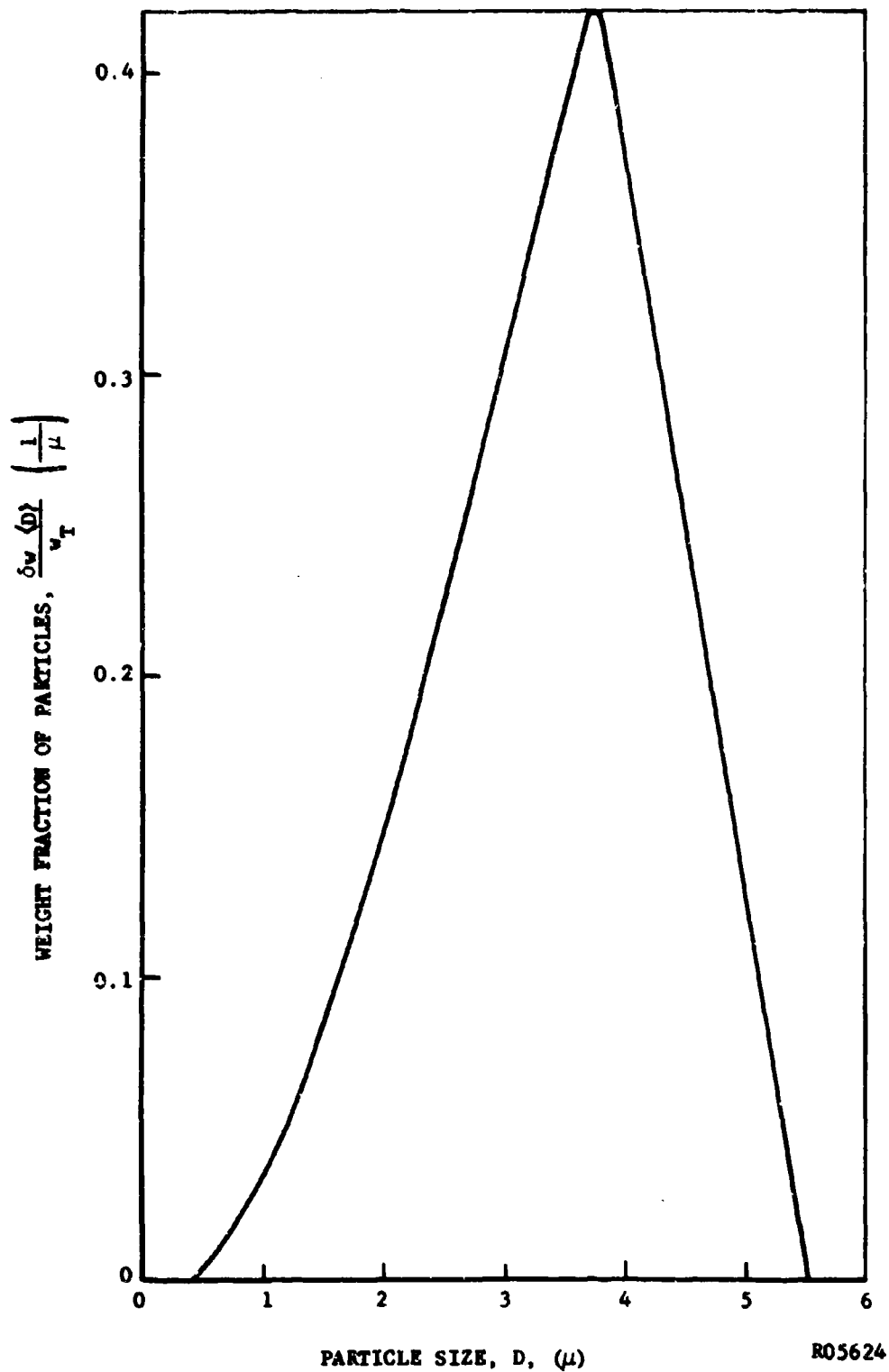


FIGURE 2-28. PARTICLE SIZE DISTRIBUTION OF ALUMINA SAMPLE OBTAINED FROM MOTOR FIRING AT 500-PSI CHAMBER PRESSURE

particle size while still keeping points A, B, and C as parameters, Figure 2-29 is obtained. The ordinate of Figure 2-29 will be  $\frac{\delta W_i \langle D \rangle}{\delta W} \cdot \frac{\delta W \langle D \rangle}{W_T} = \frac{\delta W_i \langle D \rangle}{W_T}$  with units of  $1/\mu \text{ in}^2$ .

For any one of the three points (A, B, C) it is now possible to integrate impingement over the entire particle size range. The area under these curves can be expressed as

$$\int_0^{\infty} \frac{\delta W_i \langle D \rangle}{W_T} dD = \frac{W_i}{W_T}$$

which is the weight fraction of alumina that impinged at any point. For a run time of 90 seconds, a burn rate of 500 lb/sec., and 32 percent of the propellant as alumina, the total impingement in lb/sq. in. can be calculated as a function of position. For example:

$$\begin{aligned} \text{Impingement} &= \frac{W_i}{W_T} \left( \frac{1}{\text{in.}^2} \right) \left( \frac{500 \text{ lb.}}{\text{sec.}} \right) (0.32) (90 \text{ sec.}) \\ &= \frac{W_i}{W_T} (14400) \text{ lb/sq. in.} \end{aligned}$$

This curve for impingement along the nozzle wall integrated for the total firing is shown in Figure 2-30. This is the final result desired from the cold-flow modeling test data.

### 2.7.3 100 FW2

The model of the 100 FW2 consisted only of the aft closure. Therefore, nitrogen was used as the modeling gas. As shown in Figure 2-31, the aft closure was modeled at two burn times, 16 and 54 percent of burnout. Three particle sizes were modeled, making a total of six runs.

Again, from the modeling equations (2.31) and (2.32) the particle diameter ratio and model pressure can be determined. Since the model chamber is 11 inches in diameter, a scale factor of  $\frac{D_R}{D_M} = 9.1$  is dictated. The other values which are input to the equations are as follows:

$$\rho_{P_R} = 2.28 \text{ gm/cm}^3$$

$$T_R = 6360^\circ \text{R}$$

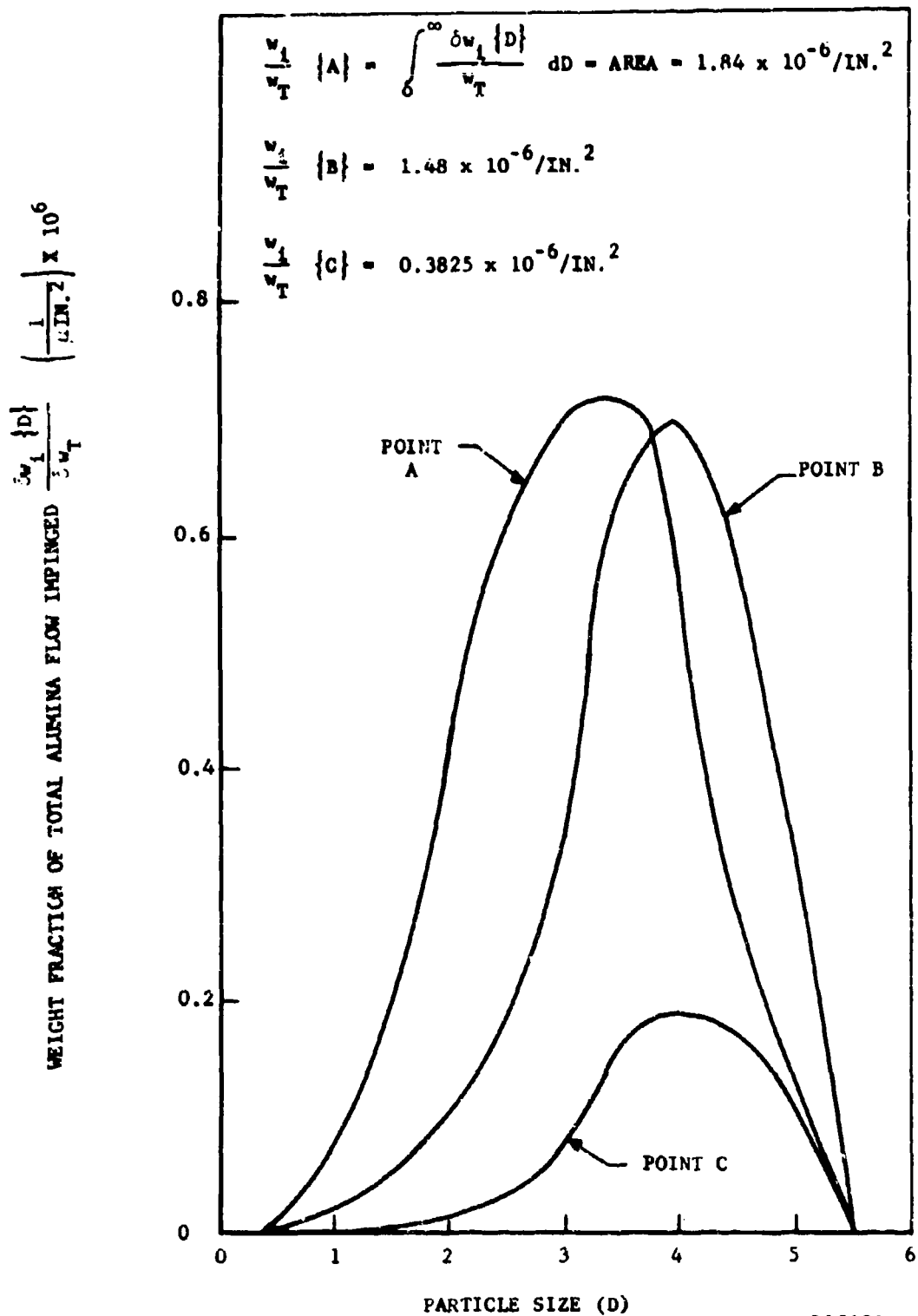


FIGURE 2-29. WEIGHT FRACTION OF TOTAL ALUMINA FLOW IMPINGED VERSUS PARTICLE SIZE FOR POINTS A, B, AND C.



### 2.7.1 SIMULATOR NOZZLE

The simulator nozzle (Figure 2-16) was a full scale model of the nozzle used in the hot firing part of this program. All impingement found on this nozzle was negligible when  $3\mu$  particles were modeled. This indicated that large agglomerated particles must have been produced in the hot firing to produce the impingement indicated in those tests.

### 2.7.2 GIMBALLED NOZZLE

In the gimballed nozzle (Figure 2-17), there was no impingement in the gimbaling section of the nozzle in either the straight or canted 5 degree position. Therefore, a full impingement study was made only on the entrance section of the straight nozzle.

It was questioned whether or not the absence of impingement in the gimbaling section was due to no particles impinging on the tapes or the velocity was too high and the particles bounced off the tape. A 90 degree wedge and a bar were placed in the exit cone (Figure 2-18) of the gimballed nozzle to check whether or not any particles could be picked up in the supersonic region. Two runs were made, one with sulfur hexafluoride and one with nitrogen as the modeling gas. A high concentration of particles were found on the wedge and bar for the sulfur hexafluoride run, but none was found for the nitrogen run. Since the molecular weight of sulfur hexafluoride is larger than nitrogen, the sonic velocity would have been lower and thus the velocity at the wedge smaller. This indicates that the higher velocity particles in the nitrogen flow may not have been picked up. On the other hand, impingement was also negligible on the gimbaling part when sulfur hexafluoride was used. (One explanation of the difference in impingement on the shapes in the exit cone with the two gases is that the differences are a function of the differences in shock lines produced and their effect on the particles.)

The gimballed nozzle which was modeled had a 63-inch diameter chamber with a 15-inch gimballed throat. It was assumed that the rocket had a total burn time of 90 seconds, a burn rate of 500 lb/sec., and an alumina loading of 32 percent. Since for subsonic flow the impingement is nearly the same when nitrogen and sulfur hexafluoride is the modeling gas, nitrogen was used for the study.

From the modeling equations (Equations 2.31 and 2.32), the particle diameter ratio and model pressure can be determined for the case of nitrogen as the modeling gas and Dow polystyrene spheres as the particles. Since the model chamber is 11 inches in diameter, a scale factor of  $D_R/D_M = 5.73$  is dictated. The other values needed to solve Equations (2.31) and (2.32) are:

$$\rho_{P_R} = 2.28 \text{ gm/cm}^3$$

$$T_R = 6360^\circ\text{R}$$

$$\rho_{P_M} = 1.05 \text{ gm/cm}^3$$

$$T_M = 480^\circ\text{R}$$

$$a_R^* = 4100 \text{ fps}$$

$$MW_R = 20.4$$

$$a_M^* = 992 \text{ fps}$$

$$MW_M = 28$$

$$\mu_R = 6.7 \times 10^{-5} \text{ lb/ft sec.}$$

$$\gamma_R = 1.18$$

$$\mu_M = 1.06 \times 10^{-5} \text{ lb/ft sec.}$$

$$\gamma_M = 1.4$$

$$P_R = 613 \text{ psia}$$

Therefore, from the modeling equations, the particle diameter ratio and the model chamber pressure are

$$\frac{D_{P_M}}{D_{P_R}} = \left[ \frac{1}{5.73} \times \frac{2.28}{1.05} \times \frac{4100}{992} \times \frac{1.06 \times 10^{-5}}{6.7 \times 10^{-5}} \right]^{1/2} = 0.496 \quad (2.33)$$

and

$$P_M = \frac{1}{0.496} \times \frac{1.06 \times 10^{-5}}{6.7 \times 10^{-5}} \times \left[ \frac{480}{5360} \times \frac{20.4}{28} \times \frac{1.18}{1.4} \right]^{1/2} \times 613 \text{ psia} = 42 \text{ psia} \quad (2.34)$$

In Equation (2.32),  $\rho_{P_R}$  and  $D_{P_R}$  correspond to the conditions in the rocket at 6360°R, and when a certain particle diameter is being modeled, it refers to the diameter of the particle at room temperature (530°R). For example, if a 2μ diameter particle is being modeled, the diameter of the particle in the model must be determined with the knowledge that the hot particle in the rocket is actually larger than 2μ. The hot diameter can be determined by conserving mass.

Mass of hot particles = mass of cold particle

$$\left( \frac{4}{3} \pi \frac{D_P^3}{8} \rho_P \right)_{\text{hot}} = \left( \frac{4}{3} \pi \frac{D_P^3}{8} \rho_P \right)_{\text{cold}} \quad (2.35)$$

or

$$\left( D_P^3 \right)_{\text{hot}} (2.28) = (2)^3 (3.7) \quad \left( D_P \right)_{\text{hot}} = 2.35\mu$$

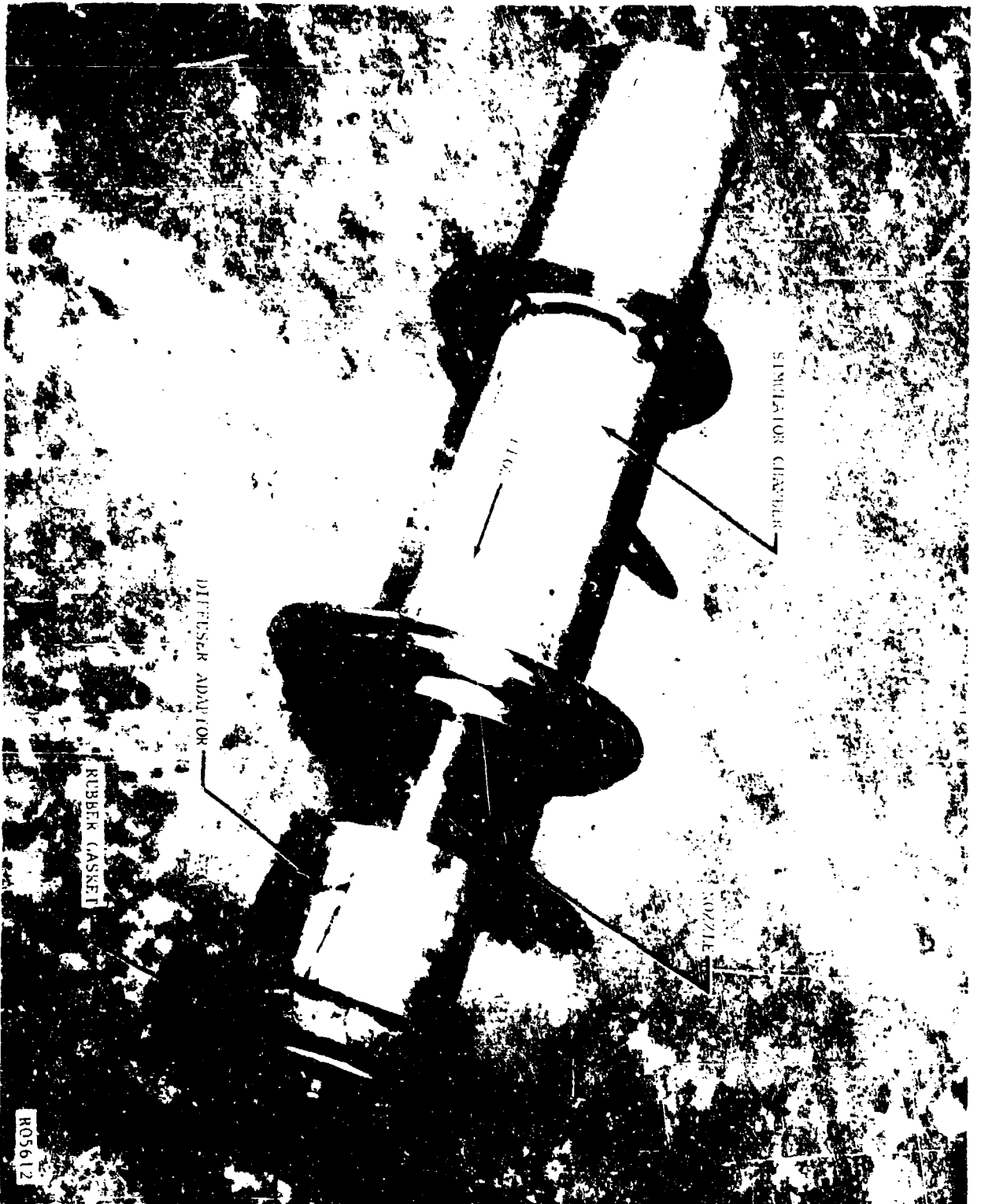


FIGURE 2-16. SIMULATOR MODEL

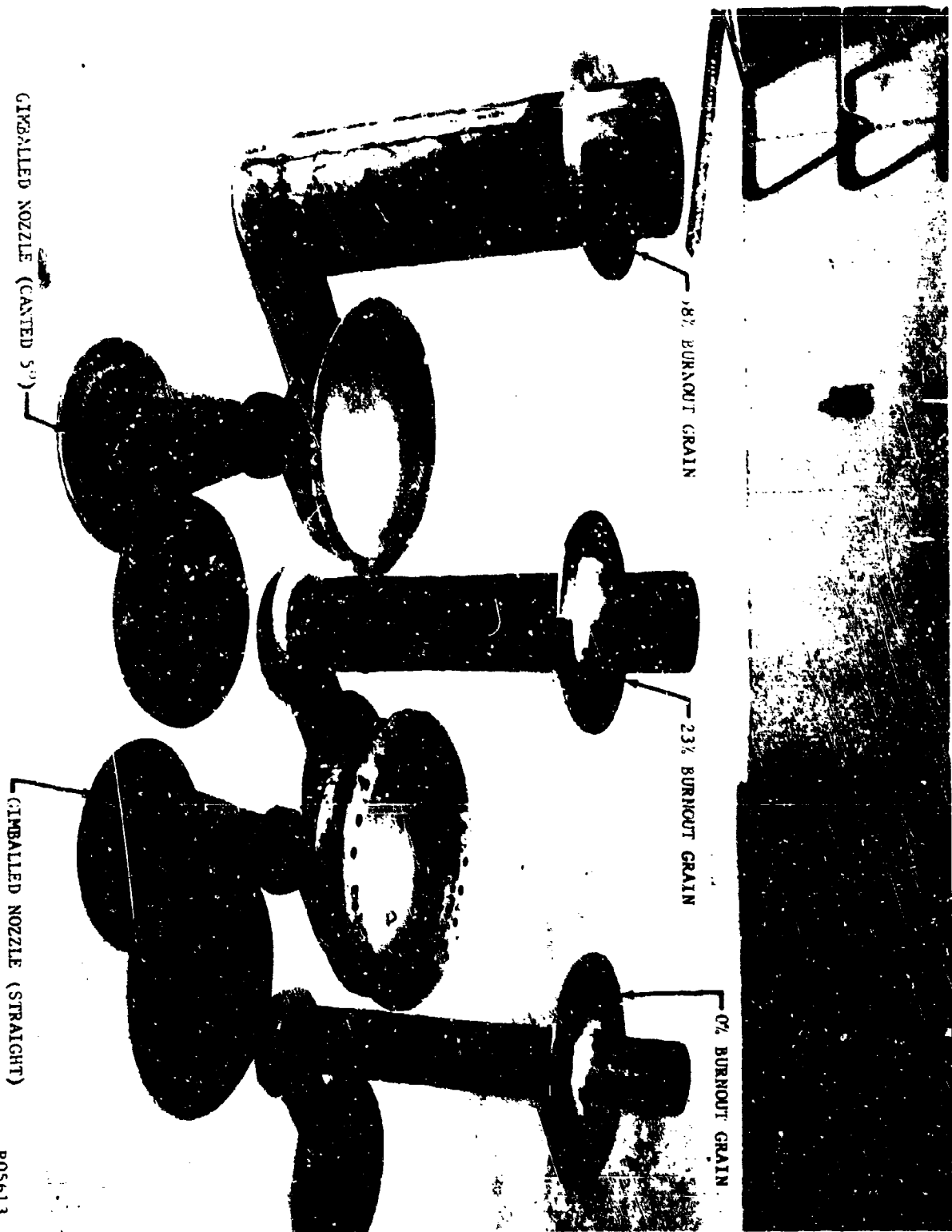


FIGURE 2-17. GIMBALED NOZZLES AND GRAIN MODELS

R05613

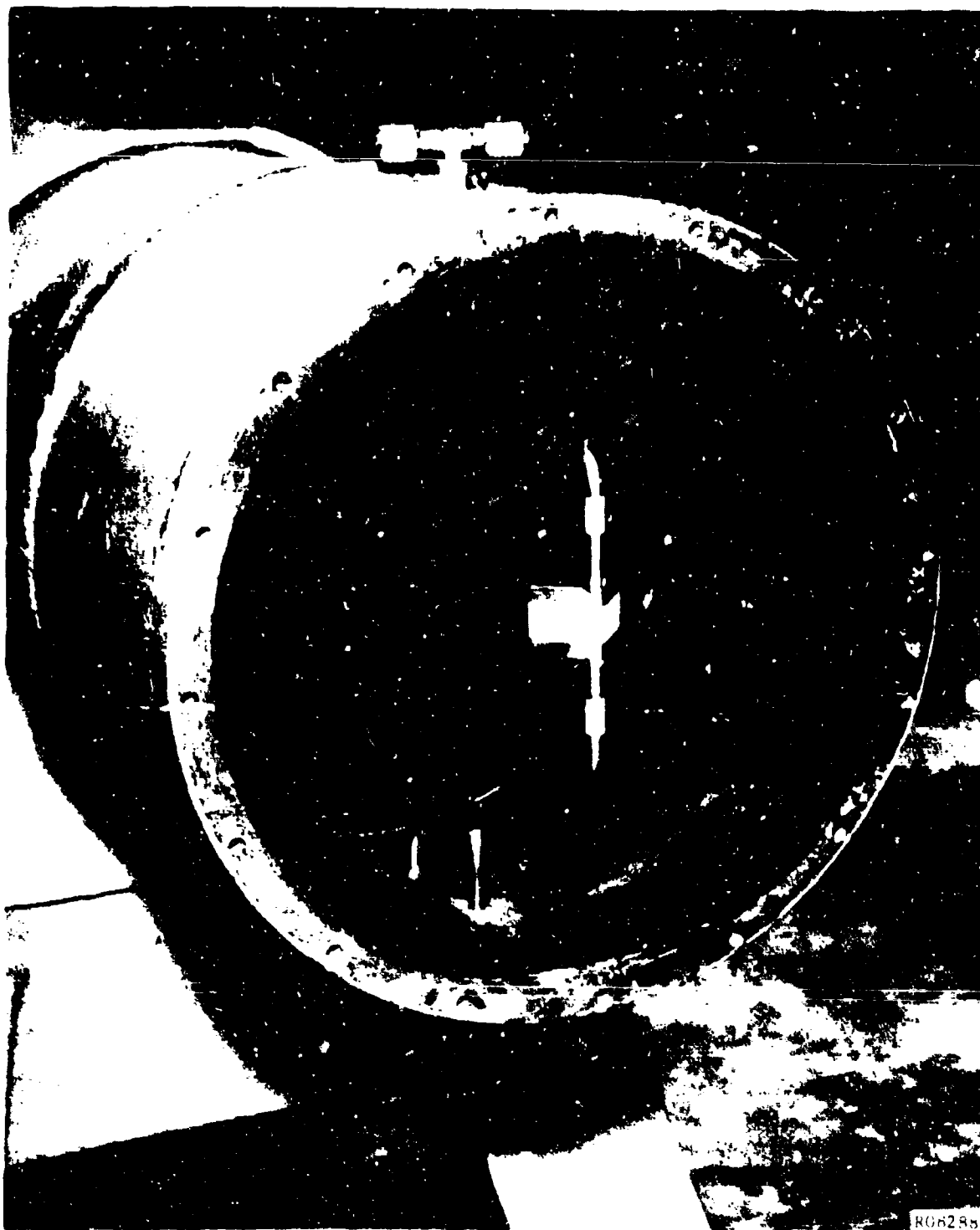


FIGURE 2-18. PARTICLE IMPINGEMENT TAPES ON WEDGE AND BAR FOR SUPERSONIC REGION OF NOZZLE

Therefore, to model a cold  $2\mu$  diameter particle with a density of  $3.7 \text{ gm/cm}^3$ ,  $\rho_P$  and  $D_{PR}$  must be  $2.28 \text{ gm/cm}^3$  and  $2.35\mu$ , respectively.

The density for aluminum oxide at  $6360^\circ\text{R}$  was taken by extrapolating the data of Kirshenbaum and Cahill.<sup>2,3</sup>

For the three sizes of polystyrene particles used, Table 2.5 shows the sizes of aluminum oxide particles being modeled.

TABLE 2.5  
MODELED PARTICLE SIZES FOR GIMBALLED NOZZLE

<u>Polystyrene Particle Dia.</u>	<u>Hot Aluminum Oxide Particle Dia. in Rocket</u>	<u>Cold Aluminum Oxide Particle Dia. from Rocket</u>
0.8 $\mu$	1.6 $\mu$	1.4 $\mu$
1.3 $\mu$	2.6 $\mu$	2.2 $\mu$
2.05 $\mu$	4.1 $\mu$	3.5 $\mu$

As shown in Figure 2-19, three grain port sizes representing three different instants in burn-time (0, 23, and 58 percent of burn-out) were needed to show the variation of impingement with time. Since three grains and three particle sizes were used, nine runs were made to develop the overall impingement picture.

Figures 2-20, 2-21, and 2-22, present the impingement data of the  $1.4\mu$ ,  $2.2\mu$ , and  $3.5\mu$  particles, respectively. The ordinate is expressed as the weight percent of that particular particle size, at that particular instant of time, impinging on the aft closure. Each data point represents the average of from 6 to 12 counts of impinged particle density in the region of the particular position along the aft closure.

An example is given to illustrate how the particles which are impinged on the tape of the model can be converted to weight percent impinged on the aft closure of the rocket. Assume counting by use of a microscope gives  $N$  particles/sq. in. on the tape at some point along the aft closure. Also, it is known that  $10^{10}$  particles were originally injected into the gas and the scale factor from the model to the rocket is 5.75. Then the weight percent impinged is

$$\frac{N}{10^{10}} \times \frac{1}{(5.75)^2} \times 100.$$

It is also interesting to note how reproducible the data are by comparing one person's particle count with another's and by comparing two tapes from the same run or from duplicate runs. These comparisons, shown in Figure 2-23 indicate reproducibility of the data.

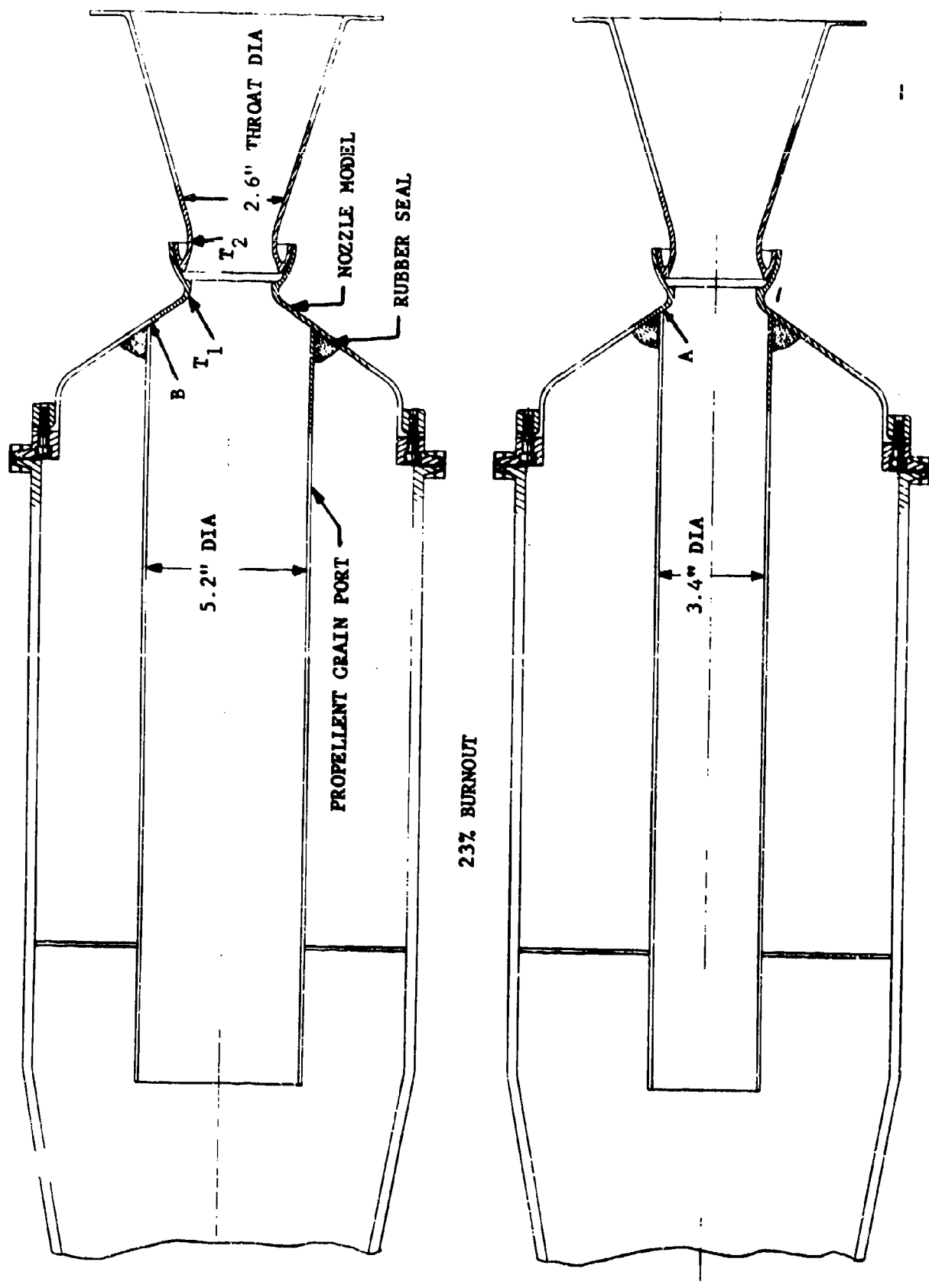


FIGURE 2-19. GIMBALED NOZZLE COLD FLOW MODELS

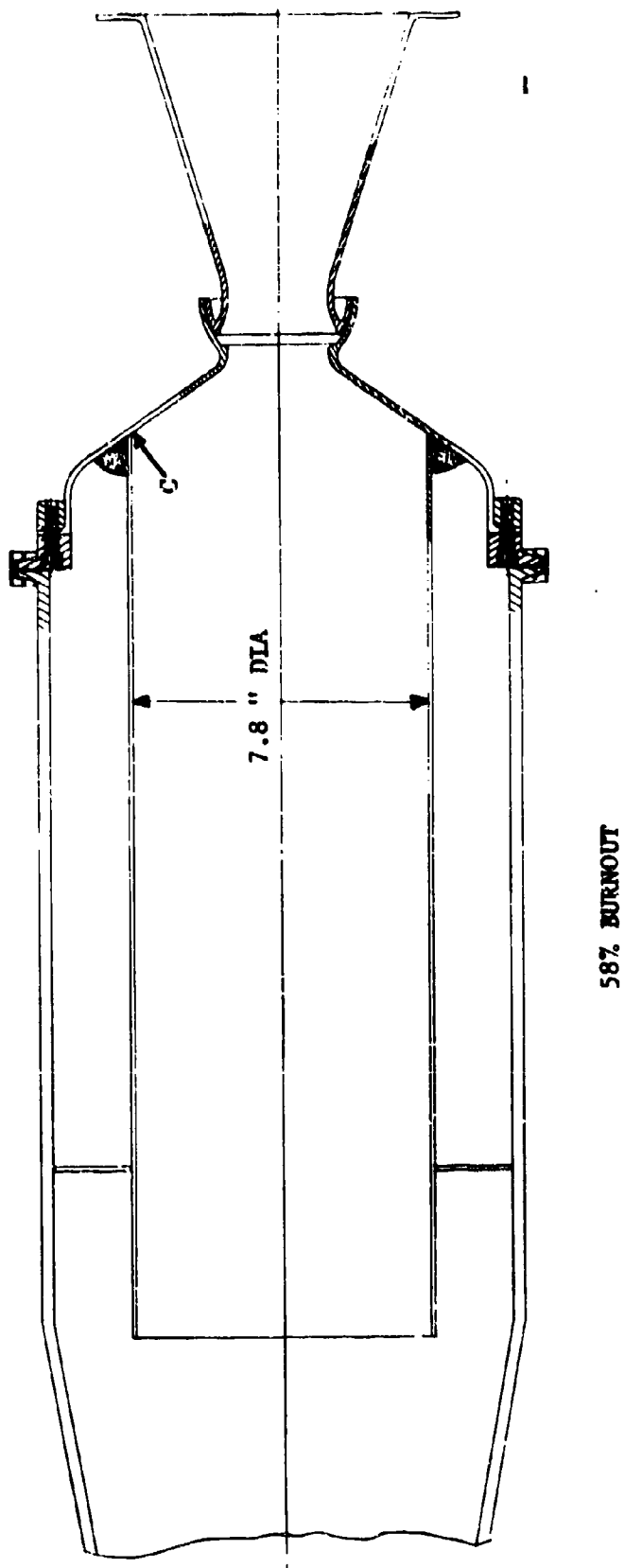


FIGURE 2-19. (CONTINUED)



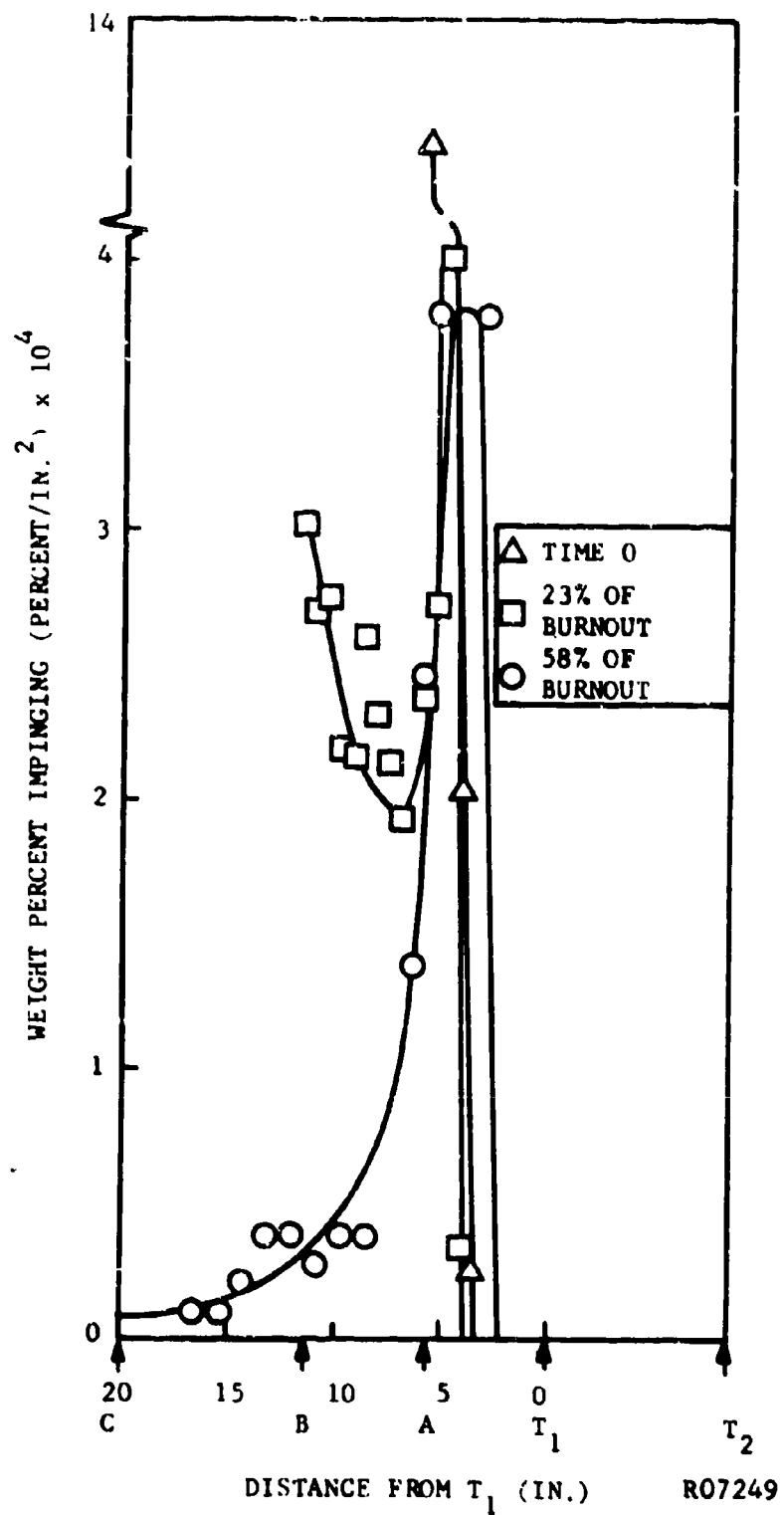


FIGURE 2-20. WEIGHT PERCENT OF 1.4<sub>μ</sub> PARTICLES IMPINGING ALONG THE AFT CLOSURE

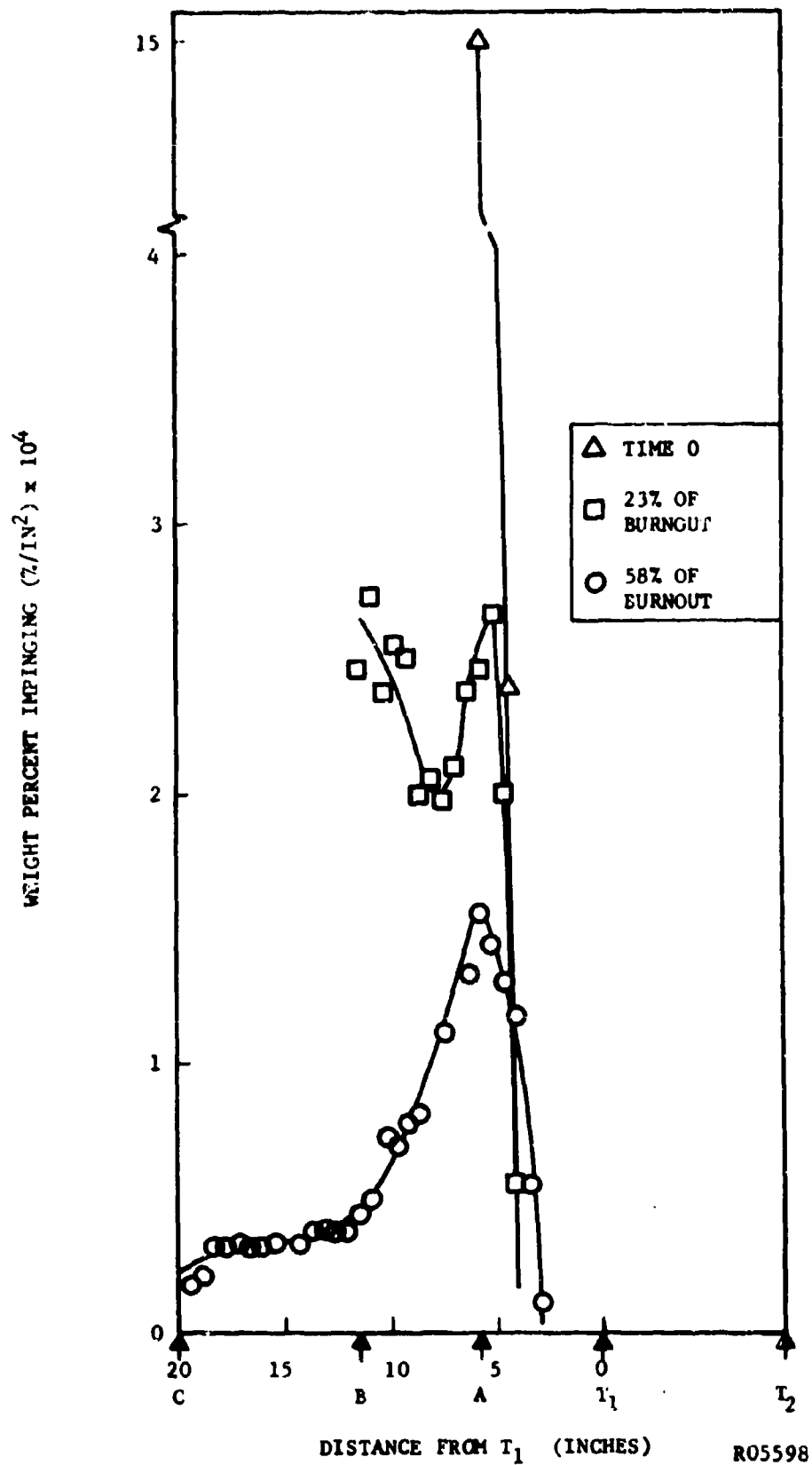


FIGURE 2-21. WEIGHT PERCENT OF  $2.2\mu$  PARTICLES IMPINGING ALONG THE AFT CLOSURE

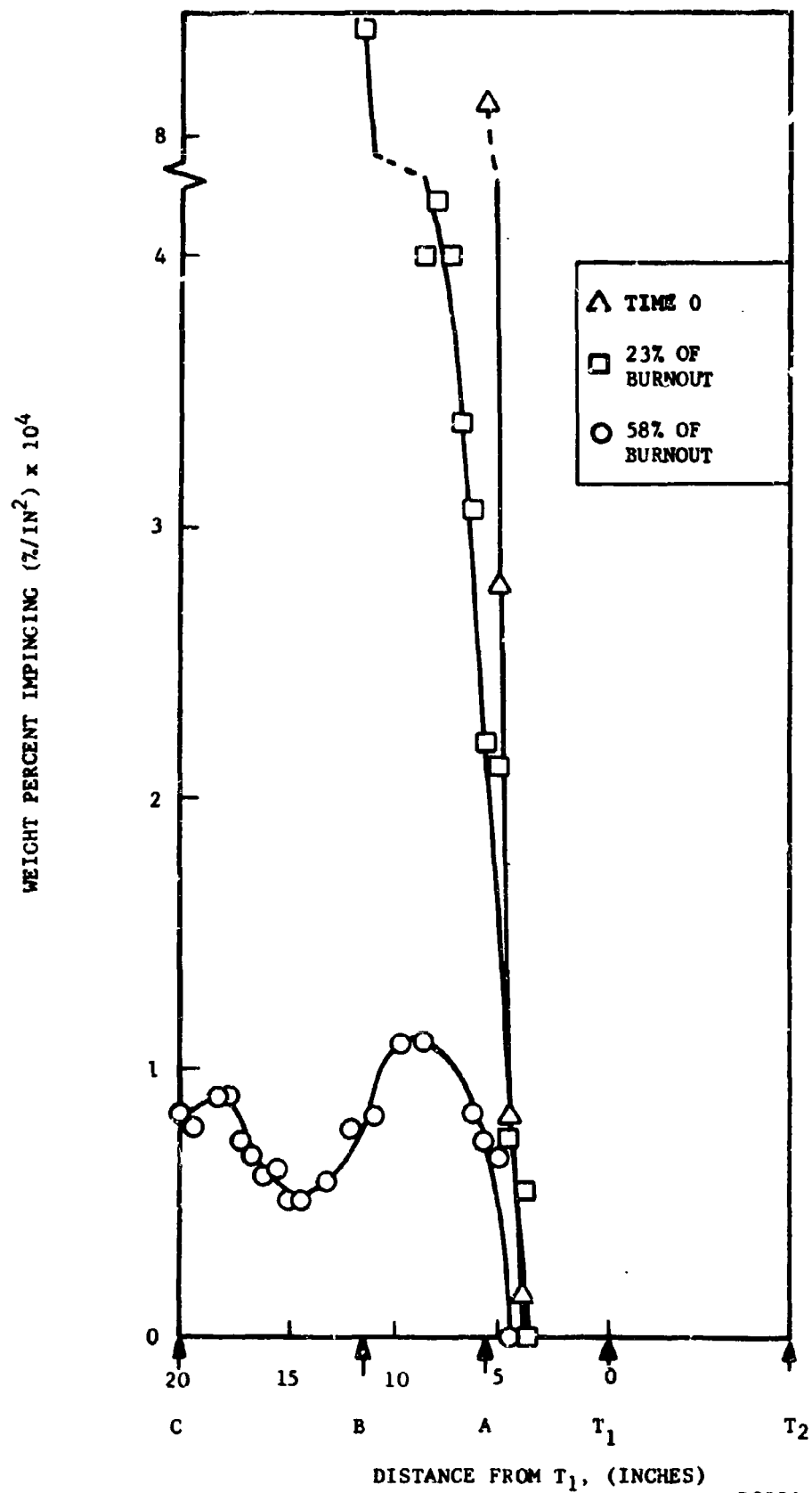


FIGURE 2-22. WEIGHT PERCENT OF 3.5 μ PARTICLES IMPINGING ALONG THE AFT CLOSURE

2-48

R05597



**R0562.**

From Figures 2-20, 2-21, and 2-22, it is now possible to develop a curve of impingement versus grain burn-time for each particle size at any point along the aft closure. Figures 2-24, 2-25, and 2-26 present such curves for points A, B, and C, of Figure 2-19, respectively. The ordinates of these curves have been changed to weight fraction impinging per square inch instead of weight percent impinging per square inch as in Figures 2-20, 2-21, and 2-22.

From the curves in Figures 2-24 through 2-26, an average weight fraction impinged can be found from each particle size at points A, B, and C by noting:

$$(100-t_b) \frac{\delta w_i \{D\}}{\delta w \{D\}} = \int_{t_b}^{100} \frac{\delta w_i \{D\}}{\delta w \{D\}} \{t\} dt \quad (2.36)$$

where D is a particular particle size

$$\frac{\delta w_i \{D\}}{\delta w \{D\}} = \text{average weight fraction impinged per sq. in. for this particle size}$$

$$\frac{\delta w_i \{D\}}{\delta w \{D\}} \{t\} = \text{weight fraction impinged per sq. in. for the same particle size as a function of time}$$

$$t_b = \text{time, percent of burnout when the point on the aft closure is first exposed to particle impingement}$$

$$\text{The integral } \int_{t_b}^{100} \frac{\delta w_i \{D\}}{\delta w \{D\}} \{t\} dt \text{ is the area under the curves of}$$

Figures 2-24, 2-25, and 2-26. Table 2.6 is a tabulation of  $\frac{\delta w_i \{D\}}{\delta w \{D\}}$ .

From Table 2.5, it is possible to obtain  $\frac{\delta w_i \{D\}}{\delta w \{D\}}$  as a function of particle size for points A, B, and C. These curves are shown in Figure 2-27. As will be explained later, the particle size range of interest is from  $0.5\mu$  to  $5.5\mu$ .

WEIGHT FRACTION IMPINGING,  $\frac{\delta w_1 \{D\}}{\delta w \{D\}} \{c\} (1/1N^2) 10^6$

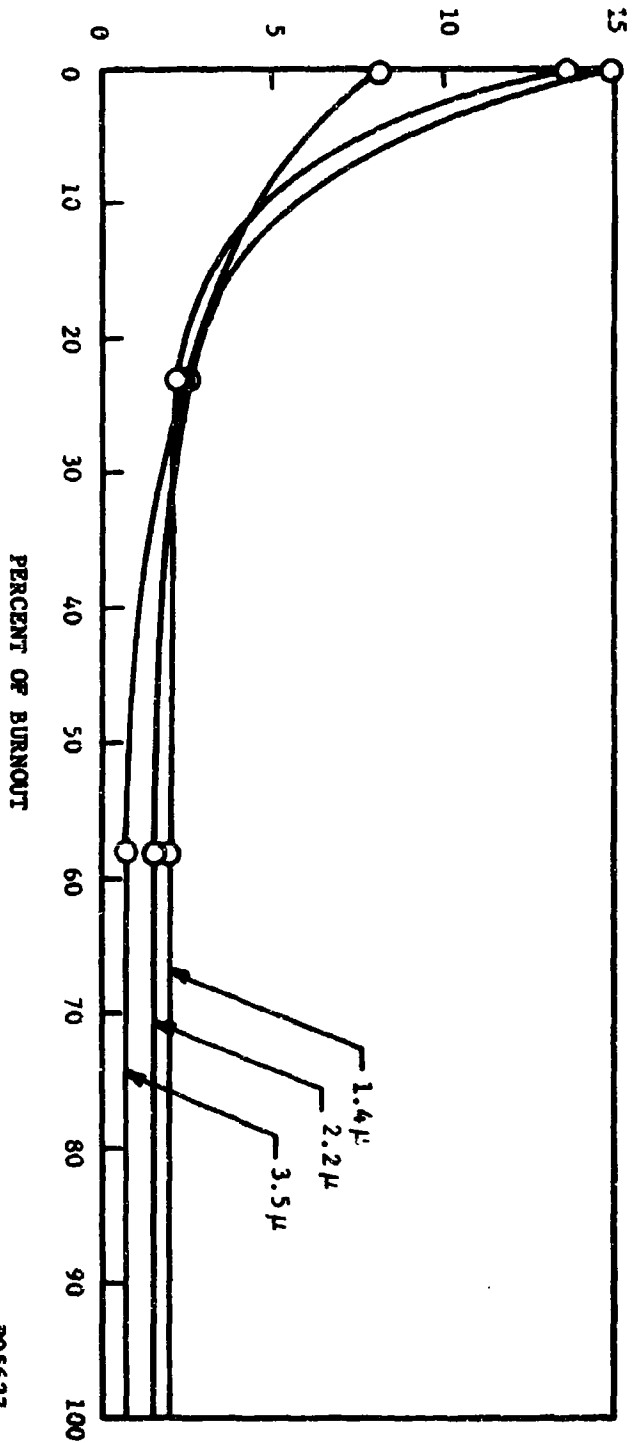


FIGURE 2-24. WEIGHT FRACTION OF 1.4 μ, 2.2 μ, AND 3.5 μ, PARTICLES IMPINGED AT POINT A VS. PERCENT OF BURNOUT

BD5627

25-2

$$\text{WEIGHT FRACTION IMPINGING } \frac{\delta w}{\delta w} \frac{\{D\}}{\{D\}} \{t\} \left( \frac{1}{2} \right) \times 10^6$$

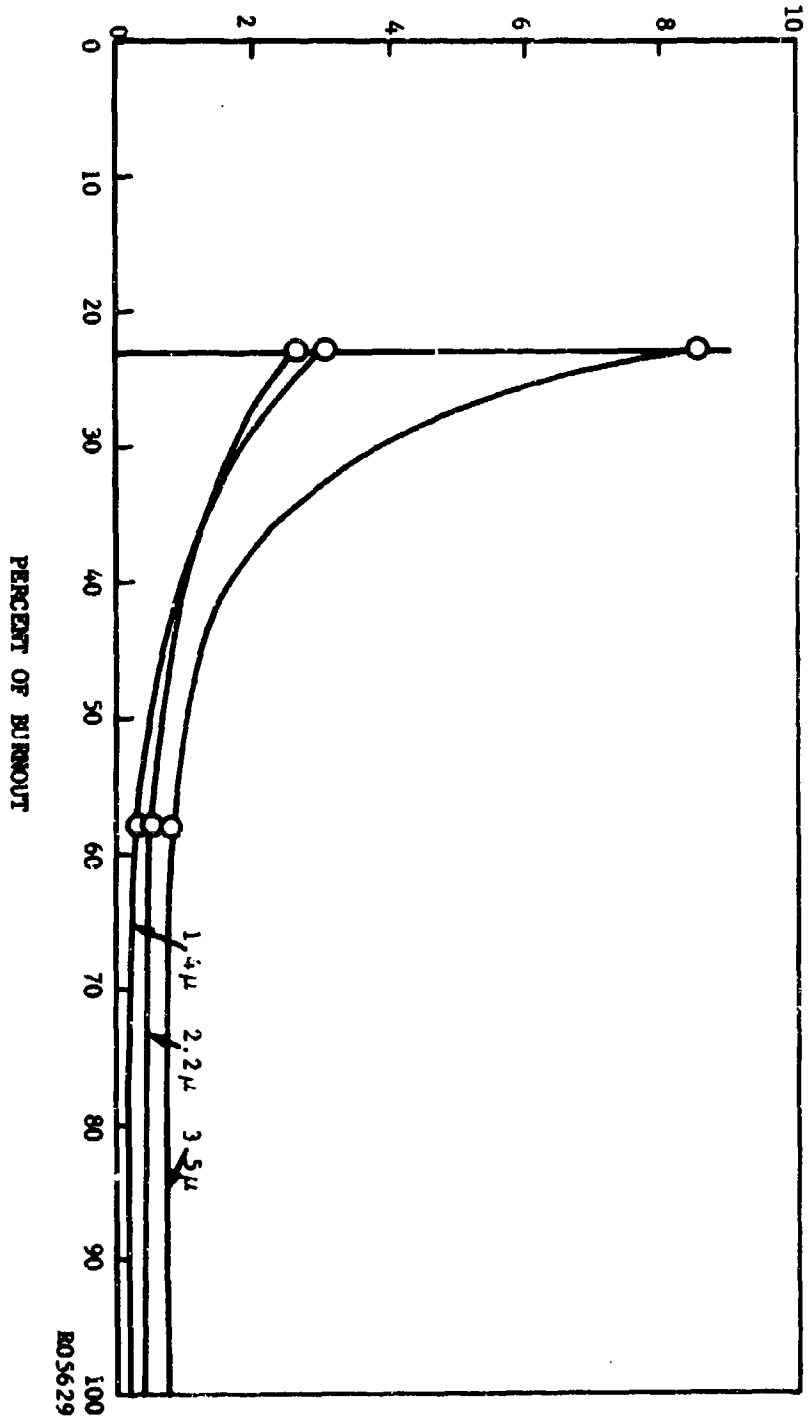


FIGURE 2-25. WEIGHT FRACTION OF 1.4μ, 2.2μ, AND 3.5μ PARTICLES IMPINGING AT POINT B VS. PERCENT OF BURNOUT

WEIGHT FRACTION IMPINGING,  $\frac{\delta_w \{D\}}{\delta_w \{D\}} \left\{ z \right\} \left( \frac{1}{\text{IN.}^2} \right) \times 10^6$

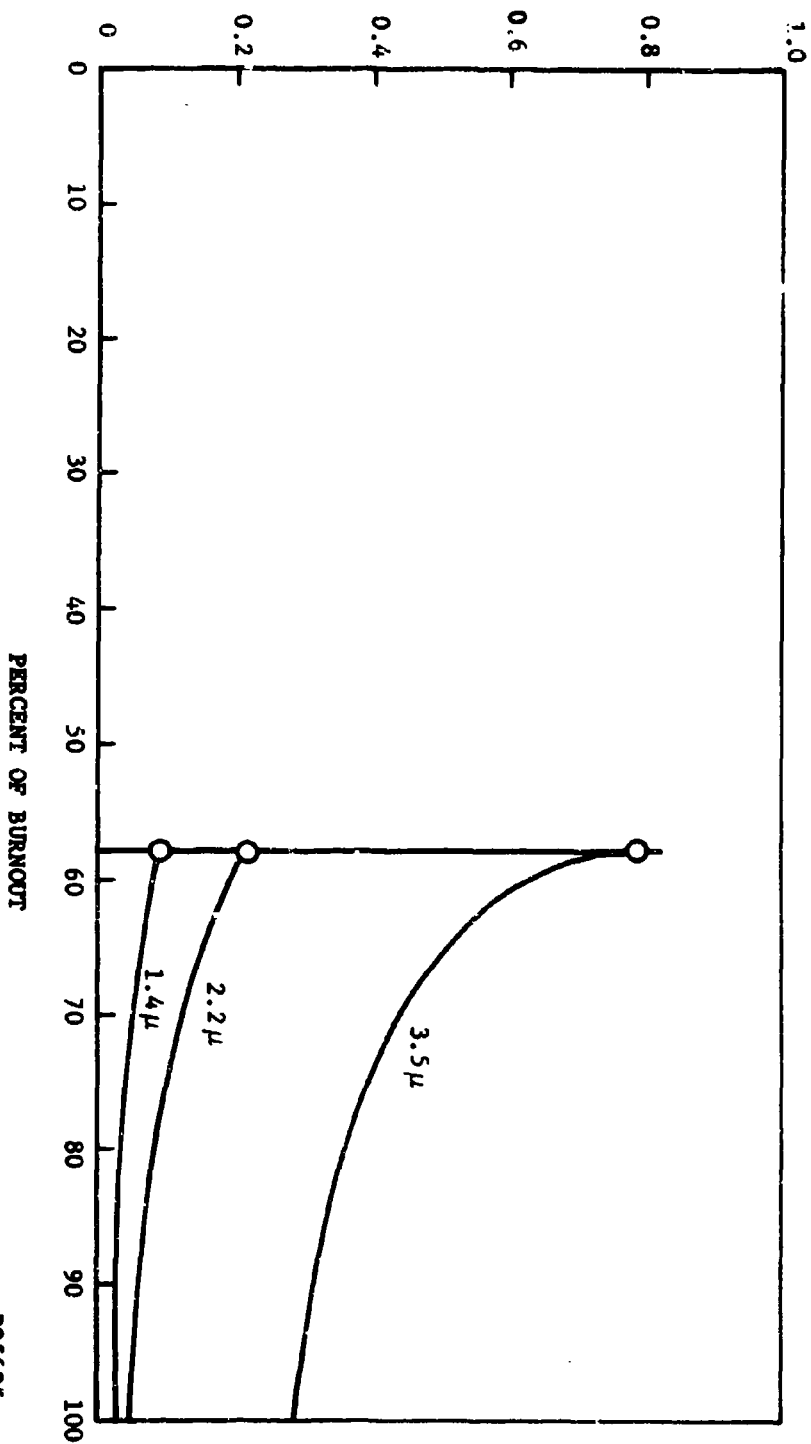


FIGURE 2-26. WEIGHT FRACTION OF 1.4μ, 2.2μ, AND 3.4μ PARTICLES IMPINGING AT POINT C VS. PERCENT OF BURNOUT

RD5625



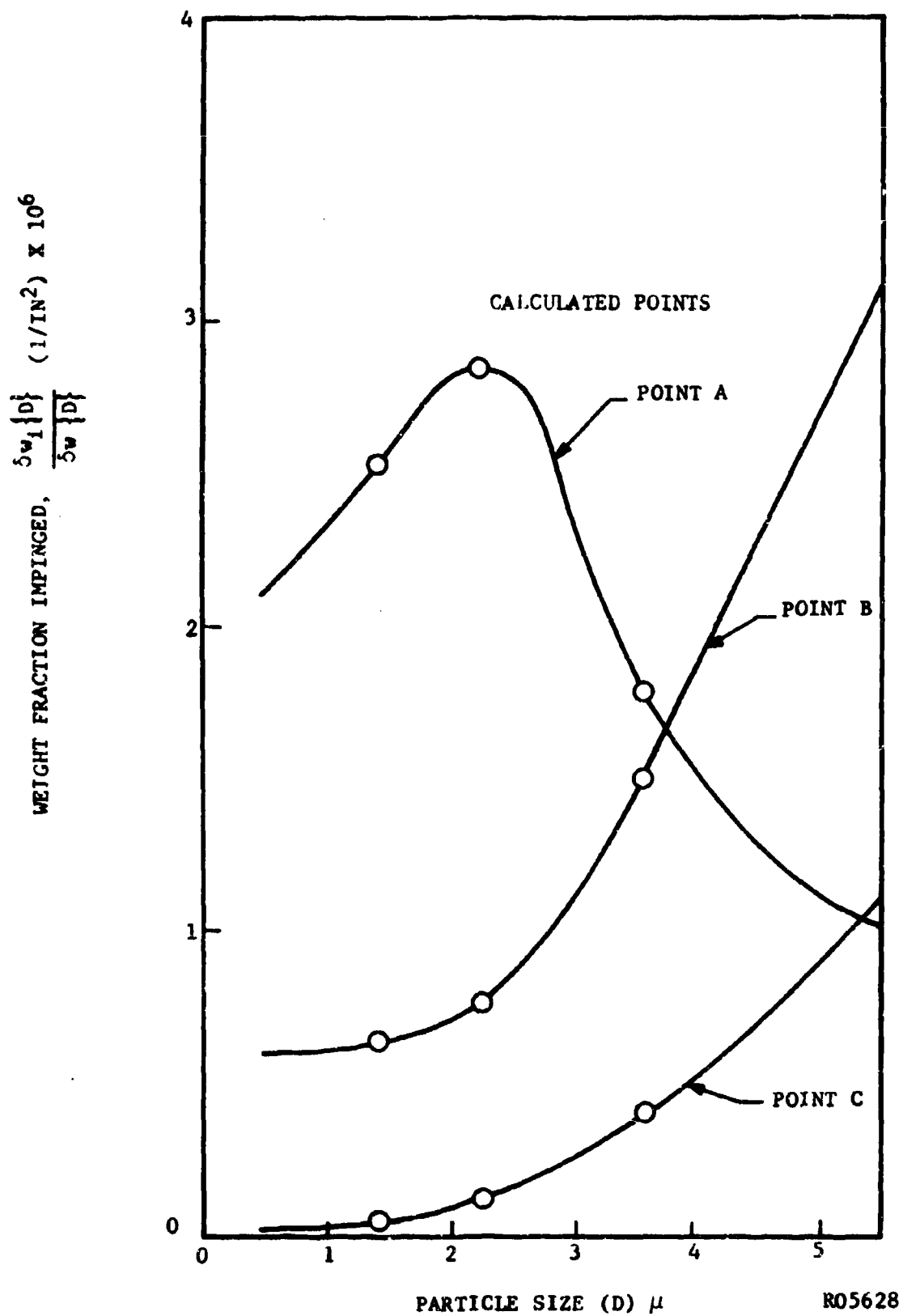


FIGURE 2-27.. AT POINTS A, B, C: ALUMINA WEIGHT FRACTION IMPINGED AS A FUNCTION OF PARTICLE SIZE

TABLE 2.6

TABULATION OF  $\frac{W_1 \langle D \rangle}{\delta W \langle D \rangle}$

Point	$t_b$ (% of Burnout)	D ( $\mu$ )	$\int_{t_b}^{100} \frac{\delta W_1 \langle D \rangle}{\delta W \langle D \rangle} \langle t \rangle dt$ (% of Burnout) $\ln^2$	$\frac{\delta W_1 \langle D \rangle}{\delta W \langle D \rangle}$ $\left  \frac{1}{\ln^2} \right $
A	0	1.4	254	2.54
A	0	2.2	285	2.85
A	0	3.5	168	1.68
B	23	1.4	49.6	0.65
B	23	2.2	59	0.77
B	23	3.5	115.4	1.5
C	58	1.4	2.1	0.05
C	58	2.2	4.6	0.115
C	58	3.5	16	0.4

The next step is to integrate impingement over the size range of particles found in a rocket. However, to do this the weight fraction of particles as a function of particle size must be known. This function can be obtained by differentiating a curve of Sehgal's<sup>2.4</sup> data for a 500 psi chamber pressure. The differential of his percent total volume below curve is shown in Figure 2-28 with units of the ordinate as  $1/\mu$  since

$$\frac{\delta W \langle D \rangle}{W_T} = d \left( \frac{W \langle D \rangle}{W_T} \right) / dD$$

where  $W_T$  is the total weight of all the alumina particles.

By multiplying the ordinate of the curves in Figure 2-27 with the ordinate of the curve in Figure 2-28 at each particle size and plotting as a function of

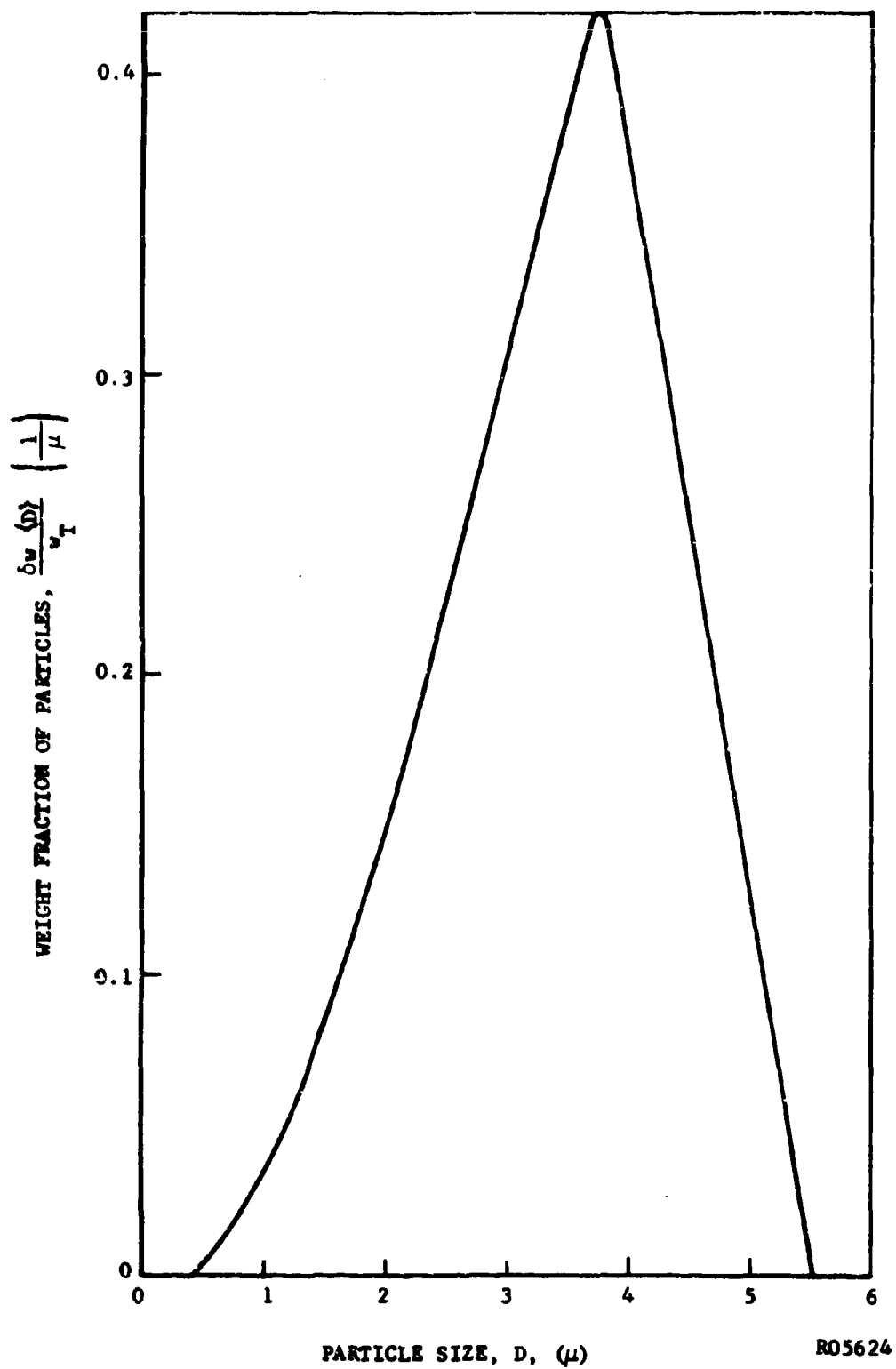


FIGURE 2-28. PARTICLE SIZE DISTRIBUTION OF ALUMINA SAMPLE OBTAINED FROM MOTOR FIRING AT 500-PSI CHAMBER PRESSURE

particle size while still keeping points A, B, and C as parameters, Figure 2-29 is obtained. The ordinate of Figure 2-29 will be  $\frac{\delta W_i \langle D \rangle}{\delta W_T D} = \frac{\delta W_i \langle D \rangle}{W_T}$  with units of  $1/\mu \text{ in}^2$ .

For any one of the three points (A, B, C) it is now possible to integrate impingement over the entire particle size range. The area under these curves can be expressed as

$$\int_0^{\infty} \frac{\delta W_i \langle D \rangle}{W_T} dD = \frac{W_i}{W_T}$$

which is the weight fraction of alumina that impinged at any point. For a run time of 90 seconds, a burn rate of 500 lb/sec., and 32 percent of the propellant as alumina, the total impingement in lb/sq. in. can be calculated as a function of position. For example:

$$\begin{aligned} \text{Impingement} &= \frac{W_i}{W_T} \left( \frac{1}{\text{in.}^2} \right) \left( \frac{500 \text{ lb.}}{\text{sec.}} \right) (0.32) (90 \text{ sec.}) \\ &= \frac{W_i}{W_T} (14400) \text{ lb/sq. in.} \end{aligned}$$

This curve for impingement along the nozzle wall integrated for the total firing is shown in Figure 2-30. This is the final result desired from the cold-flow modeling test data.

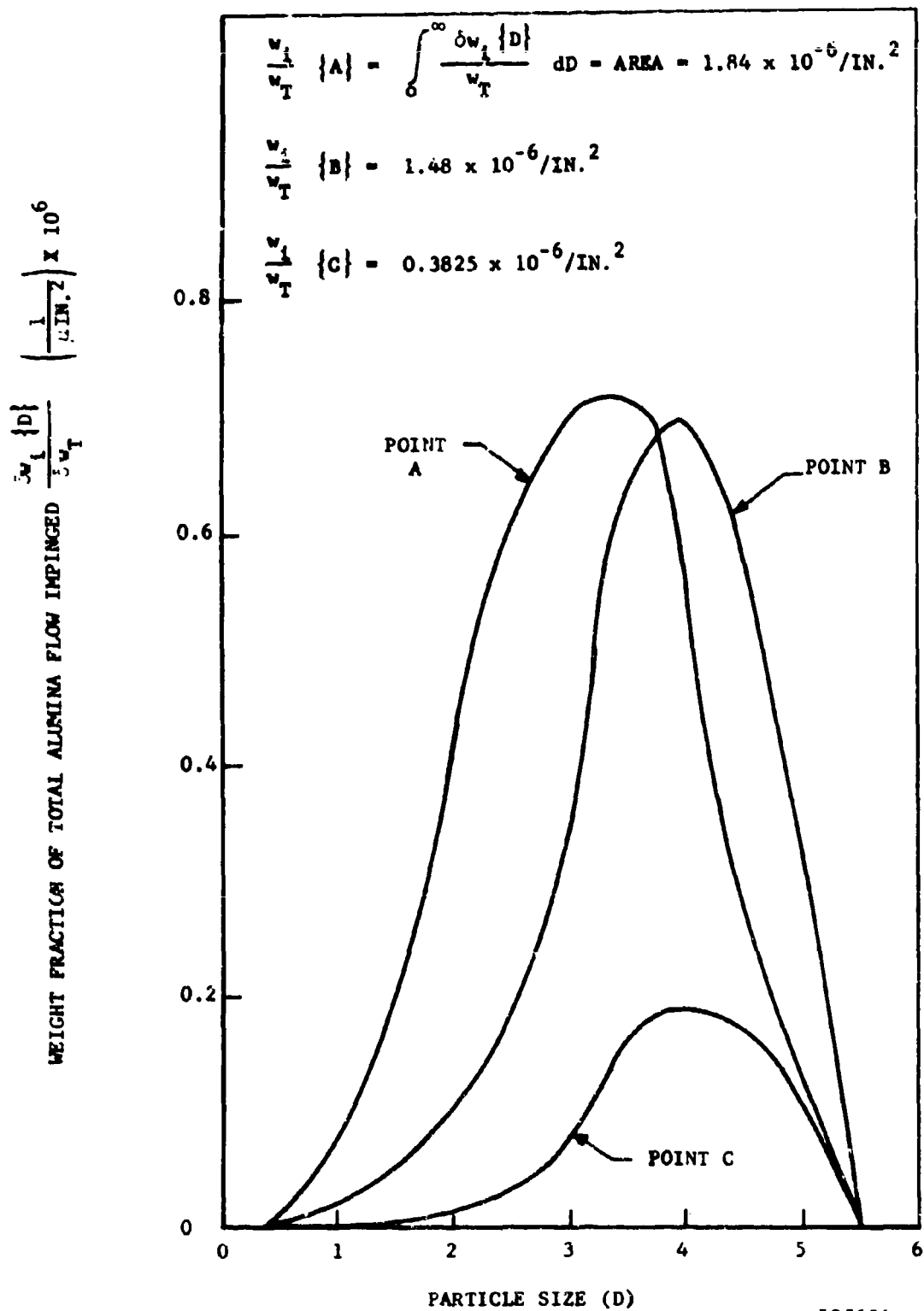
### 2.7.3 100 FW2

The model of the 100 FW2 consisted only of the aft closure. Therefore, nitrogen was used as the modeling gas. As shown in Figure 2-31, the aft closure was modeled at two burn times, 16 and 54 percent of burnout. Three particle sizes were modeled, making a total of six runs.

Again, from the modeling equations (2.31) and (2.32) the particle diameter ratio and model pressure can be determined. Since the model chamber is 11 inches in diameter, a scale factor of  $\frac{D_R}{D_M} = 9.1$  is dictated. The other values which are input to the equations are as follows:

$$\rho_{P_R} = 2.28 \text{ gm/cm}^3$$

$$T_R = 6360^\circ\text{R}$$



K05626

FIGURE 2-29. WEIGHT FRACTION OF TOTAL ALUMINA FLOW IMPINGED VERSUS PARTICLE SIZE FOR POINTS A, B, AND C.

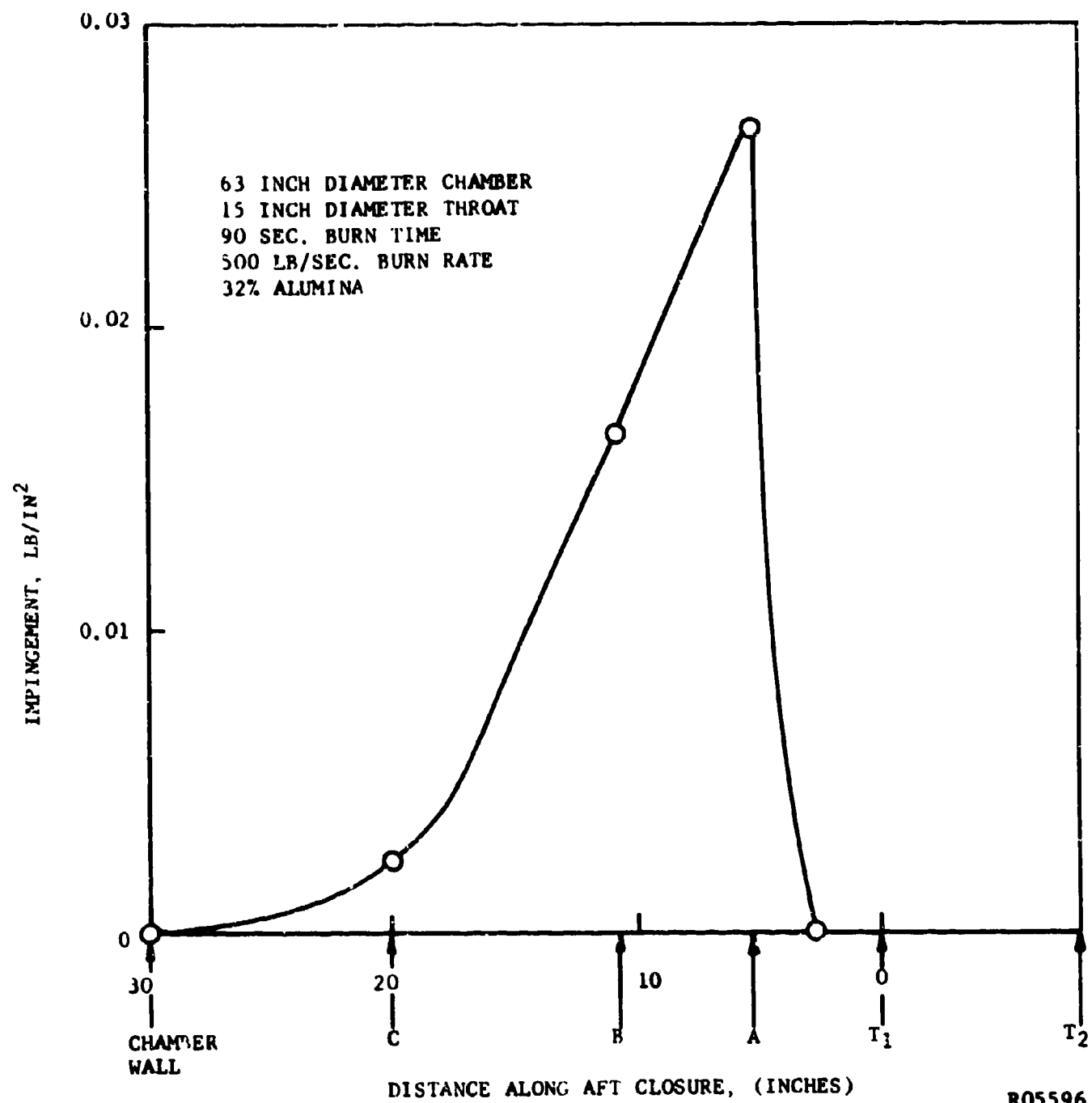


FIGURE 2-30. TOTAL IMPINGEMENT ALONG ROCKET AFT CLOSURE

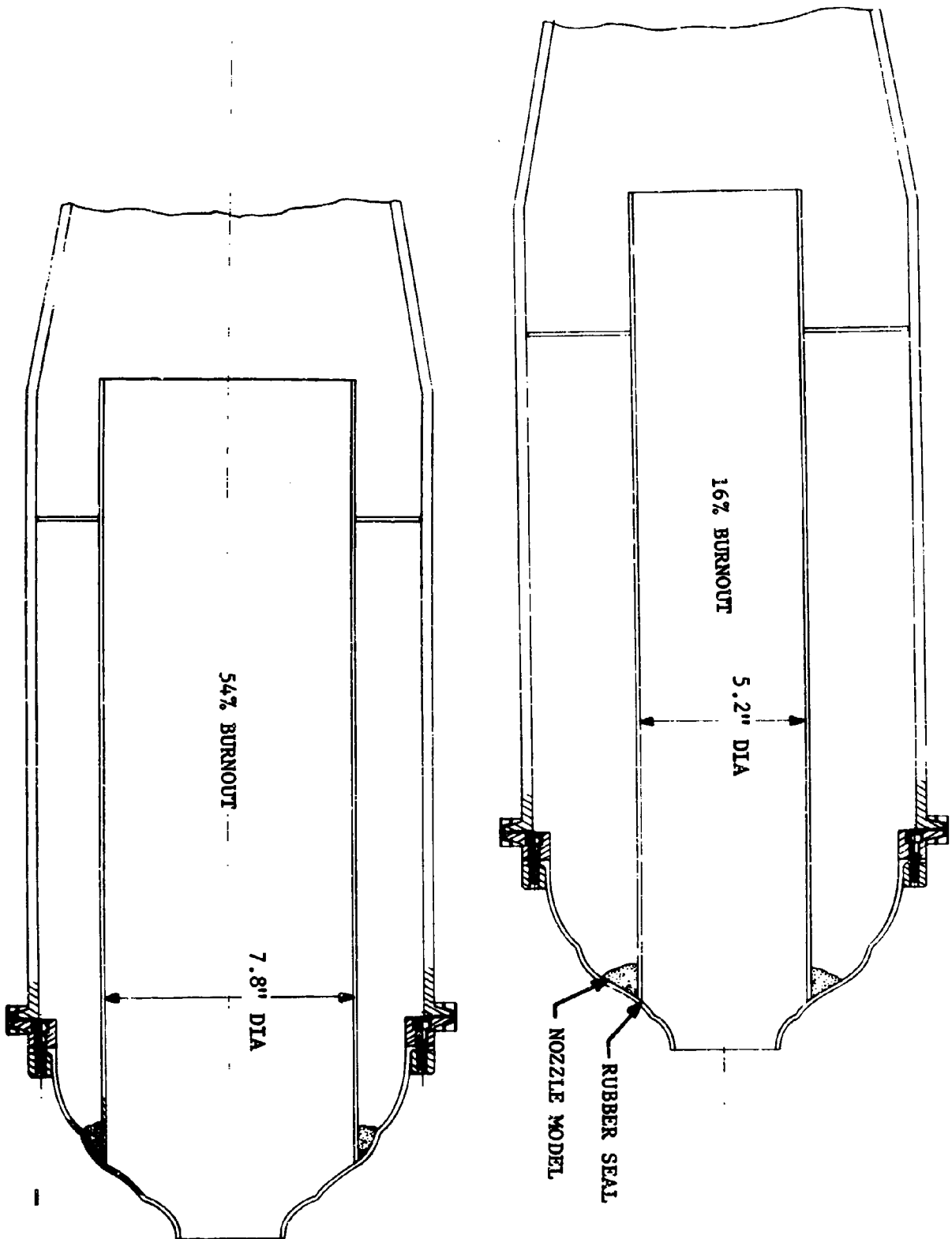


FIGURE 2-31. 100 FW2 COLD FLOW MODELS

$$\rho_{PM} = 1.05 \text{ gm/cm}^3$$

$$T_M = 480^\circ\text{R}$$

$$a_R^* = 4100 \text{ fps}$$

$$MW_R = 20.4$$

$$a_M^* = 992 \text{ fps}$$

$$MW_M = 28$$

$$\mu_R = 6.7 \times 10^{-5} \text{ lb/ft sec}$$

$$\gamma_R = 1.18$$

$$\mu_M = 1.06 \times 10^{-5} \text{ lb/ft sec}$$

$$\gamma_M = 1.4$$

$$\frac{D_{PM}}{D_{PR}} = \left[ \frac{1}{9.1} \times \frac{2.28}{1.05} \times \frac{4100}{992} \times \frac{1.06 \times 10^{-5}}{6.7 \times 10^{-5}} \right]^{1/2} = 0.395 \quad (2.37)$$

$$\frac{P_M}{P_R} = \frac{1}{.395} \times \frac{1.06 \times 10^{-5}}{6.7 \times 10^{-5}} \times \left[ \frac{480}{6360} \times \frac{20.4}{28} \times \frac{1.18}{1.4} \right]^{1/2} = 0.086 \quad (2.38)$$

For the three particle sizes used, Table 2.7 shows the sizes of alumina particles being modeled.

TABLE 2.7

PARTICLE SIZE RELATIONSHIPS IN MODELING THE 100 FW2 NOZZLE

<u>Polystyrene Particle Diameter</u>	<u>Hot Alumina Particle Diameter in Rocket</u>	<u>Cold Alumina Particle Diameter from Rocket</u>
0.8 $\mu$	2.0 $\mu$	1.7 $\mu$
1.3 $\mu$	3.3 $\mu$	2.3 $\mu$
2.05 $\mu$	5.2 $\mu$	4.4 $\mu$

For the 100 FW2, the chamber pressures are 620 psia and 643 psia at 16 and 54 percent of burnout, respectively. Therefore, the modeling pressure at 16 percent of burnout will be 53 psia and at 54 percent of burnout will be 55 psia. Figure 2-32 and 2-33 present the impingement data at 16 and 54 percent burnout, respectively. The impingement data is integrated over burn time and particle sizes found in a rocket in exactly the same manner as for the gimbaled nozzle. The final result is again the total impingement of alumina along the aft closure as shown in Figure 2-34.



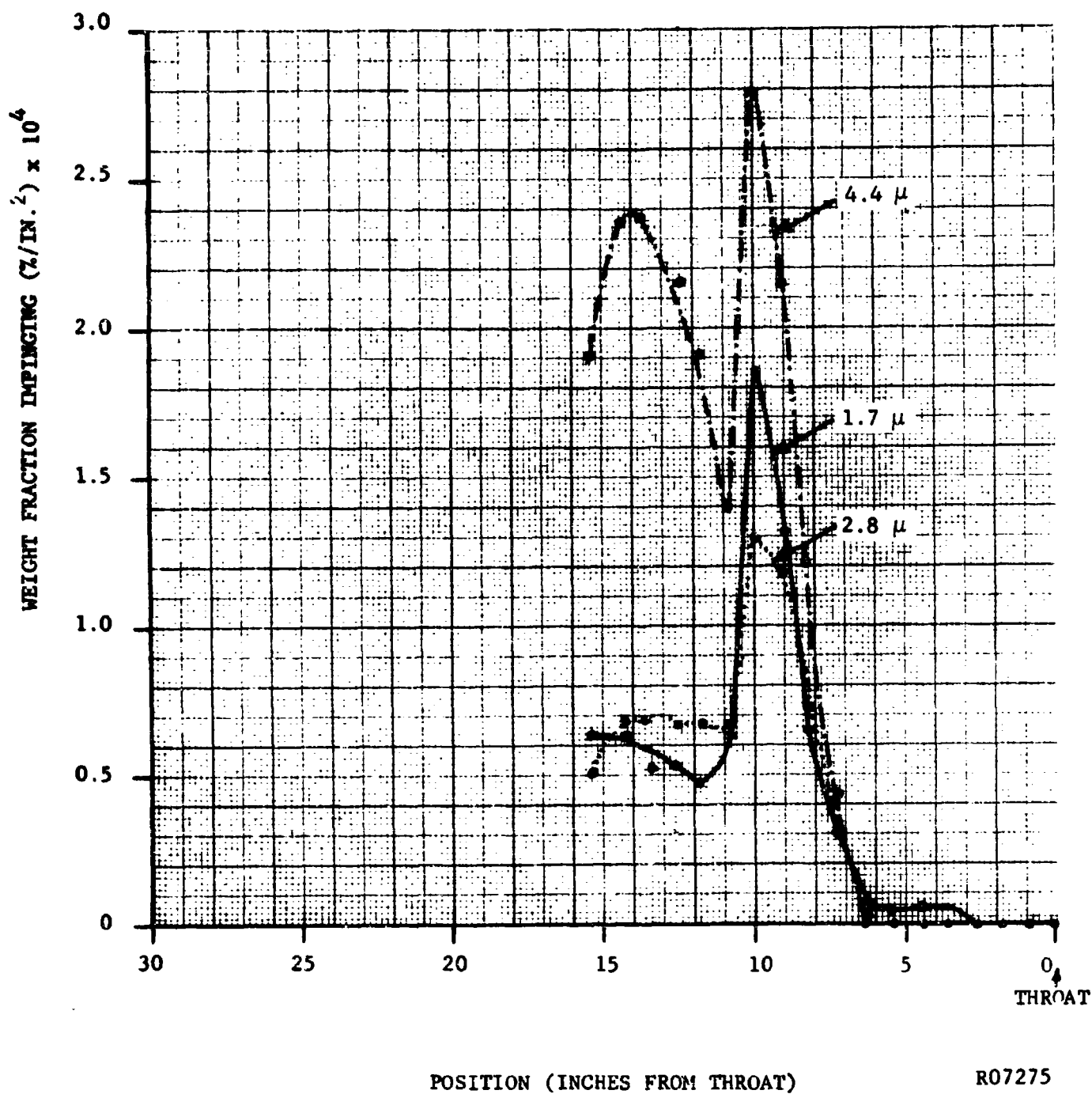


FIGURE 2-32. PARTICLE IMPINGEMENT IN 100 FW2 AT 16% OF BURNOUT

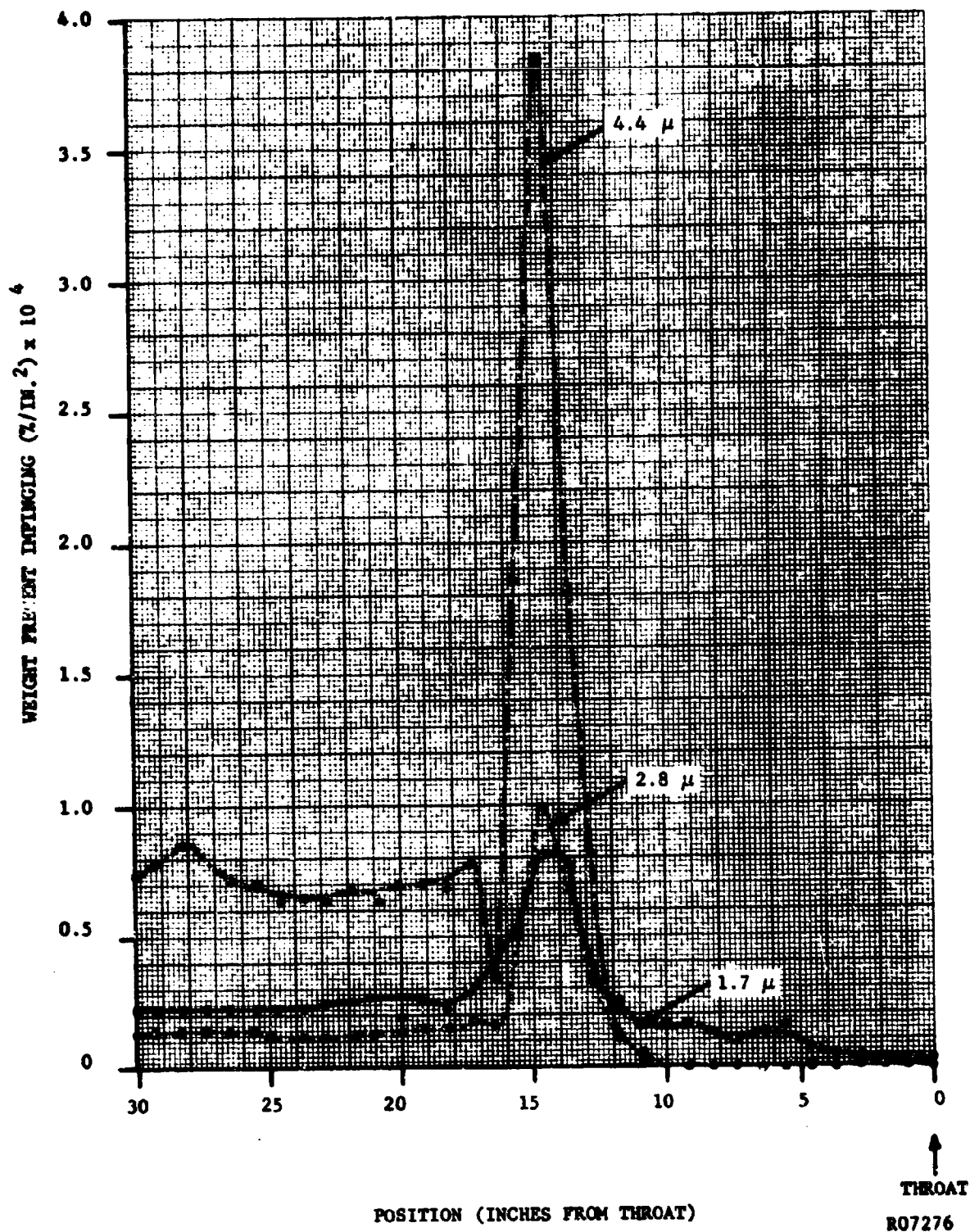
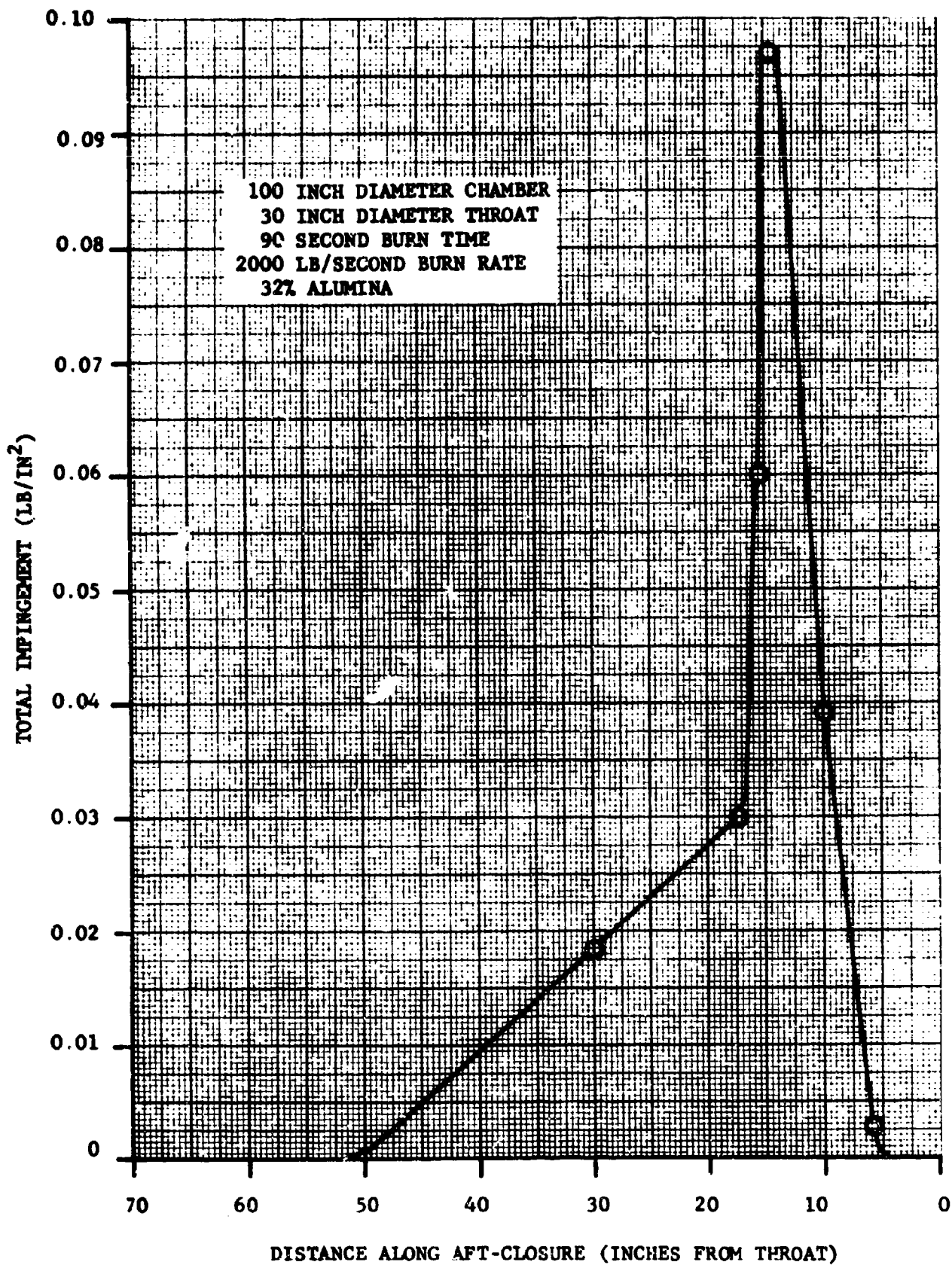


FIGURE 2-33. PARTICLE IMPINGEMENT IN 100 FW2 AT 54% OF BURNOUT



R07278

FIGURE 2-34. TOTAL IMPINGEMENT ALONG 100 FW2 AFT CLOSURE

## 2.8 PRESSURE CONTOURS

Pressure contours were measured on manometers. Figure 2-35 is a photograph taken of a pressure run with the manometers stabilized. Pressure contours were measured on two of the nozzles, (1) the gimbaled nozzle (straight) and (2) the gimbaled nozzle (canted 5 degrees). Three pressure contours were measured on the 5 degree canted nozzle: one on the outside of the turn, one on the inside of the turn, and one half way between, where no turn effects would be expected.

Figure 2-36 shows the Mach number from these pressure contours by using the one-dimensional flow tables. These runs were all made using nitrogen as the modeling gas. It is of interest to note that in the straight position, the flow did not go sonic at the first throat, but it did in the case of the 5 degree canted nozzle. This indicates more flow is realized when the nozzle is canted.

These data were used to determine the convective heat transfer for the gimbaled nozzle in section 7.

The gimbaled nozzle in straight position was axisymmetric. For this case, the mach numbers corresponding to area ratios were taken from the one-dimensional flow tables and compared to the experimental data. This comparison is shown in Figure 2-37. When sulfur hexafluoride was used as the modeling gas instead of nitrogen, there was negligible change in the Mach number contour.

## 2.9 FUTURE WORK AND APPLICATIONS

In the future, some work should be done to study the basic parameters of cold flow particle impingement modeling. That is, the effects of varying different parameters such as turbulence levels, boundary layer thicknesses, and angle of impinging gas-particle stream. Basic studies should also be carried out in the supersonic regions where particle impingement could be studied on a wedge, which can also be studied analytically.

In the course of the particle impingement modeling, the possibility of applying it to other problem areas was demonstrated. For example, flow separation in the nozzle was indicated by a step change in particle impingement. Also, impingement patterns on obstructions in the exit cone were readily shown. Of course, nozzles other than the shapes studied could be modeled. Extreme nozzle shapes and ducting for thrust vector control, where impingement might be very high, could be studied.



R08289

FIGURE 2-35. PHOTOGRAPH OF MANOMETER BANK

NO7266

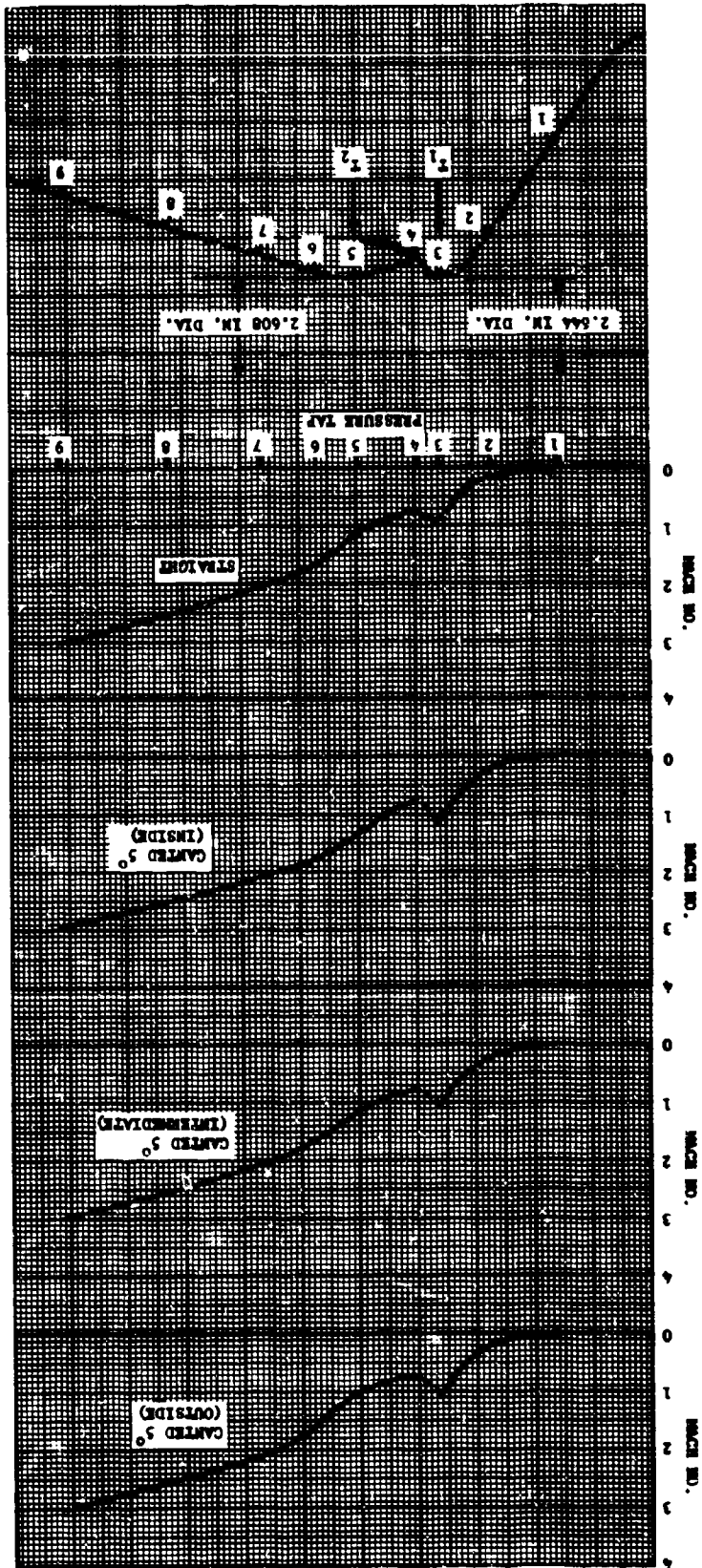
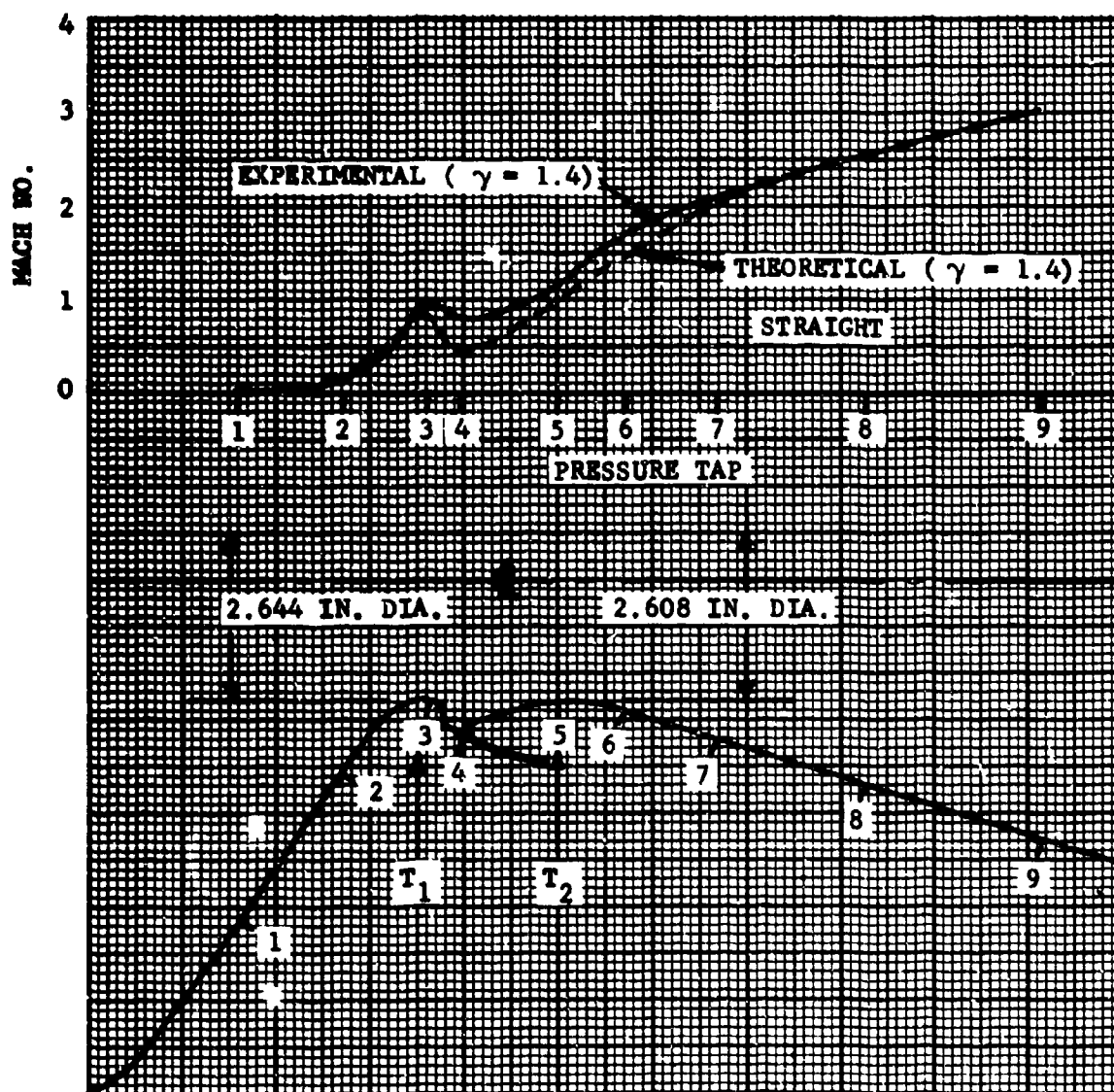


FIGURE 2-36. MACH NUMBER IN GIMBALED NOZZLE, CANTED 5° AND STRAIGHT, COLD FLOW DATA



R07265

FIGURE 2-37. COMPARISON OF EXPERIMENTAL AND THEORETICAL MACH NUMBERS IN STRAIGHT GIMBALED NOZZLE

## 2.10 REFERENCES

- 2.1 Marble, F. E., "Free Expansion Nozzles (U)", Final Report, Aeronutronic Publication No. C-1952, Dec. 31, 1962 (Confidential).
- 2.2 Kuby, W., Baier, R., Carlson, D., Hoglund, R. and Stern, N., "An Investigation of Recombination and Particle Lag Effects in Rocket Nozzles (U)", First Quarterly Technical Report, Aeronutronic Publication No. C-1824, Sept. 15, 1962 (Confidential).
- 2.3 Kirshanbaum, A. D. and Cahill, J. A., "The Density of Liquid Aluminum Oxide" Journal of Inorganic Nuclear Chemistry, 1960, Vol. 14, pp. 283-287.
- 2.4 Sehgal, R., "An Experimental Investigation of a Gas-Particle System," Jet Propulsion Laboratory, TR 32-238, March 16, 1962



## SECTION 3

### PARTICLE IMPINGEMENT IN SIMULATOR FIRINGS

#### 3.1 INTRODUCTION

Rocket motor firings with a calorimetric molybdenum nozzle were conducted with the following objectives:

- (1) To study the heat transfer to the nozzle wall due to particle impingement.
- (2) To obtain quantitative data on the influence of various concentrations of particles in the flow on heat transfer to inlet, throat, and exit cone regions of nozzles.
- (3) To study the variation in particle flow heat transfer with nozzle geometry (particularly the canted configuration).

The test firings were conducted using a rocket motor in which slurries containing various concentrations of solid particles were injected into the combustor along with hydrogen and oxygen gases. In most tests, the solid particles consisted of alumina between 1.0 and 5.0 microns in diameter. Combustion products and particles were exhausted through a molybdenum nozzle instrumented inside and outside with surface thermocouples at 15 locations to obtain the desired heat transfer data.

A total of 64 runs was conducted. The alumina concentration in the exhaust products was varied from 0 to 35 percent. Throughout the schedule of tests the formulations were designed for a constant theoretical chamber temperature of about 5100°F. The principal results of the tests are presented in Figures 3-7 through 3-18, which illustrate wall temperatures, heat fluxes, and film coefficients for various propellants, solids concentrations, and nozzle locations and geometries.

### 3.2 DESCRIPTION OF TEST APPARATUS AND RUN PROCEDURE

The rocket motor and the accompanying molybdenum nozzle are illustrated in Figure 3-1. The slurry-gas injection combination allowed a wide range of changes in combustion products. For example, with rearrangement of feeds the alumina content of the combustion gases could be eliminated or varied while allowing very little change in gaseous composition or temperature.

Combustion conditions were regulated by metering the gases with sonic orifices, and the slurry was metered by a positive displacement pump pushing across a diaphragm with a hydraulic oil output. The injector was designed for good mixing of gaseous and slurry feeds with a minimum of momenta in the direction of the nozzle. The slurry was atomized in twelve injector inlets where a single stream of the slurry admixed with an annular stream of hydrogen. This stream impinged upon the oxygen for further mixing in the combustion area at the injector end of the chamber. The solid copper injector readily accommodated the planned firings without over-heating. A photograph of the simulator engine from the injector end is shown in Figure 3-2.

Chamber wall design (graphite backed with asbestos phenolic) was patterned after other Philco motors which have withstood total firing times of around 1000 seconds, and single firing durations of over two minutes. Heat loss from the chamber was large, and was accounted for in data reduction. The step at the end of the chamber caused boundary layer break-up. Therefore, boundary layer conditions resulting from simulator chamber operation would have reduced influence on the downstream flow along the nozzle section.

The greatest number of runs consisted of injection of an alumina-water slurry into the combustion gases. Two types of alumina were used:

- (1) Linde Alumina Abrasive - type 1.0-C Highly Uniform, 1.0 micron diameter. (Poor atomization forced eventual elimination of this type)
- (2) Norton Alumina Powder, 38-1200 mesh, 2.5 micron average diameter.

Originally a gelling agent was used to maintain the alumina-water suspension. This was eliminated, however, because the gel had an adverse effect on the dispersion of particles by the injector. A modified test procedure was adopted in which the ball-milled suspension was added to the run tank immediately before firing. Any pre-run settling effects were determined to be negligible.

Two types of molybdenum nozzles were tested: an axisymmetrical and a 5-degree canted shape. Figure 3-3 is a photograph of the axisymmetrical nozzle. The throat diameter in each configuration was 1.25 inches. Figure 3-4 illustrates the distribution of thermocouple locations on the axisymmetrical nozzle. Accompanying this diagram is Table 3.1 which is a tabulation of axial distance, radial distance, and nozzle area ratio of each thermocouple installation.



3-3

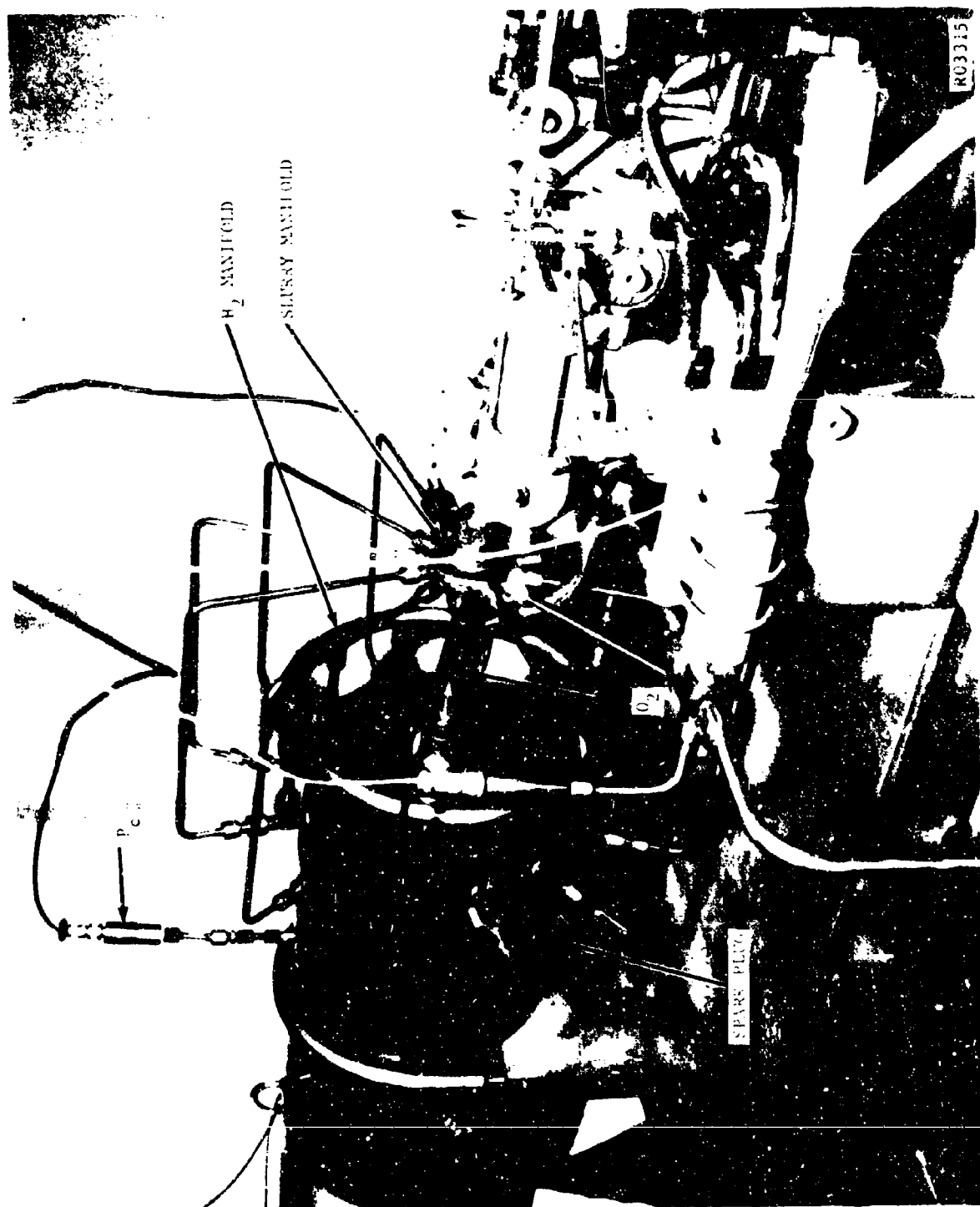


FIGURE 3-2. HEAT TRANSFER ROCKET ENGINE, INJECTOR END

3-4

MOLYBDENUM HEAT TRANSFER NOZZLE WITH:  
 CHROMEL-ALUMEL IN MOLYBDENUM,  
 "NARMAC" THERMOCOUPLE  
 1. TUNGSTEN - TUNGSTEN RHEINIUM IN  
 MOLYBDENUM, "NARMAC" THERMOCOUPLE  
 2. RHEINIUM - MOLYBDENUM, "HY CAL"  
 THERMOCOUPLE  
 3. CHAMBER RADIOMETER WITH VENTILATED  
 WINDOW  
 4.



RO3313

FIGURE 3-3. MOLYBDENUM HEAT TRANSFER NOZZLE

1/2  
 FRAMES

FE

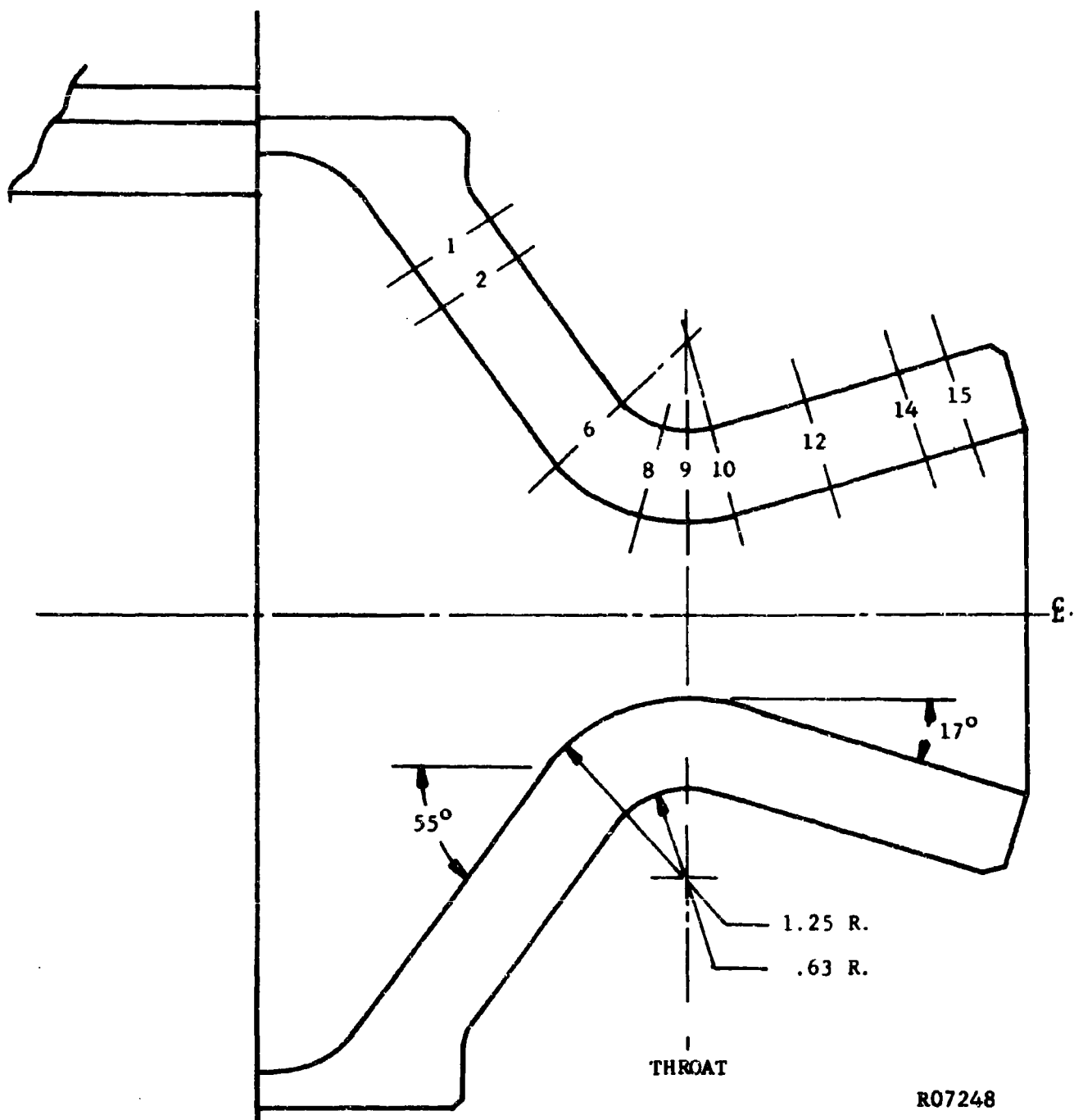


FIGURE 3-4. SURFACE THERMOCOUPLE LOCATIONS

TABLE 3.1

**MOLYBDENUM CALORIMETRIC NOZZLE GEOMETRY  
AND THERMOCOUPLE LOCATION**

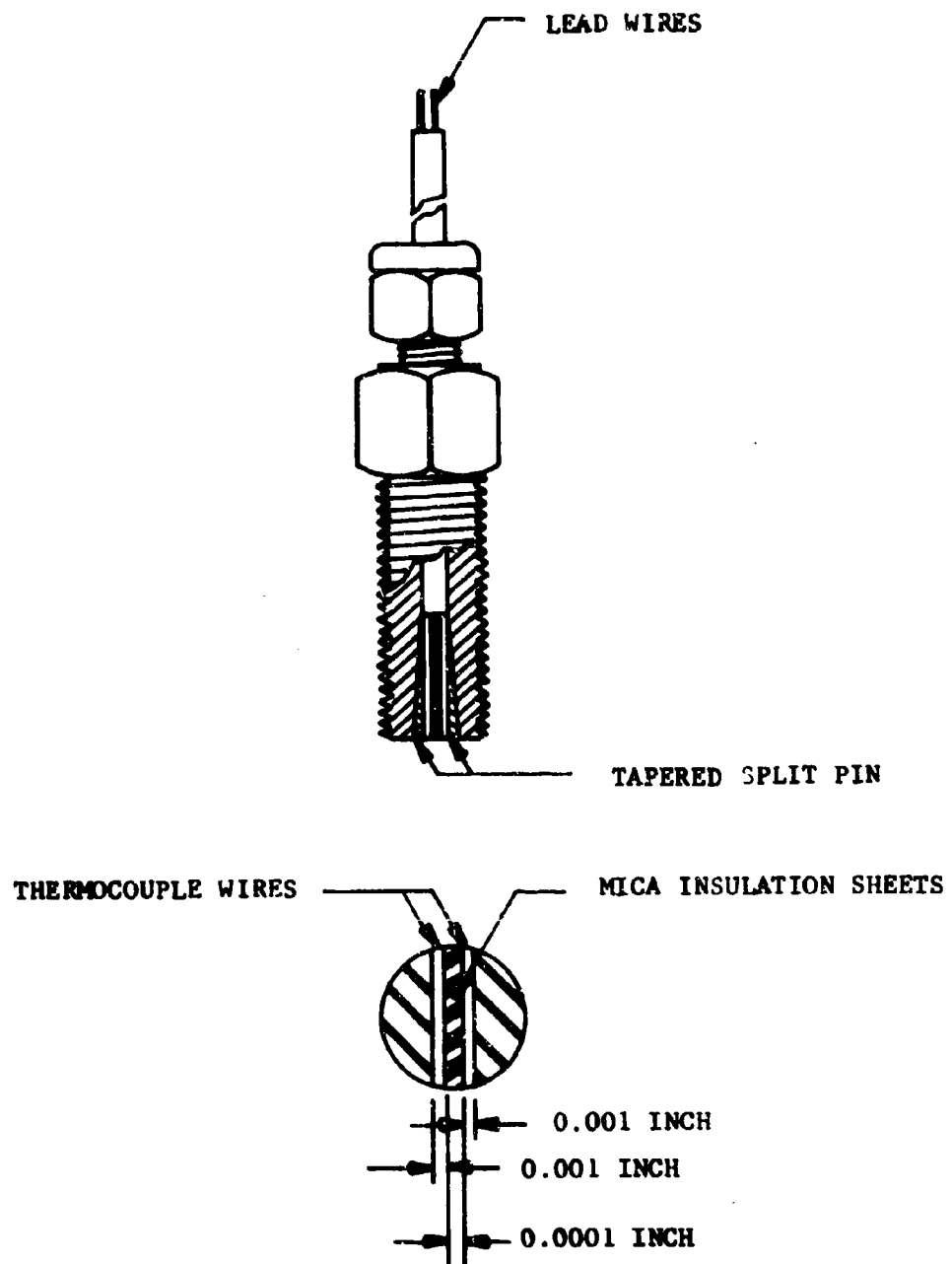
<u>Axial Distance Z, Inches</u>	<u>Radius, Inch</u>	<u>Area Ratio</u>	<u>Thermocouple Number</u>
0.418	2.405	14.8	1
0.618	2.119	11.5	2
1.290	1.159	3.44	--
1.430	0.991	2.5	6
1.990	0.667	1.14	8
2.314	0.625	1.0	9
2.638	0.667	1.14	10
2.680	0.680	1.18	--
3.318	0.867	1.92	12
3.988	1.063	2.9	14
4.328	1.162	3.47	15

Thermocouples were installed on the inside (hot) surface of the nozzle at the locations shown on Figure 3-4. During testing, many of these malfunctioned. On a typical test, data were gained from four to seven thermocouples.

Backwall thermocouples were spot-welded to the outside (cool) surface of the nozzle at four locations. Temperatures for other positions were determined by interpolation.

The majority of the thermocouples were Nanmac Model P, but a few of the same basic design made by the Thermotron Company were also used. No difference in the output of the two brands could be detected. Figure 3-5 shows the Nanmac thermocouple design. The junctions on the inside thermocouples were made flush with the nozzle to preclude surface flow disturbance. The junction was made by erosion or abrasion across the 0.0001-inch mica insulation between the two 0.001-inch thermocouple wires as shown in Figure 3-5. At hottest locations, tungsten, tungsten-rhenium junctions were used. Remaining thermocouple junctions were chromel-alumel.

In a typical test, the slurry was introduced 2.0 to 2.5 seconds after the start of hydrogen-oxygen combustion. The initial combustion period served to preheat the wall surfaces. The combustion restabilized rapidly after slurry



R07247

FIGURE 3-5. NANMAC MODEL P THERMOCOUPLE



injection and the run was normally continued for an additional two seconds. Continuous nozzle surface temperatures, chamber pressure, and flow rate data were recorded throughout each run.

To summarize the test apparatus description and run procedure, a brief tabulation is presented below:

Engine size	6" I.D. and 55" long
Throat diameter	1.25"
L*	1280"
Chamber pressure	275 psia
Injector	[12 H <sub>2</sub> + 12 slurry] on 24 O <sub>2</sub>
Propellants	
Gaseous	H <sub>2</sub> , O <sub>2</sub>
Slurry	(1) Al <sub>2</sub> O <sub>3</sub> - H <sub>2</sub> O (2) ZrO <sub>2</sub> - H <sub>2</sub> O (3) Al - CH <sub>3</sub> OH
Exhaust Solids Concentration	0 - 35%
Corresponding Solids/ Gas Ratio	0 - 0.55

### 3.3 DATA REDUCTION AND TEST RESULTS

The major step in data processing was the reduction of the transient thermocouple data to total heat flux in the nozzle. This was done on a digital computer using a modified analytical technique presented in Reference 3.1 from JPL. The equation used in the JPL analysis is for a cylindrical shape. A technique was developed to convert the analysis to conical geometry. Also, because the JPL program assumes radial conduction only, a complete 3-dimensional transient conduction analysis of the molybdenum nozzle was conducted for typical run conditions as an error check. A very versatile digital computer program termed "thermal analyzer" was used, which operates by differencing the general partial differential equation for conduction in solids. Results showed that axial conduction upstream and downstream from the throat region of the nozzle amounted to only about 5 percent of the radial heat conduction. Accordingly, it was concluded that the JPL one-dimensional analytical approach, modified for conical geometry, was sufficiently accurate for data reduction.

The radiation heat flux was estimated according to procedures explained in Section 5, and subtracted from the total to obtain heat flux due to gaseous convection and particle impingement. A "film coefficient" was then determined from the latter heat flux and the difference in fluid stagnation and wall surface temperatures. The stagnation temperature used is the theoretical flame temperature of the particular propellant combination, corrected for heat loss to the combustor walls.

The data presented is based mainly on the runs conducted during the fourth quarter of the contract period. In order to obtain proper comparisons, it was necessary to select runs on the basis of common thermocouple data. Some of the runs, therefore, were not considered for data reduction and presentation because of incomplete thermocouple recordings.

Figures 3-6, 3-7 and 3-8 show direct temperature readings at thermocouple locations 6 (inlet), 9 (throat), and 12 (exit cone), respectively, versus time elapsed from start of slurry injection. The slurry composition in these tests was alumina and water. Note that the wall temperatures remain well below the alumina solidification temperature of  $3700^{\circ}\text{F}$ . In general, the temperature response is more erratic as the solids loading ratio,  $\phi$ , is increased. The sharp peak in Figure 3-8 for  $\phi = 0.2$  indicates the presence of a local heat transfer phenomenon of an interesting transient nature due to the particles.

Figures 3-9, 3-10 and 3-11 show the film coefficients corresponding to the previous temperature data. In the inlet and throat regions, there is a definite relationship between film coefficient and alumina solids loading ratio. At the throat, the film coefficient increases by 20 to 30 percent with an increase in  $\phi$  of 0.10 to 0.20. At the inlet, the increase in film coefficient with  $\phi$  is clearly observed through most of the run times. The film coefficient increases over the  $\phi = 0$  run by 40 percent to 100 percent when injecting alumina at  $\phi = 0.30$ .

At the exit cone location (thermocouple 12), there appears to be no general correlation between solids loading ratio and film coefficient, as shown in Figure 3-11. There is, however, a very sharp momentary peak in film coefficient which calls for further investigation. Accordingly, Figure 3-12 is presented which shows the corresponding total peak heat flux at thermocouple 12. In 0.10 second, the heat flux increases from 4.0 to 13.5 Btu/sec in<sup>2</sup>. It subsequently decays to 3.5 Btu/sec in<sup>2</sup> during the remaining 0.20 second of the test.

Similar rapid increases in total heat flux were observed at inlet and throat regions during other test runs, as shown in Figure 3-13. It is hypothesized that this response is characteristic of the start-up period of solid propellant rocket operation when the nozzle walls are hot but at a temperature less than the alumina melting point. The impinging particles will converge and solidify on the wall surface until a sufficient depth of coating is formed to cause a local surface "wave" of collected molten alumina to flow downstream. On flowing downstream, the molten alumina will often pass onto an uncoated section of wall surface, causing an extreme temperature gradient and momentarily higher heat flux. After the alumina solidifies on the wall surface, the heat flux will decrease because of an insulating effect. It is probable that this process has been well represented by the heat flux data shown in Figures 3-12 and 3-13.

Figure 3-14 is a comparison of film coefficients at two circumferential locations on the throat of a canted nozzle. For this run, aluminum-methanol slurry was used to make an overall propellant aluminum content of 18.8 percent. In describing the two thermocouple locations, one should picture the canted nozzle as having one wall surface with a generally larger radius of curvature than the opposite wall. The thermocouple on this wall surface is therefore located at an "outside point." Conversely, the remaining thermocouple is located at an "inside point." As shown in Figure 3-14, the film coefficient at the outside point is about 50 percent greater than at the inside point.

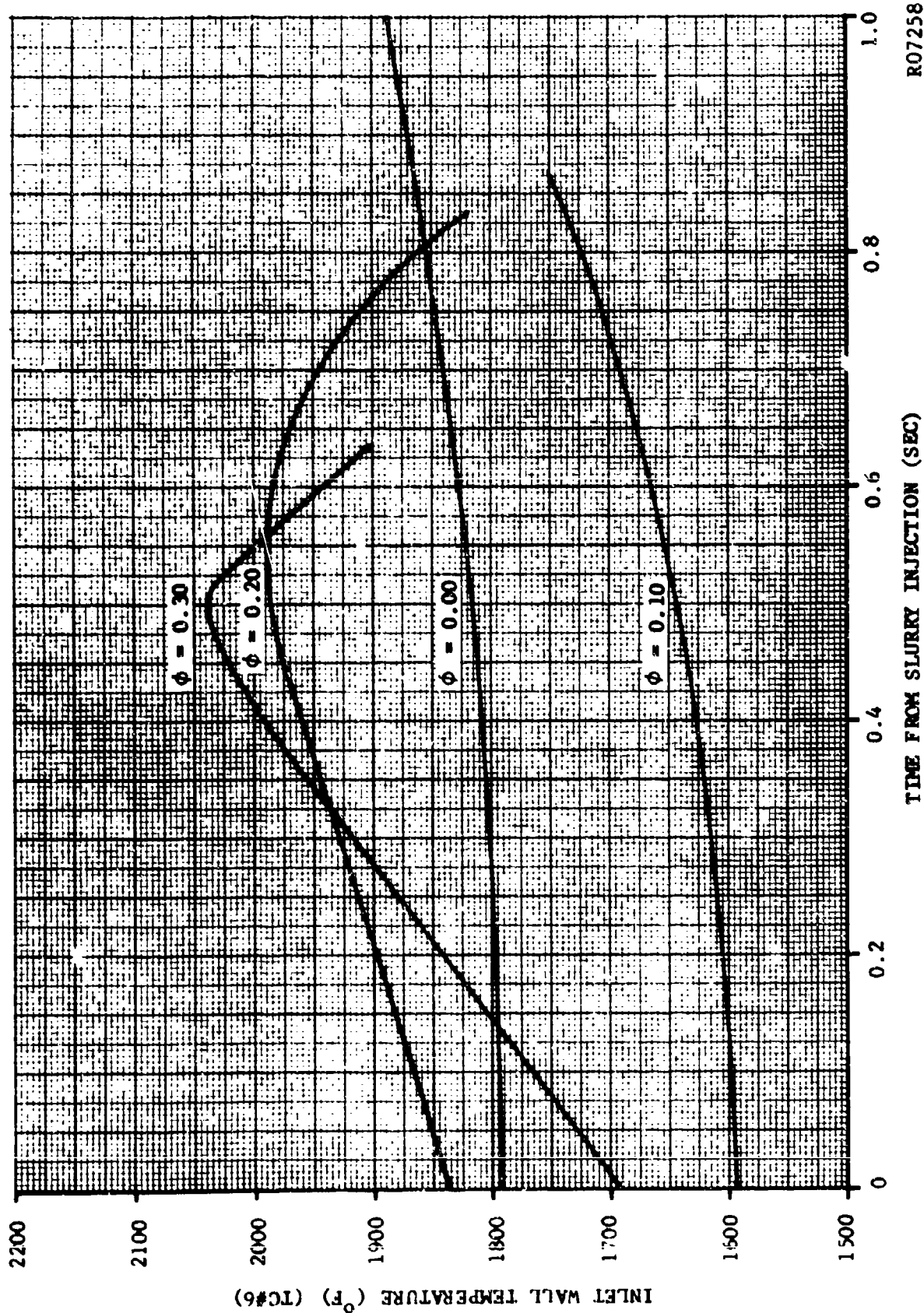


FIGURE 3-6. MEASURED INLET WALL TEMPERATURES DURING SLURRY INJECTION

R07258

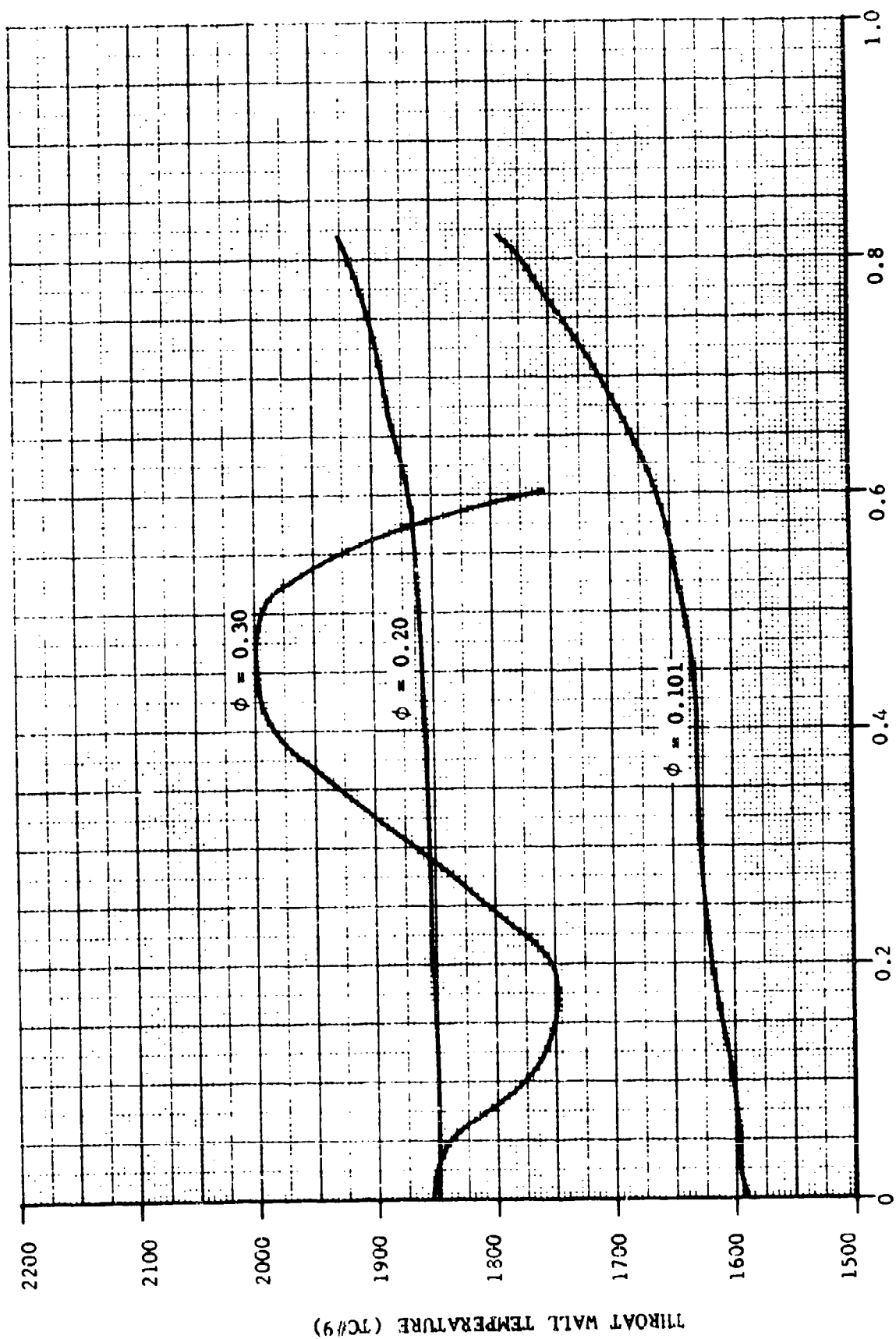
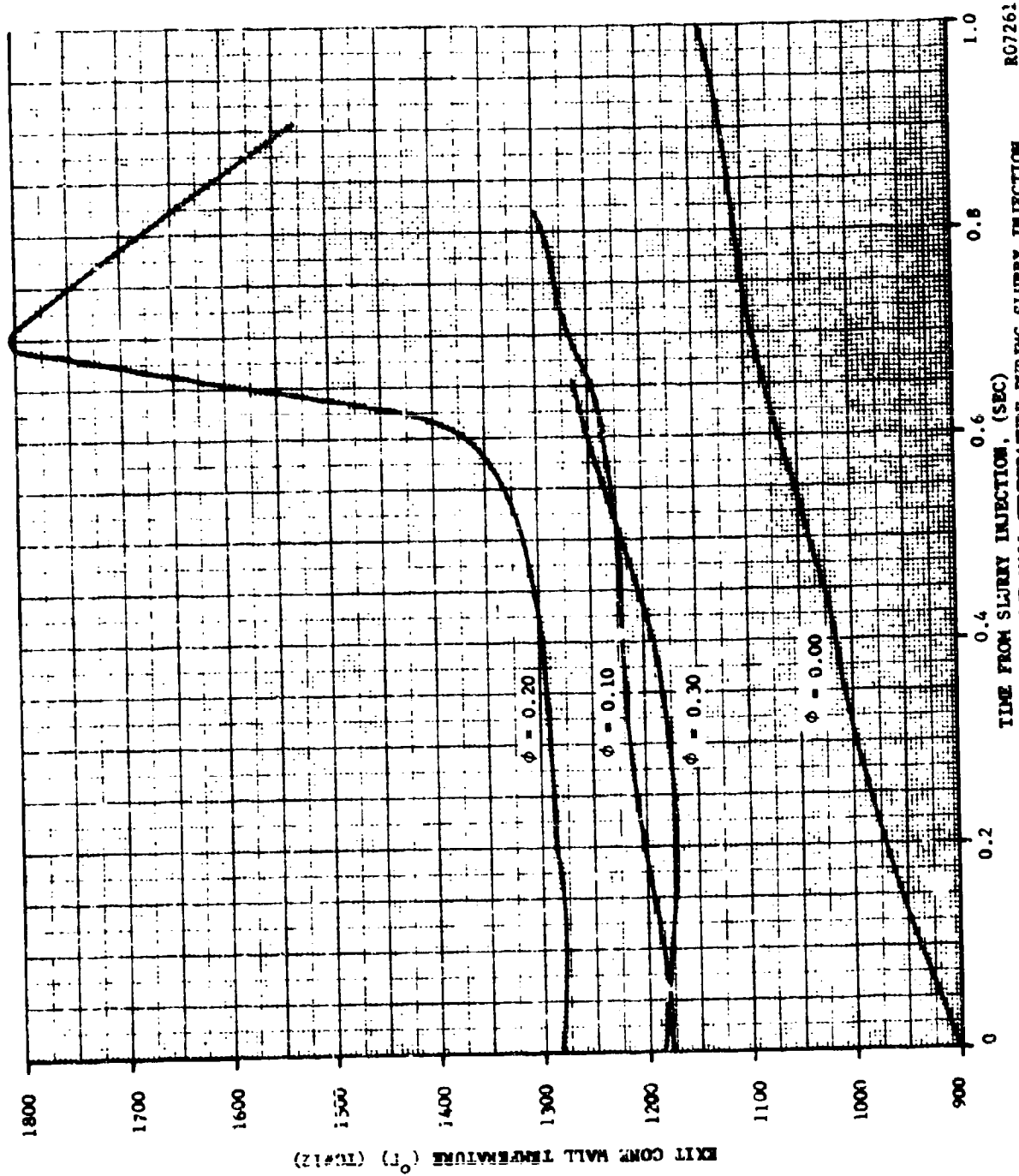


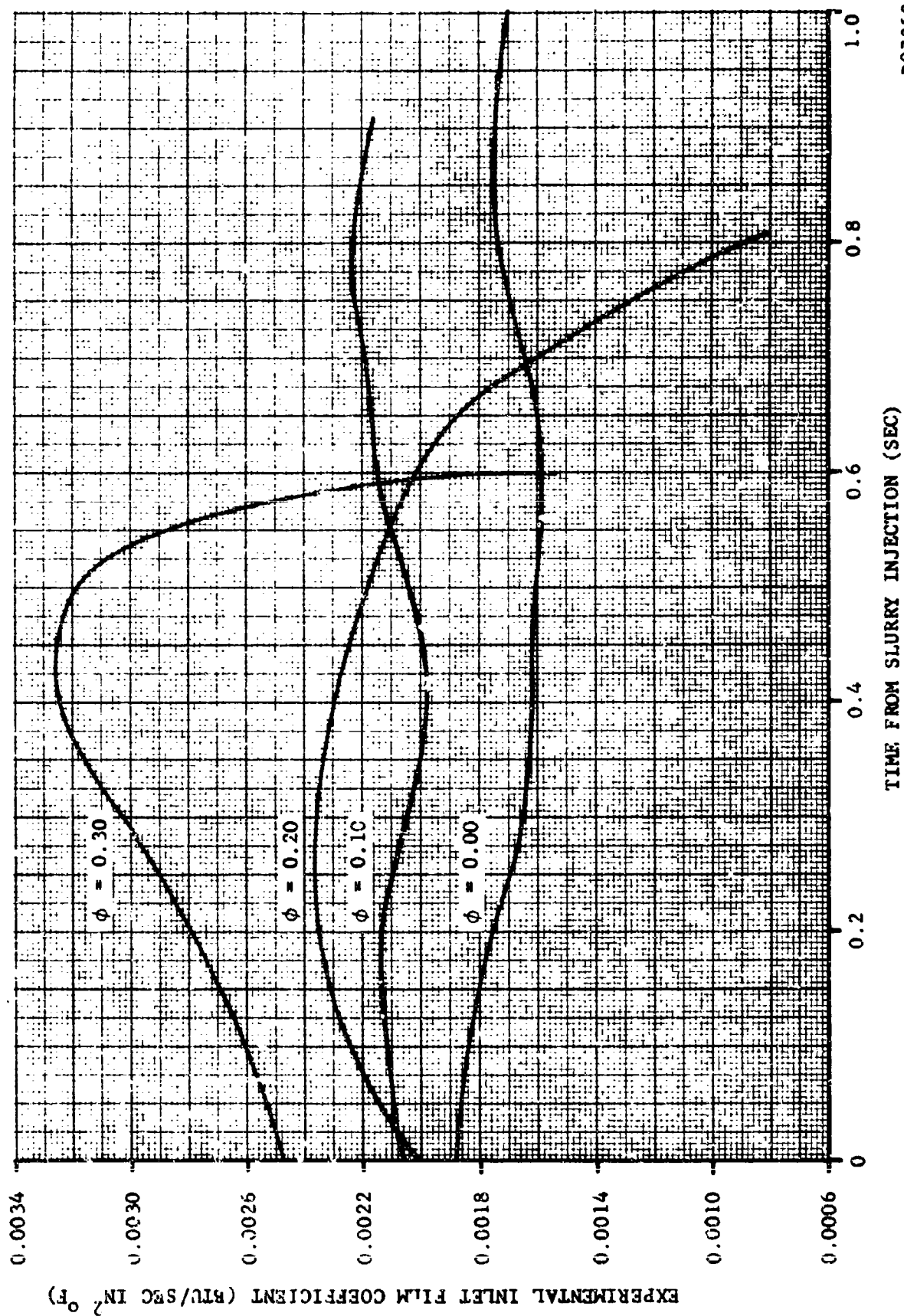
FIGURE 3-7. MEASURED THROAT WALL TEMPERATURES DURING PERIOD OF SLURRY INJECTION FOR SOLIDS LOADING RATIOS OF 0.10, 0.20, AND 0.30

R07260



R07261

FIGURE 3-8. MEASURED EXIT CORE WALL TEMPERATURE DURING SLURRY INJECTION



R07259

FIGURE 3-9. EXPERIMENTAL INLET FILM COEFFICIENT DURING PERIOD OF SLURRY INJECTION  
FOR SOLIDS LOADING RATIOS OF 0.0, 0.10, 0.20, AND 0.30

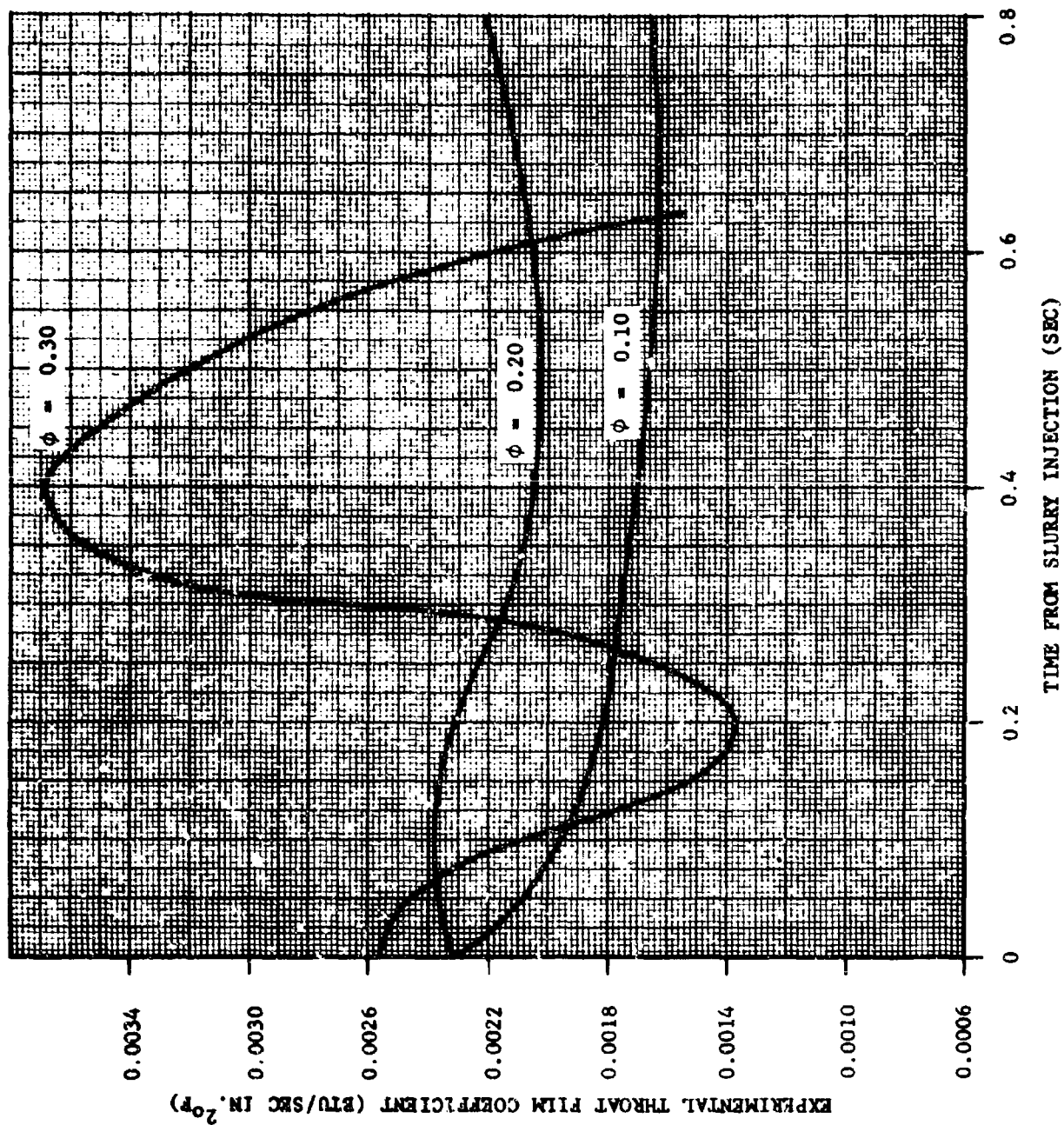


FIGURE 3-10. EXPERIMENTAL THROAT FILM COEFFICIENT VERSUS TIME FROM SLURRY INJECTION

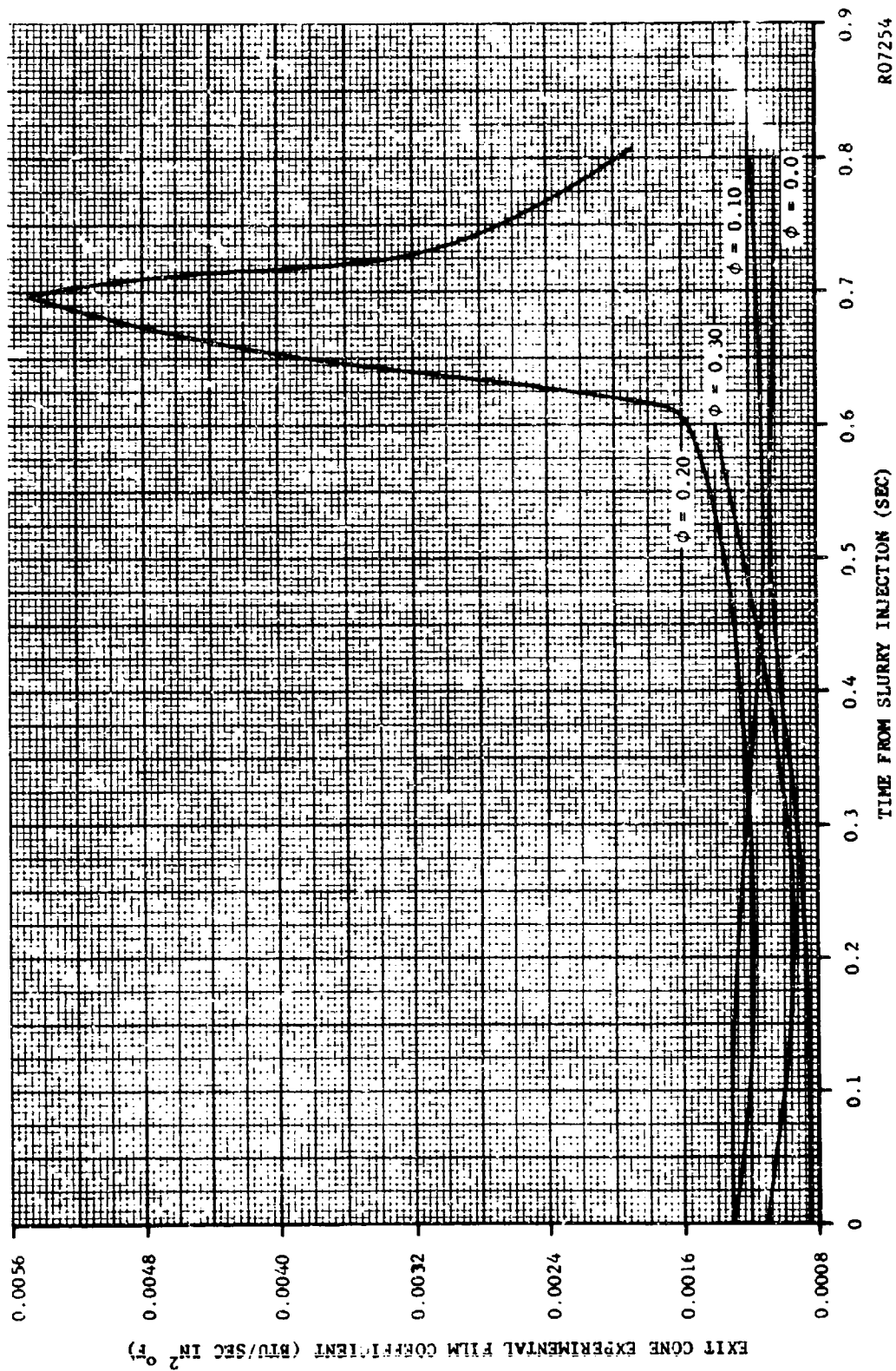


FIGURE 3-11. EXIT CONE FILM COEFFICIENT DURING SLURRY INJECTION

R07254



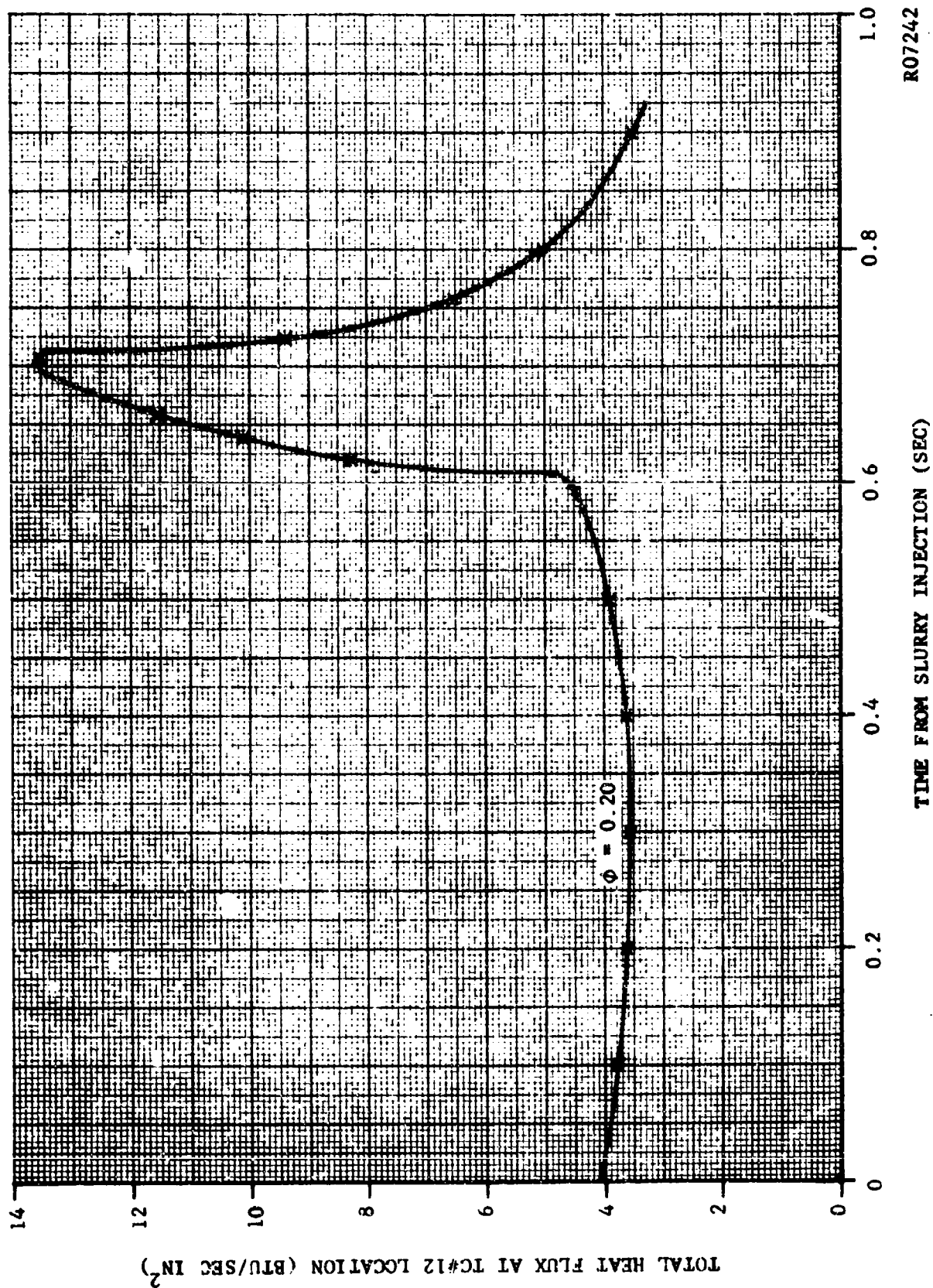
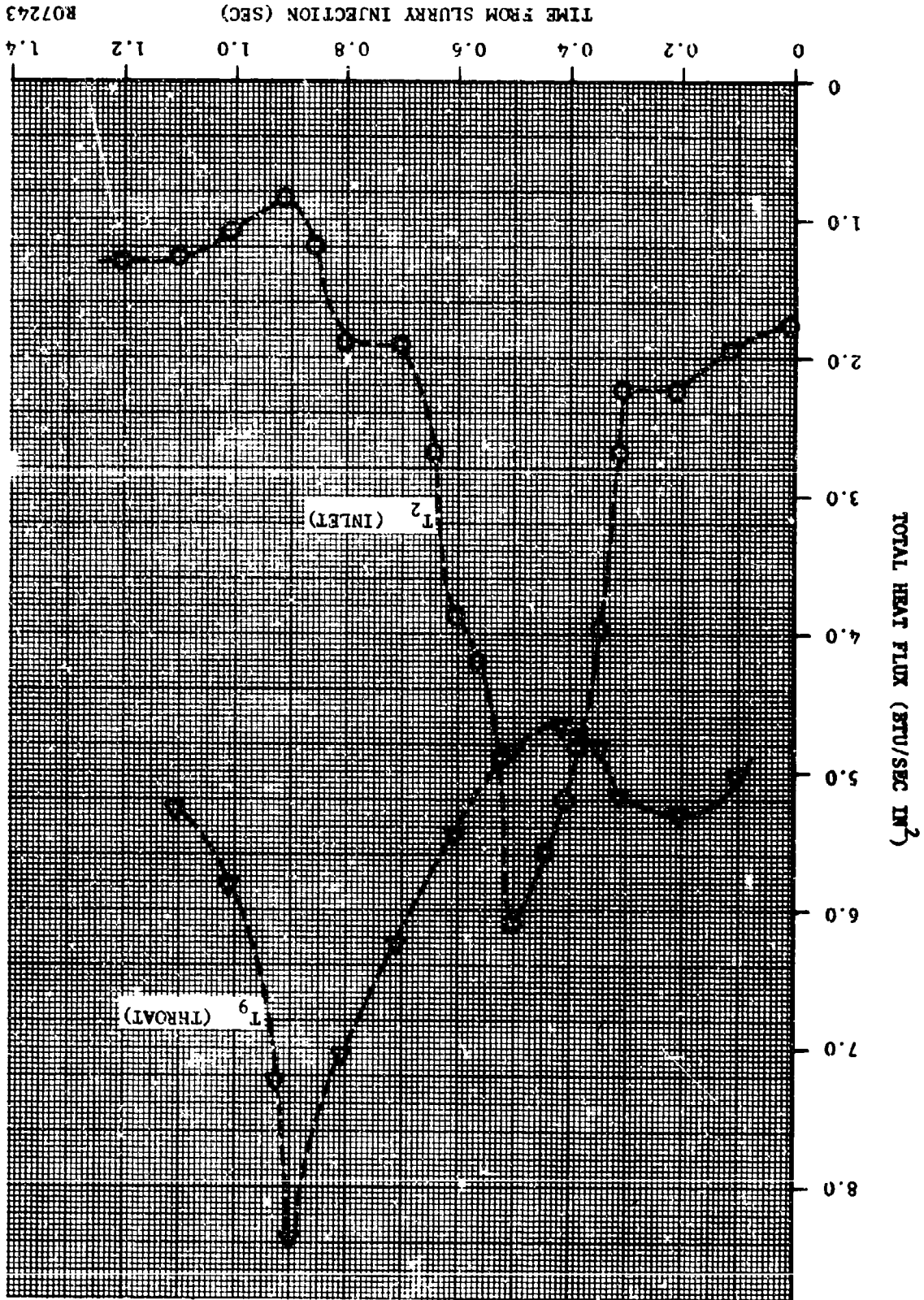


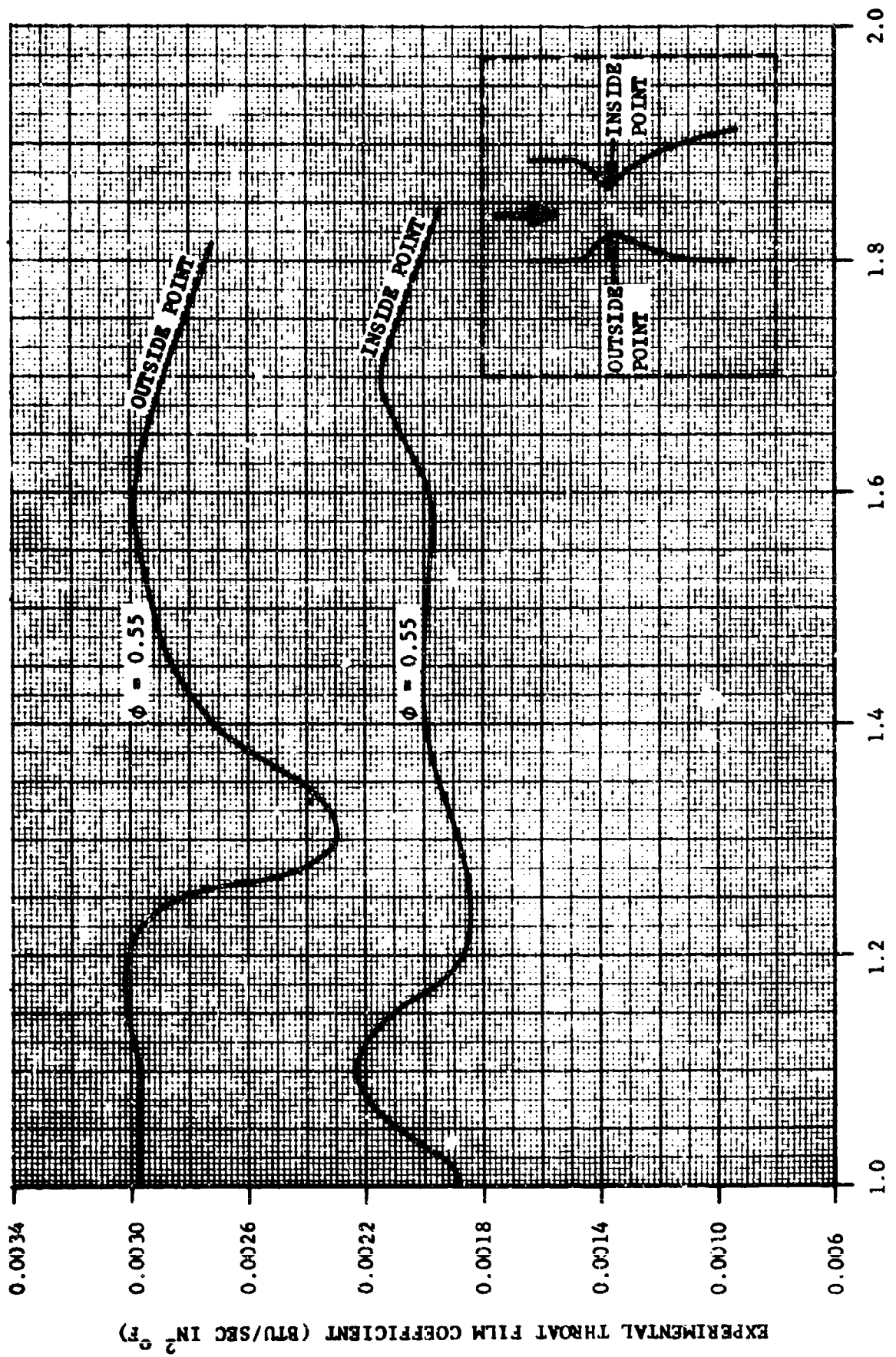
FIGURE 3-12. TOTAL HEAT FLUX AT EXIT CONE LOCATION DURING SLURRY INJECTION

R07242

FIGURE 3-13. TRANSIENT TOTAL HEAT FLUX TO SIMULATOR NOZZLE



R07243



RUN TIME (SEC)

FIGURE 3-14. THROAT FILM COEFFICIENTS FOR CANTED NOZZLE

R07241

- (1) Gaseous convection.
  - (2) Particle behavior in the flow.
  - (3) Wall coating due to impingement, adherence, and collection of particles.
  - (4) Thermal radiation.
- Testing has revealed that heat transfer from typical solid propellant exhausts to nozzle wall surfaces is physically complex. Of the following four basic mechanisms that govern the heat transfer, the unique details of (2) and (3) have been determined from the test program.
- A unique hot firing test system has been developed which permits detailed measurement of transient heat transfer along nozzles subject to solid propellant exhaust environment.

### 3.4 CONCLUSIONS

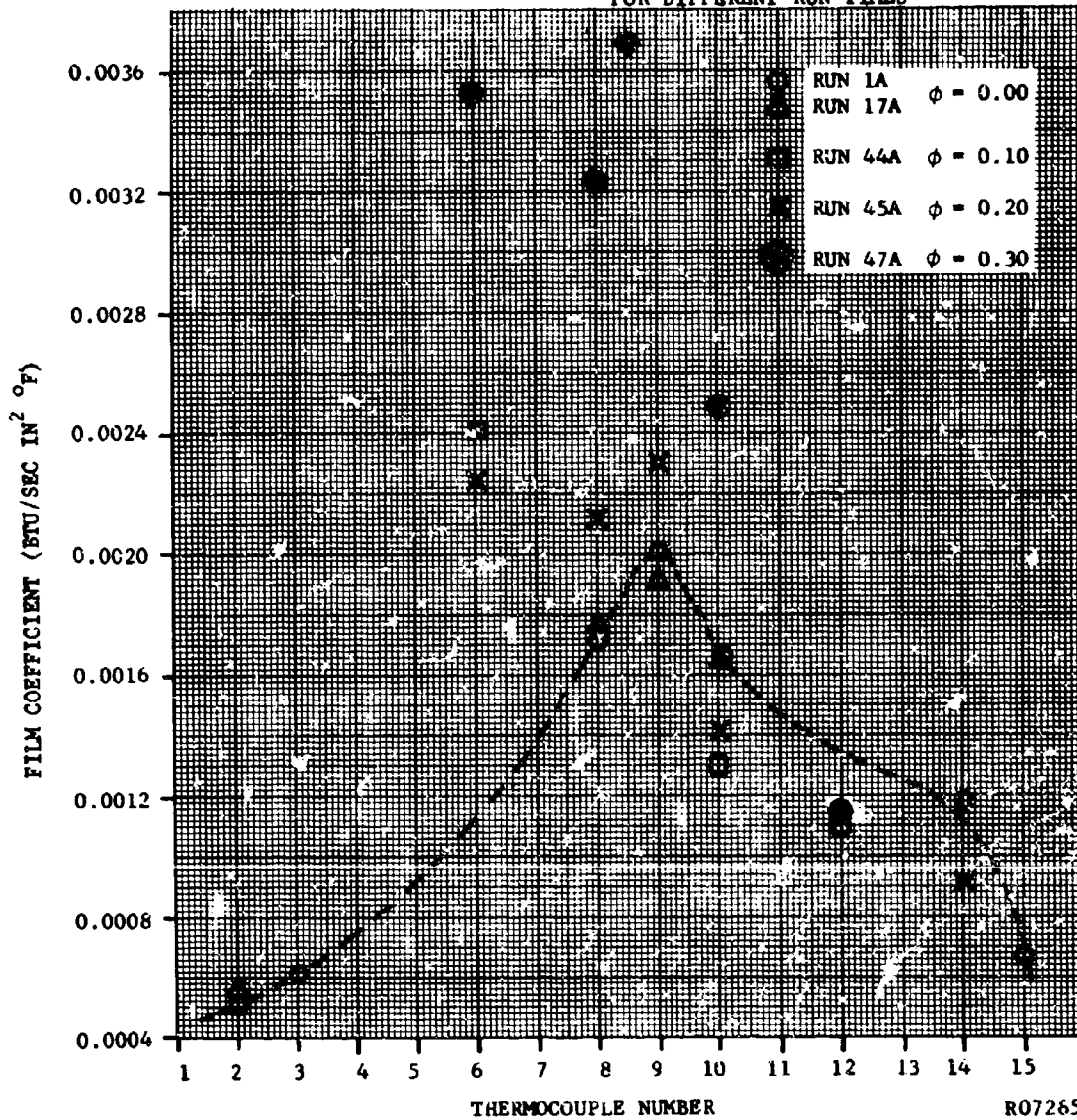
Several runs were conducted using slurries of aluminum powder and methanol to allow the study of the case of burning aluminum. The total heat flux for inlet (thermocouple 6) and exit cone (thermocouple 14) locations are shown on Figure 3-17 versus run time. The solids loading ratio for this run was 0.55. The erratic behavior of the inlet heat flux reflects presence of alumina wall coating. The exit cone heat flux appears more uniform during the run, suggesting that wall coating is minimized.

Figure 3-16 illustrates film coefficients at peak magnitudes of heat flux for thermocouple numbers from 2 to 14 for runs with alumina and zirconia slurries. As in Figure 3-15, this data is a source of information rather than a correlation with nozzle geometry. The zirconia particles were selected for comparison with alumina particles because they remain solid at the predicted combustion temperatures while alumina is molten. It appears that peak film coefficients with zirconia slurry are not as sensitive to solids loading ratio as alumina. In general, there appears to be no great difference in maximum film coefficients for zirconia with  $\phi = 0.2$  and  $\phi = 0.4$ . The chief difference between alumina coating phenomenon, which appears at the inlet section for the data of Figure 3-16, and alumina particle effects is the previously illustrated transient zirconia and alumina particle effects is the previously illustrated transient alumina coating phenomenon, which appears at the inlet section for the data of Figure 3-16.

Figure 3-15 shows film coefficients corresponding to maximum levels of heat flux recorded during several runs versus thermocouple locations, from thermocouple 2 to thermocouple 15. Because each film coefficient occurs at a different run time, Figure 3-15 is not to be used as a strict correlation for nozzle geometry, but only as a source of data presentation. In general, it shows that solid particles have the greatest influence in the entrance and throat regions of the nozzle. In the exit cone maximum values of film coefficient remained nearly the same for  $\phi = 0.2$  to  $0.30$ .

NOTE:

1. DATA POINTS AT EACH POSITION TAKEN  
FOR DIFFERENT RUN TIMES



R07285

FIGURE 3-15. FILM COEFFICIENTS AT PEAK MAGNITUDES OF HEAT FLUX  
VERSUS THERMOCOUPLE NUMBER

NOTE: DATA POINTS AT EACH POSITION TAKEN  
FOR DIFFERENT RUN TIMES

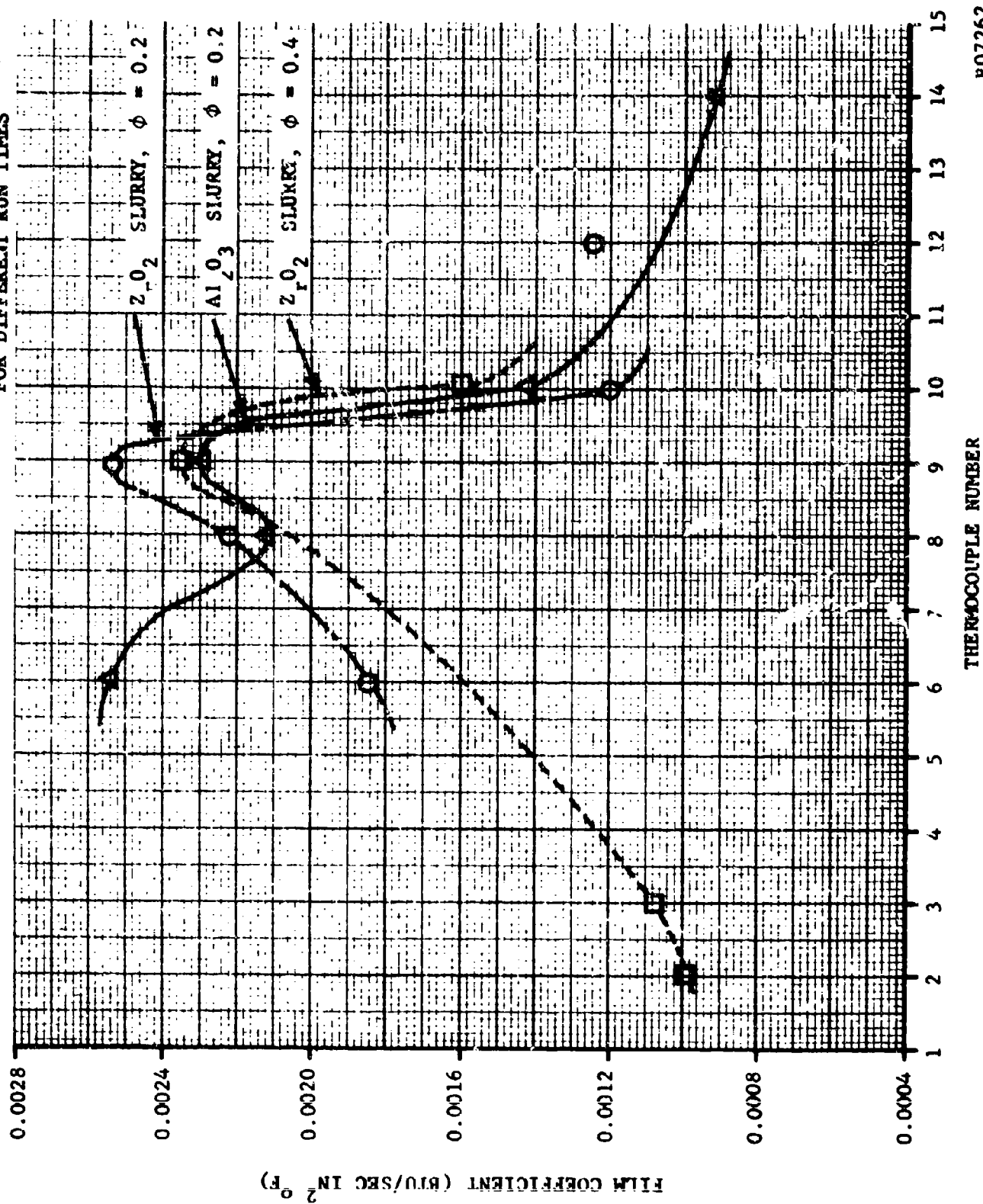


FIGURE 3-16. FILM COEFFICIENTS AT PEAK MAGNITUDES OF HEAT FLUX VERSUS THERMOCOUPLE NUMBER

R07262

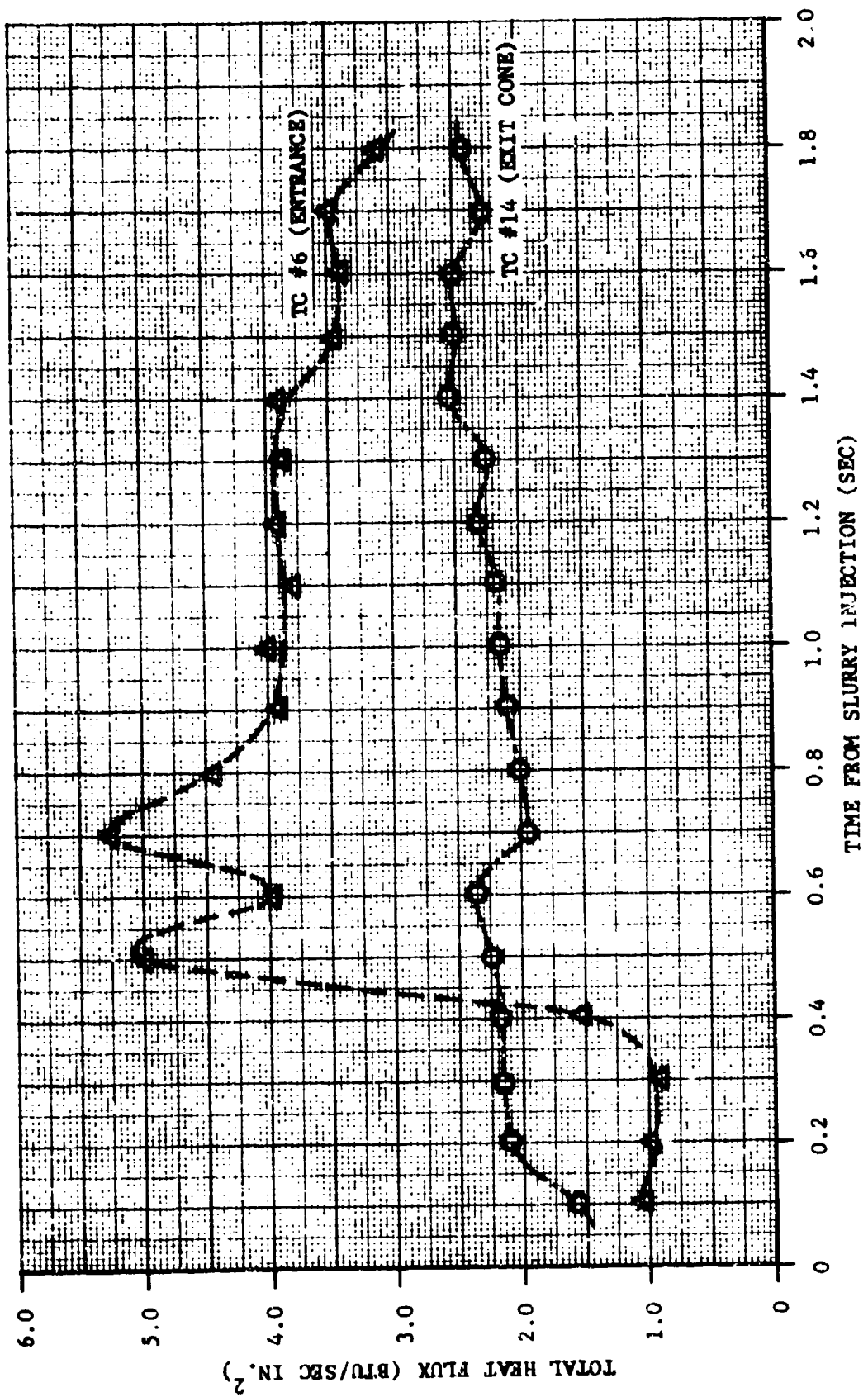


FIGURE 3-17. TOTAL HEAT FLUX AT ENTRANCE AND EXIT CONE LOCATIONS FOR ALUMINUM BURNING PROPELLANTS (18.8% ALUMINUM)



## 3.5 REFERENCES

## 3.1

Powell, W. B., Howell, G. W., Irving, J. P., A Method for the Determination of Local Transient Heat Flux in Uncooled Rocket Motors, Jet Propulsion Laboratory Technical Report No. 32-257, July 1, 1962.

The test results with canted geometry revealed that significant circumferential variation in heat transfer film coefficients--up to 50 percent--occur at the throat. For this test, aluminum slurry was injected at a solids loading ratio of 0.55.

Briefly summarizing some additional test results, it was observed that the exit cone heat transfer rates were less sensitive to solids loading and there was less tendency toward erratic behavior of heat flux due to wall coating. The latter is shown in Figure 3-17 where aluminum is burned at solids loading ratio of 0.55.

Thermal radiation heat transfer to the nozzle walls is significant in the chamber areas, but unimportant in the exit cone region, and is described in Section 5.

Briefly summarizing some additional test results, it was observed that the exit cone heat transfer rates were less sensitive to solids loading and there was less tendency toward erratic behavior of heat flux due to wall coating. The latter is shown in Figure 3-17 where aluminum is burned at solids loading ratio of 0.55.

At the higher particle concentrations ( $\phi = 0.2$  and up), wall coating effects on heat transfer become very important. As previously discussed, the wall coating can build up to a depth sufficient to initiate development of an advancing wave of liquid alumina along the nozzle wall. The resulting extreme temperature gradients will produce the momentarily very high peaks in heat flux as shown in Figures 3-12 and 3-13. The final result of wall coating is a drop in heat flux because the alumina behaves as an insulator upon solidification. The heat transfer associated with wall coating is not predictable because of its purely local and extremely transient nature. For this reason, development of general correlations relating overall heat transfer to nozzle walls is not feasible for the present sets of test conditions. Should the alumina wall coating and solidification not occur, the overall heat transfer data could probably be generalized into a correlation. This may be true, for example, of operation at wall temperatures in excess of the alumina melting point.

At the higher particle concentrations ( $\phi = 0.2$  and up), wall coating effects on heat transfer become very important. As previously discussed, the wall coating can build up to a depth sufficient to initiate development of an advancing wave of liquid alumina along the nozzle wall. The resulting extreme temperature gradients will produce the momentarily very high peaks in heat flux as shown in Figures 3-12 and 3-13. The final result of wall coating is a drop in heat flux because the alumina behaves as an insulator upon solidification. The heat transfer associated with wall coating is not predictable because of its purely local and extremely transient nature. For this reason, development of general correlations relating overall heat transfer to nozzle walls is not feasible for the present sets of test conditions. Should the alumina wall coating and solidification not occur, the overall heat transfer data could probably be generalized into a correlation. This may be true, for example, of operation at wall temperatures in excess of the alumina melting point.

Gasous convection is represented by the zero solids loading ratio data for the nozzle inlet (Figure 3-9) and exit cone (Figure 3-11). This type of nozzle heat transfer has been well documented and correlated. With the addition of particles to the flow, and in the absence of wall coating, regular increases of heat flux and convective film coefficients are observed. This is particularly evident in entrance and throat sections as shown in Figures 3-9 and 3-10. This is probably due to migration of the fluid boundary layer by particles. Similar observations of increased convective heat transfer with solid particle addition have been observed and correlated by both Farber and Morley (3.2), and Babcock and Wilcox Company (3.3) for subsonic flow in straight tubes.



- 3.2 Farber, L. and Morley, M. J., "Heat Transfer to Flowing Gas-Solids Mixtures in a Circular Tube," Ind. and Eng. Chemistry 49, pp. 1143-1150, July 1957.
- 3.3 Babcock and Wilcox Co., "Gas-Suspension Task II Final Report," and "Supplement," BAW-1201 and BAW-1207, respectively, 1960.

## SECTION 4

### ALUMINA PARTICLE EMISSIVITY - EXPERIMENTAL

#### 4.1 INTRODUCTION

In order to evaluate the radiative heat transfer characteristics of gas-particle clouds, knowledge of the particle emissivities at elevated temperatures is required. One of the objectives of this study has been to determine experimentally the spectral emissivity of alumina at temperatures ranging from the melting point ( $2320^{\circ}\text{K}$ ) to about  $2900^{\circ}\text{K}$ . The experiments were conducted using a carbon-free system in which a slurry containing only  $\text{Al}_2\text{O}_3$  and water was added to a gaseous hydrogen-oxygen flame (details of the experimental procedure are presented in Subsection 4.3).

Measurement of alumina emittance was approached in two different ways. First, an attempt was made to measure the radiation emitted from the gas-particle cloud at a location within the chamber of the test motor. It was felt that the thermodynamic state of the system could be more accurately defined at this position due to the lack of thermal lag between the particles and the gas. Also, higher temperatures could be obtained in the chamber than at the exit of an expansion nozzle. The second method consisted of measuring the emitted radiation at the exit of a throatless motor operated so as to produce a hot subsonic flow. This motor was designed to produce approximately 100 pounds of thrust at a chamber pressure of 600 psia with the nozzle in place; firings made without the nozzle were at atmospheric pressure.

In addition to the alumina emissivity tests, a series of runs was made for which the emission spectra of other radiators were observed. That is, substances such as carbon, iron oxide, and aluminum were added to the flow, and their effects on the emission spectra noted. The carbon was introduced both in particulate form (carbon black) and as liquid hydrocarbons ( $\text{C}_6\text{H}_6$  and  $\text{CH}_3\text{OH}$ ), while the iron oxide ( $\text{Fe}_2\text{O}_3$ ) and aluminum were introduced as solid particles only.

The spectra resulting when carbon was added as a solid differed markedly from those produced when a hydrocarbon was added, but since little is known of the combustion processes involved, it is difficult to attribute the results to a specific phase of the element. The effects of varying the concentration of solid  $\text{Fe}_2\text{O}_3$  in the flow were also shown.

#### 4.2 THEORY\*

The measurement of the alumina emittance is accomplished by measuring the spectral steradiancy of the alumina cloud and comparing this with the calibration steradiancy of a tungsten lamp. The cloud steradiancy may be converted to the average, or weighted, emittance of the individual particles through knowledge of the particle size distribution, mass flow rate, and gas properties at the point of measurement.

For the present study, measurements were made at wavelengths for which no gas emission bands exist ( $\lambda = 1.4, 1.78, \text{ and } 2.33\mu$ ). At other wavelengths, account must be taken of the emission and absorption characteristics of the gas, and the analysis necessarily becomes more complex. An account of the theoretical expressions for this case is presented in the Appendix.

The steradiancy of an optically thin, homogeneous (in temperature and concentration) cloud over a one dimensional path of unit area and length  $L$  is, at wavelength  $\lambda$ ,

$$R_{\lambda} = R_{\lambda}^0 \left[ L \int_0^{\infty} \epsilon_{\lambda}(r) N(r) \pi r^2 dr \right] \frac{\text{watts}}{\text{cm}^3 \text{ str}} \quad (4.1)$$

where  $\epsilon(r)$  is the size (and temperature) dependent spectral emittance of an individual particle of radius  $r$ . The size distribution may be characterized by a distribution function  $\phi(r)$ , where

$$\phi(r) = \frac{N(r)}{\tilde{N}} \quad (4.2)$$

so that Equation (4.1) becomes

$$R_{\lambda} = R_{\lambda}^0 \left[ L \tilde{N} \int_0^{\infty} \epsilon_{\lambda}(r) \phi(r) \pi r^2 dr \right] \frac{\text{watts}}{\text{cm}^3 \text{ str}} \quad (4.3)$$

\*Please turn to page 4-29 for foldout page of symbols.

The total number of particles of all sizes per unit volume,  $\tilde{N}$ , is given by the formula

$$\tilde{N} = \frac{\phi \rho}{\bar{w}} \quad (4.4)$$

where the average weight  $\bar{w}$  is

$$\bar{w} = \frac{\int_0^{\infty} N(r) w(r) dr}{\int_0^{\infty} N(r) dr}$$

$$= \frac{\int_0^{\infty} \Phi(r) w(r) dr}{\int_0^{\infty} \Phi(r) dr}$$

$$= \int_0^{\infty} \Phi(r) w(r) dr \quad \frac{\text{grams}}{\text{particle}} \quad (4.5)$$

since  $\int_0^{\infty} \Phi(r) dr = 1.$

The emittance of the individual particles is a function of particle size as shown by Equation (4.3). In order to obtain a clearer presentation of experimental results, an average, or weighted, emittance,  $\bar{\epsilon}_\lambda$ , is defined:

$$\bar{\epsilon}_\lambda = \frac{\int_0^\infty \epsilon(r) \phi(r) \pi r^2 dr}{\int_0^\infty \phi(r) \pi r^2 dr} \quad (4.6)$$

Equation (4.3) becomes, with Equations (4.4) and (4.6)

$$R_\lambda = R_\lambda^0 \left[ L \frac{\phi \rho}{\dot{w}} \bar{\epsilon}_\lambda \int_0^\infty \phi(r) \pi r^2 dr \right] \frac{\text{watts}}{\text{cm}^3 \text{ str}} \quad (4.7)$$

Equation (4.7) is the basis for determination of  $\bar{\epsilon}$  with the measurement of the cloud steradian,  $R$ . The quantities  $\phi$  and  $L$  are obtained from flow rate and geometry measurements,  $\rho$  and  $R^0$  from calculations of the state of the gas at the point of measurement, and the size distribution integral from prerun size distribution measurements. The actual data reduction techniques and equations are presented in another report.<sup>4.1</sup>

The methods of obtaining  $\rho$ ,  $R^0$ , and size distribution information were as follows. The state of the gas is calculated from theoretical data modified for heat transfer losses. Figure 4-1 shows the theoretical chamber temperature of the  $\text{H}_2 - \text{O}_2 - \text{H}_2\text{O}/\text{Al}_2\text{O}_3$  system plotted against oxidizer-to-fuel (O/F) ratio for various values of the parameters  $\phi$  and  $\psi$ . The flow is kept from accelerating and thus causing an expansion temperature drop by lowering the flow rate until the pressure drop along the chamber is small. Experimental measurement of the heat transfer losses was made by measuring chamber coolant inlet and outlet temperatures\*; the chamber temperature drop due to heat transfer then could be calculated. Some independent tests of this calculation were made by using the sodium line reversal technique to measure the gas temperature directly. The results of both the calculation and the measurement showed a relatively small loss in temperature, about 100°K in 3000°K. Therefore, as a matter of routine, the chamber temperature was taken to be the theoretical

---

\* This measurement also sufficed to indicate when steady state was reached.

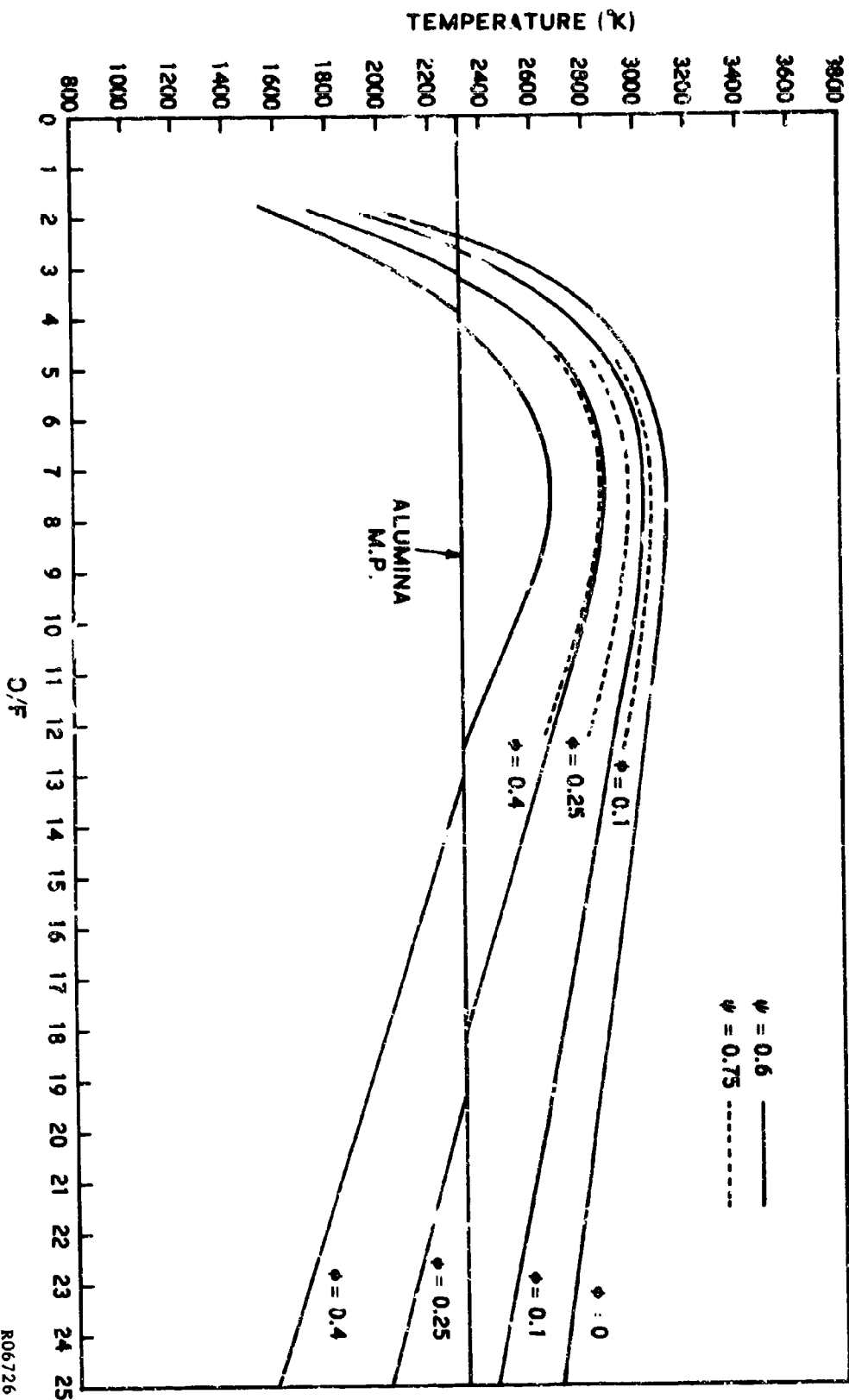


FIGURE 4-1. CHAMBER TEMPERATURE VERSUS O/F FOR  $H_2 - O_2 - H_2C/A1_2O_3$  SYSTEM

temperature less 100°K. This embodies the assumption that the heat transfer does not change significantly when particles are added, as the chamber pressure measurement was made for the gas-only system. This should be a valid assumption since the coolant temperature did not rise significantly between the gas-only and the gas-particle cases, and also because the radiative transfer could not be too much different for the two cases as can be seen by examining the spectra.

In order to determine the gas density from the equation of state, molecular weight values computed from an equilibrium flow thermochemical computer program were used in conjunction with the measured static pressure and temperature values determined as described above. This computer program also produced the temperature data of Figure 4-1.

The size distribution was examined in three different ways. First, samples of the unfired powder were run through a Micromerograph size analyzer which indicated cumulative weight versus size, and these results were analyzed by successive graphical differentiation to get a number histogram. This was in turn normalized by dividing the total area under the curve to get  $\Phi(r)$ . The resultant distribution function pertinent to these tests is shown in Figure 4-2.

Secondly, the particles were collected by a shutter probe placed on the exhaust axis about 15 feet from the exit plane. The collected samples were observed under an optical microscope and qualitative information concerning the size and shape of the particles was recorded. In most cases, the collected particles were spherical in shape.\* The largest collected particles appeared to be about 10 microns in diameter, which agreed with the distribution of Figure 4-2.

The third check of particle size distribution was obtained by measuring the attenuation of light incident upon the particle cloud (transmission tests). The transmitted lamp spectral steradiancy is

$$H_{\lambda} = H_{o_{\lambda}} e^{-L \int_0^{\infty} Q_{\lambda}^{(e)}(r) N(r) \pi r^2 dr} \quad \frac{\text{watts}}{\text{cm}^3 \text{ str}} \quad (4.8)$$

which becomes, with Equations (4.2) and (4.4),

$$H_{\lambda} = H_{o_{\lambda}} e^{-\frac{L \phi \rho}{w} \int_0^{\infty} Q_{\lambda}^{(e)}(r) \Phi(r) \pi r^2 dr} \quad \frac{\text{watts}}{\text{cm}^3 \text{ str}} \quad (4.9)$$

---

\*This also provided an independent check of the theoretical temperatures since particles fired at O/F's giving chamber temperatures below the melting point of alumina were not spherical, but angular like those put into the slurry.

112  
NAMES

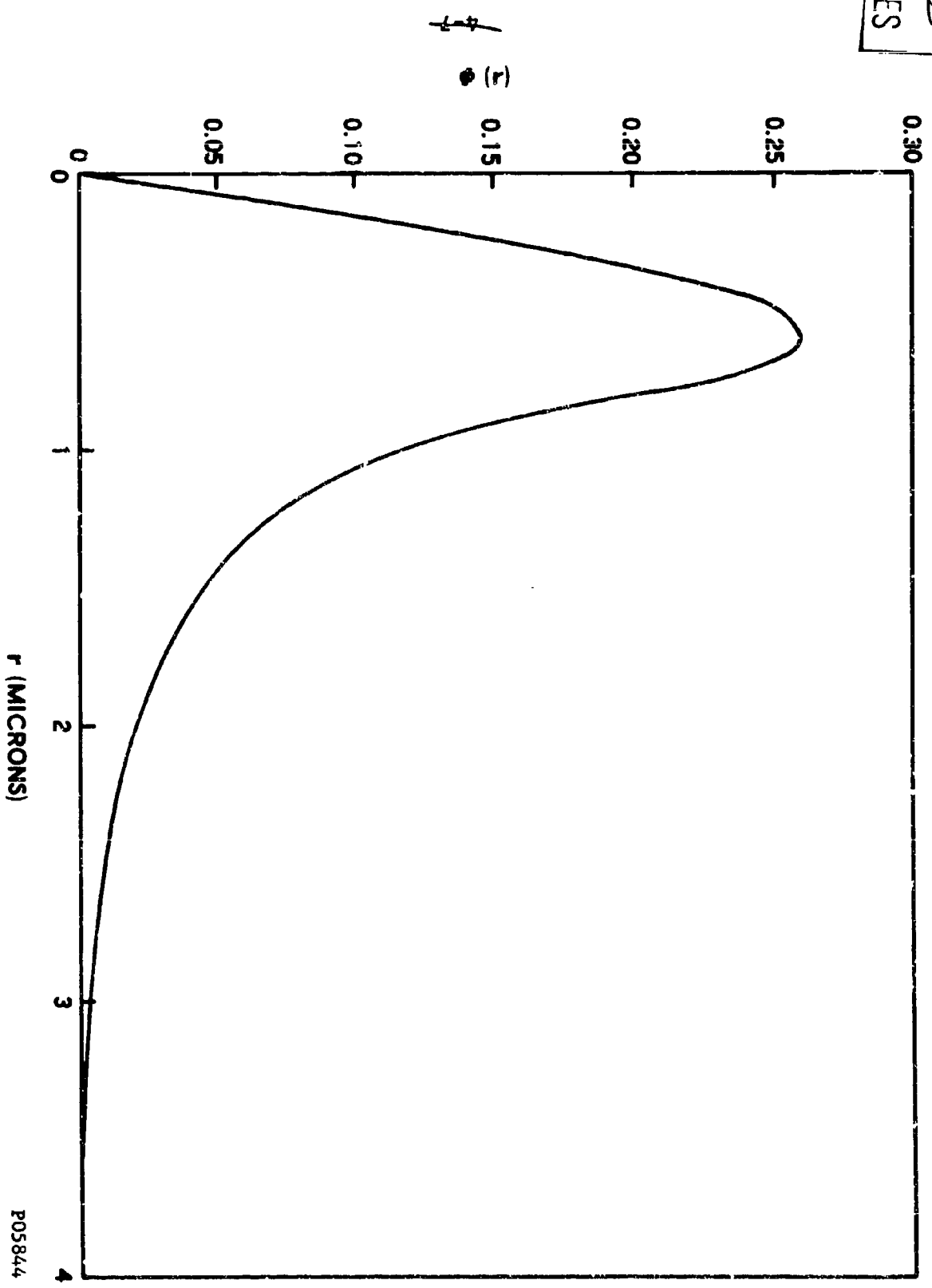


FIGURE 4-2. PARTICLE DISTRIBUTION FUNCTION VERSUS PARTICLE RADIUS

P05844



Information on  $Q^{(e)}(r)$  near the melting point of alumina is available from results of Burch and Cryvna<sup>4.2</sup> used in conjunction with the Philco Mie scattering program. In analogy to Equation (4.6), an expression for a weighted extinction efficiency factor may be written:

$$\overline{Q_{\lambda}^{(e)}} = \frac{\int_0^{\infty} Q_{\lambda}^{(e)}(r) \Phi(r) \pi r^2 dr}{\int_0^{\infty} \Phi(r) \pi r^2 dr} \quad (4.10)$$

and Equation (4.9) may be written

$$H_{\lambda} = H_{o_{\lambda}} e^{-\frac{L \Phi \rho}{w} \overline{Q_{\lambda}^{(e)}} \int_0^{\infty} \Phi(r) \pi r^2 dr \frac{\text{watts}}{\text{cm}^3 \text{ str}}} \quad (4.11)$$

The quantity  $\overline{Q^{(e)}}$  is not too sensitive to size distribution for the large particles (geometrical optics region) of this investigation, and thus the nominal values of  $Q^{(e)}(r)$  based on Burch's data and Equation (4.9) provide a measure of

$$\int_0^{\infty} \Phi(r) \pi r^2 dr$$

That is to say, the original distribution, Figure 4-2, is used with  $Q^{(e)}(r)$  to get  $\overline{Q^{(e)}}$ , and  $\overline{Q^{(e)}}$  is used in conjunction with Equation (4.11) and the experimental transmission measurement to check

$$\int_0^{\infty} \Phi(r) \pi r^2 dr$$

In the Mie region, this would not be possible as  $\overline{Q^{(e)}}$  would be highly dependent upon the distribution. The actual data reduction scheme used in analysis of the transmission tests is also described in Reference 4.1.

Note that the expressions derived in this subsection are actually for throatless motor experiments and for the chamber radiancy measurements in which a no-lag condition exists. However, by proper application of the gas-particle velocity ratios to Equation (4.4) the correct value for the particle number density,  $\tilde{N}$ , can be determined for the expansion nozzle case in which considerable velocity lag may exist between the gas and the particles. Accounting for the thermal lags, which also exist for this case, is not trivial, however. For this reason the experiments were conducted under the no-lag conditions where the state of the gas and particles could be more easily determined.

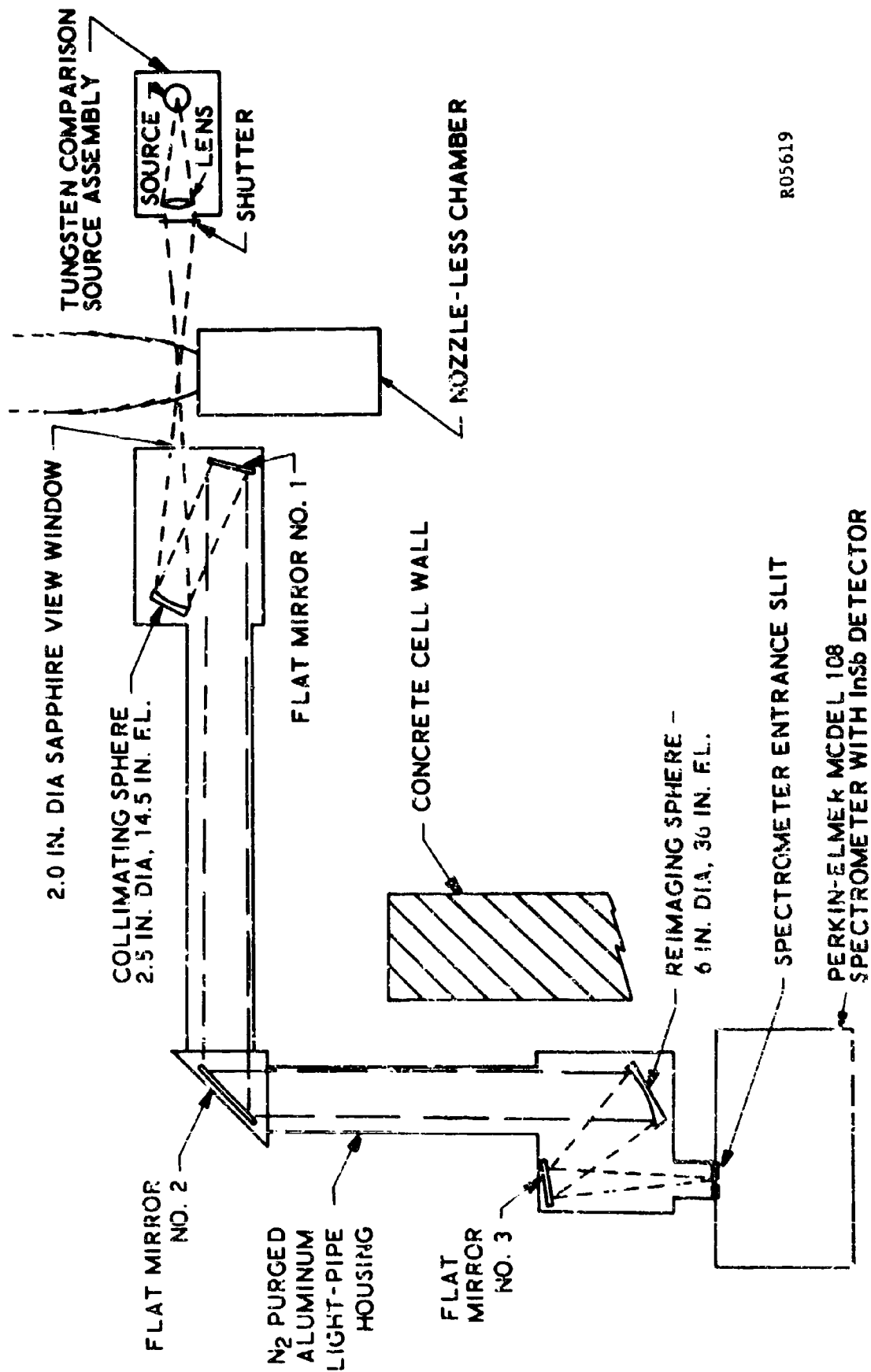
A systematic analysis of the experimental errors involved has been performed and details of the results may be obtained in Reference 4.1.

#### 4.3 EXPERIMENTAL EQUIPMENT

During the course of this contract, another study was under way at Philco Research Laboratories, under the sponsorship of Advanced Research Projects Agency (ARPA) (Contract No. NOnr 36 6(00)), directed toward further understanding of radiative properties of  $Al_2O_3$  at elevated temperatures (specifically, above the melting temperature). The interests of both studies and the equipment necessary for their completion were compatible. This allowed a larger effort in the development of the spectroscopic equipment and the optical system, and also permitted a more extensive experimental program. Some of the results reported here were also reported in the NOnr 3606 final report.4.1

The optical arrangement used in the infrared radiation experiments is shown schematically in Figure 4-3, and the spectrometer and light pipe configuration are shown in Figure 4-4. The spectrometer is a Perkin-Elmer Model 108, rapid-scan instrument utilizing a lithium fluoride prism and liquid nitrogen cooled indium antimonide photoconductive detector. In order to provide lower scan speeds than the 1-1/2 cycles per second originally available, a variable speed electric motor was connected directly to the drive shaft of the spectrometer internal drive motor. The original drive system provides for 14 discrete scan speeds ranging from 3 to 150 scans per second, and the interchangeable variable speed motor provides rates from nearly zero to 10 scans per second. Low scan rates improve the data readout and available resolution (allowing smaller slit openings) for long duration firings.

Two different test motor configurations were employed during the course of the study, one being used for the chamber radiation measurements, and the other the throatless motor previously mentioned. Although the physical dimensions of the first motor (chamber studies) are described in detail in Section 3 of this report, the characteristics of importance to the radiation studies will be mentioned here. The motor consisted of an exterior steel jacket surrounding a graphite heat sink liner (I.D. = 6.0 inches). The chamber view ports were arranged at the nozzle end. The position is indicated in Figure 4-5. The chamber port and window view are shown in Figure 3-1. A single window was used for a total radiation thermocouple-type radiometer. Preliminary spectral



R05619

FIGURE 4-3. ROCKET FLAME IMAGING SYSTEM



FIGURE 4-4. NITROGEN FLUSHED OPTICAL PIPE

views were also taken through a single window with focal point just inside the chamber wall. The setup for calibrated spectral radiancy required focusing at the center of the chamber while the tungsten filament comparison source was focused through the opposite window. Window diameter was 0.2 inch.

The smaller engine and the 500 mm Jarrell-Ash scanning grating monochromator are shown in Figure 4-6. This spectrometer was used to make the sodium line reversal measurements of chamber temperature, and has been described elsewhere.<sup>4-3</sup> The engine uses gaseous hydrogen and gaseous oxygen (as does the larger engine described in the preceding paragraph). An  $H_2O/Al_2O_3$  slurry can be injected by hydraulically forcing a piston to squeeze the slurry into the chamber at the desired flow rate. The slurry flow rate is measured in two ways: by monitoring the motion of the piston, and by recording the hydraulic fluid flow with a turbine meter. To insure good particle dispersion, the slurry is injected at four locations, each one aligned with hydrogen and oxygen injectors. Hydrogen and oxygen flow rates are obtained by measuring the pressure upstream of a calibrated sonic orifice.

Chamber pressure in the smaller engine is measured at two locations: near the injector head, and near the chamber exit. Mass flow rates are adjusted so that the chamber pressure drop is kept small and the gas state is near the stagnation value; i.e., a minimum amount of combustion energy has appeared in the form of kinetic energy of the exhaust products. This is desirable since the data reduction requires knowledge of the particle concentration and temperature, and these quantities depend upon the gas flow properties. A typical total mass flow rate is 0.4 lb/sec, and chamber pressures are about 18 and 14 psia for upstream and downstream values, respectively.

#### 4.4 RESULTS

Certain difficulties were encountered while attempting to measure the spectral emittance of an alumina-containing flame at a location within the chamber of the larger rocket motor. Calculations had been made showing that the surface temperature of the heat sink liner would not be sufficient to develop an appreciable amount of wall radiation. Erosion of the chamber wall apparently resulted in the formation of small particles which were then able to attain temperatures comparable to the gas chamber temperature. This was made evident when attempts were made to record the emission spectra (in the chamber) of a pure hydrogen-oxygen flame. Each trial resulted in the observation of an overwhelming continuum emission which is not characteristic of the  $H_2-O_2$  flame. Since no solid species were added to the flow, one possible source of the observed radiation was the presence of wall carbon particles. A visual inspection of the liner revealed roughness and erosion of the material at some points.

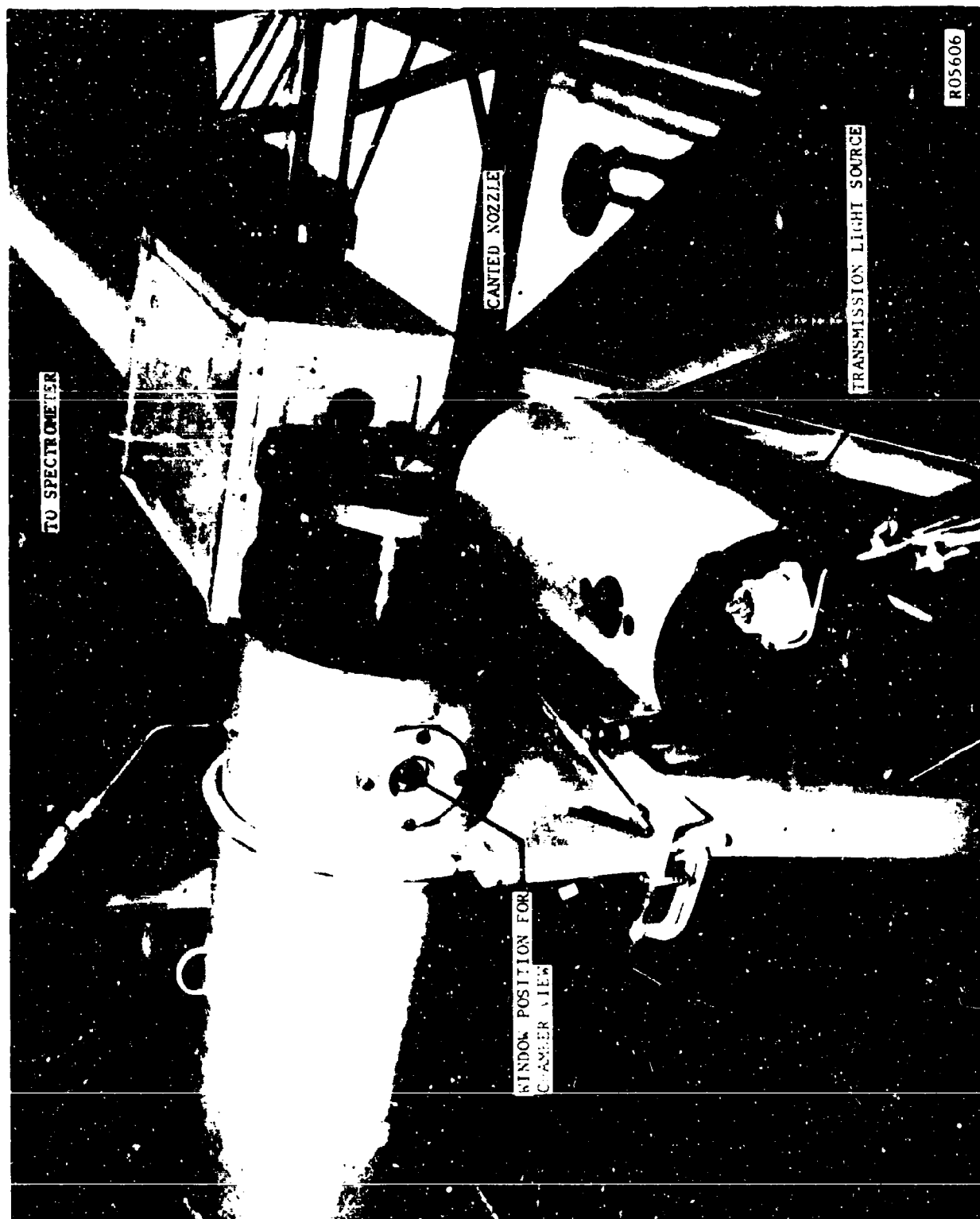


FIGURE 4-5 ENGINE AND SPECTROMETER ACCESSORIES

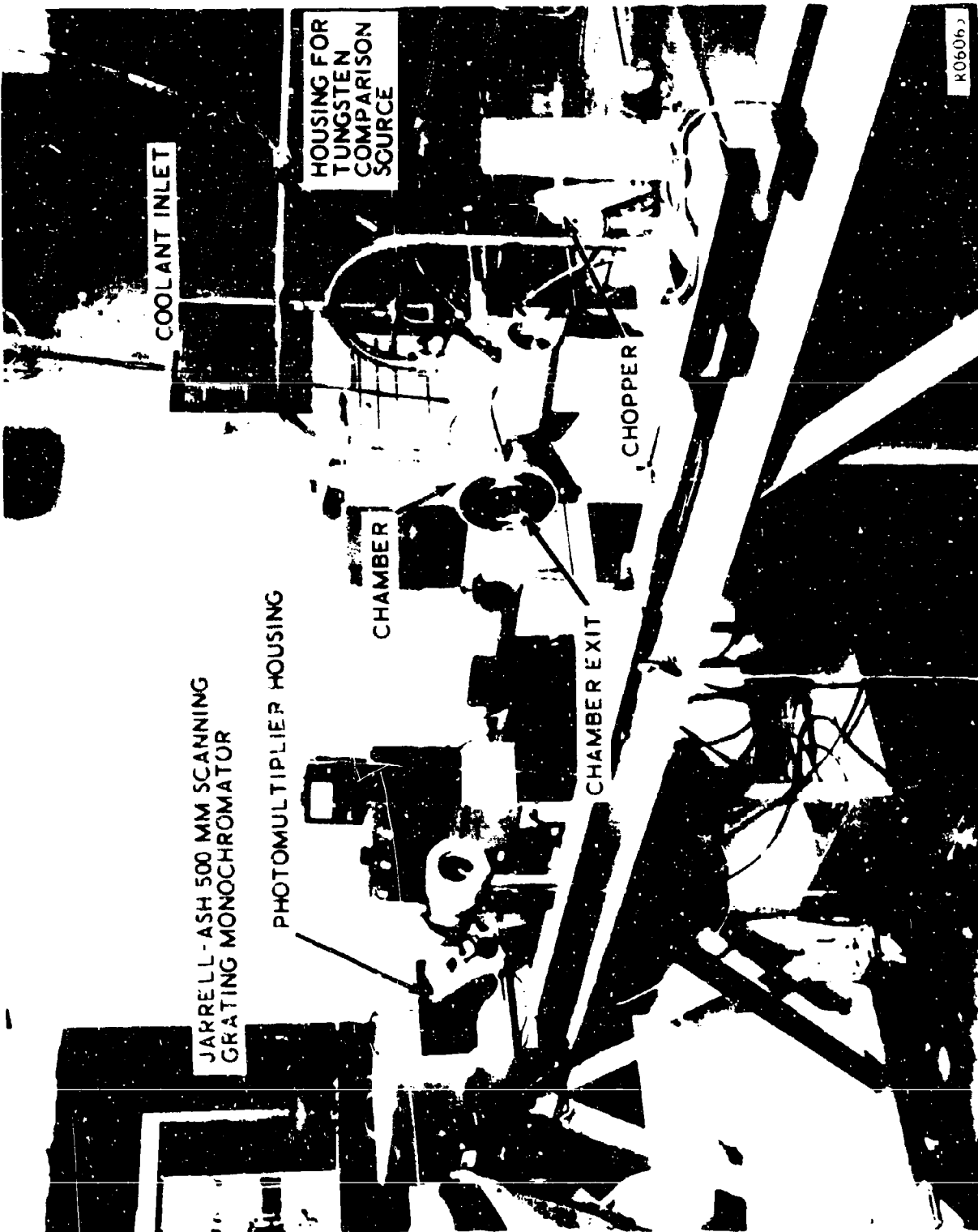


FIGURE 4-6. SMALL SLURRY ROCKET - REAR VIEW

Satisfactory operation of the system for obtaining chamber combustion spectra was critically dependent upon proper window performance. This required that the windows stay clean, intact, and that the window purge gas not be excessive. Prior to the spectral studies, the same window design was used to house an asymptotic calorimeter for total radiation data. The data were too scattered to show any reliable relationship between alumina loadings and total radiation. The causes of this could only be guessed to be such factors as excessive purge gas, recirculating flow in the conical entrance to the window, or variable effects of the graphite wall.

The final optics system, designed to properly focus the comparison source and chamber emission, produced a negligible amount of signal from the scanning spectrometer. The need for much larger windows was indicated. This factor, together with the occurrence of continuum from gas-only combustion and a number of window failures, led to the decision to focus efforts on the throatless chamber combustion.

A series of experiments designed to measure the cloud emissivity of an alumina-containing flame are described in detail in the Appendix. The results of these tests were the basis for the development of a new set of experiments designed to determine the spectral emissivity of  $\text{Al}_2\text{O}_3$  at elevated temperatures. The hot subsonic flow of the throatless rocket proved to be a valuable tool as may be seen by inspection of the results.

Figure 4-7 shows the experimentally determined spectral emissivity data due to alumina as a function of particle temperature, while Figure 4-8 shows the experimental results of Burch and Gryvnak.<sup>4.2</sup> The curve in Figure 4-7 at the lower temperatures (below 2320°K) is the result of Mie theory calculations based on alumina optical properties measured by Burch and Gryvnak and are averaged over wavelengths between one and three microns. The brackets shown on three of the data points in Figure 4-7 represent the root mean square error calculated from best estimates on measurement of data reduction and experimental uncertainties. Examination of Figure 4-8 indicates that extension to 1/2 and 3-1/2 microns may not be too bad for some practical applications. At 4 microns  $k$  is up by more than a factor of 10, and a significant error would occur with attempted extrapolation. For that data, however, one can assume that  $\bar{\epsilon}$  is proportional to  $n''$ , or  $k$ , as long as  $2\pi r/\lambda \gg 1$  and  $n'' \ll n'$  to a good approximation. Therefore the Mie theory calculations of Figure 4-7 could be extended to wavelengths of 4, 5, or 6 microns by multiplying the value shown in Figure 4-7 at  $T$ , by the ratio of  $k$  at 4, 5, or 6 microns to  $k$  at two microns for the same value of  $T$ .

Similar extrapolation of the data above the melting point is not possible because long wavelength measurements were not obtained there. The high temperature data of Figure 4-7 indicate, however, that alumina approximates a graybody at  $\lambda = 1.4, 1.78, \text{ and } 2.33 \mu$ . That is, the departures from graybody behavior are so small that they cannot be resolved within the limits set by the experimental error.



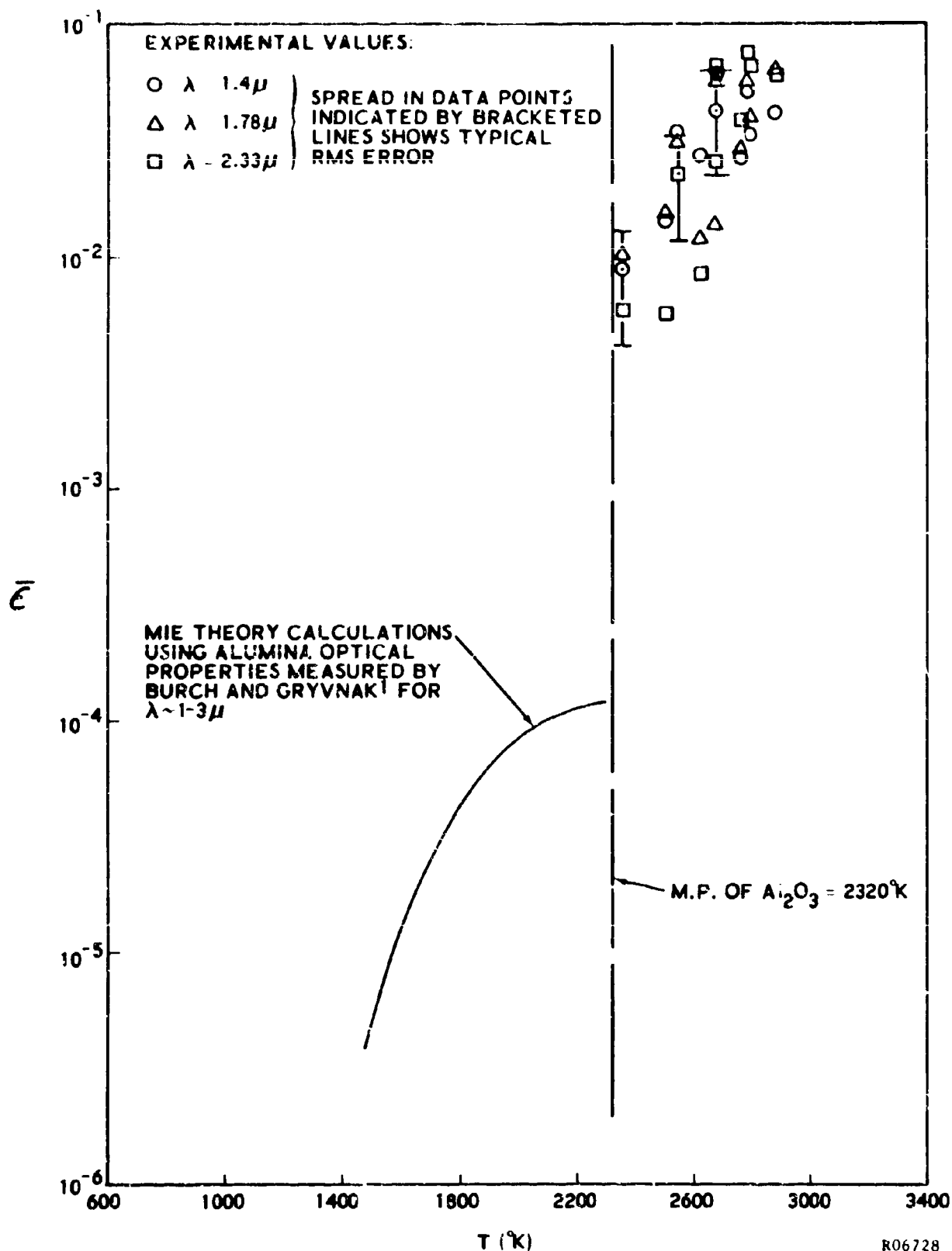


FIGURE 4-7. ALUMINA EMITTANCE FROM ROCKET ENGINE. EXPERIMENTS AND MIE THEORY CALCULATIONS BASED ON RESULTS OF BURCH AND BRYVNAK

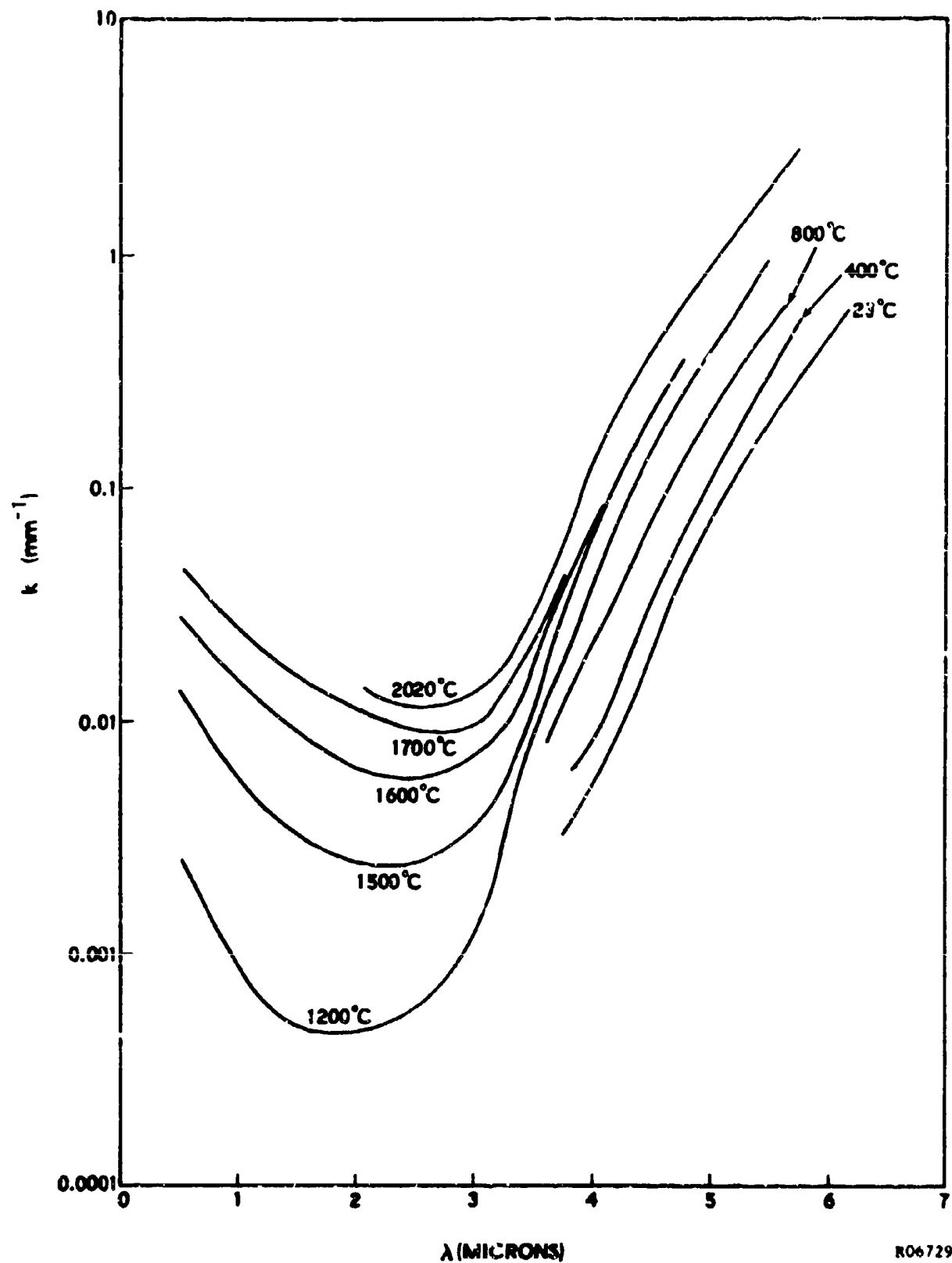


FIGURE 4-8 ALUMINA ABSORPTION COEFFICIENT VERSUS WAVELENGTH - DATA OF BURCH AND GRIVNAK

Regarding the behavior of the results, we note that a discontinuous jump in  $\bar{\epsilon}$  appears at the melting point. Burch and Gryvnak reported observing a brightness increase of one to two orders of magnitude as a portion of the alumina  $Al_2O_3$  melted and formed a molten bead in the optical path. (They could not obtain  $k$  for the liquid, however, as the bead thickness was unknown.) This observation supports the experimental results in indicating a discontinuous increase in emissance of alumina as the phase changes from solid to liquid. Since absorption and emission of electromagnetic waves depend upon conduction electrons present in the material, it can be speculated that the number of conduction electrons in the liquid phase is somewhat larger than the number present in the solid phase. This qualitative observation may be compared with results of Keyes<sup>4,4</sup> who recorded a step increase, by a factor of 13, in the RF conductivity in germanium as it melted. It remains for others, however, to explain the details of the physics of these experimental results.

The results of the small motor tests fulfill the objectives of this study. However, an attempt was made to determine the effects due to smaller particles than those used (Norton, type 38-900). Three runs were made using Norton alumina type 38-1200 (essentially a 1200 mesh particle) and Linde type 1.0-C nominally one micron particles as stated by the distributor). All three runs resulted in no measurable continuum emission. The conditions of these runs may be found in Table 4.1. Two possible explanations have been suggested for the lack of emission from these runs. The first is that the size dependency of the emissivity may be important for these smaller particles; i.e., the emissivity becomes very small for very small particles. Electron microscope photographs were made of particles collected during these three runs. The results showed that the particles ranged from 0.1 to 3 microns in diameter, with the majority being  $1\mu$  or less. The second possible explanation is that the exit temperatures were lower than expected. The photographs also showed that about 30 percent of the particles collected were unmelted, indicating temperatures very near the melting temperature of alumina. In view of the excess water present in these runs ( $\psi \approx 0.45$ ), it may be that the 100°K temperature drop observed in the earlier runs was not valid for these particular tests. No attempt was made to experimentally determine the heat losses for these experiments.

Finally, a series of nine runs was made to determine qualitatively the effects of adding solids other than  $Al_2O_3$  to the flow (namely C,  $Fe_2O_3$ , and Al). The following paragraphs and figures describe briefly the more notable results.

Figure 4-9; Run 5-B,  $H_2-O_2$  / Benzene ( $C_6H_6$ ) (4.12)

The primary feature of this run is the appearance of a very strong emission in the  $4.3\mu$   $CO_2$  band region. There is no measurable increase in continuous radiation in the 1- $3\mu$  region, and the only change in the appearance of the spectrum after the addition of  $C_6H_6$  (other than the  $CO_2$  band) is the reduction of the emission in the 1- $3\mu$  region (presumably due to the lower temperature after the addition of the benzene).

TABLE 4.1

## SUMMARY OF EXPERIMENTAL TEST DATA

Run	Q/F	$\frac{1}{2}$	$\frac{1}{\mu}$	$\frac{1}{\mu}$ (psia) <sup>**</sup>	T <sub>BP</sub> <sup>o</sup> (°K)	$\lambda = 1.4$			$\lambda = 1.78$			$\lambda = 2.33$		
						$\bar{c}$	$\frac{z}{Trans}$	$\frac{z}{Trans}$	$\bar{c}$	$\frac{z}{Trans}$	$\frac{z}{Trans}$	$\bar{c}$	$\frac{z}{Trans}$	$\frac{z}{Trans}$
20	7.65	0.222	0.75	19.32	2880	4.16 x 10 <sup>-2</sup>	0.742	0.742	6.37 x 10 <sup>-2</sup>	0.787	0.787	6.11 x 10 <sup>-2</sup>	0.676	0.676
21	15.85	0.274	0.75	15.73	2500	1.445 x 10 <sup>-2</sup>	0.691	0.691	1.524 x 10 <sup>-2</sup>	0.817	0.817	5.69 x 10 <sup>-3</sup>	0.625	0.625
22	7.67	0.414	0.75	15.12	2760	2.66 x 10 <sup>-2</sup>	0.610	0.610	2.91 x 10 <sup>-2</sup>	0.672	0.672	3.89 x 10 <sup>-2</sup>	0.660	0.660
23	10.64	0.417	0.75	16.79	2620	2.755 x 10 <sup>-2</sup>	N.A.	N.A.	1.194 x 10 <sup>-2</sup>	0.665	0.665	8.43 x 10 <sup>-3</sup>	0.606	0.606
26	7.92	0.374	0.75	22.02	2790	3.37 x 10 <sup>-2</sup>	0.582	0.582	3.91 x 10 <sup>-2</sup>	0.810	0.810	6.56 x 10 <sup>-2</sup>	0.800	0.800
29	13.71	0.234	0.75	16.79	2670	4.24 x 10 <sup>-2</sup>	0.879	0.879	1.383 x 10 <sup>-2</sup>	0.890	0.890	2.59 x 10 <sup>-2</sup>	0.809	0.809
30	16.55	0.333	0.75	16.23	2350	8.93 x 10 <sup>-3</sup>	0.345	0.345	1.015 x 10 <sup>-2</sup>	0.659	0.659	5.89 x 10 <sup>-3</sup>	0.383	0.383
32	4.08	0.307	0.75	17.20	2540	3.41 x 10 <sup>-2</sup>	N.A.	N.A.	3.23 x 10 <sup>-2</sup>	N.A.	N.A.	2.24 x 10 <sup>-2</sup>	N.A.	N.A.
34	4.77	0.308	0.75	16.68	2670	6.16 x 10 <sup>-2</sup>	0.915	0.915	5.70 x 10 <sup>-2</sup>	0.878	0.878	6.50 x 10 <sup>-2</sup>	0.850	0.850
35	5.84	0.324	0.75	16.37	2780	5.12 x 10 <sup>-2</sup>	0.483	0.483	5.70 x 10 <sup>-2</sup>	0.589	0.589	7.44 x 10 <sup>-2</sup>	0.556	0.556
7-B	6.75	0.327	0.52	22.01	2550	N.A.	0.285	0.285	N.A.	0.320	0.320	N.A.	0.329	0.329
8-B	7.03	0.220	0.40	22.20	2550	N.A.	0.289	0.289	N.A.	0.337	0.337	N.A.	0.381	0.381
9-B	6.77	0.220	0.40	21.90	2550	N.A.	0.478	0.478	N.A.	0.633	0.633	N.A.	0.637	0.637

Note: Particles used

Runs 20 - 35, Al<sub>2</sub>O<sub>3</sub>, Norton Type 38-900  
 Runs 7-B, 8-B, Al<sub>2</sub>O<sub>3</sub>, Norton Type 38-1200  
 Run 9-B, Al<sub>2</sub>O<sub>3</sub>, Linde Type 1.0-C

\*Upstream pressure tap

\*\*Exit plane pressure tap

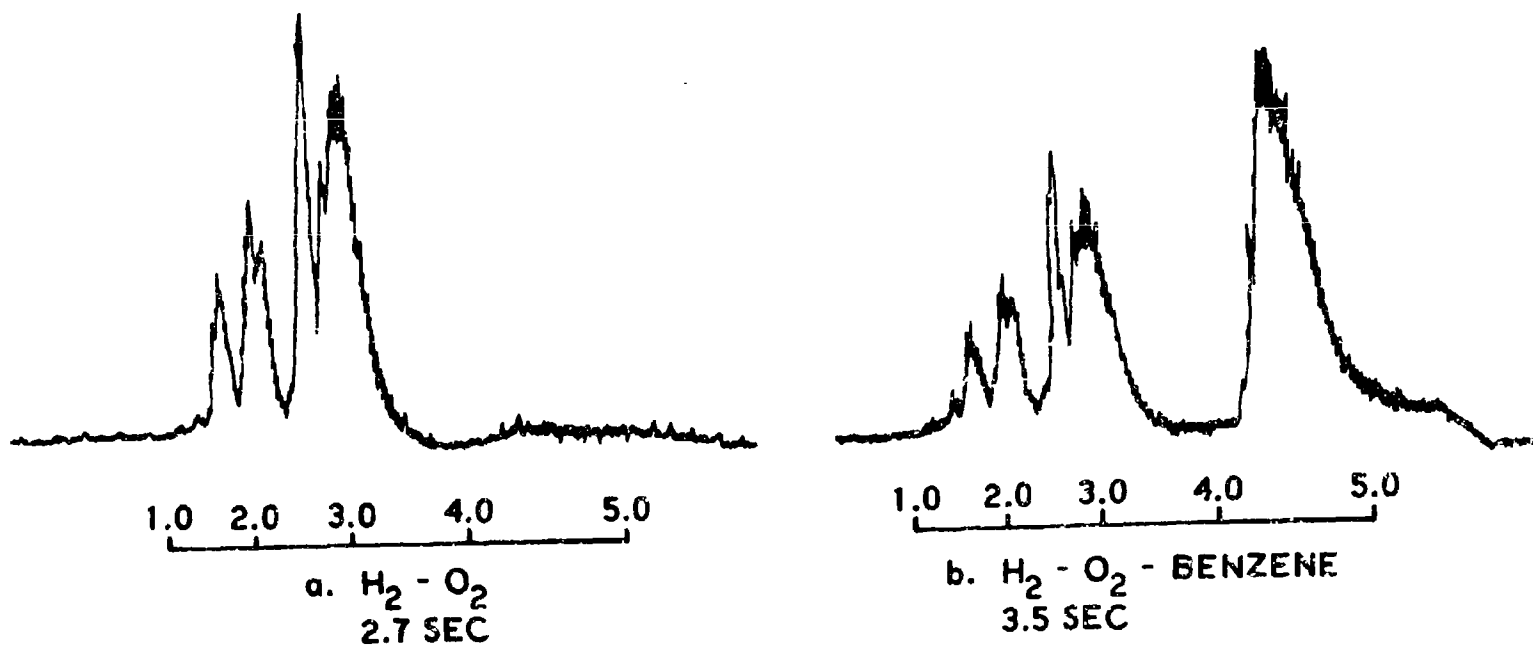


FIGURE 4-9. SAMPLE SPECTRA FROM RUN 5B

Figure 4-10; Run 3-B,  $\text{H}_2\text{-O}_2 / \text{Al-CH}_3\text{OH}$ 

(4.13)

This run also exemplifies the effect of adding carbon to the flow by showing the strong  $4.3\mu$   $\text{CO}_2$  emission characteristic of the vaporized species. In strong contrast to the previous run, the gas-only emission spectrum has been altered considerably by the appearance of a relatively strong continuum in the  $1.3\mu$  region. This additional radiation may possibly be ascribed to either the  $\text{Al}_2\text{O}_3$  resulting from the combustion of aluminum, or to some interaction between the carbon and the aluminum, or the unburned carbon in the system.

Figure 4-11; Run 1-B,  $\text{H}_2\text{-O}_2 / \text{Al-CH}_3\text{OH-C}$ 

(4.14)

The primary difference between the conditions of this run and the preceding one is in the presence of solid carbon in the flow. The carbon was introduced in the form of a powder (carbon black) added to the slurry of  $\text{CH}_3\text{OH}$  and Al. Of primary interest is the increase in radiation in the  $1\text{-}3\mu$  range with the simultaneous decrease in  $\text{CO}_2$  emission. Again, it is not possible to ascribe the emission to any one constituent, but it seems likely that the solid carbon in the flow contributed considerably to the observed changes.

Figure 4-12; Run 10-B,  $\text{H}_2\text{-O}_2 / \text{H}_2\text{O-Al}_2\text{O}_3\text{-C}$ 

(4.15)

For this run carbon black was added to an  $\text{Al}_2\text{O}_3\text{-H}_2\text{O}$  slurry, and the results are shown in the figure. The continuum emission level ( $1\text{-}3\mu$ ) produced by this run was so intense that the recording system was overdriven and complete details of the spectrum could not be obtained. It is interesting to note, however, that at the saturation level, the emission was at least five times that from the gas. Unburned carbon is again believed to be the strong continuum emitter. Another feature worth noting is the complete absence of radiation in the  $4.3\mu$   $\text{CO}_2$  band region. This spectrum is typical of those obtained when measurements were attempted in the chamber of the larger motor.

Figure 4-13; Run 12-B,  $\text{H}_2\text{-O}_2 / \text{H}_2\text{O-Al}_2\text{O}_3\text{-Fe}_2\text{O}_3$ 

(4.16)

A slurry mixture consisting of  $\text{Al}_2\text{O}_3$ ,  $\text{H}_2\text{O}$ , and 0.5 percent by weight of  $\text{Fe}_2\text{O}_3$  was added to the  $\text{H}_2\text{-O}_2$  flame during this run. The amount of  $\text{Fe}_2\text{O}_3$  corresponded to 1/2 percent by weight of the total mass of the exhaust. Of primary interest is the appreciable increase in emission in the  $1\text{-}2.3\mu$  region and the absence of any measurable change beyond the  $2.3\mu$  point. This is somewhat similar to the pure  $\text{Al}_2\text{O}_3$  emission, although the increased emission in this case cannot be ascribed with certainty to either constituent alone.

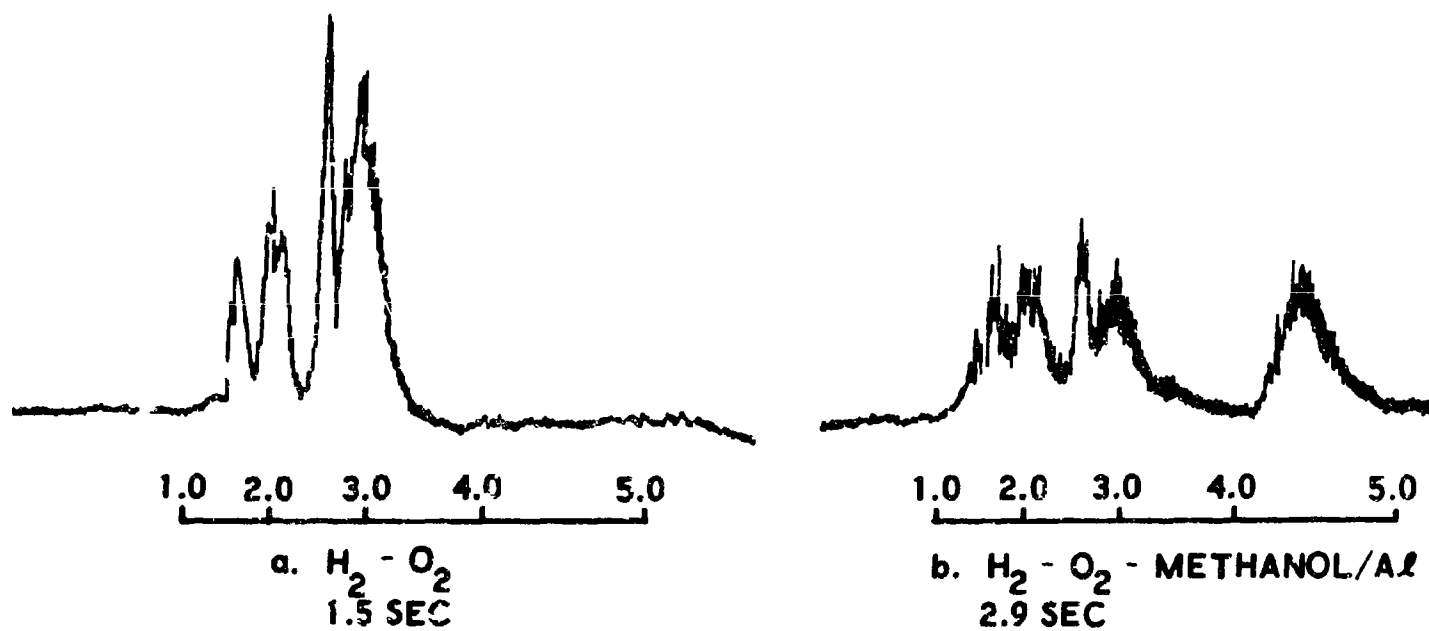
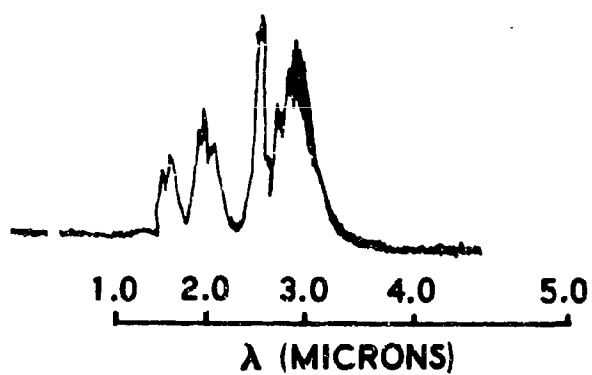
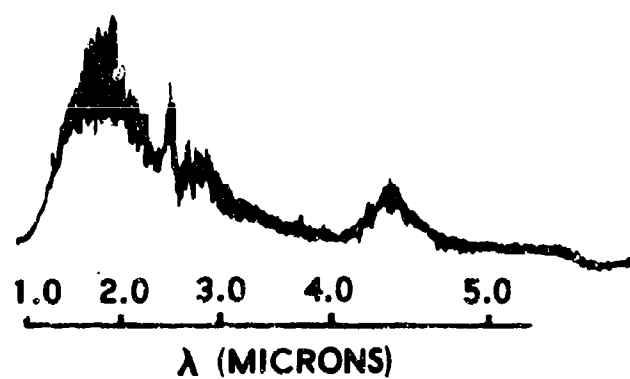


FIGURE 4-10. SAMPLE SPECTRA FROM RUN 3B



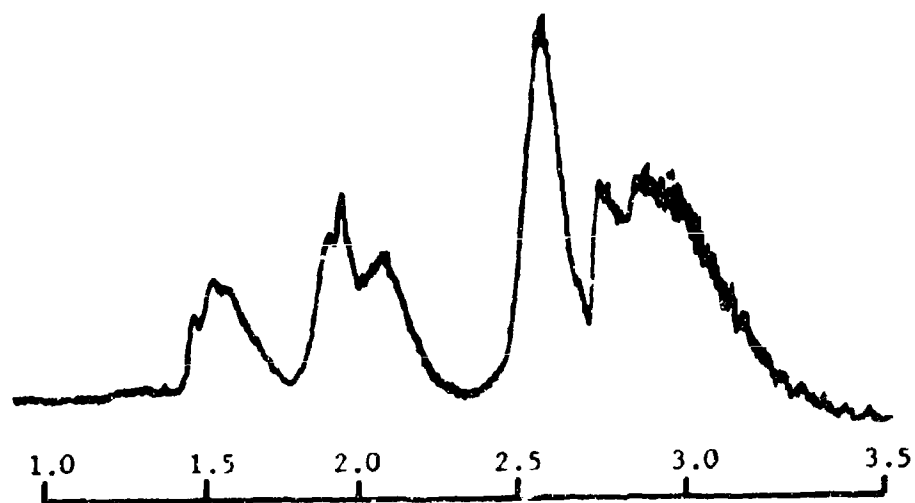
a.  $\text{H}_2 - \text{O}_2$   
1.5 SEC



b.  $\text{H}_2 - \text{O}_2 - \text{METHANOL}/\text{Al} - \text{C(s)}$   
2.9 SEC

FIGURE 4-11. SAMPLE SPECTRA FROM RUN 1B

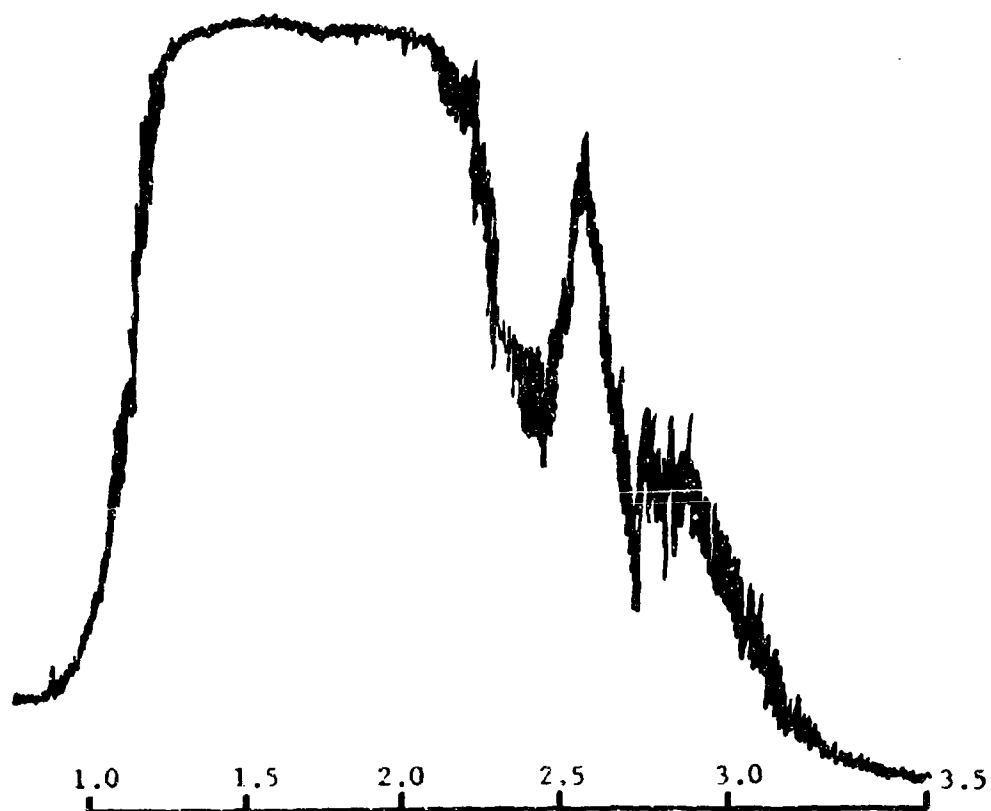




$\lambda$  (MICRONS)

a.  $H_2 - O_2$

1.6 SEC.



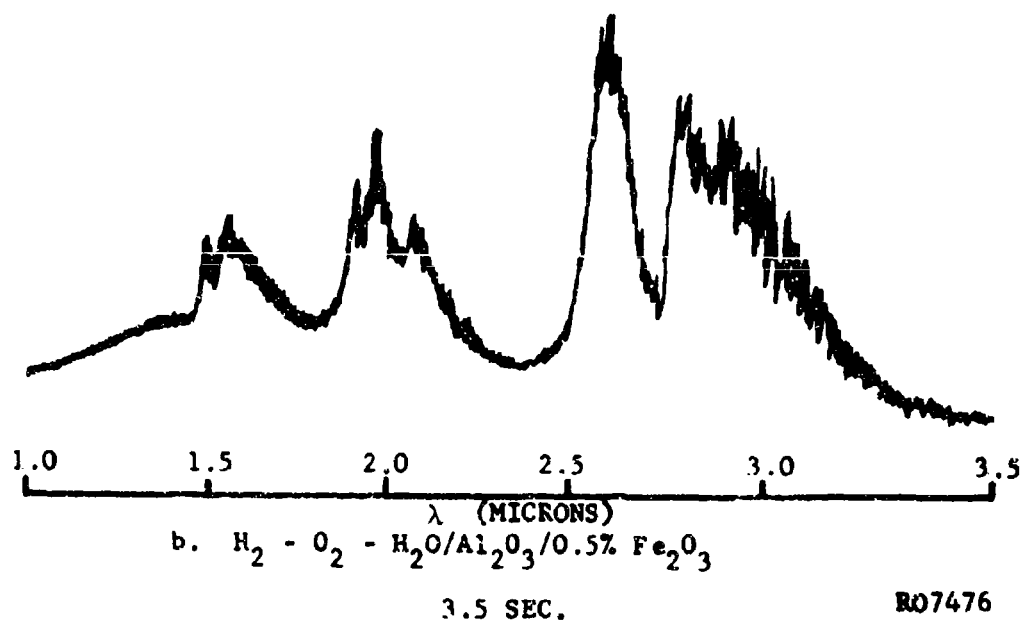
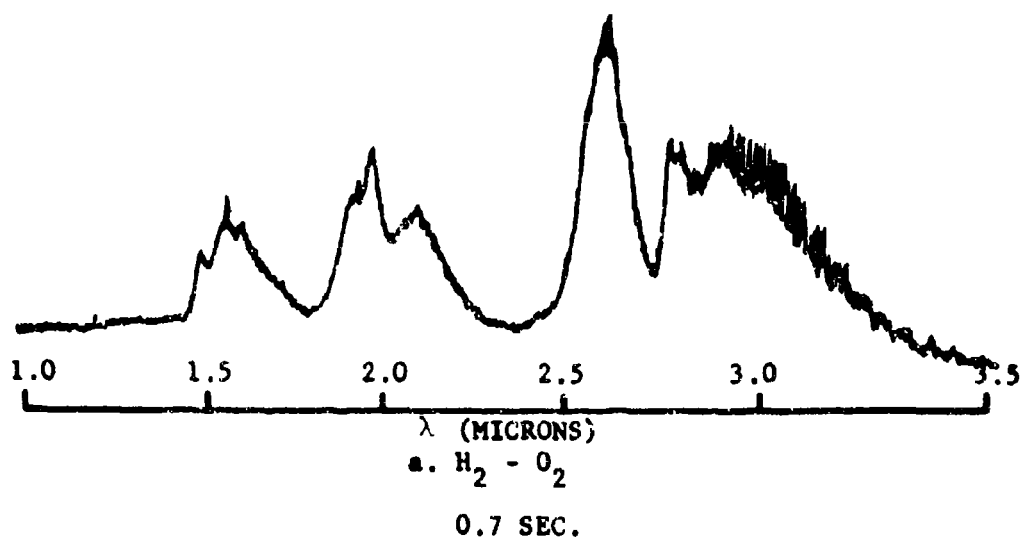
$\lambda$  (MICRONS)

b.  $H_2 - O_2 - H_2O/Al_2O_3/C$

4.0 SEC.

RO7474

FIGURE 4-17. SAMPLE SPECTRA FROM RUN 10-B



RO7476

FIGURE 4-13. SAMPLE SPECTRA FROM RUN 12-B

Conditions for this run were similar to the preceding one with the exception of an increased  $Fe_2O_3$  loading. This mixture consisted of one percent  $Fe_2O_3$  by weight of the exhaust products. The resulting increase in emission may be easily seen. In this instance, the change in radiancy level at the  $2.33\mu$  wavelength is also more apparent.

#### 4.5 CONCLUSIONS

Based upon the experiments performed during the course of these investigations, the following conclusions are drawn

##### 4.5.1 SPECTRAL EMITTANCE TESTS

Emittance of liquid phase alumina particles ranging in diameter from 1 to 10 microns is of the order 0.01 to 0.1 in the 1 to 3 micron wavelength region for temperatures between 2300 and 2900°K.

Based upon results of Reference 2, the emittance of solid  $Al_2O_3$  particles at the same wavelengths, and of the same size, varies from about  $5 \times 10^{-6}$  at 1500°K to  $2 \times 10^{-4}$  at 2300°K.

A discontinuous jump in spectral emittance in the 1 to 3 micron wavelength region occurs as alumina changes from the solid to the liquid phase.

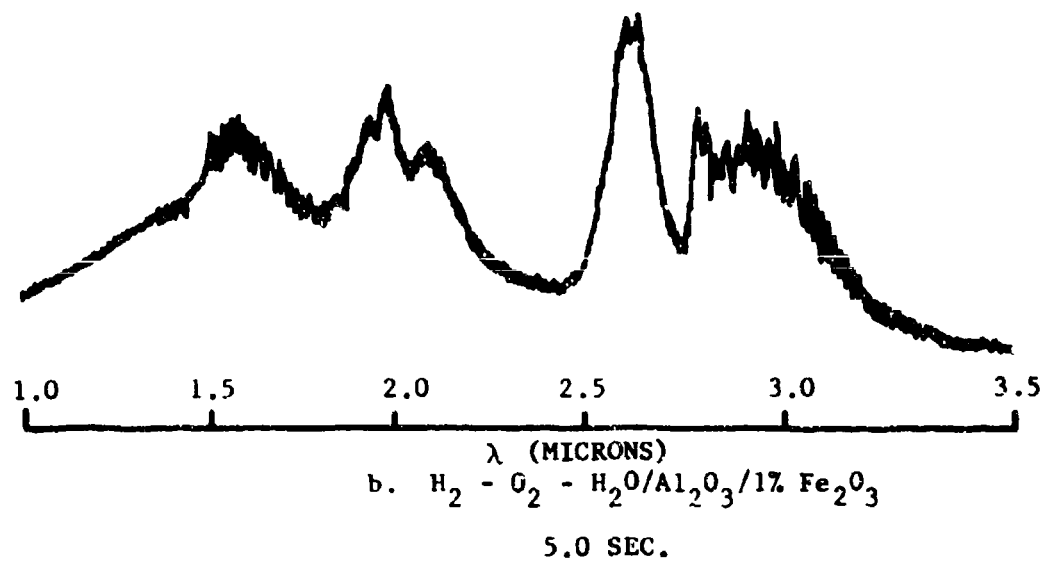
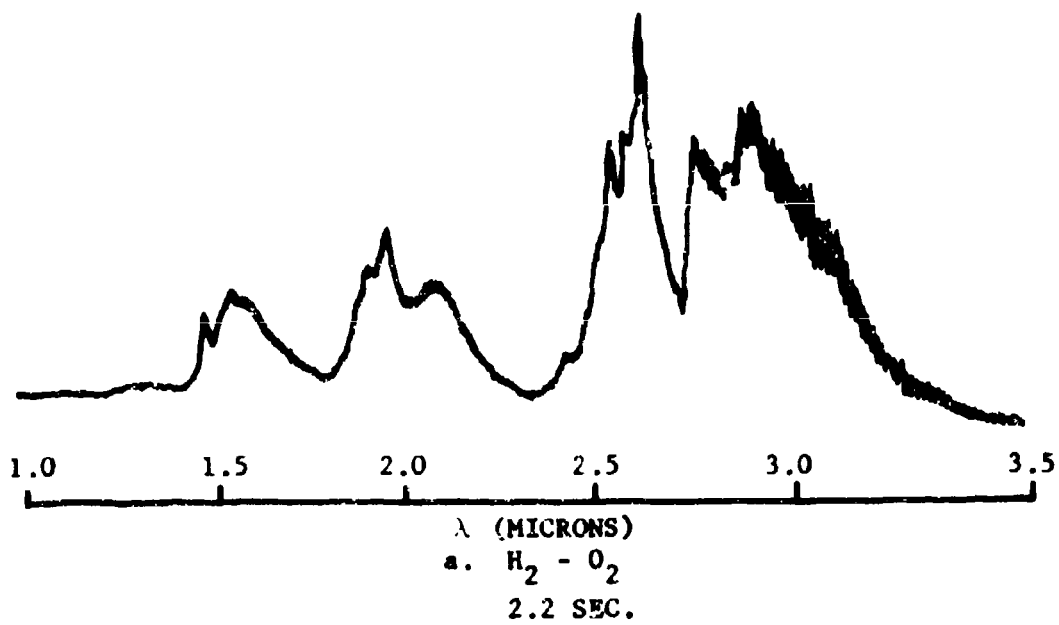
Significant increases in alumina cloud emission are produced by the addition of minor amounts of carbon or iron oxide impurities such as could occur from the burning of solid propellants.

##### 4.5.2 CLOUD EMITTANCE TESTS

In small size rockets the particle impingement on the nozzle is so serious that the simulation of the rocket plume of a large motor is not achieved

The throatless  $H_2(g)-O_2(g)$  rocket with aqueous slurry provides potentially useful devices for determining the radiation emitted by  $Al_2O_3$  particles present in rocket plumes. In particular, it allows tests to be conducted at high particle temperatures and without dynamic and thermal lag between particle and gas.

A technique was established to determine plume radiation properties by first measuring with only the fuel and oxidizer burning and then with the particulate substance present without interruption of the firing. This procedure provides an excellent demonstration of the effect of the addition of the particles.



RO7473

FIGURE 4-14. SAMPLE SPECTRA FROM RUN 11-B

The radiation emitted by the plume of a small, 100-pound thrust rocket, with one micron  $\text{Al}_2\text{O}_3$  particles added was small compared to the radiation emitted by products (mainly  $\text{H}_2\text{O}$  at atmospheric pressure) of the burning of the fuel and oxidizer alone.

#### 4.5.3 CHAMBER RADIATION TESTS

The use of a graphite-lined, heat-sink chamber is not a suitable instrument for studying the isolated radiative characteristics of materials such as alumina.

The view window design employed is not, in general, satisfactory for high pressure experiments of the type attempted. A sturdier construction should be devised to prevent damage by overpressures, and larger limiting apertures would be desirable.

#### 4.6 REFERENCES

- 4.1 Carlson, D. J. and Du Pu's, R. A., Alumina Absorption and Emittance, Aeronutronic Publication No. U-2627, 31 May 1964.
- 4.2 Burch, D. E. and Gryvnak, D., Optical Properties of Aluminum Oxide at Elevated Temperatures, Aeronutronic Publication No. U-2623, 31 May 1964
- 4.3 Carlson, D. J., ARS J. 32, 1107 (1962)
- 4.4 Keyes, R. W., Phys. Rev. 84, 367 (1951).

# NOMENCLATURE

$I$	transmitted spectral irradiance
$H_0$	incident spectral irradiance
$k$	spectral absorption coefficient per unit length
$l$	flame pathlength
$n'$	temperature and wavelength - dependent real part of the index of refraction
$n''$	temperature and wavelength - dependent imaginary part of the index of refraction
$N(r)$	number of particles per unit volume in size range between $r$ and $r + dr$
$\tilde{N}$	total number of particles of all sizes per unit volume
$p$	chamber pressure (measured)
$Q^{(e)}(r)$	spectral efficiency factor for extinction (ratio of extinction cross section to geometrical cross section) for particles in size range between $r$ and $r + dr$
$\overline{Q^{(e)}}$	spectral average extinction efficiency factor
$r$	radius of spherical particle
$R$	spectral steradiancy
$T$	temperature
$w(r)$	weight of particles in size range between $r$ and $r + dr$
$\bar{w}$	average weight for particle size distribution (see Equation (5))
$x$	geometrical dimension
$\dot{w}$	mass flow rate of propellant
$C_v$	volume concentration of particles in aqueous suspension

## GREEK

$\gamma$	spectral extinction coefficient
$\epsilon(r)$	spectral emittance of alumina particles in size range between $r$ and $r + dr$
$\bar{\epsilon}$	average spectral emittance for particle size distribution (see Equation (6))
$\lambda$	wavelength
$\rho$	gas density
$\tau$	spectral transmittance of particle cloud
$\phi$	alumina-to-gas mass ratio in gas-particle system
$\phi(r)$	particle size distribution function (see Equation (2))
$\psi$	alumina mass fraction in slurry

## SUBSCRIPTS

$\lambda$	wavelength
$o$	refers to comparison source radiancy
$g$	refers to gas value
$p$	refers to particle value
$a$	absorption (i.e. $\gamma_{pa}$ refers to volumetric absorption coefficient for particles)
$t$	total
$s$	scattering
$c$	refers to carbon value

## SUPERSCRIPIS

$o$	indicates blackbody value
-----	---------------------------

## SECTION 5

### ALUMINA CLOUD EMISSIVITY - APPLICATION TO DESIGN

#### 5.1 RADIANT HEAT FLUX FROM A TWO PHASE MIXTURE

Calculation of the radiant-heat interchange between an absorbing gas with suspended particles and its bounding surface is very difficult. This is mainly due to the complicated nature of the total emissivity of the mixture. The spectrum of an absorbing gas is composed of discrete absorption bands with the total emissivity (integrated over all wave lengths) being a function of (1) static pressure, (2) mole fraction, (3) temperature, and (4) path length. Whereas, for a particle cloud, the spectrum is similar to that of a solid surface and gas, with the total emissivity a function of (1) static pressure, (2) temperature, (3) mole fraction of gas, (4) weight ratio of particles to gas, (5) average weight of particles, (6) distribution of particle size, and (7) path length. Therefore, due to the difference in the IR spectrum of particles and gas, direct addition of total emissivities to obtain the total emissivity of the mixture is not justified. That is, the spectral emissivity obtained by direct addition of the absorption coefficients for the gas and particle cloud is valid only if the gas and particles do not influence each other in their emission (Reference 5.1).

In a 2-phase mixture, the energy emitted by the gas will, in part, be scattered by the particles. Therefore, the spectral energy emitted from an incremental volume of gas plus particles, per unit cross sectional area, and normal to a point (0) on the surface of the media's bounding surface, may be written as

$$d R_{\lambda} = \left[ \gamma_{g\lambda}^a R_{\lambda g}^0 + \gamma_{p\lambda}^a R_{\lambda p}^0 + \gamma_{p\lambda}^{sl} R_{\lambda m}^0 \right] d x \quad (5.1)$$

Please turn to page 5-21 for foldout symbol pages.

That is, the total radiation from a volume element of the cloud is the sum of (1) the individual radiating species, and (2) the energy reflected or scattered by the particles which originate at locations adjacent to the volume element. Since the incremental gas volume is optically thin, the emissivity of the gas and particles may be written as

$$\epsilon_{\lambda g} = \gamma_{g\lambda}^a d x \quad (5.2)$$

$$\epsilon_{\lambda p} = \gamma_{p\lambda}^a d x \quad (5.3)$$

Multiplication of the above emissivities by the appropriate black body energies and including the scattered energy by a defined coefficient ( $\gamma_{p\lambda}^{s1}$ ) times the appropriate black body energy ( $R_{\lambda m}^0$ ) yields Equation (5.1).

The amount of energy emitted from the volume element that reaches a point (0) is the amount transmitted through the cloud from  $x$  to 0.

$$\tau_{\lambda m} = e^{-\gamma_{t\lambda} x} \quad (5.4)$$

where

$$\gamma_{t\lambda} = \gamma_{g\lambda}^a + \gamma_{p\lambda}^a + \gamma_{p\lambda}^{s2}$$

Multiplication of Equations (5.1) and (5.4), and integrating between 0 and  $\ell$  results in the directional energy incident on a point (0) from a nonisothermal, heterogeneous cloud:

$$R_{\lambda} = \int_0^{\ell} \left[ \gamma_{g\lambda}^a R_{\lambda g}^0 + \gamma_{p\lambda}^a R_{\lambda p}^0 + \gamma_{p\lambda}^{s1} R_{\lambda m}^0 \right] e^{-\gamma_{t\lambda} x} d x \quad (5.5)$$

For the particular case of an isothermal-homogeneous cloud, Equation (5.5) reduces to

$$R_{\lambda} = \left[ \gamma_{g\lambda}^a + \gamma_{p\lambda}^a + \gamma_{p\lambda}^{s1} \right] R_{\lambda}^0 \int_0^{\ell} e^{-\gamma_{t\lambda} x} d x \quad (5.6a)$$

$$R_{\lambda} = \frac{\left[ \gamma_{g\lambda}^a + \gamma_{p\lambda}^a + \gamma_{p\lambda}^{s1} \right]}{\gamma_{t\lambda}} R_{\lambda}^0 \left[ 1 - e^{-\gamma_{t\lambda} \ell} \right] \quad (5.6b)$$



and the emissivity of the cloud is

$$\epsilon_{\lambda m} = \left[ 1 - e^{-\gamma_{t\lambda} \ell} \right] \quad (5.7)$$

assuming

$$\gamma_{p\lambda}^{s1} = \frac{s2}{p\lambda}$$

This is the case when  $\gamma_{p\lambda}^a + \gamma_{g\lambda}^a$  is of the order of  $\gamma_{p\lambda}^{s1}$ . When the scattering effect is small compared to emission, then  $\gamma_{p\lambda}^{s1} K_{\lambda m}^0$  is neglected in Equation (5.1) and Equation (5.7) becomes

$$\epsilon_{\lambda m} = \frac{\gamma_{g\lambda}^a + \gamma_{p\lambda}^a}{\gamma_{t\lambda}} \left[ 1 - e^{-\gamma_{t\lambda} \ell} \right] \quad (5.8)$$

Note that Equation (5.8) is used only when multiple scattering is neglected. Also the term  $\gamma_{p\lambda}^{s2}$  is included in the transmission term due to the influence of path length. If  $\gamma_{p\lambda}^{s2} \ll \gamma_{p\lambda}^a$  then

$$\epsilon_{\lambda m} = 1 - e^{-\left( \gamma_{p\lambda}^a + \gamma_{g\lambda}^a \right) \ell} \quad (5.8a)$$

As noted before, the above equations assume that the emission of the species in the cloud do not influence one another.

The spectral emissivity of an optically thin particle cloud (neglecting gaseous emission) was discussed in detail in Section 4. By applying the same physical definitions and empirical relations as was done in Equation 4.7 of Section 4, an expression for an optically thin particle cloud may be written:

$$\epsilon_{\lambda p} = \frac{R_{\lambda}}{R_{\lambda}^0} = \frac{\bar{\epsilon}_{\lambda} \phi \rho_p \ell}{\bar{W}} \int_0^{\infty} \Phi(r) \pi r^2 dr \quad (5.9)$$

where the particle density (number of particles per unit volume) is given as  $N = \phi \rho_p / \bar{W}$ ;  $\rho_g = PM/RT$ ;  $\bar{M}$  is the gas molecular weight and  $\phi = \rho_p / \rho_g$  if  $U_g = U_p$ . (Assumed no thermal or velocity lag exists between gas and particles.)

In the experiments discussed in Section 4, the emissivity,  $\bar{\epsilon}_{\lambda}$ , which represents the emissivity of an average size particle, was found by use of Equation (5.9). The integral

$$\int_0^{\infty} \Phi(r) \pi r^2 dr$$

for the experiment was found to be  $6.5 \times 10^{-8} \text{ cm}^2$ , with  $\bar{W} = 5.6 \times 10^{-11} \text{ gms}$  and  $\ell = 2.0 \text{ inches}$ .

The experiments were limited to atmospheric pressure and only the emissivity of the particles at wavelengths of 1.4, 1.78 and 2.33  $\mu$  was reported. These three wavelengths of  $\text{Al}_2\text{O}_3$  emission correspond to regions where  $\text{H}_2\text{O}$  has no absorption, thus justifying the  $\text{Al}_2\text{O}_3$  spectral emissivity.

From the data and experimental accuracy given in Section 4 it was found that the selection of a constant  $\bar{\epsilon}_\lambda$  between 1 and 3  $\mu$  is feasible. Since the experiments are only applicable between 1 and 3  $\mu$  and data are nonexistent at other wavelengths, one must assume  $\bar{\epsilon}_\lambda$  between 0 and 1  $\mu$  and between 3  $\mu$  and  $\infty$  in order to determine the total emissivity. To be conservative,  $\bar{\epsilon}_\lambda$  was chosen as 1, between 3  $\mu$  and  $\infty$  and equal to  $\bar{\epsilon}_{1-3}$  between 0 and 1  $\mu$ . With this, Table 5.1 was constructed and shows  $\epsilon_{1-3}$  and  $\epsilon_{\text{total}}$ . Comparing the two emissivities, one can see the importance of the unity emissivity assumption at low  $\tilde{N} \ell$ , even though the amount of black body radiation between 0 and 1  $\mu$  and 3  $\mu$  and  $\infty$  is small (see %BB in Table).

TABLE 5.1  
SAMPLE ALUMINA PARTICLE CLOUD TOTAL EMISSIVITIES  
FOR ALUMINA IN THE LIQUID PHASE

Temperature (°K)	$\tilde{N} \ell$	%BB* (0-1)	%BB (3- $\infty$ )	$\epsilon_{1-3}$	$\epsilon_{\text{total}}$
4230	$0.438 \times 10^{10}$	13	19	0.0007	0.017
4500	$0.438 \times 10^{10}$	16	17	0.0010	0.015
4800	$0.438 \times 10^{10}$	20	14	0.0023	0.014
5025	$0.438 \times 10^{10}$	23	13	0.0041	0.015
5190	$0.438 \times 10^{10}$	25	12	0.0050	0.015
4230	$4.38 \times 10^{10}$	↓	↓	0.025	0.20
4500	$4.38 \times 10^{10}$	↓	↓	0.035	0.19
4800	$4.38 \times 10^{10}$	↓	↓	0.076	0.20
5025	$4.38 \times 10^{10}$	↓	↓	0.13	0.24
5190	$4.38 \times 10^{10}$	↓	↓	0.16	0.25
4230	$43.8 \times 10^{10}$	↓	↓	0.22	0.37
4500	$43.8 \times 10^{10}$	↓	↓	0.30	0.42
4800	$43.8 \times 10^{10}$	↓	↓	0.55	0.61
5025	$43.8 \times 10^{10}$	↓	↓	0.75	0.79
5190	$43.8 \times 10^{10}$	↓	↓	0.82	0.84
4230	$120 \times 10^{10}$	↓	↓	0.50	0.59
4500	$120 \times 10^{10}$	↓	↓	0.63	0.69
4800	$120 \times 10^{10}$	↓	↓	0.89	0.90
5025	$120 \times 10^{10}$	↓	↓	0.98	0.99
5190	$120 \times 10^{10}$	↓	↓	0.99	0.99

\* %BB (0-1): Percent black body radiation in the wavelength range of 0 to 1  $\mu$ .

With the variation of  $\bar{\epsilon}_\lambda$  with temperature and wavelength known, Equation (5.8a) was employed to determine the spectral emissivity of the cloud. (Note that  $\gamma_{g\lambda}^a$  is zero at the three wavelengths chosen for analysis.) Calculation of  $\epsilon_{\text{total}}$  was obtained from the basic definition of emissivity; that is

$$\begin{aligned}\epsilon_T &= \int_0^\infty \epsilon_\lambda R_\lambda^0 d\lambda / \sigma T^4 \\ &= \epsilon_{0-1} \int_0^1 R_\lambda^0 d\lambda / \sigma T^4 + \epsilon_{1-3} \int_1^3 R_\lambda^0 d\lambda / \sigma T^4 \\ &\quad + \epsilon_{3-\infty} \int_3^\infty R_\lambda^0 d\lambda / \sigma T^4\end{aligned}$$

where monochromatic emissivity may be taken out of the integral when constant in the specified wave band.

For temperatures below the melting point of  $\text{Al}_2\text{O}_3$ , the data of Burch<sup>5.2</sup> was used and the variation of  $\bar{\epsilon}_\lambda$  with  $\lambda$  assumed similar to that of  $K_\lambda$  ( $K_\lambda$  is the absorption coefficient obtained from experiment with data between 0 and  $6\mu$ ). At wavelengths larger than  $6\mu$ ,  $\bar{\epsilon}_\lambda$  can readily be assumed equal to 1 based on the Burch and Gryvnak correlations.

Figure 5-1 is a plot of the total alumina cloud emissivity. The total emissivity is plotted versus temperature for constant  $\tilde{N} \ell$ . Where

$$\tilde{N} \ell = 7.57 \times 10^{11} \frac{\phi P \bar{M} \ell}{T} \quad (\text{Particles/ft}^2)$$

and

$$P = \text{psia}$$

$$\ell = \text{ft}$$

$$T = {}^\circ\text{R}$$

In order to compute the total  $\text{Al}_2\text{O}_3$  particle cloud emissivity for a given combustion chamber, one must know the particles-to-gas weight ratio ( $\phi$ ), pressure (P), temperature (T), and gas molecular weight (M). Then assuming  $\bar{w}$  and  $\int_0^\infty \Phi(r) \pi r^2 dr$  equal to Reference 5.2, Figure 5-1 may be used to find  $\epsilon_{\text{total}}$ .

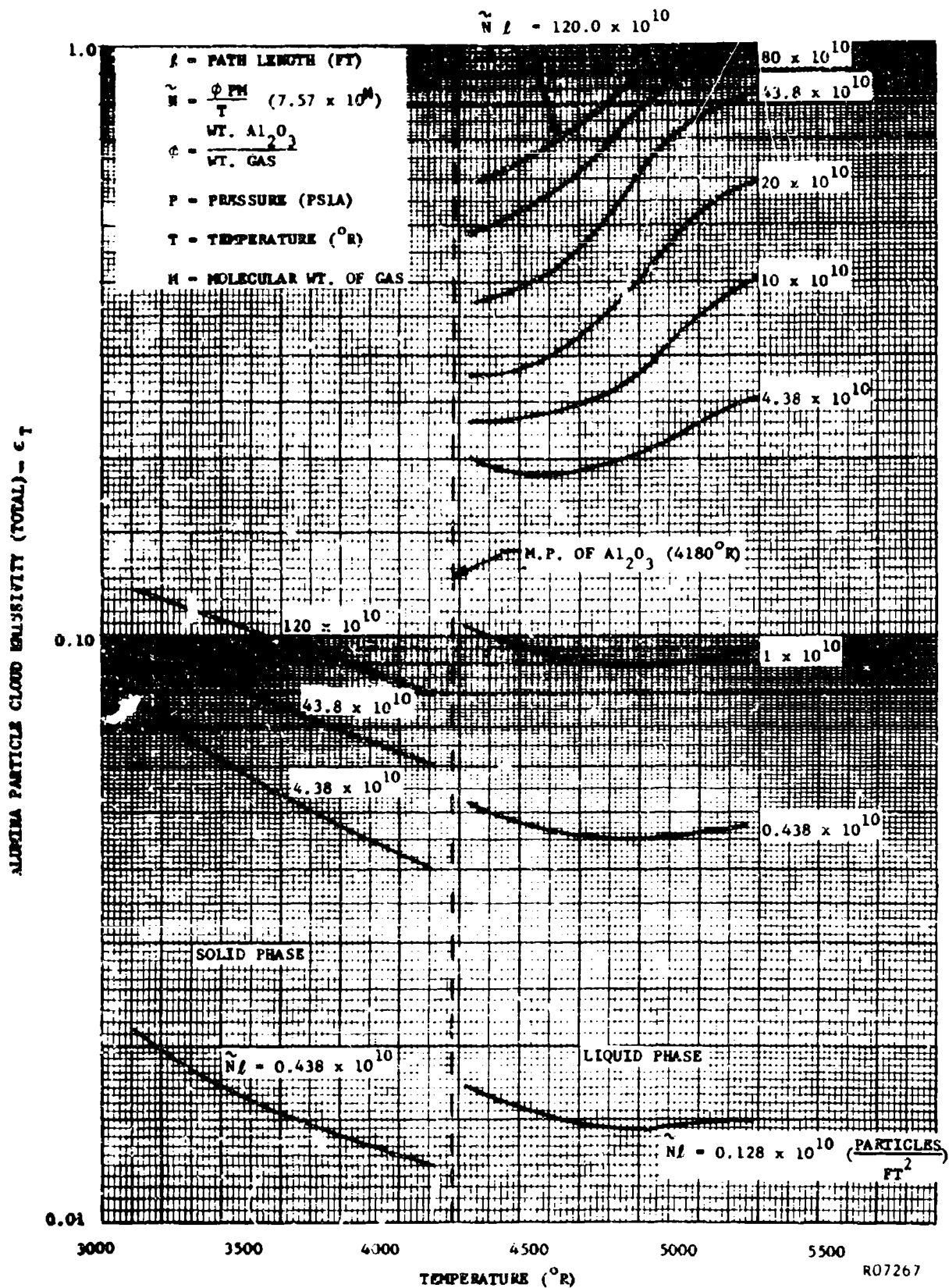


FIGURE 5-1. TOTAL  $Al_2O_3$  PARTICLE CLOUD EMISSIVITY  
(TRANSPARENT GAS) VERSUS TEMPERATURE

## 5.2 CALCULATION OF THE RADIANT HEAT FLUX IN A NOZZLE

The radiative heat fluxes are to be calculated for various parts of the 100 FW-2, large gimbaled, and simulator nozzles with emphasis on the following cases.

- (1) Inlet radiant heat flux to the 100 FW-2 nozzle.
- (2) Radiant heat flux throughout the gimbaled nozzle.
- (3) Radiant heat flux throughout the transient simulator nozzle.

Therefore, in this subsection, the purpose is to devise an approximate method to compute the radiant heat flux for the above cases using the results of subsection 5.1.

An analytical method for calculating the radiation heat flux to surfaces adjacent to the nozzle and produced by rocket exhausts containing alumina particles has been developed by Morizumi and Carpenter (Reference 5.3). The exhaust plume was essentially isobaric and at a temperature below the melting point of alumina. By dividing the plume into segments and devising an expression for the effective emissivity and temperature, the approximate radiant heat flux from the plume cloud may be found by a numerical solution. Calculation of the radiant heat exchange in a rocket nozzle is more complicated due to the nonisobaric flow, wall irradiation, and complicated geometry. Therefore, a more simplified approach to the problem was selected.

The radiant heat exchange inside an enclosure with gray walls and filled with an absorbing medium is most easily found by using the network method (reference 5.4 and 5.5). That is, the radiant heat flux to an incremental area  $A_1$  can be written as

$$q_1 = \frac{\epsilon_1}{1 - \epsilon_1} [E_1 - J_1] \quad (5.10)$$

$$= \iint_{\psi, \beta} \frac{[J_1 - E_m]}{\pi} [1 - e^{-\gamma_t s}] \sin \beta \cos \beta \, d\beta \, d\psi \quad (5.11)$$

$$+ \sum_{n=1}^k \int_{A_n} \frac{[J_1 - J_n]}{\pi} [e^{-\gamma_t s}] \frac{\cos \theta_1 \cos \theta_2}{s^2} \, dA_n$$

where

$$1 - e^{-\gamma_t s} = \text{emissivity of absorbing media}$$

and  $e^{-\gamma_t s} = \text{transmissivity of absorbing media.}$

When either the absorbing medium has nonuniform emission and transmission or the enclosure's shape is unsymmetrical with respect to  $A_1$ , Equation (5.11) is almost impossible to integrate. Also the coefficient,  $\gamma_{t,1}$ , for an absorbing gas with suspended particles may be a very complicated function of  $\beta$ ,  $\psi$ , and  $\theta$ . For example, in a rocket nozzle the combustion products are undergoing acceleration and thus the pressure and temperature (depending of course on the specific heat ratio) are a function of axial position. Since  $\gamma_p^a$  and  $\gamma_g^a$  for the absorbing media are strong functions of temperature and pressure, integration is made impossible by conventional means. However, for an enclosure with a simple shape and absorbing media with uniform emission to a local area  $A_1$ , Equation (5.11) may be simplified considerably. By inspection of Equation (5.11) one may recognize the equality.

$$A_1 \int_{A_n} \frac{\cos \theta_1 \cos \theta_2}{\pi s^2} dA_n = A_1 F_{1-n} \quad (5.12)$$

Also, let  $\epsilon_t$  represent the equivalent emissivity of the absorbing media; i.e.,

$$\epsilon_t = \int_0^\pi \int_0^{2\pi} \frac{1 - e^{-\gamma_t s}}{\pi} \sin \beta \cos \beta d\beta d\psi \quad (5.13)$$

If the absorbing media consists only of an absorbing gas, Equation (5.13) may be recognized as the gas emissivity that is plotted in standard text books (reference 5.6 and 5.7). That is

$$\epsilon_T = 1 - e^{-\gamma_g^a s}$$

Defining  $\tau = e^{-\gamma_t s}$ , equivalent transmissivity, and assuming isothermal conditions, Equation (5.10) and (5.11) may be rewritten as

$$q_1 = \frac{\epsilon_1}{1 - \epsilon_1} [E_1 - J_1] \quad (5.14)$$

$$= \sum_{n=1}^k F_{1-n} \tau_{1-n} [J_1 - J_n] + \epsilon_T [J_1 - E_m] \quad (5.15)$$

With the absorbing media consisting of an absorbing gas with suspended particles, the specification of the combined (particles and gas) emissivities and transmissivities can only be based on experimental knowledge (previously discussed). The presence of particles also increases the number of variables which effect  $\epsilon_T$  and  $\tau_{1-n}$ . Therefore, additional assumptions are required before Equations (5.14)

and (5.15) can be applied to the three cases discussed previously. These assumptions are presented below in detail.

- (1) When particles are suspended in an absorbing gas, the monochromatic emission of the resulting mixture may be expressed according to Equation (5.7). The transmissivity ( $\tau_\lambda$ ) has been investigated for an  $Al_2O_3$  cloud, and it has been found that  $\gamma_\lambda^g \sim \gamma_\lambda^a$ . The product  $F_{1-N} (J_n - J_1)$  is small in a rocket nozzle which has essentially isothermal walls. That is, when the walls of a nozzle are approximately isothermal, and radiosities ( $J$ ) of neighboring incremental areas are nearly equivalent for large values of the view factor, it may be assumed that the first term in Equation (5.15) is small and may be neglected.
- (2) The emissivity of a particle cloud is expressed in Equation (5.7), alteration of which will approximately give the total cloud emissivity. Assuming  $\alpha_\lambda = \epsilon_\lambda$ , the total emissivity of the particles may be found under a variety of nozzle conditions by use of Figure 5-1. Using the curves of McAdams, the total emissivity of various absorbing gases present in the particle cloud may be found. Combining the particle and gas emissivity by

$$\epsilon_p = 1 - e^{-\gamma_p \ell} ; \quad \epsilon_g = 1 - e^{-\gamma_g \ell} \quad (5.14) \quad (5.15)$$

$$\text{and} \quad \epsilon_T = 1 - e^{-(\gamma_p + \gamma_g) \ell} \quad (5.16)$$

the mixture emissivity is found. As was discussed in Section 5.1, this assumes (1) the particles and gas do not influence each other in emission, and (2) it is possible to add the total absorption coefficients, just as it is possible to add the monochromatic coefficients for noninteracting substances. The combined emissivity as given in Equation (5.16), neglects the scattering coefficient included in Equation (5.7). In the experiments performed during this contract period, emphasis was maintained on the emission properties of clouds. Time was not available for an intensive investigation of the scattering coefficient  $\gamma_p^s$  and the dependence of path length on the validity of Equations (5.14) and (5.15). Therefore, it is proposed, at a later time, to concentrate interest on the phenomena of light scattering by a two phase mixture approaching optically thick conditions.

- (3) To eliminate the complication of a nonisothermal absorbing medium in Equation (5.11), it is assumed that the static temperature of the media at the axial position of  $A_1$  represents the average temperature at which the integrated emission of the nonisothermal gas to the point in question is evaluated. This assumption is reasonable

if the view factor from  $A_1$  to the gas volume at  $T_{\text{static}}$  is large, and the emission ( $\epsilon_T$ ) from this gas volume is not sufficiently different from neighboring volumes.

- (4) The pressure for evaluating the emissivity of both the particles and gas is taken at the static pressure of  $A_1$ . The justification of this choice is similar to that of the static temperature.
- (5) The mean beam length at which both the particle and gas emissivity is evaluated will depend on the axial location in the nozzle.
  - (a) Convergent Section: Here the length is assumed equivalent to that of a semi-infinite cylinder with irradiation to the center of the base. This choice is based on the fact that as the inlet angle of the nozzle approaches 90 degrees the convergent section will become a semi-infinite cylinder. For large inlet angles, this assumption seems reasonable.
  - (b) Throat: A path length is chosen which is 1.4 times the diameter of the throat. This is based upon the irradiation to a point on the curved surface of an infinite cylinder, the volume of which represents the approximate absorbing media radiating to the throat.
  - (c) Divergent Section: In the divergent section, the mean beam length is assumed equivalent to the geometry described in (b), but the diameter is taken as the nozzle diameter at the point in question.
- (6) In using Equations (5.14) and (5.15) to compute the heat flux from a particle cloud, it must be assumed that the particles are uniformly distributed and the distribution of large and small particles is constant for a given nozzle cross section. The particle density found from Assumptions (3), (4), and (5) have already included this phenomena.
- (7) Assuming that the particles in a nozzle do not cross the gas stream lines is in essence equivalent to Assumption (6). However, the effect of this assumption upon the accuracy of the calculation is largely dependent upon nozzle geometry and conditions. In very large nozzles, particle slippage is greatly reduced.
- (8) Along with Assumptions (6) and (7), it must be assumed that no thermal or velocity lag exists between the particles and gas. This assumption is feasible in the convergent section, but in high acceleration regions, one may question its applicability.



Using the above assumptions, Equations (5.14) and (5.15) become,

$$q_1 = \frac{\epsilon_1}{1 - \epsilon_1} [J_1 - E_1] = \epsilon_T E_m - J_1 \quad (5.17)$$

When calculating the radiant heat flux to a black wall, one may eliminate the assumption of a gray absorbing media (monochromatic emissivity is independent of wave length) by using

$$q_1 = \epsilon_T E_m - \alpha_T E_1 \quad (5.18)$$

where  $\epsilon_T$  is evaluated at the media temperature and  $\alpha_T$  at the surface temperature. The radiative heat transfer coefficient is defined as:

$$h_r = q_1 / T_{ad} - T_i \quad (5.19)$$

where

$$\frac{T_{ad}}{T_s} = \frac{1 + \frac{\gamma - 1}{2} m^2}{1 + \frac{\gamma - 1}{2} m^2} \quad (5.20)$$

### 5.3 RESULTS

#### 5.3.1 100 FW-2 AND GIMBALED NOZZLE

Since the 100 FW-2 and gimbaled nozzle walls are ablative, the emissivity may be taken as unity. With the propellant conditions calculated at various stations in the nozzle, Equations (5.18 through 5.20) were used to find the radiative heat flux.

The radiant heat fluxes in the chamber and throat regions of both the 100 FW-2 and gimbaled nozzles represent the heat flux from a black particle cloud. Therefore, all the assumptions of the preceding section are eliminated except Number (3). That is, the radiation from an opaque particle cloud is independent of geometry, and one must only make a choice of cloud black body emission temperature in the calculation of the radiant heat exchange.

Table 5.2 presents the radiant heat interchange at the chamber and throat location of the 100 FW-2 nozzle. The chamber conditions are:  $T_c = 6350^\circ R$ ,  $P_c = 610$  psia, and  $\phi = 0.45$ .

TABLE 5.2  
RADIATION HEAT FLUXES IN THE 100 FW-2 NOZZLE

LOCATION	WALL TEMP ( $^{\circ}\text{K}$ )	$h_r$ (3tu/in <sup>2</sup> sec $^{\circ}\text{F}$ )	$q_r$ (8tu/in <sup>2</sup> sec)
Chamber	1500	0.0010	5.4
Chamber	3000	0.0015	5.1
Throat	1500	0.00089	4.3
Throat	3000	0.0012	4.0

Figure 5-2 presents the radiation heat flux that exists at various positions in the gimbaled nozzle. Calculation of these heat fluxes are made by utilizing the procedure of subsection 5.2. The figure shows the effect of wall temperature on radiation, which is expected since the difference in  $T_w$  is being compared. The dotted lines are regions of uncertainty; that is, regions that may not be strictly classified as either the chamber, throat, or divergent section of the nozzle (see Assumption (5)).

The importance of the radiative heat flux in the inlet section of the gimbaled nozzle is shown in Figure 5-3. The parameter  $h_r/h_c$  was obtained by calculating  $h_r$  as explained in subsection 5.2 and using the heat transfer coefficient plotted in Figure 7-8. The two heat transfer coefficients are then added to obtain  $(h_c + h_r)$ . Note that the sum  $(h_c + h_r)$  is not defined as the total heat flux, since the particle impingement contribution is omitted.

The increasing effect or importance of radiation with burning time is explained by an investigation of  $h_c$ . Comparison of Figure 5-2, 5-3, and 5-4 shows that  $h_c$  decreases with burning time due to the combined effect of increasing the redevelopment length of the boundary layer (pressure gradient and redevelopment) to the throat and low wall temperature.

Figure 5-4 presents the variation of the radiant to total heat flux with axial location in the exit portion of the gimbaled nozzle. Wall temperatures of 4000 and 1000 $^{\circ}\text{K}$  are presented. The radiative and convective heat transfer coefficients were calculated using the same procedure as Figure 5-4.

### 5.3.2 SIMULATOR NOZZLE

The simulator walls were made of molybdenum. With the emissivity of oxidized molybdenum found from Reference 5.8, and the thermochemical properties of the  $\text{H}_2\text{-O}_2$  plus  $\text{Al}_2\text{O}_3$  slurry in nozzle obtained from a thermodynamic computer program, the radiant heat transfer was completed. The method of calculation was outlined in subsection 5.2.

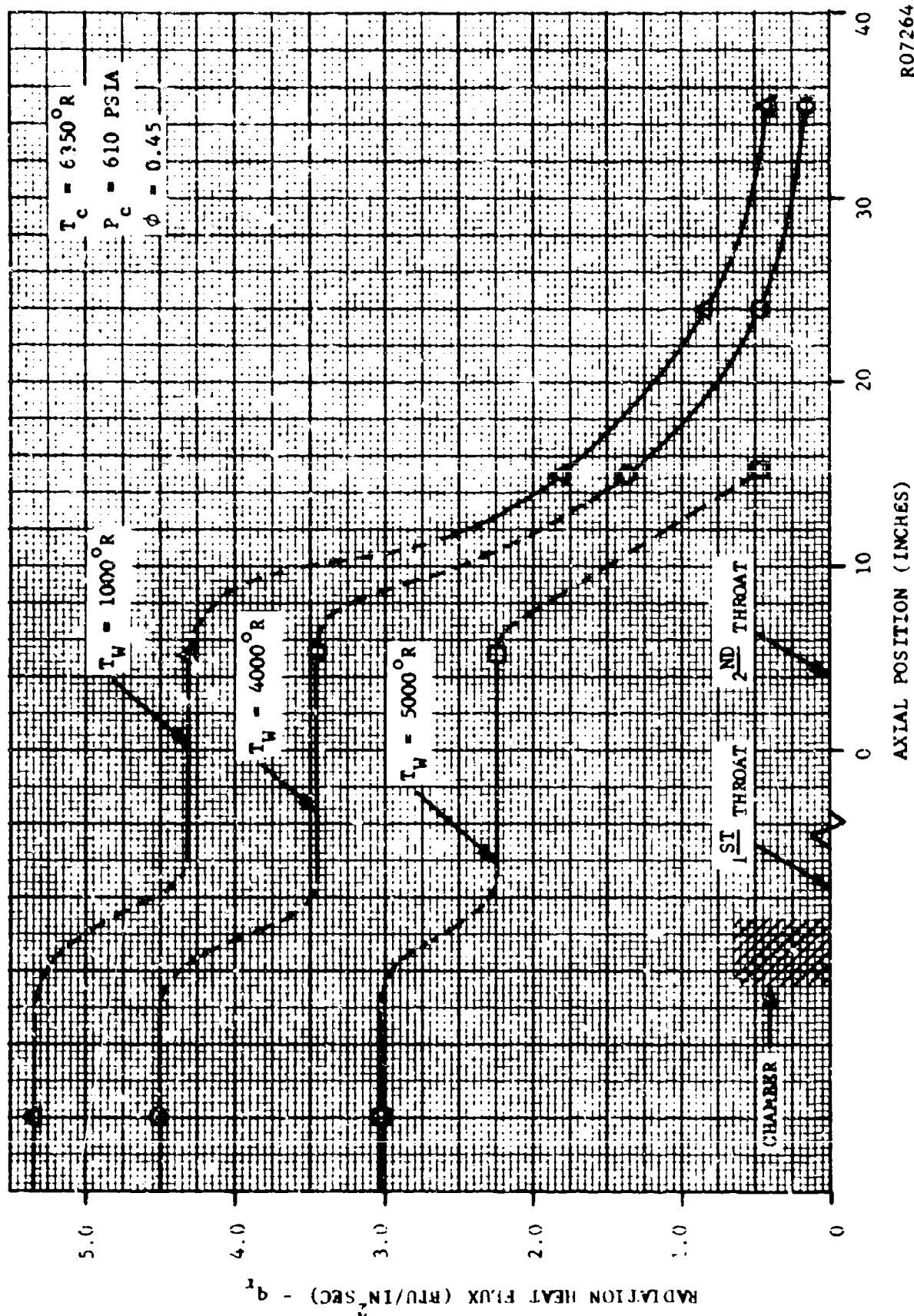


FIGURE 5-2 PREDICTED RADIATION HEAT FLUX VERSUS NOZZLE POSITION FOR GIMBALLED NOZZLE

R07264

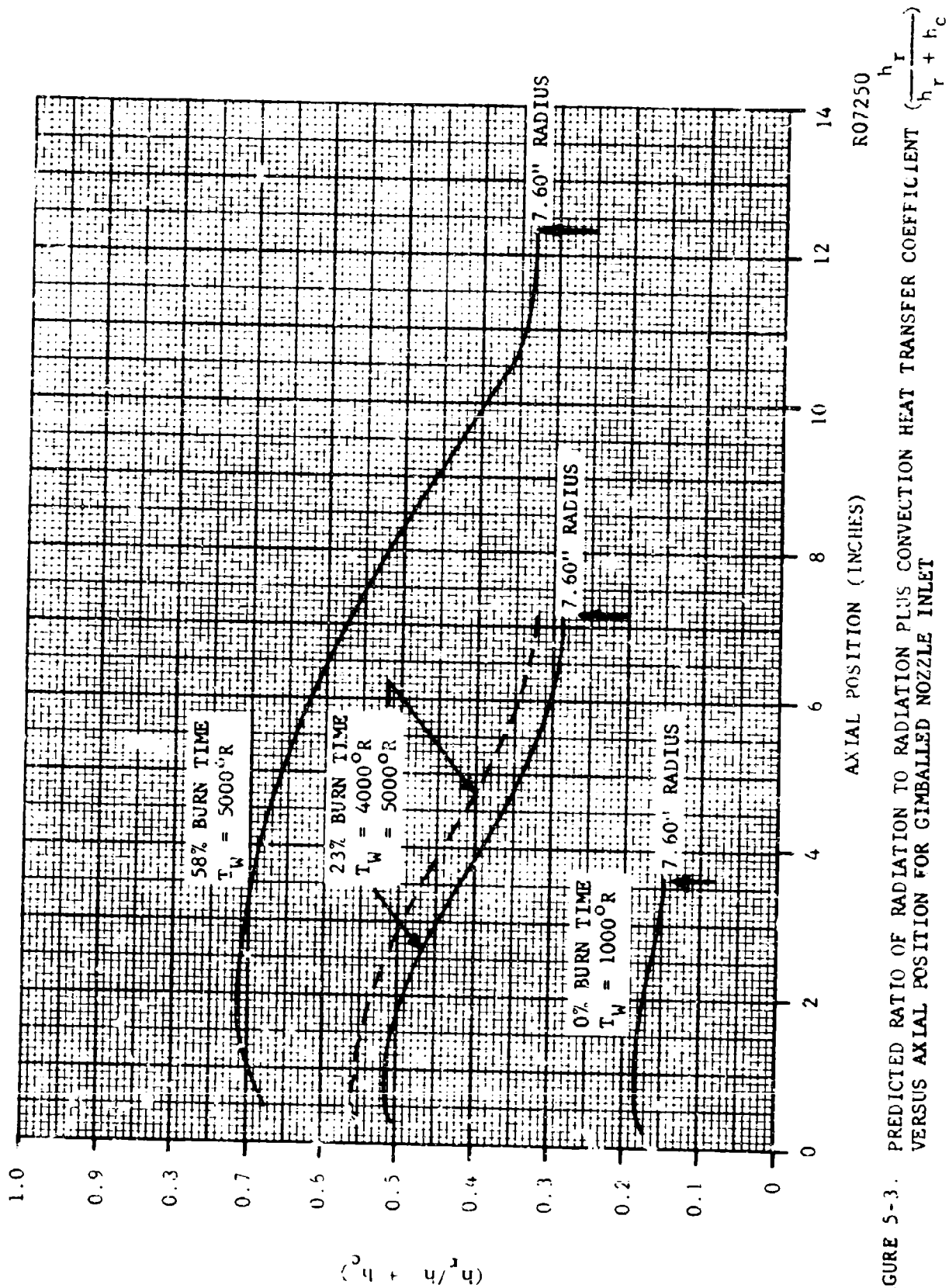


FIGURE 5-3. PREDICTED RATIO OF RADIATION TO RADIATION PLUS CONVECTION HEAT TRANSFER COEFFICIENT ( $\frac{h_r}{h_r + h_c}$ ) VERSUS AXIAL POSITION FOR GIMBALED NOZZLE INLET

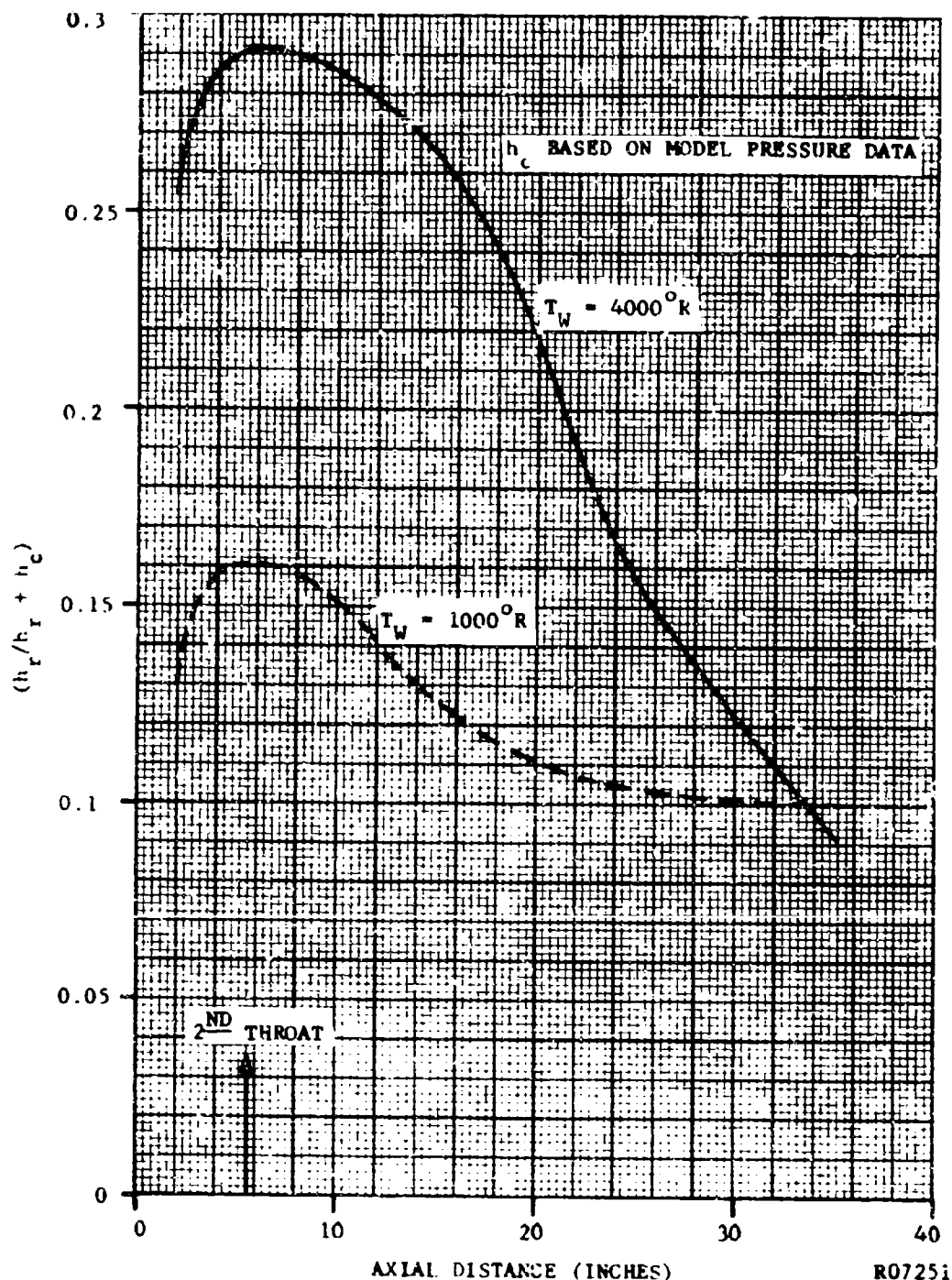


FIGURE 5-4. PREDICTED RATIO OF RADIATION TO RADIATION PLUS CONVECTION HEAT TRANSFER COEFFICIENT VERSUS AXIAL POSITION FOR GIMBALLED NOZZLE EXIT

The importance of particle cloud radiation in the simulator nozzle is shown in Figure 5-5, in which it can be seen that the amount of radiation heat flux is roughly doubled with the addition of  $Al_2O_3$  particles. In the calculation of the ratio  $(h_r/h_c + h_r)$ , the effect of the particles on the convective transfer is essentially omitted. That is, the convective heat transfer coefficient of Section 7 was simply added to the calculated radiation component.

Figure 5-6 is similar to 5-5 except the total heat flux ( $h_t$ ) is found from experiment and the radiation is based upon the experimental flame temperature. Comparison of Figures 5-5 and 5-6 results in a large discrepancy for the inlet section of  $\phi = 0$ . This deviation is attributed to mainly the difference in the calculated and experimental convective heat flux.

### 5.3.3 CONDITIONS WHEN UNITY CLOUD EMISSIVITY APPLIES

Black body conditions of a particle cloud in a rocket nozzle are shown in Figure 5-7; that is, determination of nozzle conditions required to produce a cloud total emissivity between 0.97 and 1.0 are plotted in Figure 5-7, and the use of the figure requires the same assumptions as were made in the construction of Figure 5-1.

In using Figure 5-7, the path length in an actual nozzle is obtained by use of Assumption (5) and rewritten here as:

$$\begin{aligned} \text{Path length} &= \text{local diameter in inlet and outlet sections of nozzle} \\ &= 1.4 \text{ times the throat diameter in the throat region.} \end{aligned}$$

The parameter  $\phi \bar{M}$  is the product of the ratio of particle to gas weight and gas molecular weight. Typical gas molecular weights are 18 for  $H_2 - C_2$  and 21 for 100 FW-2 propellant.

### 5.4 CONCLUSIONS

The total alumina cloud emissivity is presented for general cloud thermodynamic properties.

Predication of the emissivities are approximate and should be used only for an order of magnitude estimate. However, for a cloud with negligible multiple scattering as compared to self absorption, Figure 5-1 represents a good conservative prediction of cloud emission.

The radiation in actual rocket nozzles has been found empirically. The method used in the calculation was approximate although the importance of alumina cloud radiation as a mode of heat flux was shown; and found to be as large as 50 percent of the total heat flux.

Nozzle conditions to produce blackbody effects in the particle cloud have been developed by applying existing experimental data. It was found, for example, that with thermodynamic properties of  $T = 5200^\circ R$ ,  $P = 350$  psia, alumina loading ( $\phi$ ) = 0.5, and gas molecular weight ( $M$ ) = 20.0; the cloud emissivity may be taken at unity for path lengths greater than 14 inches.

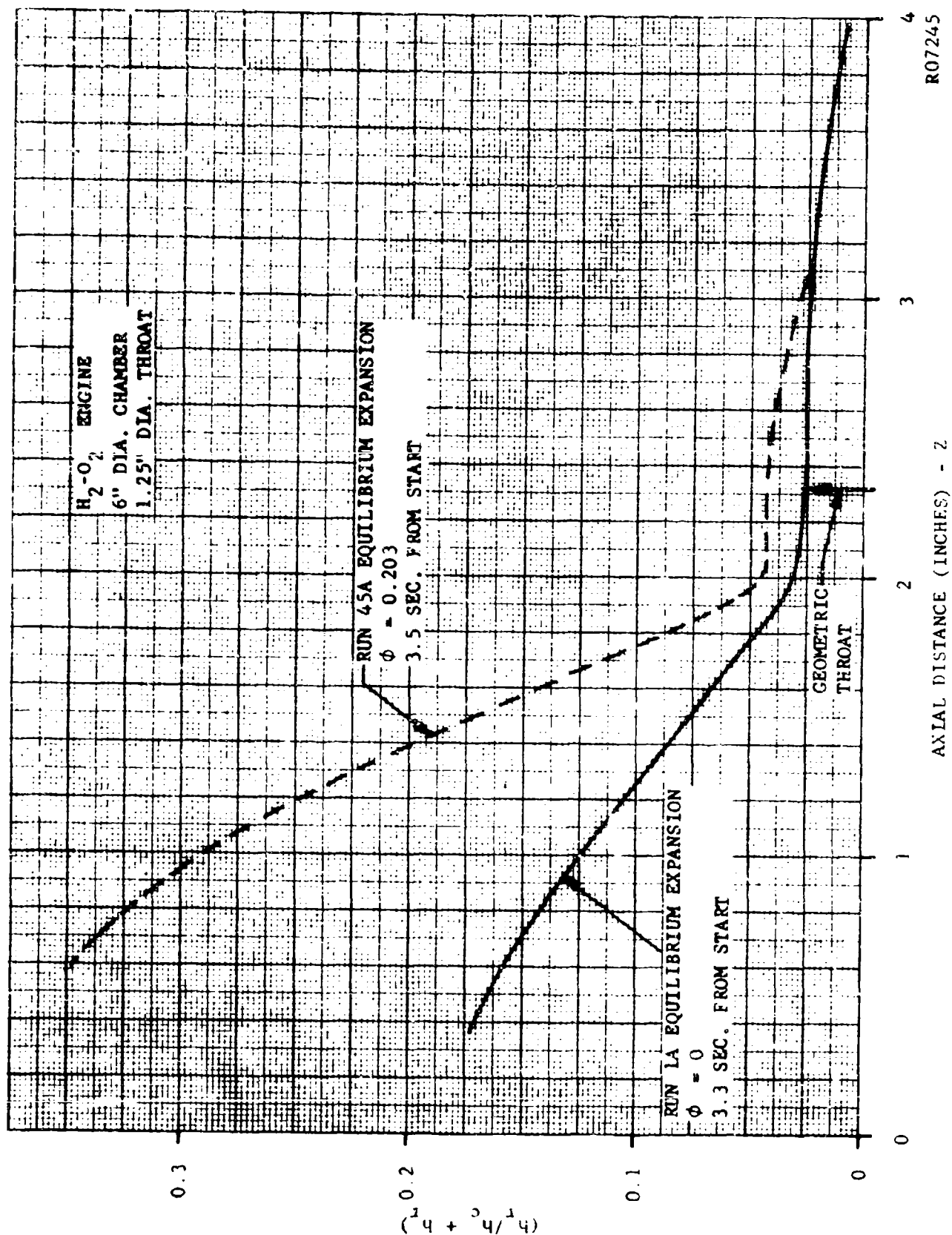


FIGURE 5-5. PREDICTED RATIO OF RADIATION TO RADIATION PLUS CONVECTION

R07245

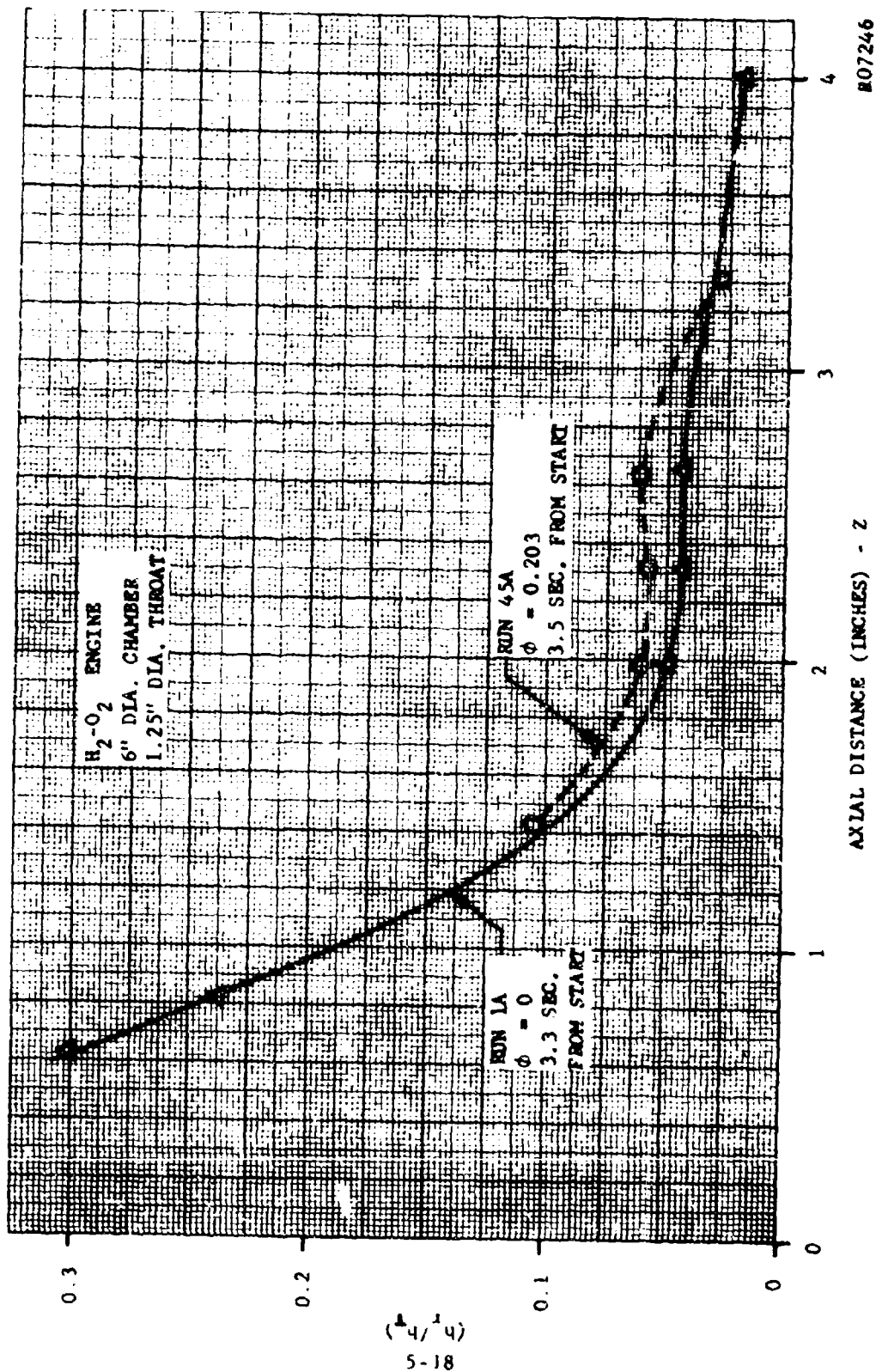


FIGURE 5-6. SEMI-EXPERIMENTAL RATIO OF RADIATION TO TOTAL HEAT TRANSFER COEFFICIENT VERSUS AXIAL POSITION FOR MOLYBDENUM SIMULATOR NOZZLE RUNS 1A AND 45A

807246



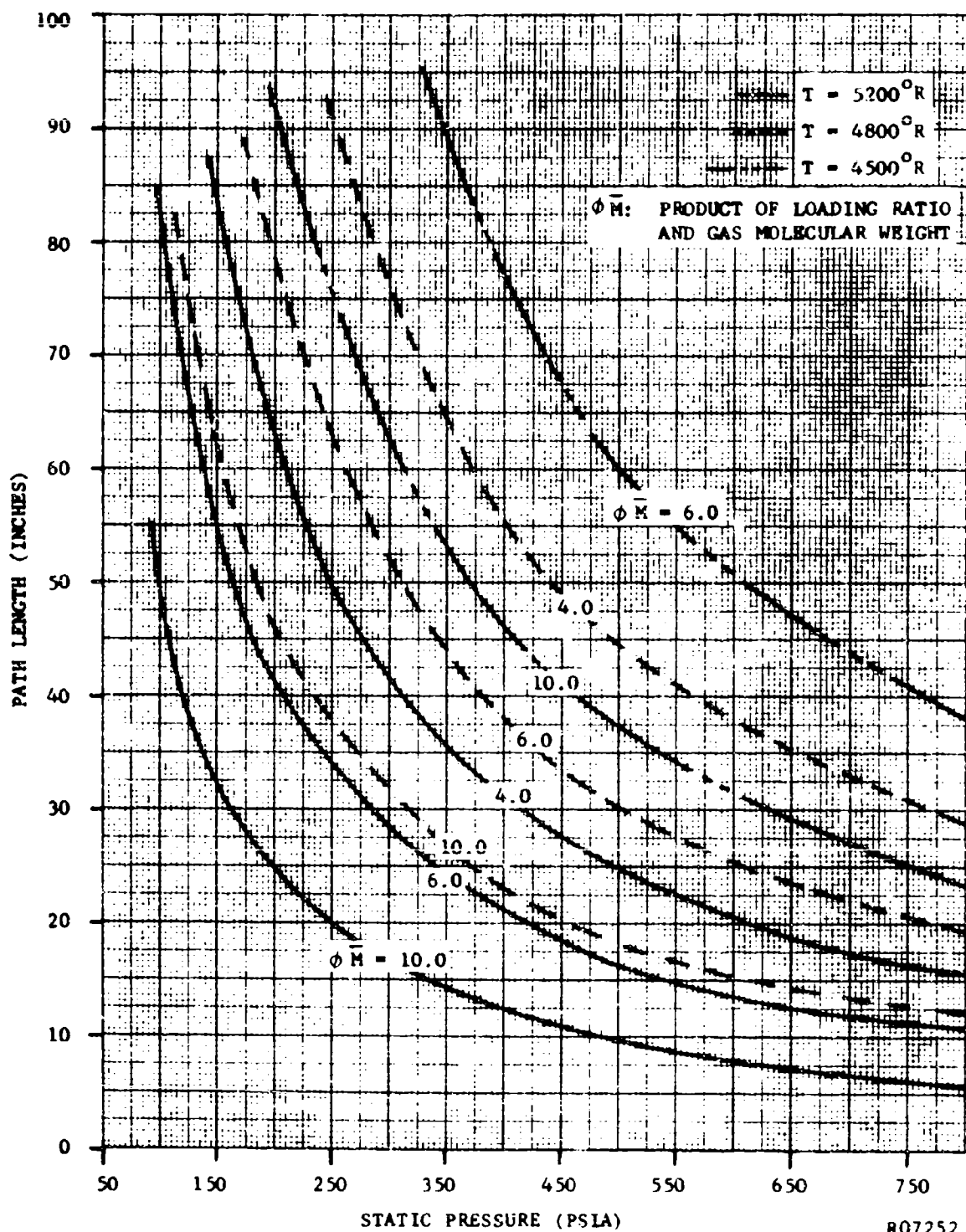


FIGURE 5-7 PATH LENGTH REQUIRED FOR GIVEN PRESSURE AND  $\phi \bar{M}$  OF AN  $\text{Al}_2\text{O}_3$  PARTICLE CLOUD TO PRODUCE BLACK BODY CONDITIONS

## 5.5 REFERENCES

- 5.1 Eckert, E. R. G., Drake, R. M. Heat and Mass Transfer, Second Edition, McGraw-Hill (1959)
- 5.2 Carlson, D. J. et. al Alumina Absorption and Emittance, Aeronutronic Publication No. U-2627, Contract NONr 3606(00), May 1964.
- 5.3 Morizumi, S. J. and Carpenter, H. J., "Thermal Radiation from the Exhaust Plume of an Aluminized Composite Propellant Rocket." AIAA Aerospace Sciences Meeting, New York, January 20, 1964.
- 5.4 J. T. Bevens, R. V. Dunkle, "Radiant Interchange Within an Enclosure", Trans ASME, February 1960.
- 5.5 A. K. Oppenheim "Radiation Analysis by Network Method", Trans ASME, Vol 78, 1956.
- 5.6 McAdams, W. H. Heat Transmission, 3rd Edition, McGraw-Hill, (1954).
- 5.7 Kreith, F., Principles of Heat Transfer, International Textbook Co., (1961).
- 5.8 Goldsmith, A; Hirschhorn, H. J.: and Waterman, T. E. Thermophysical Properties of Solid Materials, Volume III, WADC Tech. Report 58-476, November 1960.

## NOMENCLATURE

[illegible]

## SECTION 6

### SAMPLING OF MICRON-SIZED PARTICLES

Particles in the size range of 0.5 to 6 microns in diameter were used in the modeling and in the hot firings. In both cases, there was a need to capture and observe the particles of the gas streams.

Picking up the polystyrene particles by impingement on sticky tape in the impacting sampler allowed a check of the sticky tape as an impingement detector on the nozzle model. The particle samples were then used in the development of a microscope technique for counting the impinged particles. It also indicated whether or not the particles were dispersed individually by the atomizing system.

Sampling of the rocket particles allowed a check on whether or not the particles were melted and on how well they were dispersed or agglomerated in the rocket.

The May-Welchman particle analyzer, which was used, consisted of four brass sampling nozzles mounted in a square ring at right angles to each other in cascade. Opposite each nozzle was an impingement slide where the particles were collected from the turning gas stream. The largest nozzle, first stage, received the rocket exhaust and collected relatively large particles, and passed on the part not collected to the next nozzle. The fourth nozzle had the smallest cross section and collected the finest particles. Its collection chamber was connected to a gas aspirator. Only the fourth stage was normally used in order to provide a complete sample of all particle sizes on one slide. Nozzle throat dimensions for the fourth stage were 14mm x 0.6mm in the shape of a rectangular slot.

The sampling apparatus was developed especially for the rocket plume using the May-Welchman apparatus. It was mounted in a device (Figs 6-1&6-3) having a neoprene sealed shutter to (1) maintain steady vacuum conditions in the nozzle system before sampling, (2) pick up a small enough sample to show discrete particles, and (3) omit sampling extraneous dust before the firing. The shutter was actuated by a solenoid. Sampling time was a function of the duration of the current pulse to the solenoid (approximately 1/10 second) and the spring tension on the shutter mechanism. The sampling time was held constant at approximately 1/5 second for all samples. The apparatus was mounted in the center of the rocket plume approximately 30 feet from the nozzle exit.

The exhaust particles were collected on clear glass microscope slides. Different surface treatment of slides included double-sided Scotch tape, translucent Scotch tape No. 810, standard transparent Scotch tape, and the cleaned surface of the glass slide itself. The clean glass slide produced the most readable samples.

From an examination of the particle samples several conclusions could be drawn:

- (1) Not all the particles issuing from the throatless motor were molten when conditions were set for a chamber temperature of 5100°F.
- (2) There was very little agglomeration of particles in the throatless engine.
- (3) The engine with the molybdenum nozzle for particle impingement studies produced a wide variety of particles: spherical, crystalline, agglomerated. This is expected since it is known that a considerable amount of alumina ran down the nozzle entrance and was then broken up at the throat.

Figure 6-2 shows some of the particle displays produced by photographs of the sampler impact area from various firings.

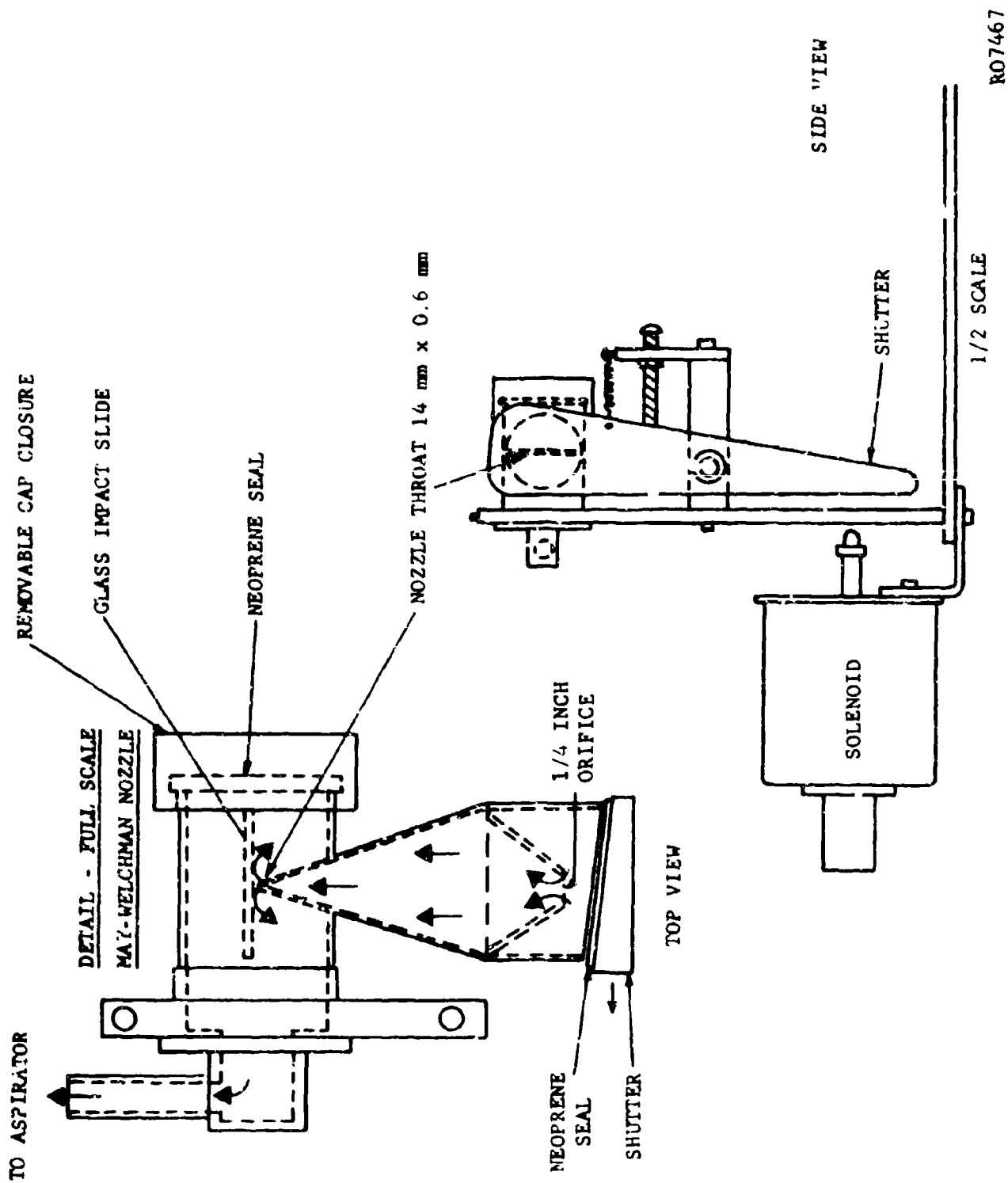
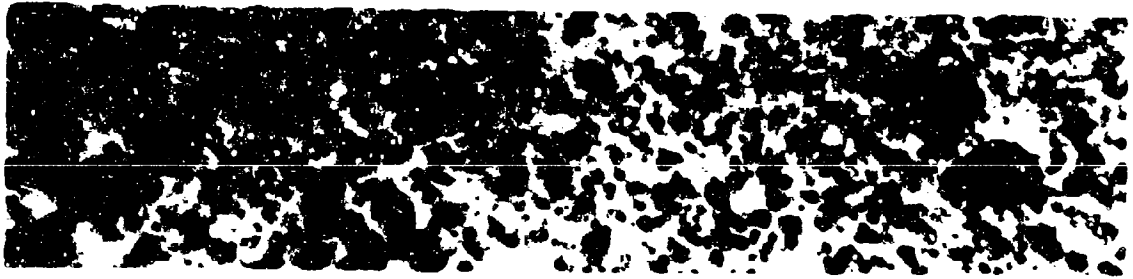


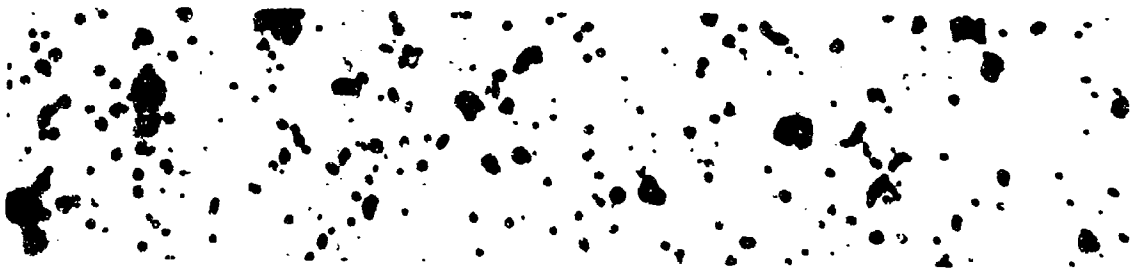
FIGURE 6-1. APPARATUS FOR SAMPLING ROCKET EXHAUST



MOLY NOZZLE  $\phi = 0.3$   $AL_2O_3$  1000X



MOLY NOZZLE  $\phi = 0.3$   $AL_2O_3$  1000X



MOLY NOZZLE  $\phi = 0.2$   $AL_2O_3$  1000X



THROATLESS ENGINE  $\phi = 0.2$   $AL_2O_3$  10,000X

FIGURE 6-2. SAMPLED ALUMINA PARTICLES

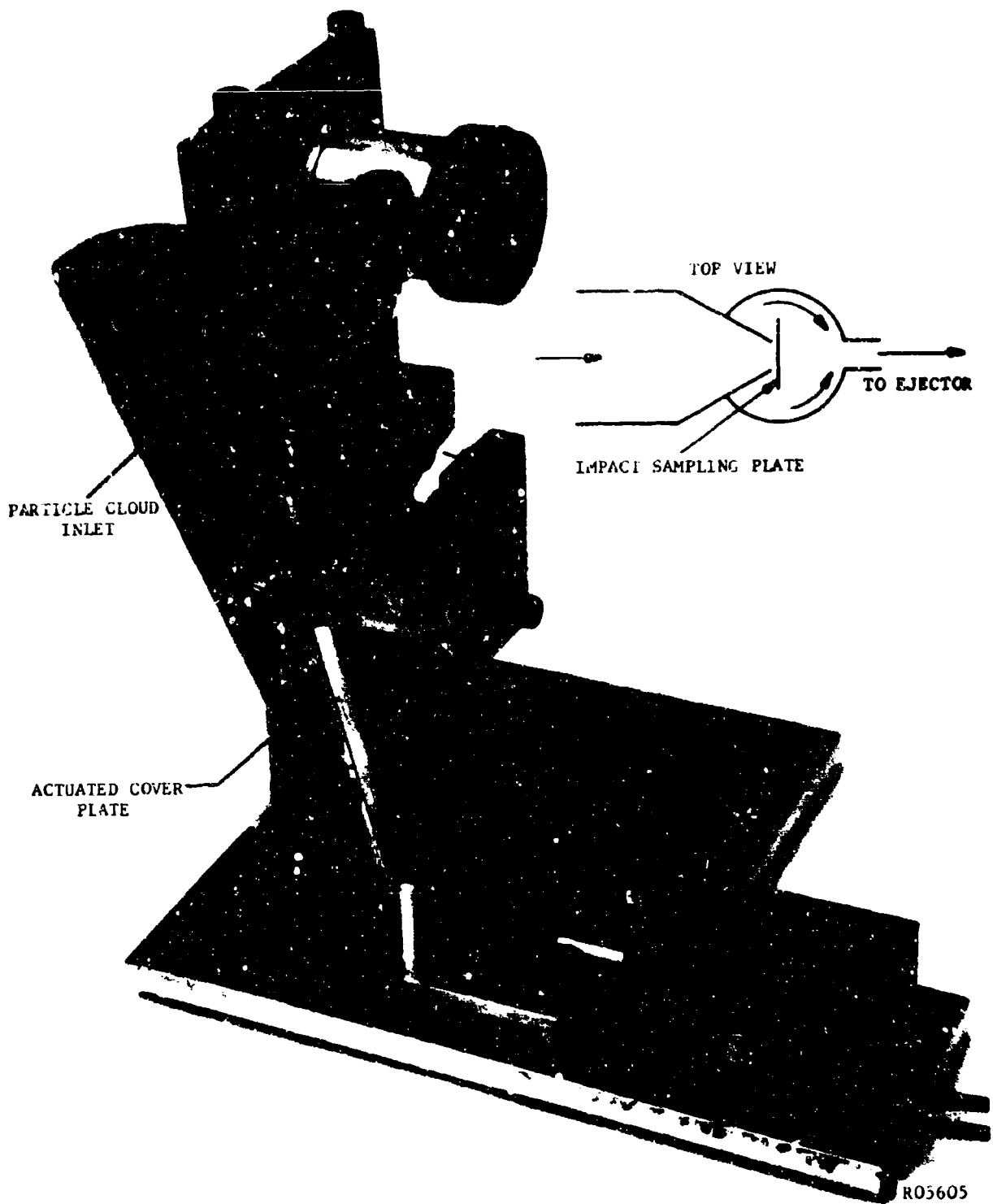


FIGURE 6-3. EXHAUST CLOUD PARTICLE SAMPLER



**BLANK PAGE**

## SECTION 7

### CONVECTIVE HEAT TRANSFER ANALYSES

#### 7.1 INTRODUCTION

Although the emphasis in this program has been placed on the enigma of the condensed phase and radiation energy transport mechanisms, there is still much to be learned to define accurately the convective process. In most cases, the condensed phase and radiation contributions to total heat transfer in solid propellant nozzles are of the same order as the errors commonly associated with the convective predictions.

References 7.1 to 7.4 contain rather general treatments of the important aspects of the nozzle heat transfer problem. Some of the more important conclusions which can be drawn from these and other studies of nozzle heat transfer include:

- (1) For the nozzles of interest in this program, the convective heat transfer is a consequence of turbulent boundary layer development.
- (2) Chemical effects due to (1) dissociation and recombination, (2) nozzle wall ablation or pyrolysis, and (3) corrosion are not negligible.
- (3) Physical modification of the boundary layer due to the surface blowing is important.
- (4) Surface roughness, resulting from the condensed phase interaction with the nozzle wall or physical erosion, may significantly influence boundary layer development.

- (5) It is a good approximation to assume that radiative and convective effects are additive when the radiative flux is significantly less than the convective flux.
- (6) The direct addition of condensed phase impingement and convective effects is regarded as a first approximation which, in some cases, may be very poor.
- (7) Non-ideal combustion and non-equilibrium nozzle expansion considerations can reasonably be avoided for the present purposes.

The interaction effects among the various modes of energy transfer are omitted from consideration in this work. The consequences of this can be illustrated by the following example. The convective heat transfer to an ablating or pyrolyzing nozzle surface will lead to the injection of gaseous ablation products into the boundary layer. The injection tends to reduce the convective transport by altering the physical boundary layer parameters, surface shear, and boundary layer chemical composition. Chemical reactions, usually endothermic, between the combustion and ablation products can further reduce the convective heat flux to the wall. Since these effects are proportional to the mass addition rate, which depends on the convective heat transfer, equilibrium will be attained, and the net convective transport will be less than for the case of no injection. Under these conditions, if there is also radiation heat transfer, mass addition rates will increase and the convective heat transfer will be reduced. Consequently, simple addition of radiation and convection is conservative. On the other hand, the impingement of condensed phases on the nozzle surface will tend to increase the boundary layer turbulence level near the wall. This will tend to increase the convective heat transfer so that simple addition of the effects will not be conservative. Clearly, when these coupling effects are neglected and the simplified theoretical results are forced to fit experimental measurements, the effective heats of ablation of the wall material ( $Q_{eff}^*$ ) will be higher than expected. Preliminary results obtained from current work at Philco suggest that film cooling and chemical reaction effects could increase the apparent heat capacity of charring and non-charring ablators by factors of 2 to 5, or more, respectively.

The primary objective in presenting these introductory remarks has been to establish the context within which the convective heat transfer results apply. They also serve to emphasize the need for caution in the interpretation of the results. Following a brief description of the calculation method, the results for three specific nozzle designs will be presented and discussed.

## 7.2 METHOD OF CALCULATION

The method of calculating rocket nozzle turbulent boundary layer growth and convective heat transfer described in Reference 7.4 has been used exclusively. The actual calculations were accomplished on an IBM 7094 digital computer. Reference 7.4 provides an excellent description of both the theory and the computer program input requirements. Briefly, the method features the simultaneous solution of the boundary layer integral momentum and energy equations. One-seventh power profiles of velocity and temperature are used to approximately determine the boundary layer shape parameters. The skin-friction coefficient and Stanton number are evaluated as functions of boundary layer thickness from the best available semiempirical relations. The computer program provides a number of useful options, including choices of (1) one dimensional flow or arbitrary Mach number distribution and (2) enthalpy or temperature driving potentials. Although a number of criticisms may be raised against this method of calculation, it is one of the best available, and it was found to be both convenient and economical for the present purposes. The important inputs to the program and the assumptions made will be discussed briefly before presenting the results of the computations.

All heat transfer calculations require the initial definition of the chamber conditions, combustion product properties throughout the nozzle, and the nozzle geometry. Subsidiary thermochemical computer programs are used to calculate chamber conditions, given the original propellant composition and the desired chamber pressure. The combustion products are then expanded isentropically for both the frozen and equilibrium flow assumptions. These calculations provide the chemical composition, ratio of specific heats, and specific heat data required for the convection analysis. A secondary hand calculation is used to relate pressure and mach number when wall static pressure distributions are available from experiment. Normally the equilibrium expansion assumption is preferred, in which case the isentropic exponent,

$$\gamma_{eq} = \left( \frac{\partial \ln p}{\partial \ln \rho} \right)_s,$$

evaluated in the throat region, is taken as an average value to represent the flow. The equilibrium specific heat,

$$c_{p,eq} = \left( \frac{\partial H}{\partial T} \right)_p,$$

calculated throughout the expansion is not the appropriate value to use in boundary layer calculations. However, such values can be used to determine an approximate average value when the nozzle surface temperatures are known or assumed. When an average specific heat is so determined, the temperature driving potential is used to calculate heat transfer.

The specification of the nozzle wall temperatures is normally an important and complex problem. Most of the calculations were performed under the assumption of constant wall temperature, primarily for convenience. Actual wall temperatures vary with time, axial position, and wall material. Additionally, gas properties and friction coefficients were evaluated at the film reference temperature.

The Prandtl number, stagnation viscosity, and the temperature dependence of the viscosities were determined from the data given in Reference 7.6. The free stream stagnation temperatures were taken equal to the ideal values for the measured or time averaged chamber pressures. The heat transfer program assumes a recovery factor of 0.89 in calculating adiabatic wall temperatures.

In all the calculations, the boundary layer is assumed to grow from an initial momentum thickness slightly greater than zero. Similarly, the initial ratio of thermal to velocity boundary layer thicknesses is taken to be slightly greater than unity. The effects of these relatively arbitrary specifications die out rapidly and do not seriously compromise the results. It should also be noted that during the initial development of the boundary layer, laminar flow is normally expected whereas the calculations regard the entire boundary layer development as turbulent. Consequently, the first heat transfer coefficient calculated is not accurate. However, the first point is expected to be directionally correct, as it should be higher than the succeeding point or points due to the importance of the boundary layer development length effect.

Consistent with the recommendations of Reference 7.4, a boundary layer interaction exponent of 0.1 was chosen for all convection calculations. This quantity provides for the effective increase in the heat transfer coefficient when the boundary layer energy thickness exceeds the momentum thickness.

A few additional assumptions concerning the nozzle geometry and boundary layer starting points are required. These are briefly discussed along with the results of the calculations for each particular nozzle examined.

### 7.3 RESULTS

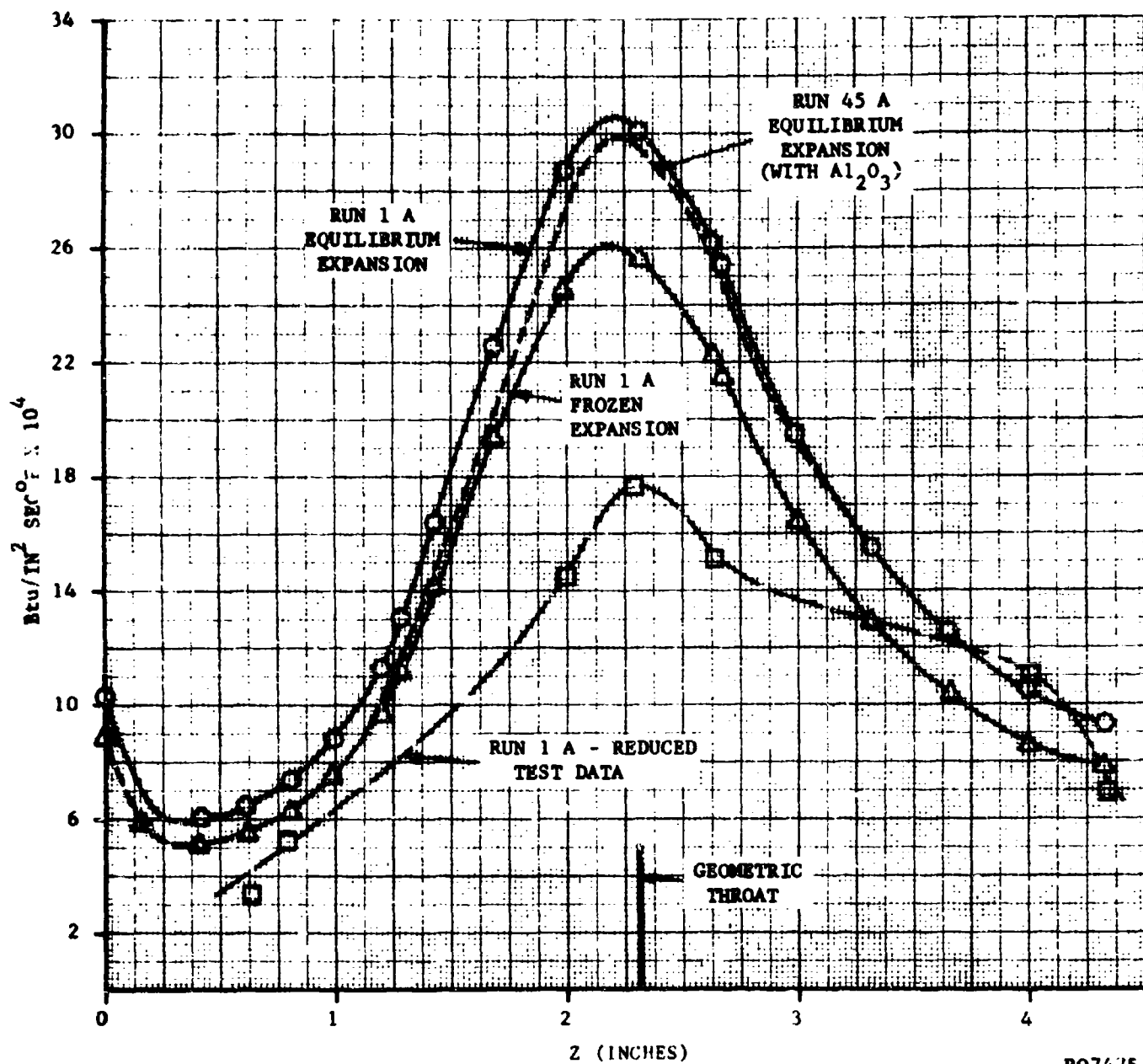
Calculations were performed for three different nozzles. The results are presented separately. Note that, except where noted otherwise, the symbols which appear in the figures which follow represent calculated points, not experimental measurements.

#### 7.3.1 MOLYBDENUM CALORIMETRIC NOZZLE

The molybdenum nozzle geometry and thermocouple locations are shown in Figure 3-5 and in Table 7.1. The convective heat transfer for Run 1A, frozen and equilibrium expansion, and Run 45A are shown in Figure 7-1 for comparison. The boundary layer was assumed to start on the conical (55 degrees) inlet section at a radius equal to the chamber (grain port) radius. It was necessary to fit a smooth curve to the available thermocouple data to provide an adequate wall temperature distribution. Heat transfer coefficients were calculated at a single time near the

TABLE 7.1  
MOLYBDENUM SIMULATOR NOZZLE GEOMETRY  
AND THERMOCOUPLE LOCATION

<u>Axial Distance Z, Inches</u>	<u>Radius, Inch</u>	<u>Area Ratio</u>	<u>Thermocouple Number</u>
0	3.0	23.0	-
0.418	2.405	14.8	1
0.618	2.119	11.5	2
0.808	1.847	8.7	3
0.998	1.575	6.35	4
1.198	1.289	4.25	5
1.290	1.159	3.44	-
1.430	0.991	2.4	6
1.689	0.793	1.61	7
1.990	0.667	1.14	8
2.314	0.625	1.0	9
2.638	0.667	1.14	10
2.880	0.680	1.18	-
2.998	0.773	1.53	11
3.318	0.867	1.92	12
3.658	0.966	2.39	13
3.988	1.063	2.9	14
4.328	1.162	3.47	15



RO7475

FIGURE 7-1. PREDICTED AND EXPERIMENTAL CONVECTIVE HEAT TRANSFER COEFFICIENT VERSUS NOZZLE AXIAL POSITION FOR MOLYBDENUM CALORIMETRIC NOZZLE

end of the run when chamber and wall temperature conditions were reasonably stable (3.3 seconds). It should be noted that these results must be interpreted as corresponding to the theoretical flame temperature with a recovery factor of 0.89. For the purpose of calculating viscosity, the composition of the combustion gases was assumed to be 90 percent  $H_2O$  - 10 percent  $H_2$ . Also shown in Figure 7-1 are convective coefficients calculated directly from test data of Run 1A. As shown, the theoretical coefficients for frozen expansion in the throat region are 50 percent higher than those found experimentally. In the entrance and high area ratio exit cone locations, theoretical and experimental coefficients are more nearly equal.

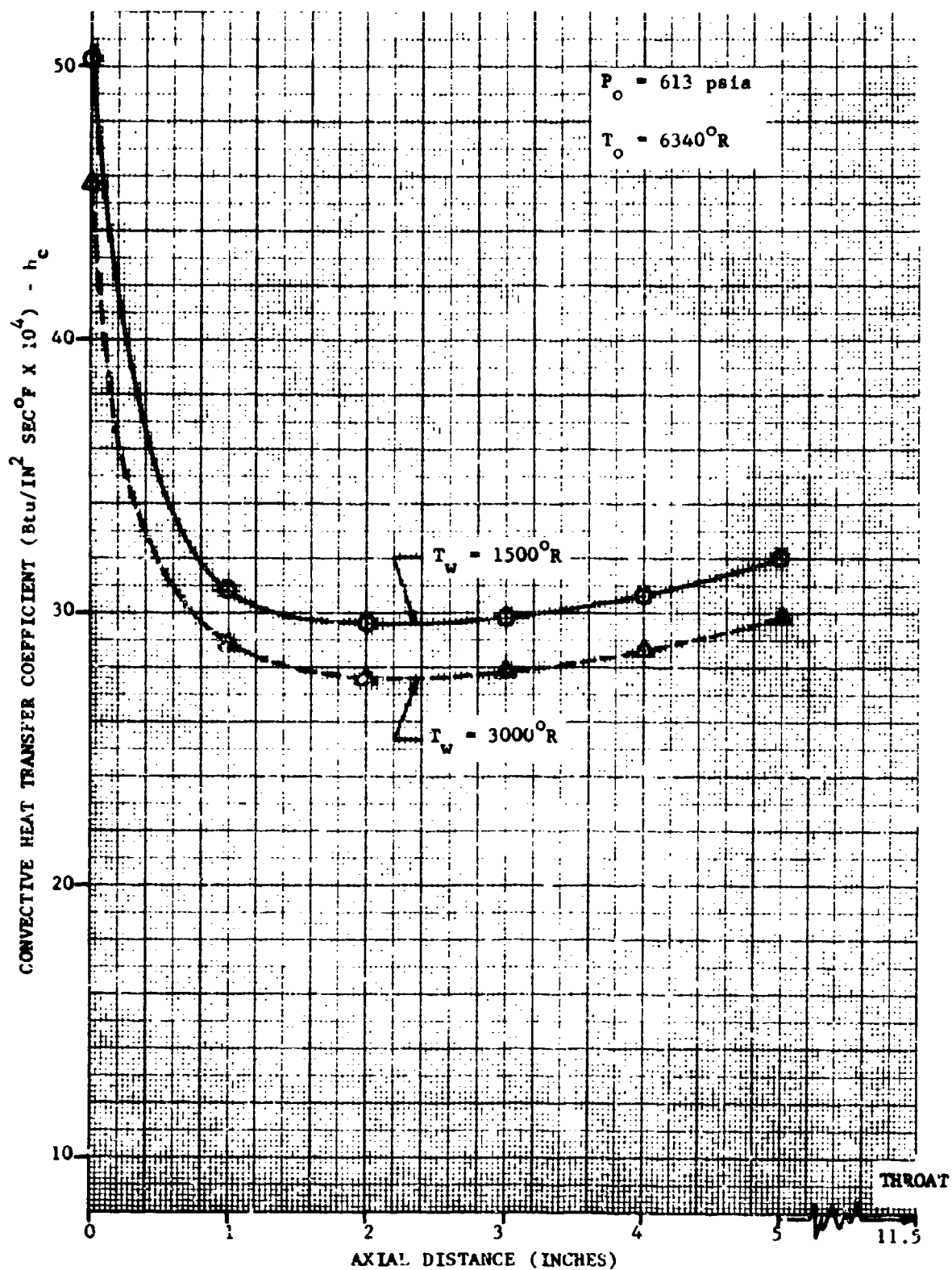
### 7.3.2 100FW-2 NOZZLE INLET

Convection coefficients calculated for the soft ablator portion of the 100FW-2 nozzle inlet are presented in Figures 7-2 through 7-6. Each of these figures represents a particular time during the firing, and, consequently, it was necessary to determine the appropriate ablator geometry at each time. The initial and final contours were known from the inlet design and post test measurements (Reference 7.5). At 5 seconds, it was assumed that the exposed portion of the original contour was unchanged. At the end of firing, 90 seconds, the post test measured contour was assumed. The 19.5, 50, and 75 second contours were constructed by assuming that the insulation surface regression was a linear function of the time it was exposed. In all cases, the heat transfer calculations were stopped at the point where the soft insulation met the graphite substrate, and they were started at the point where the propellant grain met the soft insulation. The assumed geometries are shown in Table 7.2. The two curves shown in each of the figures are a consequence of assuming constant wall temperatures of 1500 and 3000°R. Considerably less difference would be observed if the combustion gas properties and friction coefficients had been evaluated at free stream conditions. The combustion gas viscosity was determined by assuming proportional contributions by the major gas components using the data of Reference 7.6. The values of the convection coefficients near  $Z = 0$  can certainly not be regarded as accurate due to the uncertainty of the grain burning and flow field details in this region. In general, Figures 7-2 through 7-6 show the expected trend of decreasing heat transfer coefficient with increasing distance from the origin of the boundary layer. This trend would, of course, indicate that the linear insulation recession rate assumption was not accurate, unless one of the other heat transfer modes has a reverse tendency.

### 7.3.3 GIMBALL NOZZLE

A full scale gimballled nozzle was scaled down (5.75 to 1), and the wall pressure distributions were measured in both the straight and canted (5 degree) positions. The convective heat transfer has been calculated, using the modeling pressure data, for the full scale nozzle. The 100FW-2 propellant and chamber pressure were assumed for these calculations. Because of the severe interruption in the nozzle contour upstream of the throat, it was necessary to calculate the heat transfer in the inlet and throat-exit sections separately.





R07488

FIGURE 7-2. PREDICTED CONVECTIVE HEAT TRANSFER COEFFICIENT VERSUS AXIAL DISTANCE FOR 100FW-2 AFT CLOSURE AT 5 SECONDS

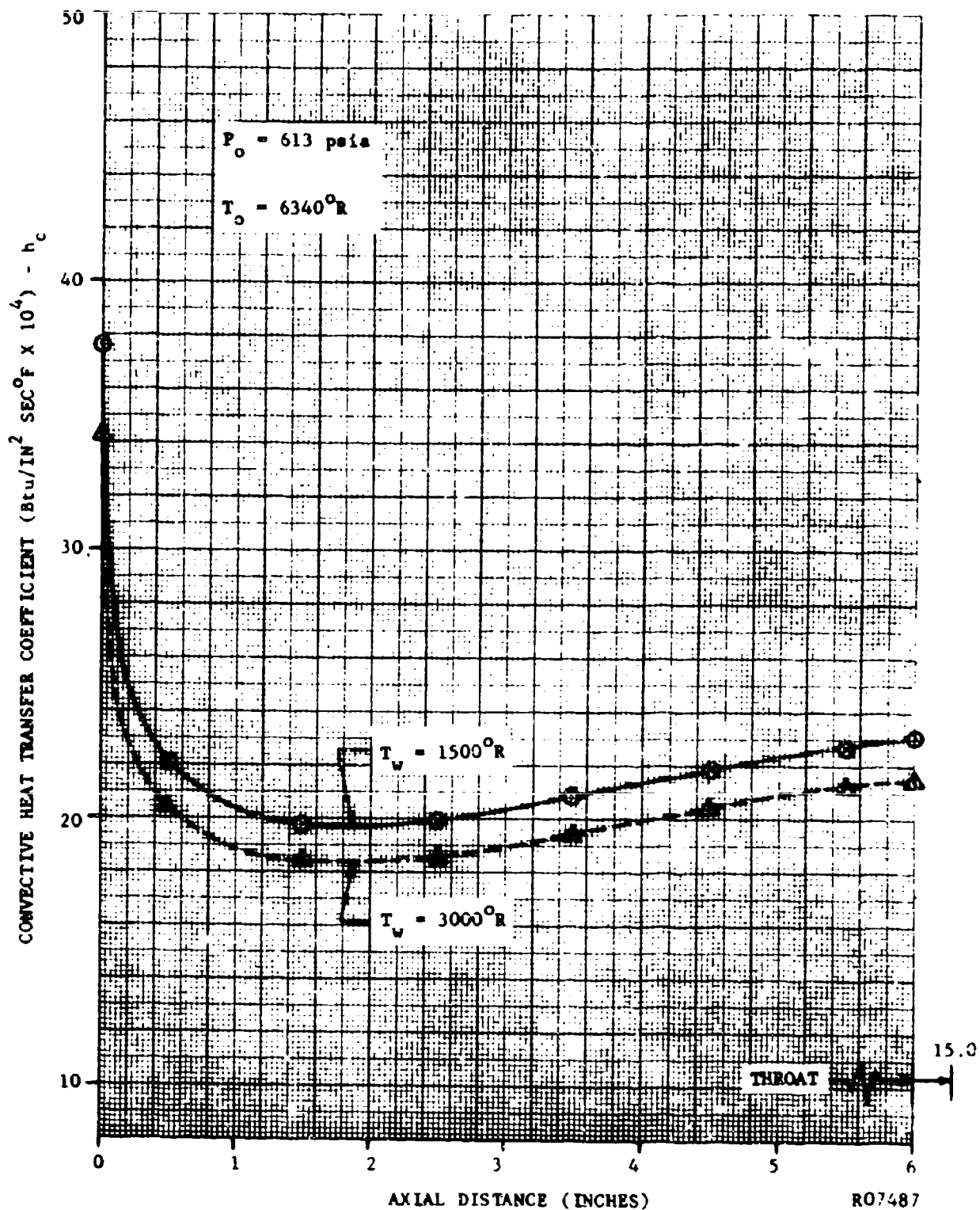
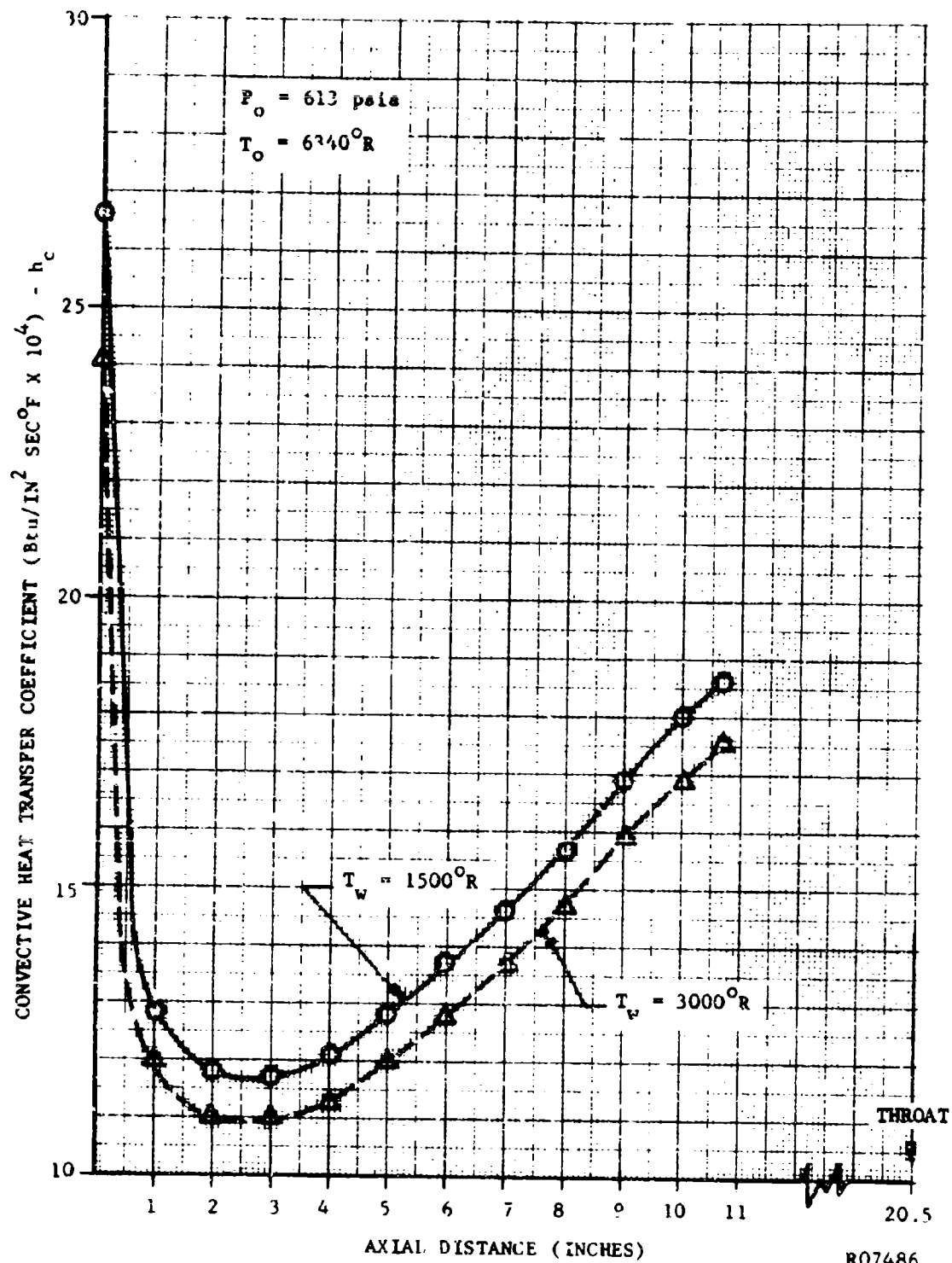


FIGURE 7-3. PREDICTED CONVECTIVE HEAT TRANSFER COEFFICIENT VERSUS AXIAL DISTANCE FOR 100FW-2 AFT CLOSURE AT 19.5 SECONDS



R07486

FIGURE 7-4. PREDICTED CONVECTIVE HEAT TRANSFER COEFFICIENT VERSUS AXIAL DISTANCE FOR 100FW-2 AFT CLOSURE AT 50 SECONDS

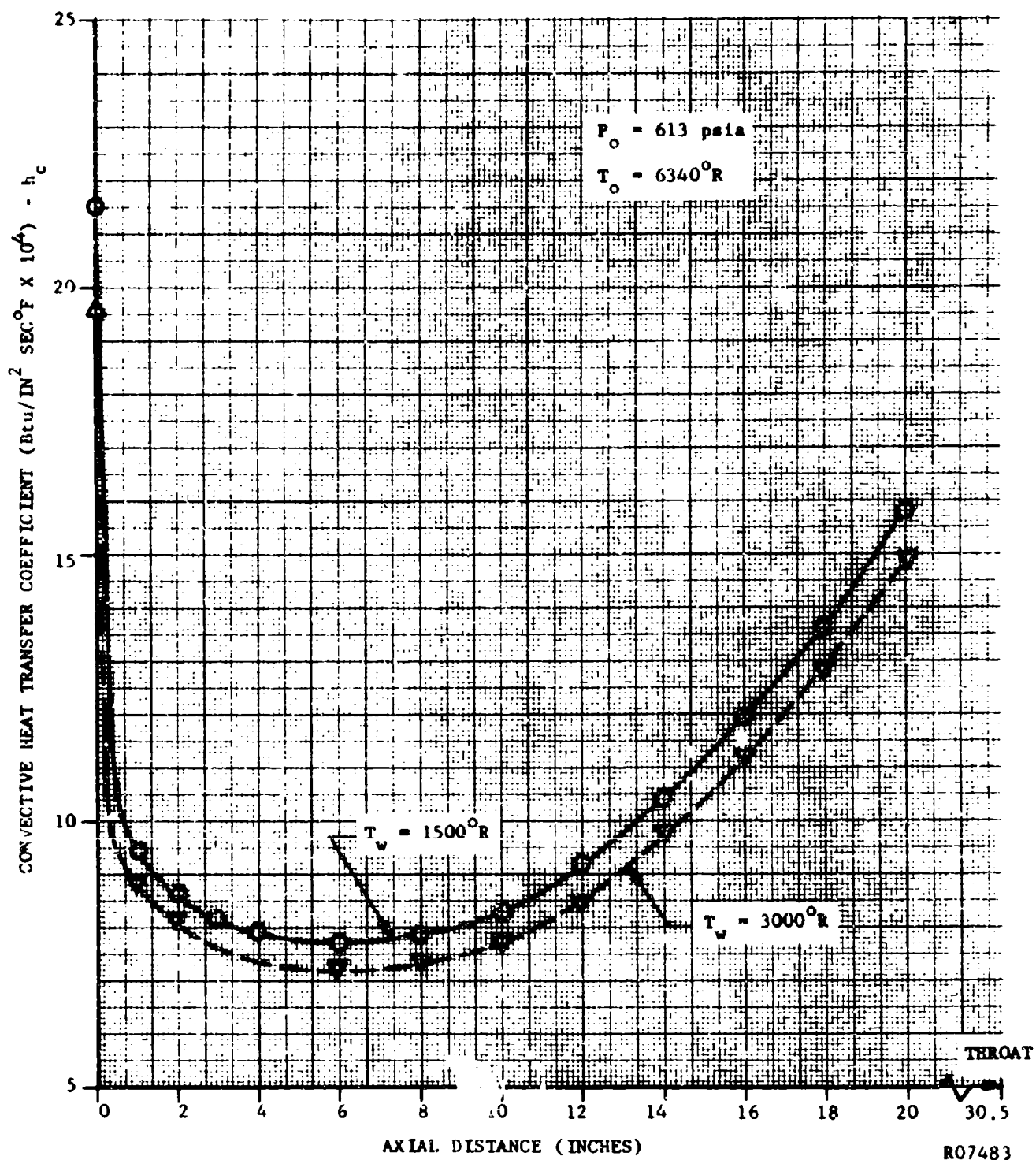
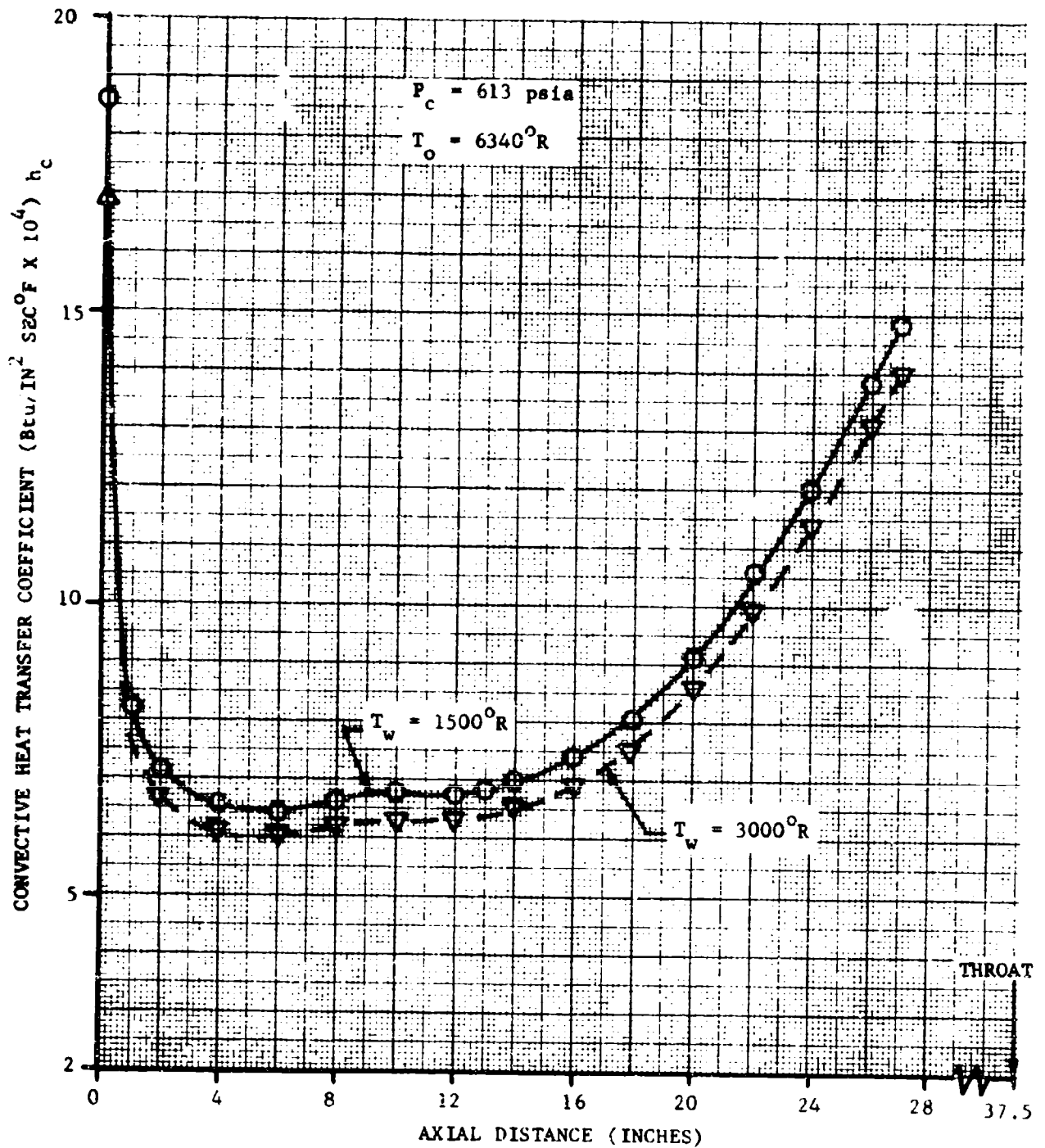


FIGURE 7-5. PREDICTED CONVECTIVE HEAT TRANSFER COEFFICIENT VERSUS AXIAL DISTANCE FOR 100FW-2 AFT CLOSURE AT 75 SECONDS



R07479

FIGURE 7-6. PREDICTED CONVECTIVE HEAT TRANSFER COEFFICIENT VERSUS AXIAL DISTANCE FOR 100FW-2 AFT CLOSURE AT 90 SECONDS

TABLE 7.2

## 100FW-2 NOZZLE INLET GEOMETRY:

5 Seconds After Ignition

<u>Axial Position</u> <u>Z, Inches</u>	<u>Radius</u> <u>Inches</u>	<u>Axial Position</u> <u>Z, Inches</u>	<u>Radius</u> <u>Inches</u>
0.0	20.87	4.0	17.68
1.0	19.84	5.0	17.02
2.0	19.02	11.5	- throat - 14.20
3.0	18.35		

19.5 Seconds After Ignition

0.0	26.77	4.5	21.22
0.5	25.92	5.5	20.52
1.5	24.62	6.0	20.25
2.5	23.35	15.0	- throat - 14.27
3.5	22.22		

50 Seconds After Ignition

0.0	36.22	7.0	26.17
1.0	34.97	8.0	24.87
2.0	33.67	9.0	23.67
3.0	32.02	10.0	22.67
4.0	30.37	10.7	22.17
5.0	28.87	20.5	- throat - 14.41
6.0	27.37		

75 Seconds After Ignition

0.0	43.77	11.0	35.37
1.0	42.17	12.0	34.17
2.0	41.17	13.0	32.57
3.0	41.15	14.0	30.97
4.0	40.87	15.0	29.67
5.0	40.37	16.0	28.37
6.0	39.77	17.0	27.7
7.0	39.07	18.0	26.17
8.0	38.17	19.0	24.97
9.0	37.47	20.0	23.87
10.0	36.47	30.5	- throat - 14.53

90 Seconds After Ignition

0	50.0	15.0	38.47
1.0	49.1	16.0	37.60
2.0	48.2	17.0	36.68
3.0	47.3	18.0	35.59
4.0	46.4	19.0	34.39
5.0	45.5	20.0	32.87
6.0	44.6	21.0	31.49
7.0	43.8	22.0	30.09
8.0	42.3	23.0	28.87
9.0	41.3	24.0	27.80
10.0	41.2	25.0	25.64
11.0	41.0	26.0	25.57
12.0	40.47	27.0	24.57
13.0	39.87	37.5	- throat - 14.65
14.0	39.20		

The results for the inlet section are shown in Figures 7-7 through 7-9 for grain burn times of 0, 23, and 58 percent respectively. The geometry is given in Table 7-3. In Figure 7-7, the wall temperature (graphite phenolic) was taken to be constant at  $1000^{\circ}\text{R}$  to approximately represent the starting conditions. The two curves in Figure 7-8 represent assumed wall temperatures of  $4000$  and  $5000^{\circ}\text{R}$ . Similarly the curves in Figure 7-9 represent  $5000$  and  $6000^{\circ}\text{R}$  surface temperatures. Although these temperatures are arbitrary, they are thought to cover the range of wall conditions which might realistically be expected. The boundary layer calculations were started at the propellant grain - wall contour junction. The calculations were all stopped at a radius of 7.60 inches which corresponds to the first throat radius in the modeling nozzle. The pressure measurements were not used in these calculations. Figure 7-10 compares the Mach number distribution corresponding to the one dimensional flow assumption with the Mach numbers determined from the model inlet pressure taps. The differences are not regarded as especially significant compared to the errors which could arise from fairing a curve through the three data points.

The calculated heat transfer coefficients for the throat-exit section of the full scale, gimbaled nozzle are shown in Figures 7-11 through 7-13. The geometry and Mach number distributions are given in Table 7.4. Figure 7-11 compares the heat transfer for the one dimensional flow assumption with that calculated using the modeling wall pressure distribution for a  $5000^{\circ}\text{R}$  isothermal wall. Also shown are the results for a non-isothermal wall. Here the wall temperature was taken at  $6000^{\circ}\text{R}$  in the throat section, and then varied uniformly to the local free stream static temperature at the last wall point in the exit cone. This temperature distribution is quite arbitrary, but it averages about  $5000^{\circ}\text{R}$  while decreasing from  $6000^{\circ}\text{R}$  to about  $4000^{\circ}\text{R}$ . Figure 7-12 compares the heat transfer coefficients determined for isothermal walls at  $1000$  and  $4000^{\circ}\text{R}$  with the nozzle in the straight position and using the modeling pressure data to determine Mach number. The  $5000^{\circ}\text{R}$  wall temperature values shown in Figure 7-11 were not replotted because they are very close to the  $4000^{\circ}\text{R}$  results. The one-dimensional calculations are replotted for comparison. Figure 7-13 presents the data for the nozzle in the canted position. Modeling pressure data was used to determine the Mach number distribution for each of the three curves. The results are also based on the assumption of a  $5000^{\circ}\text{R}$  isothermal wall condition. The canted nozzle wall coordinates are referred to the axial centerline of the exit cone. The boundary layer was started 5.40 inches upstream of the 15.0 inch diameter throat. This is apparently a reasonable assumption, because it is extremely doubtful that the boundary layer formed in the nozzle entrance section could persist across the major discontinuity in the contour between the two throats. The initial Mach number of 0.80 was determined from the model pressure measurement at station 4, and was the same for both the canted and straight configurations.

#### 7.4 CONCLUSIONS

In comparing the predicted heat transfer coefficients for the molybdenum nozzle with the values obtained from Kun IA, as shown in Figure 7-1, large differences are observed in the throat region. Referring to Figure 1 of reference 7.7, it is evident that transitional boundary layer flow could occur in the

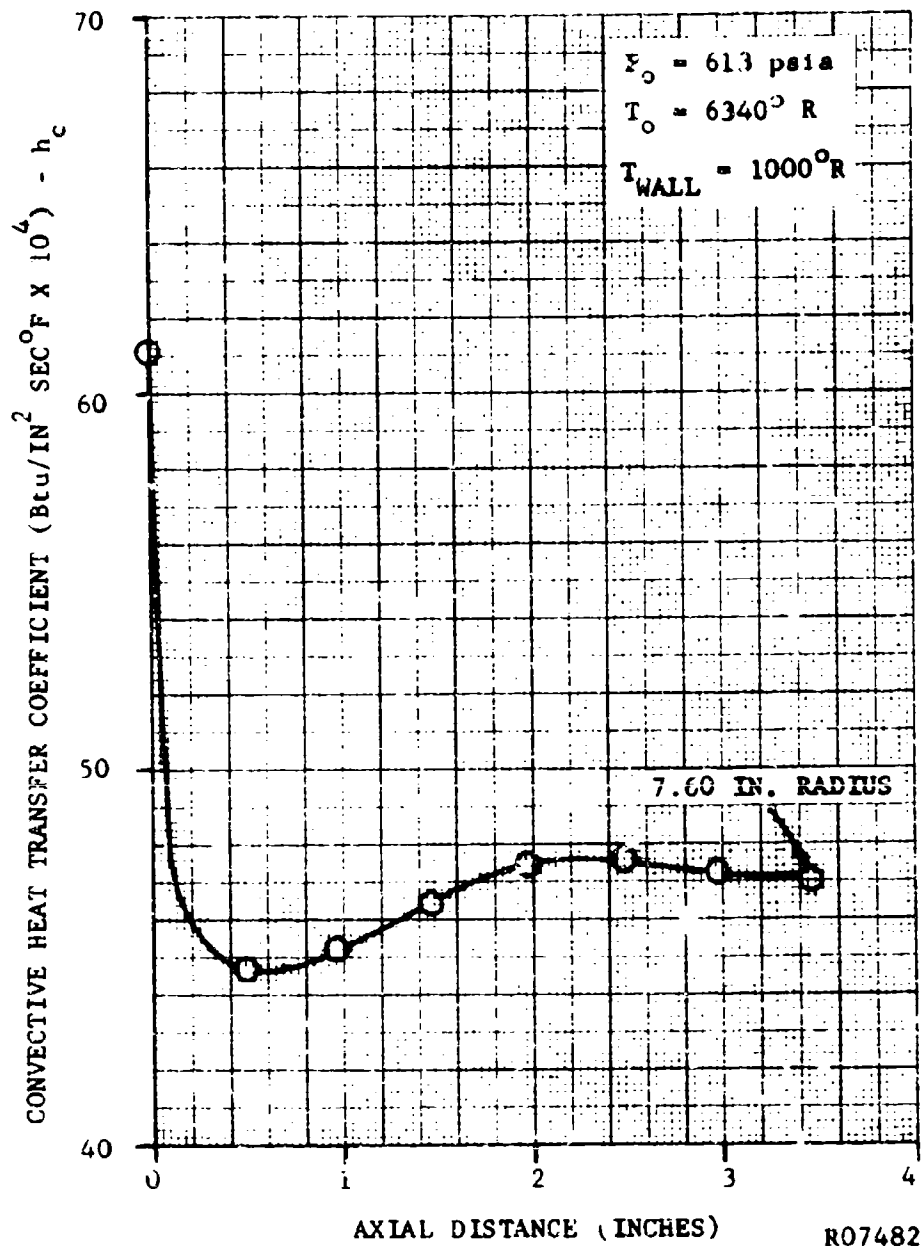


FIGURE 7-7. PREDICTED CONVECTIVE HEAT TRANSFER COEFFICIENT VERSUS AXIAL DISTANCE FOR GIMBALLED NOZZLE INLET AT 0% BURN TIME



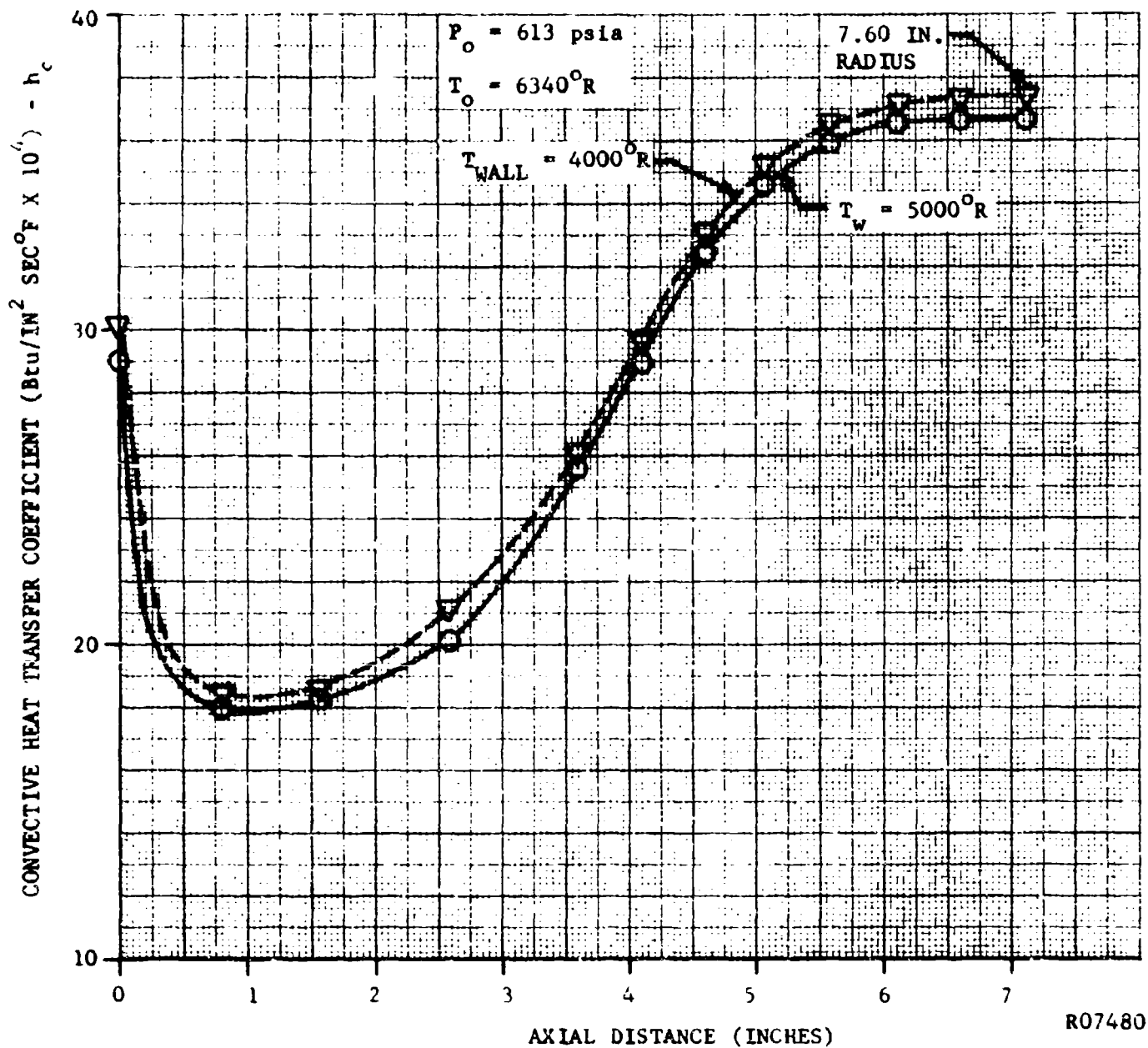


FIGURE 7-8. PREDICTED CONVECTIVE HEAT TRANSFER COEFFICIENT VERSUS AXIAL DISTANCE FOR GIMBALED NOZZLE INLET AT 23% BURN TIME

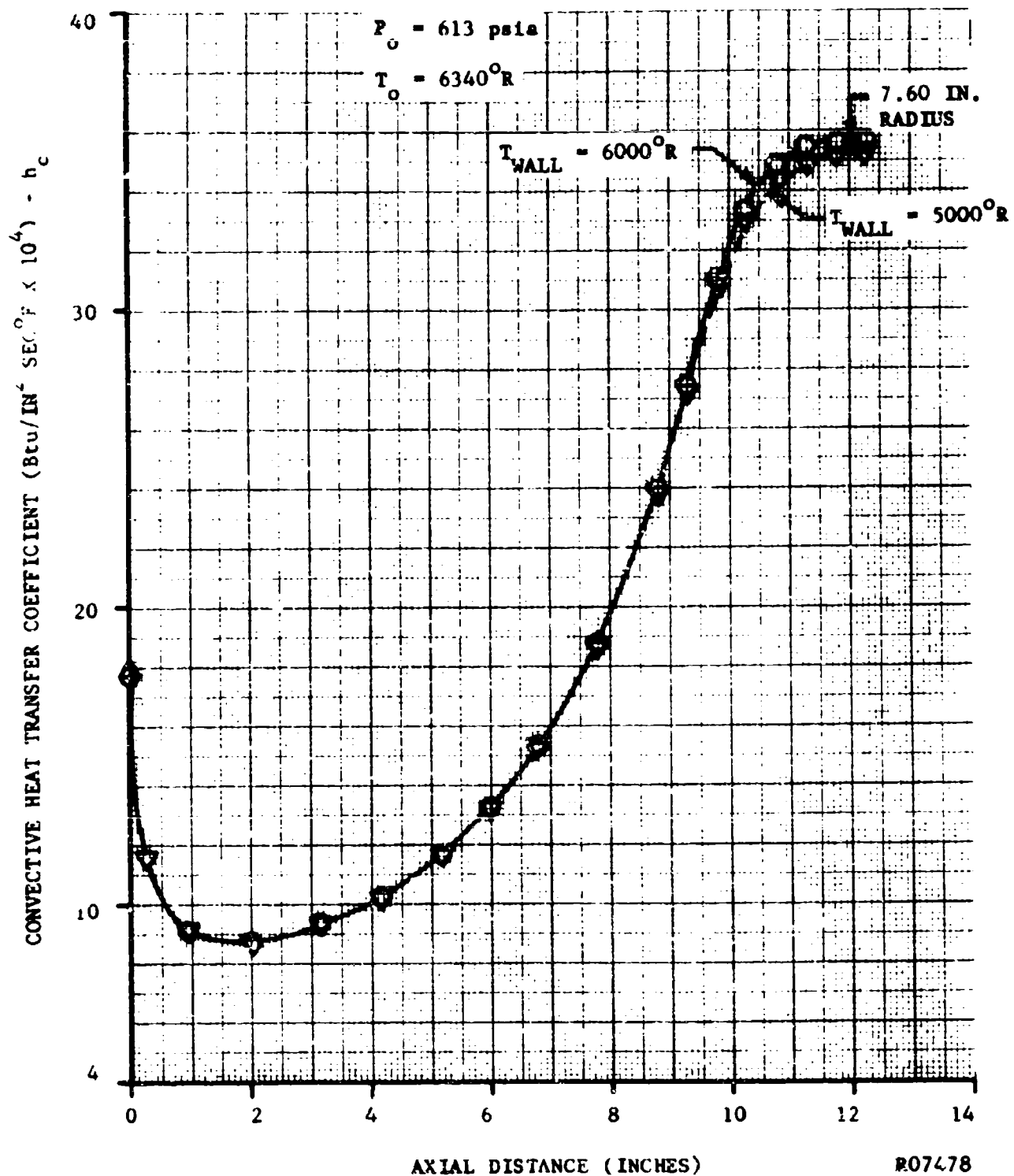


FIGURE 7-9. PREDICTED CONVECTIVE HEAT TRANSFER COEFFICIENT VERSUS AXIAL DISTANCE FOR GIMBALED NOZZLE INLET AT 58% BURN TIME

TABLE 7.3

## GIMBAL NOZZLE INLET GEOMETRY

<u>0% Grain</u>		<u>23% Grain</u>		<u>58% Grain</u>	
Axial Position <u>Z, Inches</u>	Radius <u>Inches</u>	Axial Position <u>Z, Inches</u>	Radius <u>Inches</u>	Axial Position <u>Z, Inches</u>	Radius <u>Inches</u>
0.0	9.78	0.0	14.95	0.0	22.4
0.5	9.05	0.8	13.80	0.95 — (1) —	21.05
1.0	8.45	1.6 — (2) —	12.65	2.05	19.45
1.5	8.10	2.6	11.25	3.2	17.85
2.0	7.86	3.6	9.78	4.2	16.45
2.5	7.73	4.1	9.05	5.2	14.95
3.0	7.66	4.6	8.45	6.0	13.80
3.5 — (3) —	7.60	5.1	8.10	6.8 — (2) —	12.65
4.6 -Throat-	7.50	5.6	7.86	7.8	11.25
		6.1	7.73	8.8	9.78
		6.6	7.66	9.3	9.05
		7.1 — (3) —	7.60	9.8	7.45
		8.2 -Throat-	7.50	10.3	8.10
				10.8	7.86
				11.3	7.73
				11.8	7.66
				12.3 — (3) —	7.60
				13.4 -Throat-	7.50

NOTE: — ( ) — Indicates location of pressure tap number shown in circle.

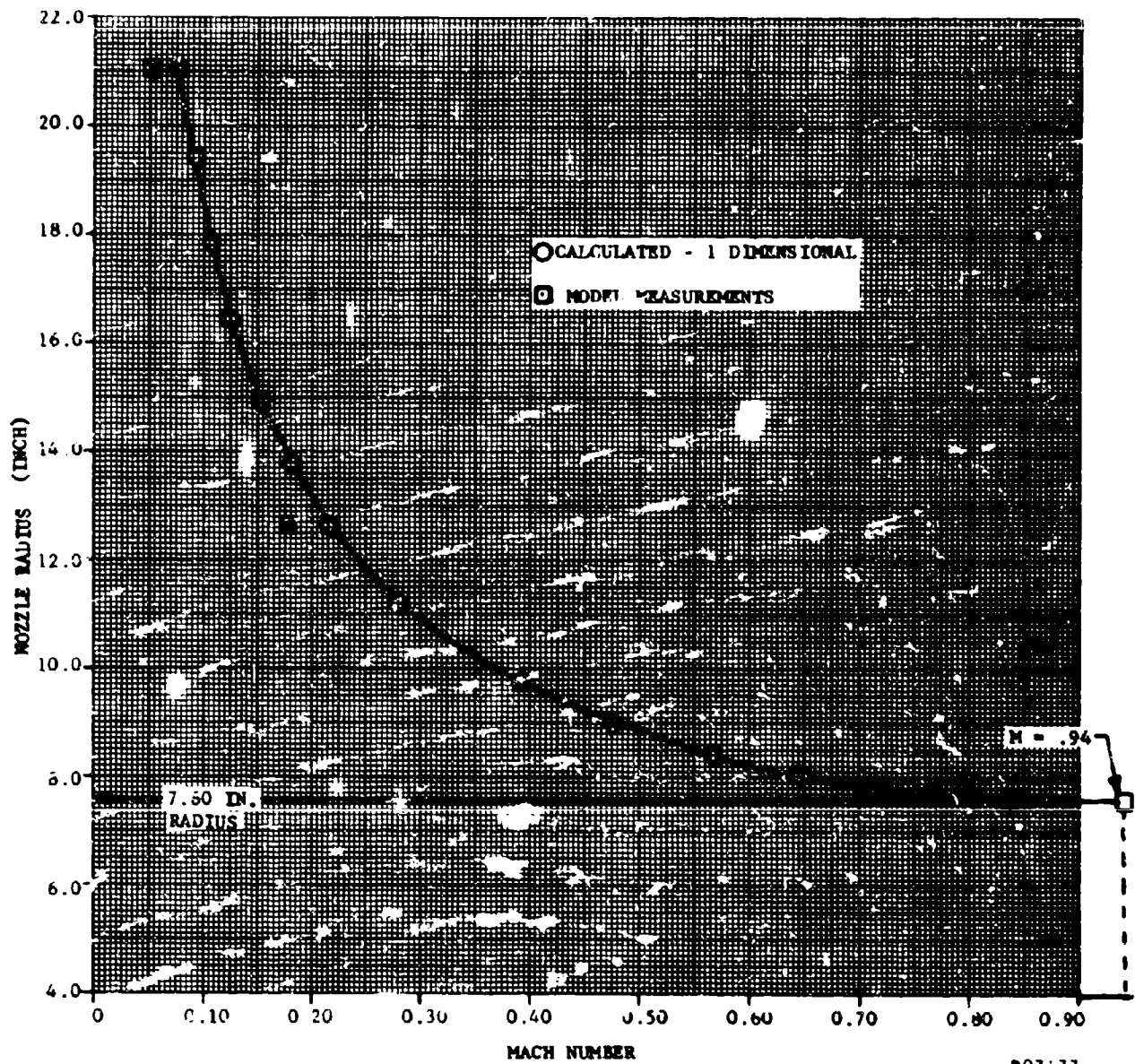


FIGURE 7-10. COMPARISON OF MACH NUMBERS FOR ONE DIMENSIONAL AND MODEL FLOW FOR GIMBALED NOZZLE INLET AT 55% BURN TIME

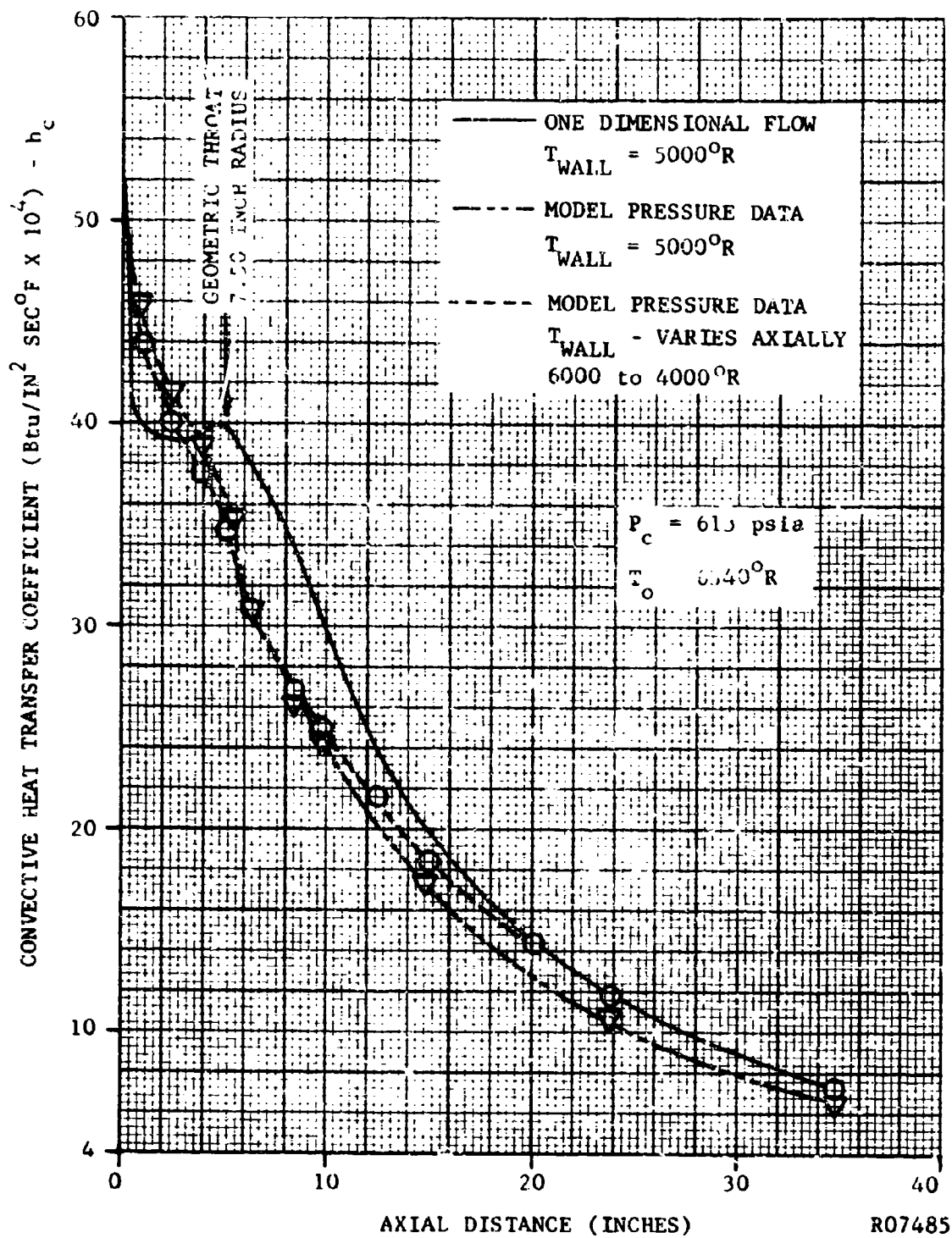


FIGURE 7-11. PREDICTED CONVECTIVE HEAT TRANSFER COEFFICIENT VERSUS AXIAL DISTANCE FOR GIMBALED NOZZLE THROAT - EXIT STRAIGHT CONFIGURATION

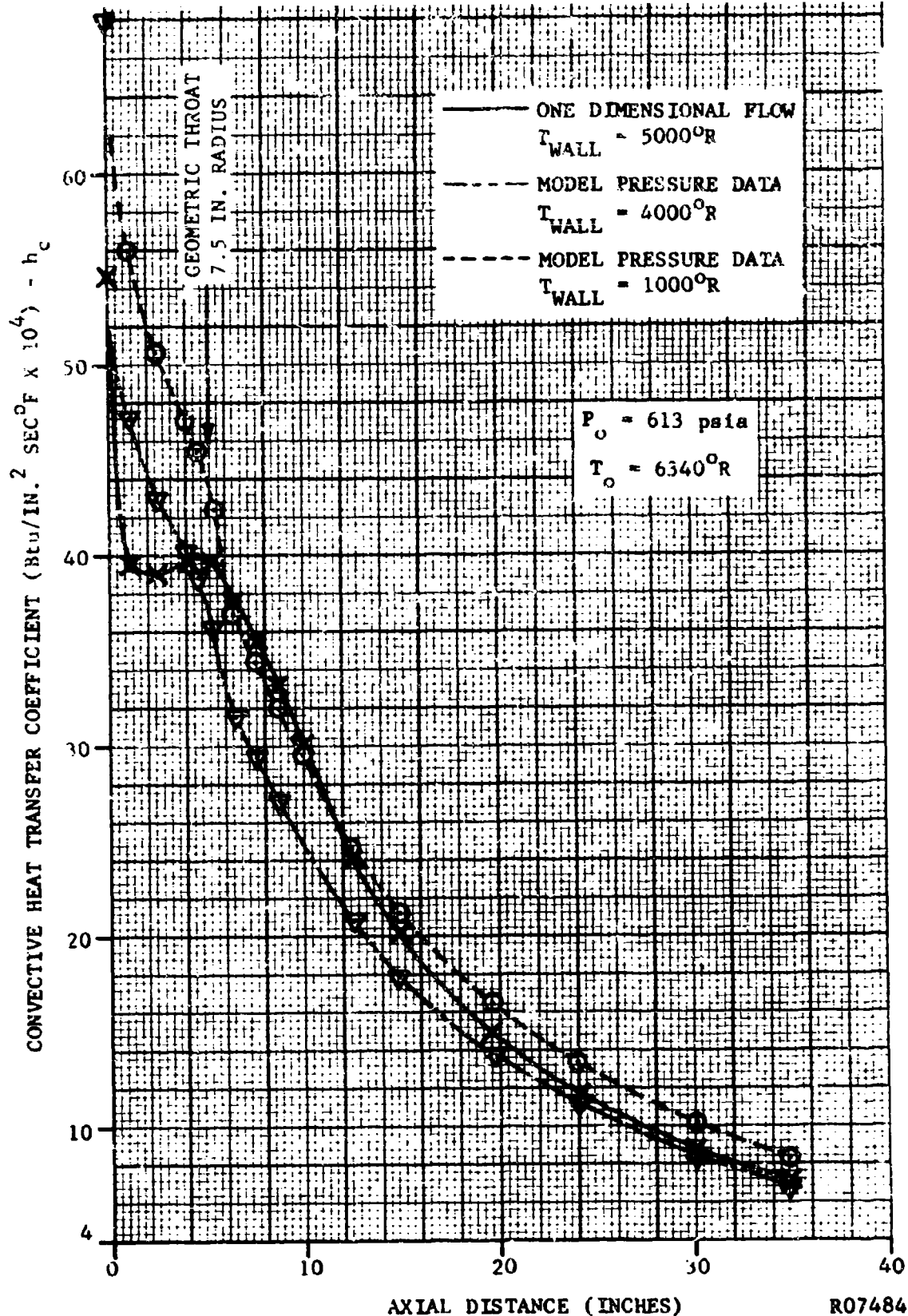


FIGURE 7-12. PREDICTED CONVECTIVE HEAT TRANSFER COEFFICIENTS VERSUS AXIAL DISTANCE FOR GIMBALED NOZZLE THROAT - EXIT STRAIGHT CONFIGURATION

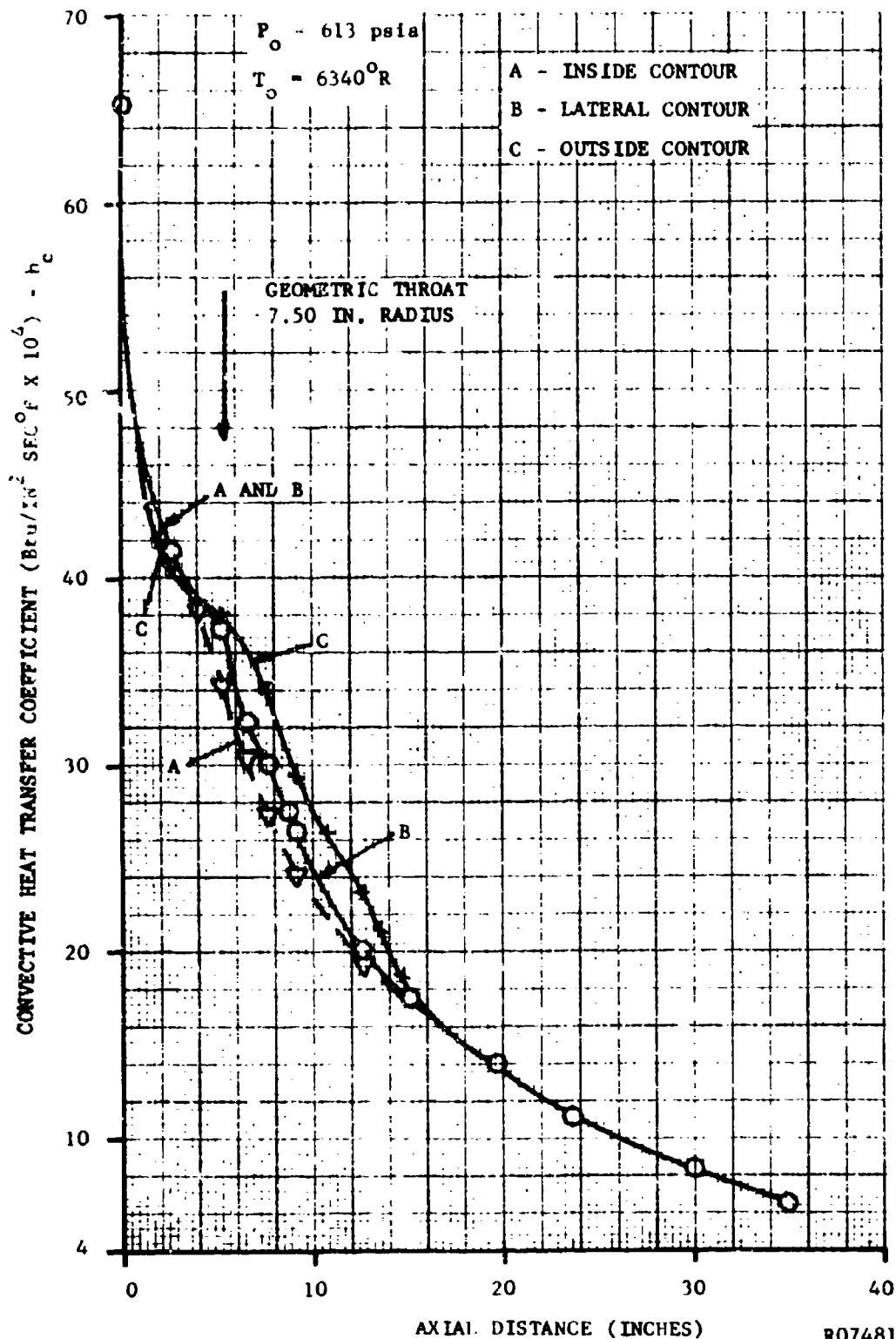



FIGURE 7-13. PREDICTED CONVECTIVE HEAT TRANSFER COEFFICIENTS VERSUS AXIAL DISTANCE FOR GIMBALLED NOZZLE THROAT - EXIT CANTED ( $5^\circ$ ) CONFIGURATION

TABLE 7.4

GIMBALED NOZZLE THROAT-EXIT GEOMETRY  
AND MACH NUMBER DISTRIBUTION

Straight Position				Canted - Inside Contour				Canted - Lateral Contour				Canted - Outside Contour			
Axial Position Z, Inches	Radius Inches	Mach No.		Axial Position Z, Inches	Radius Inches	Mach No.		Axial Position Z, Inches	Radius Inches	Mach No.		Axial Position Z, Inches	Radius Inches	Mach No.	
0.0	8.90	0.80	4	0.0	8.90	0.90	4	0.0	8.90	0.80	4	0.0	8.90	0.80	4
1.12	8.48	0.85		1.12	8.48	0.89		1.12	8.48	0.85		1.12	8.48	0.81	
1.83	8.22	0.90		1.83	8.22	0.95		1.83	8.22	0.89		1.83	8.22	0.83	
2.53	8.00	0.95		2.53	8.00	1.02		2.53	8.00	0.94		2.53	8.00	0.85	
3.23	7.80	1.01		3.23	7.80	1.11		3.23	7.80	1.00		3.23	7.80	0.88	
3.95	7.65	1.10		3.95	7.65	1.19		3.95	7.65	1.05		3.95	7.65	0.91	
4.20	7.60	1.13	5	4.63	7.56	1.26		4.63	7.56	1.11	5	4.63	7.56	0.95	
4.63	7.56	1.16		5.40	7.50	1.35		5.33	7.505	1.16		5.33	7.505	0.98	
5.40	7.50	1.30		5.60	7.51	1.38		5.40	7.50	1.25		5.40	7.50	1.05	
6.50	7.60	1.50		6.50	7.60	1.51		6.50	7.50	1.43		6.50	7.60	1.20	
7.60	7.71	1.56		7.60	7.71	1.60		7.60	7.71	1.50		7.60	7.71	1.30	
8.70	7.93	1.64		8.70	7.93	1.66		8.70	7.93	1.60		8.70	7.93	1.48	
9.15	8.00	1.66	6	9.15	8.00	1.73		9.15	8.00	1.63	6	9.15	8.00	1.51	
9.95	8.22	1.71		9.95	8.22	1.77		9.95	8.22	1.69		9.95	8.22	1.62	
12.65	9.07	1.87		12.65	9.07	1.91		12.65	9.07	1.87		12.65	9.07	1.74	
14.75	9.80	1.99	7	14.75	9.70	1.99		15.00	9.80	1.99	7	15.00	9.80	1.99	
19.67	11.20	2.18		19.67	11.20	2.15		19.67	11.20	2.14		19.67	11.20	2.14	
24.00	12.52	2.33	8	23.63	12.45	2.28		23.63	12.45	2.28	8	23.73	12.48	2.28	
30.07	14.38	2.51		30.07	14.38	2.48		30.07	14.38	2.48		30.07	14.38	2.48	
35.00	15.87	2.64	9	35.00	15.87	2.64		35.00	15.87	2.64	9	35.00	15.87	2.64	

NOTE:  Indicates location of pressure tap number shown in circle.



throat for diameter Reynolds numbers ranging from about 340,000 to 740,000. The Reynolds throat number for Run IA was approximately 520,000, and is well within the transitional range. This suggests that the throat heat transfer coefficient could be about 0.0013, compared to the measured value of 0.0018 Btu/in<sup>2</sup>·sec F. This difference is not unreasonable, considering the potential influences of heat transfer, combustion phenomena and nozzle inlet geometry on boundary layer transition. However, it may also be observed that the best turbulent boundary layer correlation shown in Figure 1 of reference 7.7 is in very close agreement with the experimental value for Run IA. Consequently, the possibility that the boundary layer in the throat is not fully turbulent is neither positively accepted or rejected. There are, of course, other experimental variables, such as the distribution of the injected water which could account for the low heat fluxes observed.

For all the other nozzles examined in this study, the throat Reynolds numbers are outside the range for transitional flow suggested in reference 7.7. Further, the comparison of theory with experiment for liquid engine firings shown in reference 7.4 indicates that the Elliott, Bartz, Silver method may tend to predict low rather than high heat transfer coefficients for the nozzles considered here. Again, it is emphasized that there is much to be learned about the fundamental nature of the convective heat transfer processes in rocket nozzles.

The predicted heat transfer rates for the 100FW-2 nozzle inlet show several important trends which, although they are not unexpected, should be emphasized. First, the relative insensitivity of the heat transfer rate to the choice of surface temperature is evident at each of the firing times (Figures 7-2 to 7-6). The results also graphically display the competition of the development length and acceleration effects on the heat transfer. In the first few inches (small Z), the boundary layer thickens, and the convective coefficient decreases, roughly as the distance to the one-fifth power, as suggested by flat plate theory. In the region where the main stream flow is accelerating, the coefficients rise again, and would ultimately reach a maximum at the nozzle throat. It is evident that the heat transfer coefficients at any point along the inlet surface will be dependent on the distance over which the boundary layer has developed before reaching the point in question. That is, the local convective heat transfer coefficient will exhibit a significant inverse dependence on the time after ignition. The calculated heat transfer coefficients were subsequently used, along with the radiation and condensed phase heat flux contributions, to estimate the effective  $Q^*$  for the aft-closure liner.

The heat transfer results for the gimbaled nozzle inlet appear to be quite insensitive to wall temperature at high surface temperatures. Figure 7-7 indicates that the combination of low wall temperature and short boundary layer development length can lead to relatively higher coefficients during the initial phase of combustion. Since this is the time when the ablative mass addition occurs at the greatest rate, the net heat transfer rates could exhibit the opposite tendency in the actual motor. Because the calculated coefficients are rather high, the wall erosion rate is likely to be higher than might otherwise be expected.

The results for the throat-exit region of the gimalled nozzle are rather interesting. Again, a major dependence of the results on the choice of the surface temperature is not observed. The results obtained under the assumption of one-dimensional flow reflect the effect of the initial boundary layer development, which would not appear if the "pipe flow" or "simplified Bartz" type analyses had been used to calculate the convective coefficients. The use of the Mach number distribution, as determined from the modeling pressure data, has the interesting effect of completely eliminating the peak in the convective coefficient at the nozzle throat. This suggests that the nozzle surface just upstream of the geometric throat will be subjected to an unusually severe environmental interaction leading to high erosion rates. Figure 7-13 suggests that the effect of nozzle canting is to introduce about a 20 percent variation in the convective coefficient around the nozzle circumference. It is also noted that the effects are confined to the vicinity of the throat with the greatest deviations from the uncanted results occurring downstream of the throat.

## 7.5 REFERENCES

- 7.1 Armour, W. H., et al, Applied Research for Advanced Cooled Nozzles, Aeronutronic Publication No. C2382, Contract AF 04(611)-8387, RTD-TDR-63-1122, January 1964 (Confidential).
- 7.2 Armour, W. H., et al, A Review of Nozzle Concepts for Future Solid Propellant Rocket Motors, Philco Research Laboratories Report No. U-2551, RPL-TDR-64-8, March 1964.
- 7.3 Rosner, D. E., Convective Heat Transfer with Chemical Reaction, ARL 99, Part 1, August 1961
- 7.4 Elliott, D. B., Bartz, D. R. and Silver, S. Calculation of Turbulent Boundary-Layer Growth and Heat Transfer in Axisymmetric Nozzles, California Institute of Technology, J.P.L. TR. No. 32-387, February 1963.
- 7.5 100FW2 Motor Firing Report, Large Solid Rocket Program, No. 0434-01514-T6, Aerojet General Corp., April 1962.
- 7.6 Svehla, R. A., Estimated Viscosities and Thermal Conductivities of Gases at High Temperatures, NASA TR. R-132, 1962.
- 7.7 Brinsmade, A. F., et al, Heat Transfer in Nozzle Systems (U), Quarterly Technical Summary Report, July 1963, Allegany Ballistic Laboratory, ABL/ARPA/QTSR-3 (Confidential)

## SECTION 8

### PREDICTION OF EROSION RATES FOR 100 FW2 AFT CLOSURE

At the completion of Contract AF 04(611)-7047, 30 October 1962, 8.1 a preliminary attempt was made to predict insulation erosion rates for the 100 FW2 aft closure using calculated convective and radiative heat transfer rates and estimated rates of particle impingement. In view of the results of cold flow modeling studies completed under the present contract, a refinement of this prediction was investigated, taking into account revised estimates of convective and radiative heat transfer as well.

#### 8.1 SUMMATION OF HEAT FLUXES

The total heat transfer to the aft closure surface was considered to consist of three components:

(1) Convective:

$$q_c = h_c (T_o - T_w) \quad (8.1)$$

(2) Radiative:

$$q_r = \epsilon \sigma (T_p^4 - T_w^4) \quad (8.2)$$

(3) Impingement:

$$q_p = \dot{m}_p C (T_p - T_w) \quad (8.3)$$

where

$q_c$  = convective heat flux per unit area

$h_c$  = convective heat transfer coefficient

- $T_o$  = stagnation temperature  
 $T_w$  = wall temperature  
 $q_r$  = radiative heat flux per unit area  
 $\epsilon$  = effective emissivity  
 $\sigma$  = Stefan-Boltzmann constant  
 $T_p$  = particle temperature  
 $q_p$  = impingement heat flux per unit area  
 $\alpha$  = particle energy accommodation factor  
 $\dot{m}_p$  = mass rate of particle flux per unit area  
 $C$  = average particle heat capacity

All calculations of instantaneous heat fluxes were converted, for purposes of predicting erosion rates, to time-average heat fluxes by the three mechanisms at any given station along the aft closure. The average flux at a given station was defined as

$$(q)_{avg} = \frac{1}{t_e - t_s} \int_{t_s}^{t_e} q \, dt \quad (8.4)$$

where

- $(q)_{avg}$  = time-average heat flux  
 $t_e$  = total burn time  
 $t_s$  = time at which a given station is exposed by burning back of the propellant grain  
 $q$  = instantaneous heat flux (either  $q_c$ ,  $q_r$ , or  $q_p$ )  
 $t$  = time

The average convective heat fluxes were derived by computer integration of instantaneous heat fluxes, based on profiles of convective heat transfer coefficient, " $h_c$ ," calculated for several different times during the firing. The average radiative heat flux was the same at all points and was calculated directly from Equation (8.2). Inasmuch as integrated values of

$$\dot{m}_p = \int_{t_s}^{t_e} \dot{m}_p \, dt$$

were available directly from the results of the cold flow modeling studies, only hand calculations likewise were required to determine time-average values of " $q_p$ ."

The following assumptions were made in all calculations:

- (1)  $T_o \approx T_p \approx 6340^\circ R$
- (2)  $\epsilon \approx 1.0$
- (3)  $\alpha \approx 1.0$

Calculations were performed for two possible values of wall temperature:

- (1)  $T_w = 1500^\circ R$
- (2)  $T_w = 4000^\circ R$

The time-average heat fluxes computed for the three mechanisms and the two wall temperatures are shown in Figure 8-1 as functions of the tangential distance along the aft closure, where "zero" is defined as the point where the aft closure meets the 100-inch diameter case, and where the throat then is located at distance 53.4 inches. It is seen that convective and radiative heat fluxes are of the same order of magnitude, whereas impingement heat flux calculated from the new modeling data, generally is so low as to be virtually insignificant.

The time-average heat fluxes shown in Figure 8-1 can be converted into time-average erosion rates as follows:

$$\Delta \approx \left( \frac{1}{\rho_i - \rho_c} \right) \frac{q_{total}}{Q^*} \quad (8.5)$$

where

- $\Delta$  = time-average erosion rate
- $\rho_i$  = density of virgin insulation
- $\rho_c$  = density of porous char
- $Q^*$  = "effective heat of ablation" of insulation

and where

$$q_{total} = q_c + q_r + q_p \quad (8.6)$$

(Time-average values are assumed)

This calculation presupposes that the insulation ablates to a weak char which is then mechanically removed, so that only the density difference between the virgin material and the char is counted as undergoing the ablation process. Densities typical of the 100 FW2 insulation were taken to be:

$$\begin{aligned} \rho_i &\approx 80.5 \text{ lb/ft}^3 \\ \rho_c &\approx 24.2 \text{ lb/ft}^3 \end{aligned}$$

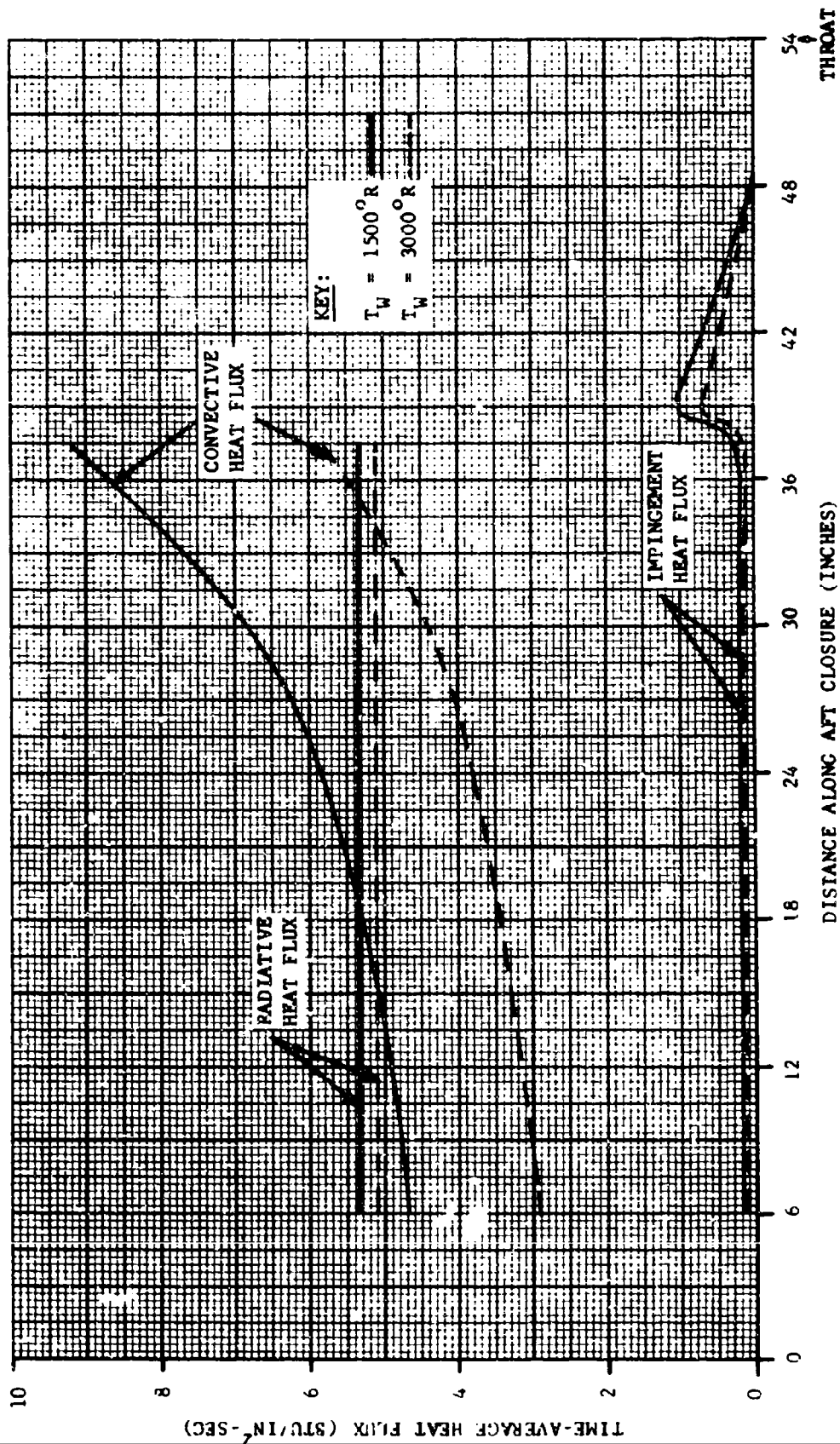


FIGURE 8-1. CALCULATED AVERAGE HEAT FLUXES FOR 100-FW-2 AFT CLOSURE

R07244

## 8.2 ESTABLISHING $Q^*$ FOR THE WALL MATERIAL

The primary assumption involved in the conversion of heat flux rates into erosion rates is the choice of a value for the "effective heat of ablation,"  $Q^*$ . This quantity, which should not be expected to be the same as any "heat of ablation" measured in the laboratory under static conditions, must include the otherwise-unaccounted-for effects of blowing, mechanical shearing, and the like.

Originally, attempts were made to predict erosion rates matching those actually measured, with " $Q^*$ " assigned a single, constant value throughout. These attempts proved unsuccessful; hence, a  $Q^*$  relationship dependent on heat flux was investigated. Inasmuch as both the radiative and the impingement heat fluxes were essentially constant throughout the region of interest (true, time-average erosion rates actually are measurable only between distance points 14.4 inches and 37.4 inches in Figure 8-1),  $Q^*$  was assumed to be an arbitrary power function of average " $q_c$ ," the convective heat flux. The wall temperature was taken to be 1500°R, since this case would maximize the relative importance of the convective contribution. The empirical relationship for  $Q^*$  best fitting the measured time-average erosion rates then was:

$$Q^* \approx (3.22 \times 10^6) (q_c)^{-2.503} \quad (8.7)$$

where

$Q^*$  = effective heat of ablation, Btu/lb

$q_c$  = convective heat flux, Btu/in.<sup>2</sup> - sec

Total time-average erosion rates predicted by Equations (8.5), (8.6), and (8.7) are compared in Figure 8-2 to the measured average rates calculated as

$$\dot{\Delta}_{\text{exptl.}} = \frac{\Delta_{\text{exptl.}}}{t_e - t_s} \quad (8.8)$$

where

$\dot{\Delta}_{\text{exptl.}}$  = time-average erosion rate

$\Delta_{\text{exptl.}}$  = erosion depth measured at a given station along the aft closure

### 8.3 INTERPRETATION OF THE ANALYSIS

The "predicted" curve based upon the empirical  $Q^*$  relationship is seen to fit the experimental curve very well, except possibly in the distance region 30 inches to 36 inches. Actual  $Q^*$  values required to fit the measured data ranged from 56,000 Btu/lb at position 14.4 inches down to 12,500 Btu/lb at position 37.4 inches. The latter value is in the range of previous estimates<sup>8.1</sup> of effective heat of ablation under rocket firing conditions, while the former value definitely appears too high. Perhaps the measured erosion rates  $\Delta_{\text{exptl}}$  are subject to large errors in the region of the 14.4-inch point owing to small values of both  $\Delta_{\text{exptl}}$  and  $(t_e - t_s)$  in this region.

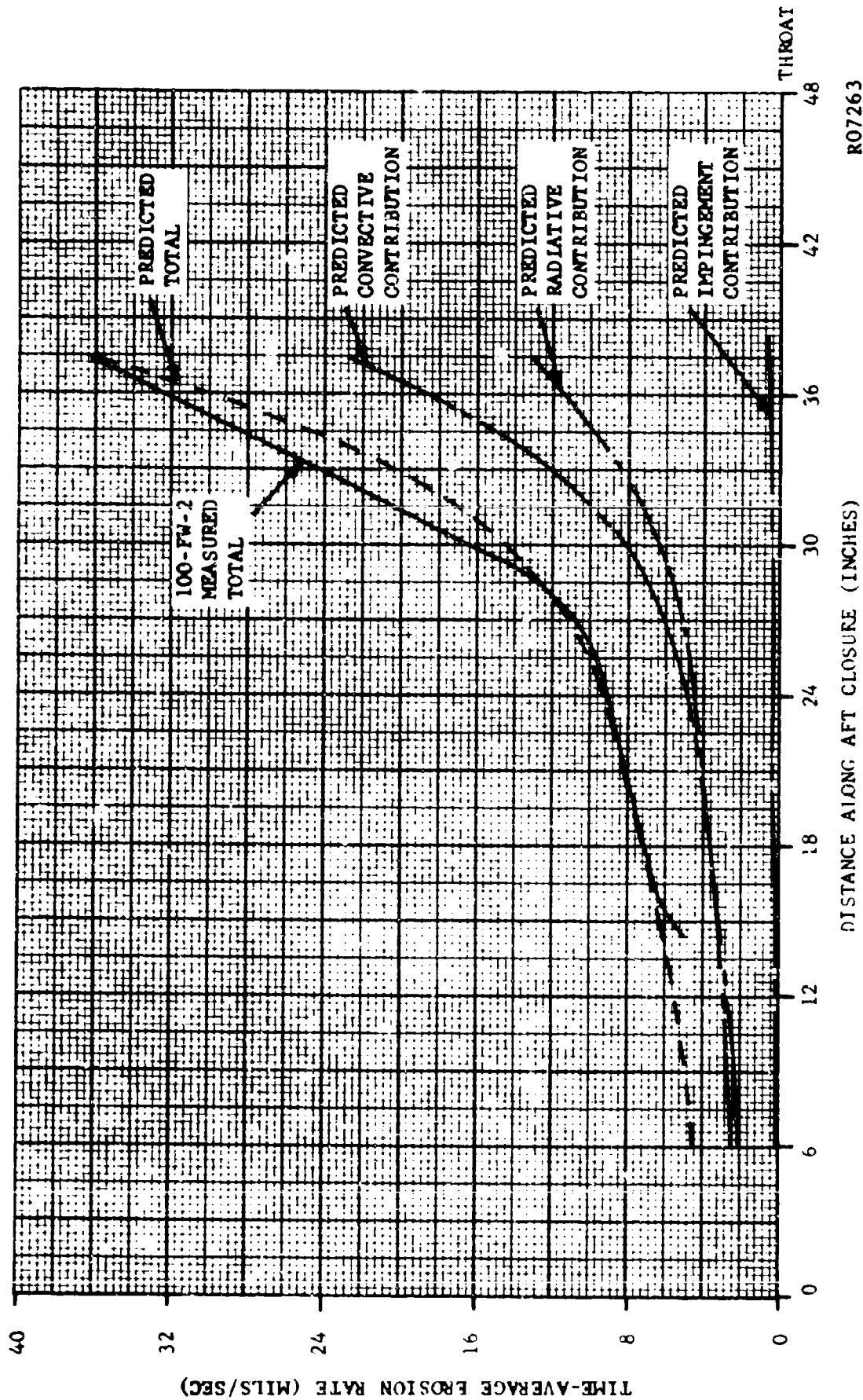
Upon examination of the individual contributions to total predicted erosion rate, (each is plotted against distance in Figure 8-2), the contribution of impingement heat flux, " $q_p$ ", again is seen to be negligible. The question naturally arises whether a more reasonable fit of measured erosion rates might be obtained by assigning a value much greater than unity to the "particle energy accommodation factor,"  $\alpha$ , or, in other words, by taking mechanical erosion to be an important result of particle impingement. It can be seen, however, that the shape of the experimental curve would not be matched even by taking " $\alpha$ " to be as high as 10; for example, because the peak in particle flux (Figure 8-1) occurs downstream of the last point (37.4 inches) at which a measured erosion rate value could be determined. (Beyond this point, the insulation had burned back to the graphite backing during the course of the firing).

In Figure 8-3, measured and predicted erosion rates for the 100 FW2 aft closure are plotted versus local Mach number for comparison with similar data reported by Aerojet-General Corporation<sup>8.2</sup> for the 100 FW2 aft closure. Correlation versus Mach number in the region of interest appears only to change the relative shapes of the curves, and does not suggest any new or better empirical approach to the prediction of erosion rates.

### 8.4 FUTURE WORK

In conclusion, a quite sophisticated and detailed analytical procedure for studying nozzle environment effects in a given nozzle has been demonstrated. However, a real test of the validity and utility of the method has not been completed. A larger number of designs, varying in scale and geometry, should be similarly analyzed to develop more correspondence between the real and predicted environmental effects. This would lend itself to (1) a better evaluation of the particle impingement validity, (2) increased reliability in the predictions made by such an analysis, and (3) increased ability to indicate a consistent method of applying the analysis to various designs.





R07263

FIGURE 8-2. COMPARISON OF MEASURED EROSION RATE VERSUS EROSION RATE PREDICTED FROM EMPIRICAL  $Q^*$  VERSUS  $Q_c$  RELATIONSHIP ( $T_w = 1500^\circ R$ )

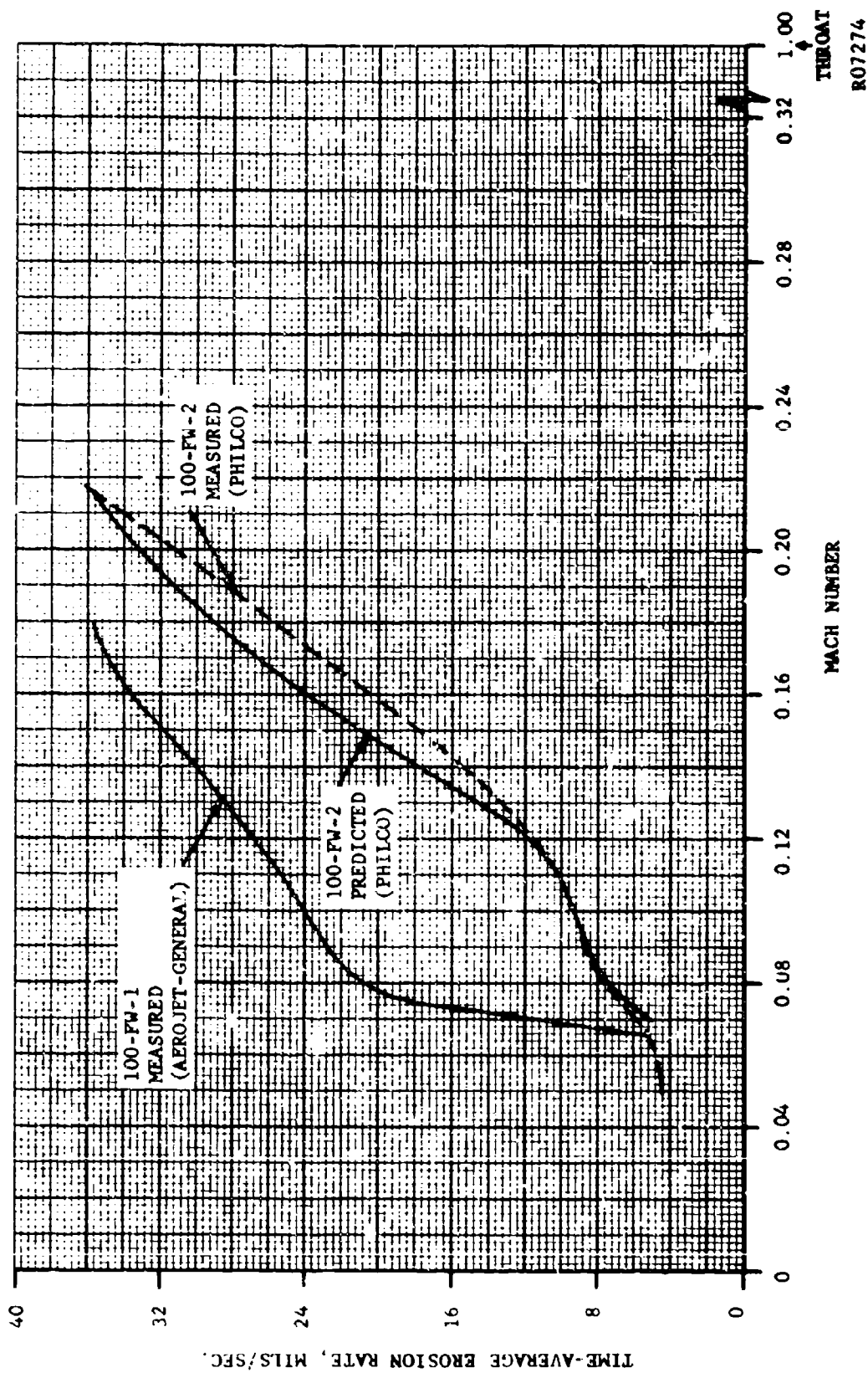


FIGURE 8-3. COMPARISON OF EROSION RATES CORRELATED AGAINST LOCAL MACH NUMBER

## 8.5 REFERENCES

- 8.1 "Detail Design Optimization of Solid Propellant Rocket Motor Aft-Closure Nozzle Combinations (U)," Contract AF 04(611)-7047, 30 October 1962.
- 8.2 100FW2 Motor Firing Report, Large Solid Rocket Program, No. 0434-01514-T6, Aerojet General Corp., April 1962.

## SECTION 9

### SUMMARY AND RECOMMENDATIONS

There are certain limitations and uncertainties associated with some aspects of the work. These need to be outlined clearly. A straightforward evaluation of the work is needed for intelligent planning of future work. Therefore, a concise evaluation is presented in the form of this summary with recommendations.

A very useful particle sampler has been developed. Small enough samples can be taken to avoid agglomeration, and to display all the particles in proper number distribution on one slide. The sample is not subject to fractionation by air currents or variable particle sedimentation rates such as might occur in simple exposed slide sampling. This tool can be applied to motors of various sizes and propellant formulations, and to sampling various portions of the nozzle effluent cross section. This would furnish much needed data for nozzle performance analysis where particle size is a factor.

Further tests with the sampler would be worthwhile. Very large particles might tend to bounce from the glass slide upon impact. While this does not appear to be the case for the tests conducted, this factor should not be overlooked. If this is the case, multistage sampling could be used to allow lower collection velocities for the large particles.

The cold flow particle impingement modeling technique has a highly sophisticated analytical basis. The results are consistent and reproducible. More varied designs than those modeled in this program should be studied to demonstrate the effectiveness of the technique. Cases having more severe particle impingement would be interesting. Since the cold flow modeling conditions typically do not model the boundary layer thickness studies in which the boundary layer is varied should be conducted. This same technique of analysis and facility design would make a very interesting study using dyed droplets impinging on blotter surfaces. The technique can be applied to a study of particle impingement through shock waves and to the detection of flow separation regions in supersonic flow. Correct particle size distribution data for a given motor is necessary for accuracy in cold flow modeling studies.

A cold flow modeling technique has been developed and demonstrated for determining nozzle wall pressure contours. By using this data in convective heat transfer analysis, the nozzle material heat load severity is indicated. The severe heat flux problems of one particular design have been revealed.

Emissivity values for alumina have been established up to a temperature of 5200°F. The data are applied to the calculation of radiative heat flux values to the nozzle wall for various motor sizes, pressures, and alumina loadings. However, the calculation is only approximate, since many assumptions were required to handle the complexities in geometry, particle flow field, and thermal gradients through the field of view in the nozzle. The values calculated probably represent a lower limit of radiation, since unburned carbon and propellant additives are seen to add significantly to the radiation.

While this work was conducted mainly with a hydrogen-oxygen-alumina flame, similar studies are needed on actual propellant or simulated propellant firings. More work is needed on chamber window viewing technique. Studies must be made, as in this work, on flames with known particle size distributions, if scaling laws are to be inferred. Particle size distribution in the large motors must be known if the scaling laws are to be applied to them.

Application of the work of this program to the detailed analysis of heat fluxes to two large nozzle designs has been demonstrated. This allows conclusions to be drawn on the relative importance of the various heat flux modes, and on the implications of various geometries for the severity of nozzle attack. However, the study of more cases, and the input of the nozzle wall reaction products, is needed to demonstrate more convincingly the utility of the method in evaluating proposed designs.

A technique has been demonstrated for directly measuring particle impingement heat fluxes. The experiment involved a specialized case where a relatively cool inert wall was used. The next step is to study particle impingement effects in a similar manner, but with a hotter nozzle wall and one which reacts to the environment by ablating or eroding.

## APPENDIX A

### STUDIES OF TOTAL EMISSION FROM A $H_2-O_2-Al_2O_3$ PLUME USING A 1-INCH ROCKET MOTOR

#### A.1 INTRODUCTION

The presence of aluminum oxide particles in the exhaust products of rocket motors warrants detailed study in order (1) to permit a better understanding of thrust losses due to lack of equilibrium between particles and gas, (2) to gain information on effect of particle addition on radiant heat transfer to rocket nozzles, and (3) to understand the radiation emitted by the plume from the standpoint of plume detection.

The radiant properties of a cloud of particles whose sizes are comparable to the wavelength of light can in principle be determined by (1) determining from Mie theory the particle emission, absorption, and scattering cross sections as a function of particle size, wavelength of light, and particle material electrical properties, which presumably are temperature dependent; (2) solving a radiative transfer problem using the above particle cross sections for the particular geometry involved. (If there exists interaction between the radiation and the gas dynamics then the radiative transfer problem must be solved simultaneously with the gas dynamics, but this additional complication is set aside.)

The calculation of the radiant properties of a rocket plume heavily laden with aluminum-oxide particles is hampered by the lack of knowledge of the wavelength and temperature dependence of the electrical properties of  $Al_2O_3$ . A major aim of experimental research in this area is the determination of particle emission (absorption) and scattering cross sections. The determination of this information as a function of wavelength, over all wavelengths, is a large order. A second aim of experimental work is to determine the integrated effects of the particle emission by determining the total radiation. This is of particular importance when the aim of the work is the prediction of the radiant heat transfer of a given rocket motor cloud. Total radiation (i.e., integrated with respect to wavelength) experiments generally do not give enough information to permit an understanding of detailed processes of the radiant emission.

The following discussion describes a method of experimentally determining the particle emission and scattering cross sections and describes the results of attempting such experiments.

## A.2 EXPERIMENTAL MEASUREMENT OF OPTICAL PROPERTIES OF A CLOUD OF SCATTERING-EMITTING PARTICLES

The complete radiative transfer problem for a given cloud of particles of arbitrary refractive index generally will be awkward to solve. Furthermore, it is undesirable to base the reduction of experimental data on a solution to a radiative transfer problem that is, itself, unverified by independent experiment. For these reasons, it is desirable to design the experiments in such a way that the results can be interpreted by recourse to the solution of only a trivial radiative transfer problem. By performing tests at small optical depths for scattering it is possible to obtain results that can be directly interpreted. In the equations given below, the presence of scattering by particles (i.e., a change of direction of propagation of incident light) will be accounted for, insofar as it results in an attenuation of the directly emitted light from a given point in space. However, the additional component of radiation that results by scattering at the point of radiation originating at other locations is not included, and the results can be expected to hold only when multiple scattering is not large. For this reason it is desirable to perform tests at various optical depths in order to observe the dependence of the results on particle concentration. If results are found to be concentration dependent, then only those obtained by extrapolating to zero concentration can be considered valid.

### Radiant Intensity Due to Gas and Particles at Unequal Temperatures

The radiation generated at a volume element of unit cross section and thickness,  $dx$ , is due to a gas of temperature,  $T_g$ , having a volumetric emission cross section,  $\gamma_g$  ( $\text{cm}^{-1}$ ), and a suspension of particles having a volumetric absorption (emission) cross section of  $\gamma_{pa}$  ( $\text{cm}^{-1}$ ) is

$$\left[ \gamma_g R(T_g, \lambda) + \gamma_{pa} R(T_p, \lambda) \right] dx \quad (\text{A-1})$$

where

$R(T, \lambda)$  = Spectral radiancy at wavelength  $\lambda$  due to a blackbody at temperature  $T$ .

This radiation will suffer attenuation due to the self absorption by the gas, absorption by the particles, and scattering by the particles. The total attenuation in traversing the distance  $x$  from the interior to the surface of the medium at  $x = 0$  is

$$\exp(-\gamma_t x) \quad (\text{A-2})$$

where

$$\gamma_t = \gamma_{ps} + \gamma_{pa} + \gamma_g \quad (A-3)$$

and

$$\gamma_{ps} = \text{scattering cross section of the particles per unit volume (cm}^{-1}\text{)}.$$

Integrating the product of expressions (A-1) and (A-2) over the length zero to L gives the following results for the steradiance of the gas-particle mixture:

$$R_p(\lambda) = \frac{\gamma_{pa}}{\gamma_t} (1 - e^{-\gamma_t L}) R(T_p, \lambda) + \frac{\gamma_g}{\gamma_t} (1 - e^{-\gamma_t L}) R(T_g, \lambda) \quad (A-4)$$

Equation (A-4) applies at a wavelength where the gas emits strongly, as in the case of the sodium D line emission when a sodium compound is added, or at other wavelengths where the gaseous species emit characteristic radiation.

At a spectral region where no gaseous emission occurs, Equation (A-4) reduces to

$$R_p(\lambda) = \frac{\gamma_{pa}}{\gamma_{pa} + \gamma_{ps}} R(T_p, \lambda) \left( 1 - e^{-(\gamma_{pa} + \gamma_{ps}) L} \right) \quad (A-5)$$

The question arises as to whether the particle temperature can be determined by observation of the radiation emitted by the particle cloud. If a transmission test is made to determine

$$e^{-(\gamma_{pa} + \gamma_{ps}) L}$$

and the spectral steradiance is measured, the product

$$\frac{\gamma_{pa}}{\gamma_{pa} + \gamma_{ps}} R(T_p, \lambda)$$

is determined. However, further information on the ratio of

$$\frac{\gamma_{pa}}{\gamma_{pa} + \gamma_{ps}}$$

is necessary in order to determine particle temperature, and this information is usually not available.



If carbon is present and is in thermal equilibrium with the gas, as would be expected due to the small sizes of carbon particles, then Equation (A-4) applies if  $\gamma_g$  is replaced by  $\gamma_g + \gamma_c$  where  $\gamma_c$  is the absorption cross section per unit volume due to carbon. (The scattering by carbon particles is generally small compared to absorption; see references A.1 and A.2.) When carbon is present, the determination of the radiation solely due to  $MgO$  or  $Al_2O_3$  particles is not possible without making tenuous assumptions. If the radiation due to particles other than carbon is of interest, then one should eliminate sources of radiation of comparable magnitude.

A direct method of learning the radiation properties of a particle cloud is to perform a total radiation test by means of a spectrally neutral radiation transducer such as a thermopile. In this type of experiment, the total radiation is measured and can be directly related to particle cloud emissivity if particle temperature is known. The application of this type of information to solve the large scale rocket motor heat transfer problem may or may not offer difficulty.

### A.3 EXPERIMENTS ON SMALL ROCKET ENGINE

#### A.3.1 EXPERIMENTAL PROCEDURE

Experiments were performed on a 100 lb-ft thrust engine using gaseous hydrogen and oxygen as propellants and an aqueous slurry of aluminum oxide particles. A description of the rocket motor which was designed with a heat sink copper combustion chamber and a nozzle of porous tungsten impregnated with silver, is given in Table A.1. The engine was found to operate at all desired O/F ratios without tendency toward unstable combustion.

TABLE A.1

Motor I.D.	1 i ch
Motor Length	10 inches
Throat Diameter	0.300 inch
Exit Diameter	0.7 inch
Exit Area Ratio	6.02
Contraction Ratio	11.1
$L^*$	11i inches

The propellant flow rate control and flow rate measurements were achieved by use of calibrated critical orifices. Pressures were measured upstream and downstream of the critical orifices by means of pressure transducers, and gas temperatures were measured by welding thermocouples to the outside of the propellant feed lines upstream of orifices and wrapping lines with insulation. This method of measuring gas temperature is not fully satisfactory, since the

tubing thermal response time is somewhat long, but conventional thermocouples protected in wells are probably almost as slow and were found to be a source of excessive leakage

The slurry consisted of a mixture of 60 percent by weight aluminum oxide, 40 percent by weight of water and was fed into the combustion chamber by means of a pneumatic piston. The aluminum oxide used in the slurry was a grinding compound (Norton Co. Type 1-C metallurgical alumina) consisting of 99.98 percent  $\gamma$ - $\text{Al}_2\text{O}_3$  of nominal 1 micron size. Particles were rounded but nonspherical and were far more uniform in size than most commercial grades of alumina powder. It is believed that the use of the metallurgical grade alumina provided a much greater control over injected particle size than would otherwise have been possible. The particles were received in five separate packages which were blended together by stirring overnight in a paddle-type mixer. Particles as received, and also after mixing, were highly agglomerated but could be de-agglomerated in small quantities by pressing between a microscope slide and cover glass if water or oil was used as an immersion medium. The unagglomerated particles display Brownian motion when suspended in water and observed in a high power (970X) optical microscope with an oil immersion objective. No attempt was made initially to de-agglomerate the particles prior to injection into the rocket as it was believed that combustion and shear due to turbulence in the combustion chamber might accomplish this. More detail on particle processing eventually used is given below. Additional instrumentation used on the tests were the usual spectral intensity measurements at  $\lambda = 0.59\mu$ , transmission tests in the same wavelength interval, and total radiation tests. Total radiation measurements were made by means of a commercial rapid response thermocouple with a KBr window that passes all radiation in the  $0.4\mu$  to  $25\mu$  interval. This device is spectrally neutral and receives more than 99.5 percent of all energy emitted by a blackbody at  $2500^\circ\text{K}$ , thus permitting a total or integrated (with respect to wavelength) radiation measurement to be made.

Transmission-emission measurements were initially made at a position 6mm downstream of the exit plane of the rocket nozzle where the propellant gases were expanded approximately to atmospheric pressure. The first few firings of the engine revealed the usual minor defects which were corrected without serious delay. Initial firings were made at an O/F of about 2.8 in order to maintain the chamber temperature low enough to prevent melting of the particles, thereby assuring good size control; i.e., sizes all equal to original sizes of injected particles. Under these conditions (Runs 63-2-I and J), no particle radiation or gas radiation was detected, and low O/F firings were discontinued. High O/F firings (K, L, and M) revealed more interesting but unexpected results. When particles were first injected, no immediate increase in radiation was detected by the total radiation detector, but as the slurry mix was continued a gradually increasing signal was recorded. This signal corresponded to the increase in a shower of large "sparks" observed visually in the plume. Examination of the nozzle revealed heavy deposition on entrance and exit regions. It was concluded that the shower of sparks was due to the shedding of large droplets by the shearing action of propellant gases. A second observation was that the transmission of the plume as measured by the optical

system was nearly 100 percent even with high particle flow rates. It was concluded that the rocket was not functioning as a simulator perhaps because the particles were agglomerated and were being deposited on the nozzle in excessive amounts due to large velocity.

The alumina slurry was then subjected to further processing in order to achieve de-agglomeration. It was found that the use of 1/2 percent by weight of trisodium phosphate as a wetting agent followed by overnight mixing on a ball mill (25 percent volume of alundum balls, about 1 cm in diameter, added) achieved a high degree of de-agglomeration of the individual particles. The slurry mixture was vastly more fluid in consistency and could probably have been further enriched with  $\text{Al}_2\text{O}_3$ . Some tendency toward settling of the particles remained, and although this was not considered serious, the particles were loaded into the piston immediately before firing in order to minimize settling. The use of a noncarbonaceous gelling compound to prevent settling would be an improvement for the slurry in future tests.

The de-agglomerated particles were then fired in the rocket (Runs N, O, P and Q), and it was observed that the shower of sparks was reduced but still present, that transmission remained very high ( $\sim 96$  percent), and that simulation of rocket motor firing was not achieved. In a discussion that ensued to determine the course of action to be pursued, a work was cited in which a small solid propellant rocket was fired, and the investigator found that extensive nozzle deposits were formed with attendant shedding of large, droplet-sized, particles. It was decided that further firing of the BRACE engine per se would be of no value because of its very small size, and that attempts should be made to fire the motor without a nozzle in the hope of eliminating droplet shedding. The firing sequence was modified to provide a delay before slurry injection of about 1 to 2 seconds. Optical measurements were made on all succeeding runs at a position 14 mm downstream of the exit plane of the throatless rocket motor.

The first firing (Run R) conducted after these modifications were made showed that combustion could be sustained without the nozzle although the photomultiplier in the monochromator was overdriven and no transmission measurement was obtained. Runs S and T were successful, and transmission was observed to decrease with increasing particle weight fraction--no sparks were observed. A series of runs (Runs U to Z) were conducted very close to stoichiometric O/F in which gas and gas plus particle radiation were measured as particle fraction,  $\phi$ , was varied. A second series of runs (Runs AA, BB, CC) were also conducted at higher total mass flows with O/F as before and  $\phi$  varied. In all cases the radiation was only perceptibly increased (over the level due to the gases (mainly  $\text{H}_2\text{O}$  only) when the slurry was injected into the combustion chamber.

Alumina particles ejected by the throatless rocket were captured directly on a greased slide, and also on plain slides, by the cascade impactor for a number of runs. Examination of these slides showed that all captured particles were spherical with many agglomerates formed on the slides consisting of very small particles and also some larger single spherical particles ranging up to about 10 microns. The fact that the particles recovered after firing were spherical

indicates that the alumina had been heated above its melting point (2320°K), but no detailed information on size distribution of recovered particles is possible, because of the extreme difficulty of collecting a truly representative sample. (It was also observed that the de-agglomerated particles, if stored for four days in an aqueous suspension, would spontaneously re-agglomerate. It is therefore conceivable that some of the large particles recovered on the slides were results of re-agglomeration in the slurry prior to firing, but this is improbable since the slurry was used very soon (four hours) after being removed from the ball mill.

A number of temperature measurements by observation of sodium D line with and without a background source of known temperature were made during the first portion of the firing when only the  $H_2-O_2$  were flowing. At this portion of the firing, only a trace amount of sodium is present, and the concentration of sodium is likely to vary between the time that the gas (Na D line) emission is observed and the gas plus lamp emission is observed. The temperatures so measured are, therefore, not considered accurate and varied widely from 2400°K to 3000°K about a mean value of 2680°K even though O/F was held constant. These measurements are considered the best available estimates of the gas temperature in the absence of the dilution effect of the slurry. The raw data has been reduced to an intermediate form and is presented in Figures A-1 and A-2 and Table A.2. Figure A-1 is a plot of the plume transmission versus particle weight fraction. The data shows a wide scatter around a straight line which corresponds to a mean diameter of 0.8 micron. Transmission tests were also conducted on the de-agglomerated particles in an aqueous suspension with the same equipment that is used on the rocket motor. This data, shown in Figure A-2, shows a curvature on a log-linear plot which may be due to forward scattering being received by the photocell. As concentration is increased, the forward scattering increases to cause a departure from the usual exponentiated transmission law. This type of error is discussed in Reference A.3 and can be corrected for by plotting [specific turbidity or  $\gamma = 1/L \ln(1/T)$  divided by concentration] versus concentration, Figure A-3. The value of specific turbidity at zero concentration is free from error due to forward scattering and can be used to determine mean size. The result obtained was 0.5 micron which appears to be a reasonable value.

### A.3.2 DATA REDUCTION

#### a. Particle Scattering of Gas Emitted Radiation

A brief study was made to determine if the increased radiation measured while the particles were flowing was merely due to a change in the angular distribution of the radiation emitted by the gaseous species. Since the important radiating specie is  $H_2O$ , the emission bands are at wavelengths of 1.1, 1.38, 1.87, 2.7, 6.3 and 20 microns. According to Penner,<sup>A.4</sup> the last three of these bands account for 95 percent of the total intensity of the  $H_2O$  emission. It was estimated, based on the fact that the transmission was 42 percent for a particle fraction of 0.365 (Run Z), that under such circumstances the transmission would increase to 83 percent for the 2.7 $\mu$   $H_2O$  emission band. Most runs were conducted at lower particle fractions, and transmission would be even higher. On this

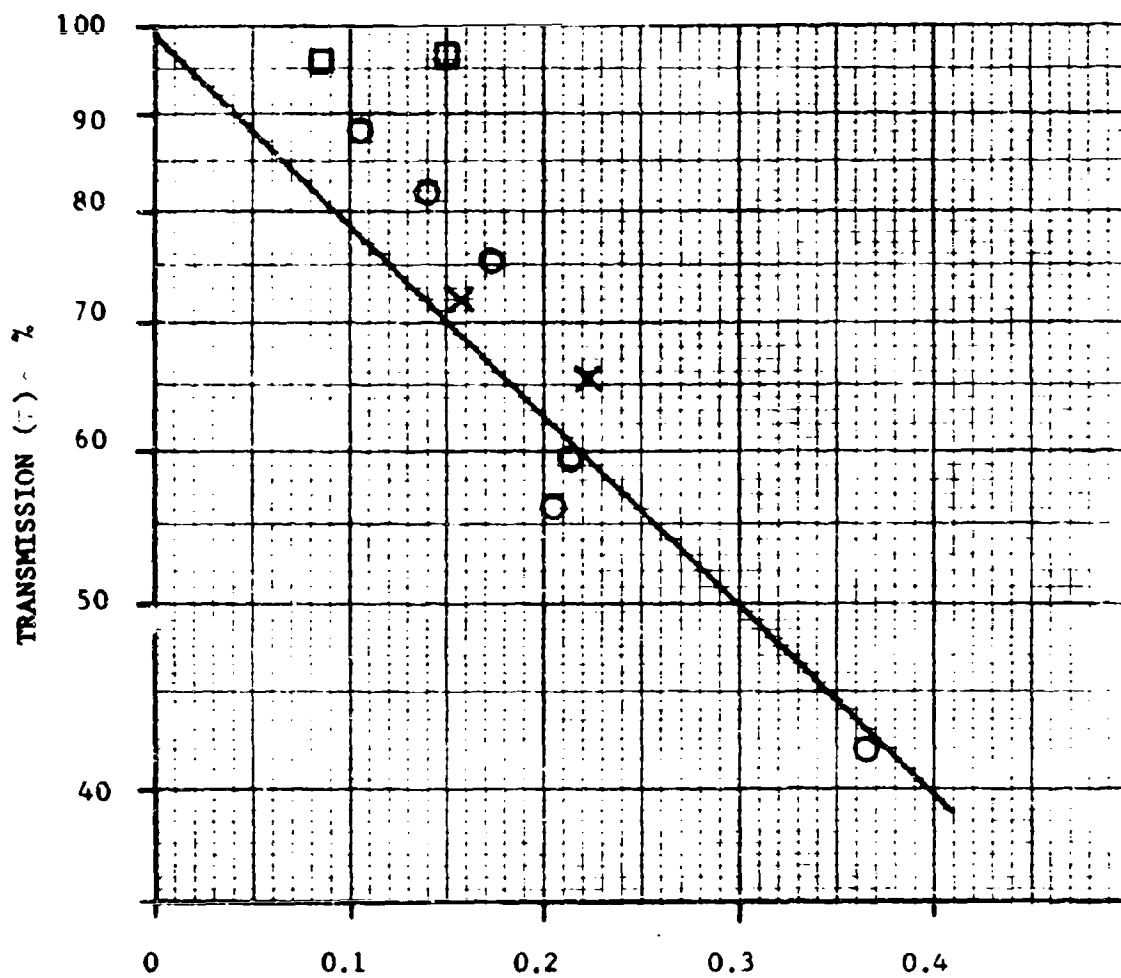


FIGURE A-1. PARTICLE WEIGHT FRACTION,  $\phi$

RO7470

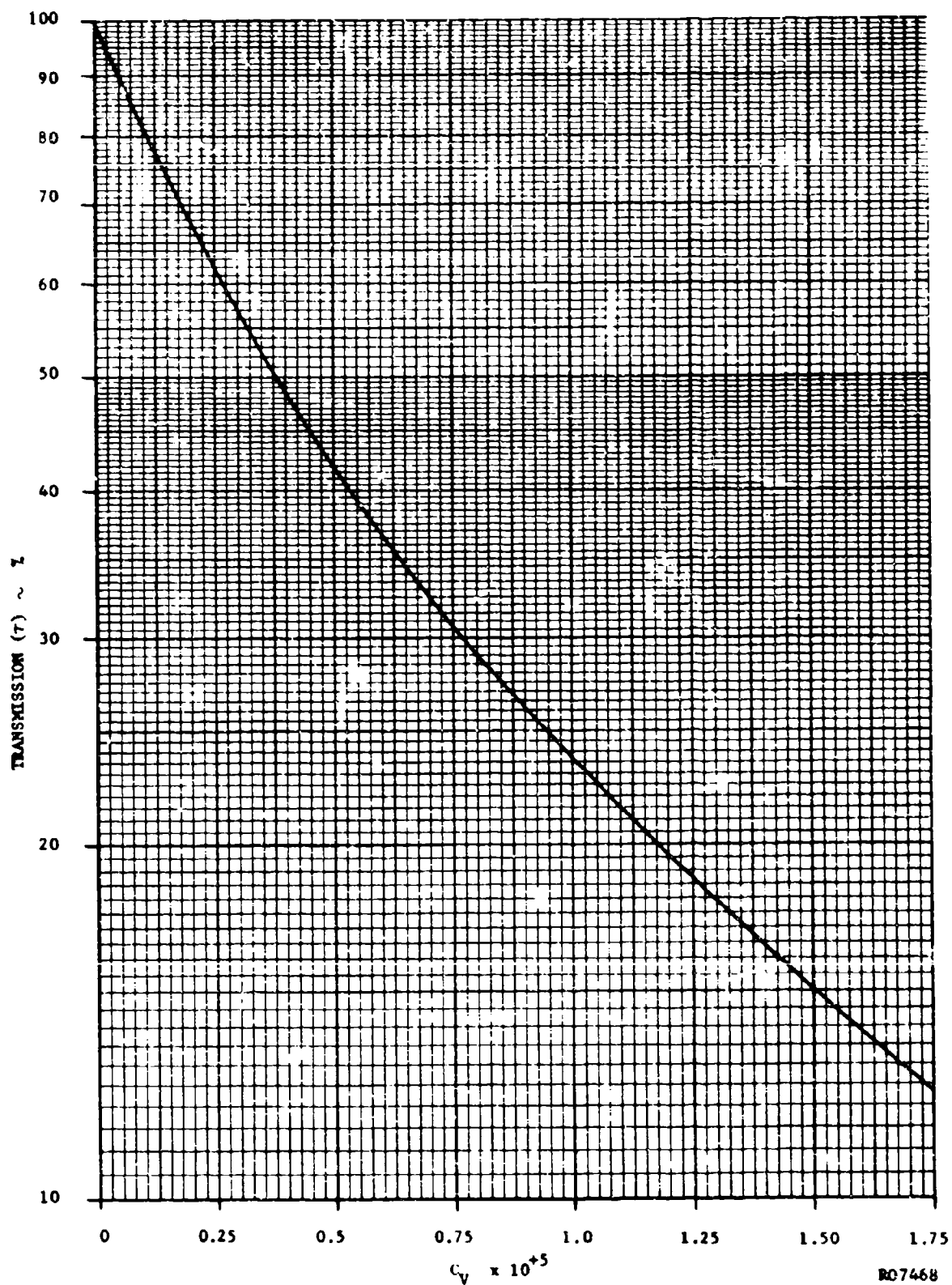


FIGURE A-2. TRANSMISSION VERSUS VOLUME FRACTION

TABLE A.2

SUMMARY OF DATA (See Notes Below)

Run No.	O/F	P <sub>c</sub> psia	$\phi$	$\dot{w}_{\text{gas}}$ lbm/sec	T <sub>2</sub> °K see below	T <sub>2</sub> <sup>1</sup> °K see below	N <sub>g</sub> watt cm <sup>-2</sup> ster <sup>-1</sup>	$\epsilon_g$	N <sub>pg</sub> watt cm <sup>-2</sup> ster <sup>-1</sup>	$\epsilon_{pg}$	$\frac{t}{\tau}$
U	8.02	47	0.106	0.158	2550	2380	0.55	0.0059	0.60	0.0078	88.3
V	7.92	49	0.140	0.160	2510	2380	0.57	0.0061	0.58	0.0081	82.3
W	7.83	50	0.174	0.164	2470	2350	0.56	0.0060	0.60	0.0090	75.6
X	7.85	49	0.211	0.167	2430	2280	0.57	0.0061	0.60	0.0095	56.2
Y	7.82	53	0.211	0.168	2420	2320	0.52	0.0056	0.57	0.0092	59.6
Z	7.87	55	0.365	0.191	2230	2220	0.50	0.0054	0.54	0.0120	42.0
AA	8.13	55	0.040	0.281	2630	2220	0.48	0.0051	0.62	0.0072	85.6
BB	8.09	62	0.159	0.288	2490	2080	0.46	0.0049	0.66	0.0096	72.5
CC	8.11	65	0.223	0.303	2410	2080	0.46	0.0049	0.74	0.0122	65.8

P<sub>c</sub> = Chamber pressure at head end of motor $\phi$  = Mass fraction of particles to gaseous products of combustion $\dot{w}_g$  = Mass flow of gaseous productsT<sub>2</sub> = Temperature of mixture of particles and gas calculated by adjusting the mean measured temperature prior to slurry injection for the dilution effect of the slurryT<sub>2</sub><sup>1</sup> = Temperature of mixture of particles and gas determined by Sodium D line measurement with slurry flowingN<sub>g</sub> = Integrated radiant intensity of gases formed by burning (H<sub>2</sub>(g) and O<sub>2</sub>(g) prior to the injection of slurry $\epsilon_g$  = Normal total emissivity of gases prior to injection of slurryN<sub>pg</sub> = Integrated radiant intensity of gases plus particles $\epsilon_{pg}$  = Normal total emissivity of gases plus particles $\frac{t}{\tau}$  = Optical transmission of plume

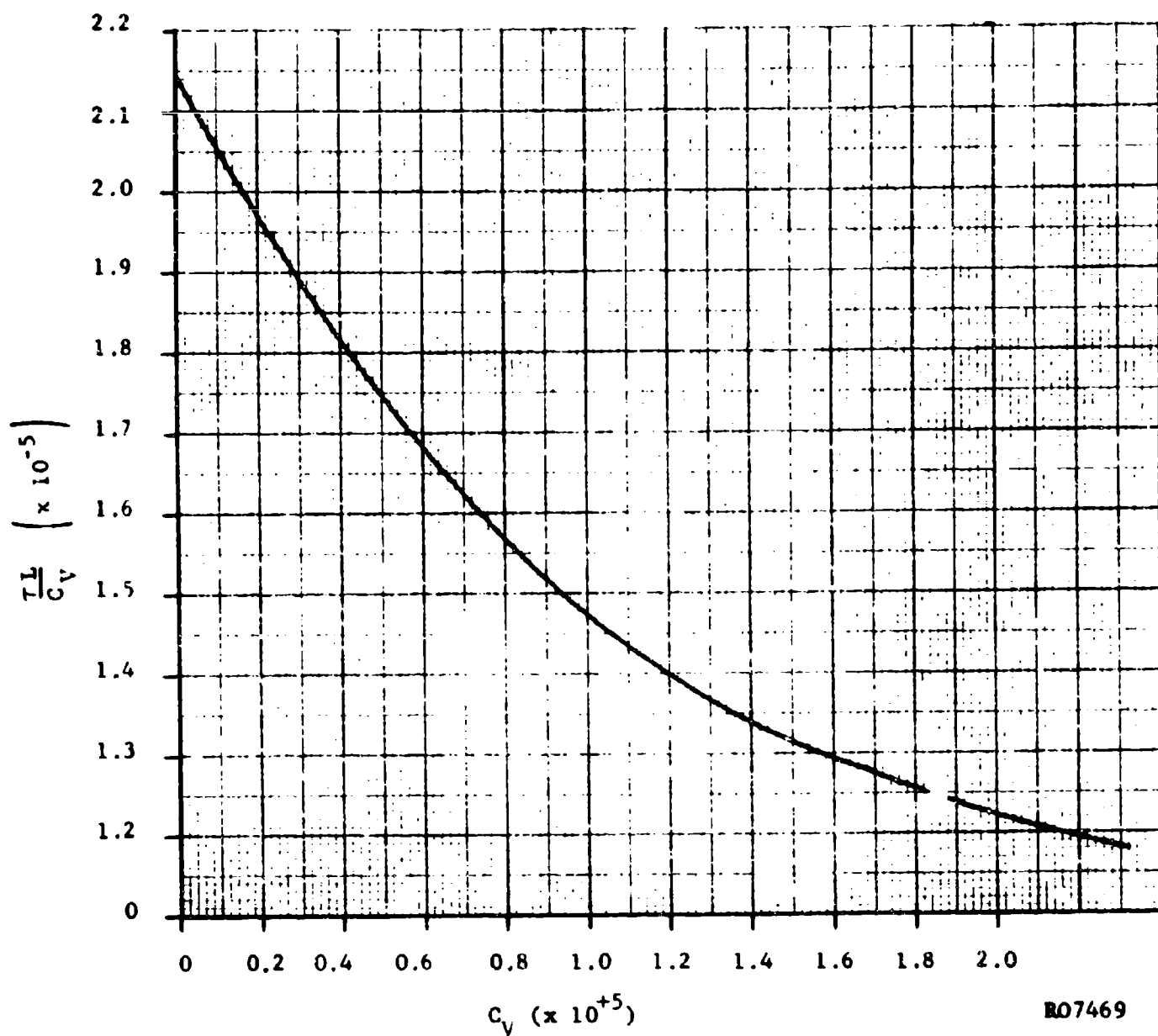


FIGURE A-3. SPECIFIC TURBIDITY VERSUS VOLUME FRACTION



basis, one can say that the optical depth for scattering is small for all important  $H_2O$  bands. Therefore, the possibility that the increased radiation measured in the normal direction is due to scattering by the particles, causing a change of angular distribution of energy emitted by  $H_2O$  with no net change in total heat transfer, is unlikely. The increase in the total radiation signal with the slurry flowing is attributed to particles emitting. This premise is further confirmed by the fact that at the visible wavelength of 0.59 micron, where no radiation was observed without the slurry, a detectable continuum was noted only when the particles are present.

#### b. Particle Cloud Emissivity

Since the optical depth for scattering of  $H_2O$  radiation by the particles is small, the particle cloud emissivity can be determined by subtracting the corrected steradiancy  $R_g(T_2)$  due to the  $H_2O$  from the measured steradiancy due to the particles plus gas,  $R_{pg}(T_2)$ . The particle cloud normal emissivity was then found by dividing by the steradiancy due to the blackbody at the temperature,  $T_2$ , that was found experimentally with the slurry flowing:

$$\epsilon_p = \frac{R_{pg}(T_2) - R_g(T_2)}{R_B(T_2)} \quad (A.5)$$

The experimental results reduced in this manner are plotted in Figure A-4.

The data falls on two lines corresponding to the different gas flow rates of 0.16 to 0.30 lb/sec for runs AA, BB, and CC. Each of these two series of the data shows moderate scatter, but the best guess seems to be that the data falls on straight lines corresponding to the two flow rates. Several unsatisfactory explanations can be offered for the variation of plume emissivities at the two different flow rates. One of these is the following. At the higher flow rates, the flow is choked at the exit plane of the motor due to heat addition, and the exit plane pressure is higher than atmospheric. The gases then expand in a diverging, supersonic jet upon leaving the nozzle resulting in a drop in the temperature ( $T_2$ ) and reduced  $H_2O$  emission measured in runs AA, BB, CC even though  $\dot{O}/\dot{F}$  ratio is held very nearly constant (see Table A.2; sodium lines were in reversal only for the last three runs, lamp current held constant). Particle cloud emissivity measured high presumably because of the greater depth and mass flow of particles. This picture would be expected to cause a reduced plume transmission, but this result was not obtained. It is this latter point that seems to be difficult to reconcile; while the particle steradiancy increased on the last three runs where lower temperatures were measured, the plume transmission shows no difference for equivalent value of  $\phi$  than on the previous six runs.

In any event, the data obtained from the earlier six runs are considered more self-consistent, and for that reason, to be the more reliable. The difficulty in interpreting the results of the last three data points is attributed to an uncertainty of particle velocity, cloud thickness, and hence particle

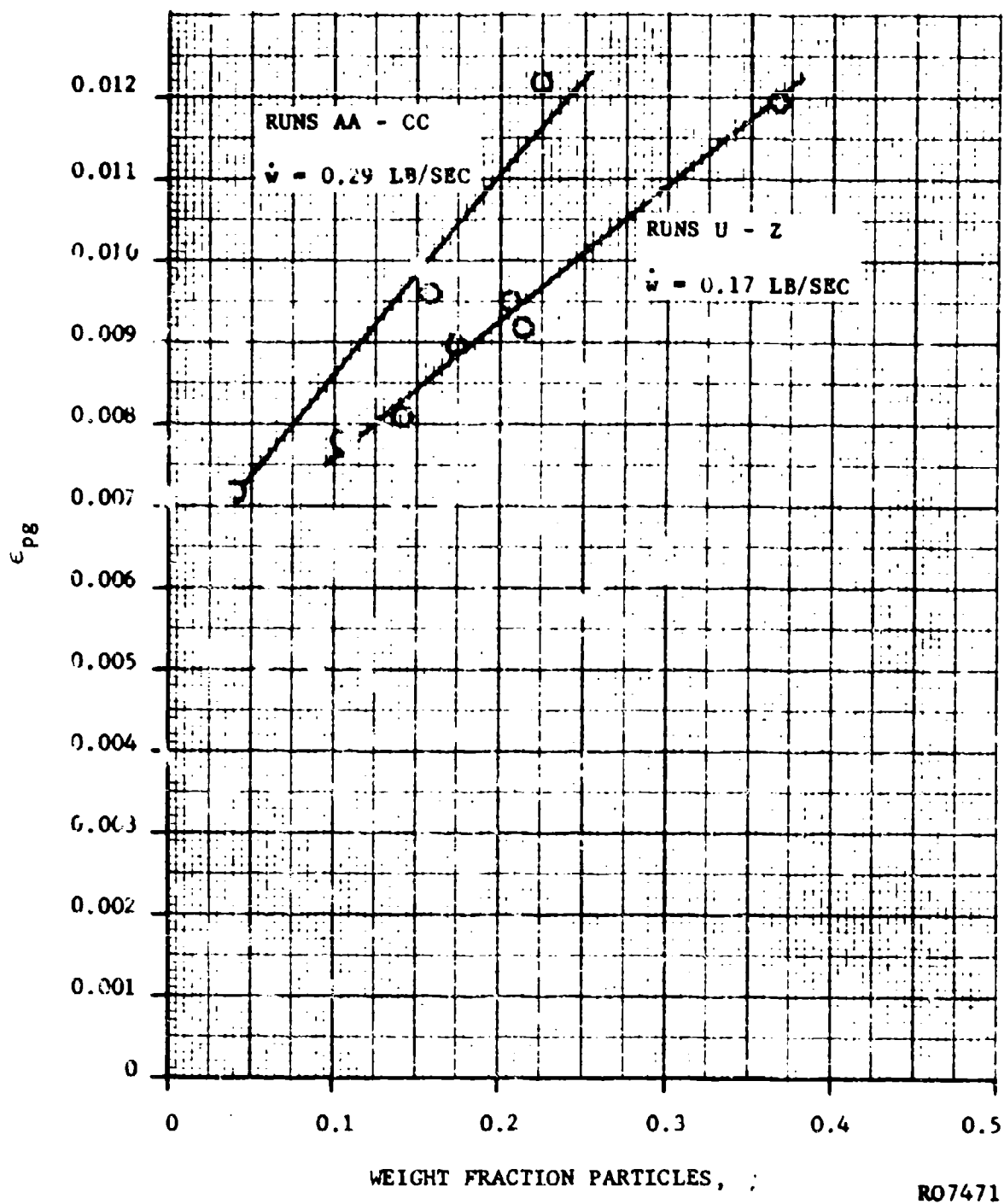


FIGURE A-4. EMISSIVITY OF PARTICLES OF  $Al_2O_3$  PLUS  $H_2O$

concentrations. Possible existence of similar uncertainties in the results of Runs U to Z cannot be overruled. Such uncertainty can be eliminated in future tests by performing a measurement of static pressure just upstream of the exit plane, and adjusting the flow rate so that atmospheric pressure is not exceeded at this point.

#### A.4 INTEGRATED RADIATION MEASUREMENTS

Measurements of the integrated radiation (i.e., the radiation emitted over all wavelengths) emitted by the particles were made by means of a fast response thermocouple with KBr window (Perkin-Elmer thermocouple and standard preamplifier). Radiation emitted by the rocket plume was collected by a spherical on-axis mirror and brought to a focus at the detector, which consisted of a blackened gold strip with a fine thermocouple attached. The photosensitive area of the transducer was  $0.2 \times 2.0$  mm, and the entire window size was about 4.0 mm in diameter. The mirror and detector assembly were enclosed in an aluminum box with a single opening to which an iris diaphragm was mounted. The box was purged with dry nitrogen to prevent atmospheric moisture from damaging the hygroscopic KBr window.

The fast response thermocouple uses a mechanically chopped radiation signal at 13 cps in order to generate an ac output which allows discrimination of signal at a dc level that does not depend on ambient temperature and other factors. It was found that the output of the thermocouple was relatively sensitive to chopping frequency (e.g., a reduction of from 13 to 11 cps increased signal by 10 percent), and for this reason a strobotach was used to adjust chopping wheel speed immediately before calibration or daily prior to a series of tests. The thermocouple signal was amplified in the preamplifier and amplifier and was recorded on the oscilloscope without rectification as an ac signal.

The radiometer was calibrated by means of a commercial blackbody cavity (Infrared Industries Model 404) up to a level of steradiancies of  $4.83 \text{ watts cm}^{-2} \text{ ster}^{-1}$  corresponding to a temperature of  $1278^\circ\text{K}$ . In calibrating the radiometer, the front face of the blackbody cavity and the thermocouple were used as the conjugate focal points. In performing measurements on the rocket plume, the optics were arranged so that a point on the axis of the mirror and the thermocouple were conjugate focal points. Both the image of the blackbody cavity and the image of the plume were large compared to the target area of the detector. To provide a check on the stability of the radiometer, a sub-standard calibration was used on a daily basis before each run. This was accomplished by deflecting the light from the tungsten ribbon filament lamp into the radiometer by means of a front surface mirror located at the image of the lamp on the rocket axis. It was believed that if a sharp image of the lamp was projected onto the transducer then the day-to-day alignment of the mirror would be too critical to provide a meaningful check of the stability of the radiometer. An additional lens was therefore inserted in the optical system in order to defocus the image of the lamp on the thermocouple and eliminate the need of a highly critical alignment of the mirror. The irradiancy at the thermocouple with the defocussing lens in position was very close to the irradiancy due to the rocket plume itself.

Erratic performance of the radiometer was noted during the first series of tests, its sensitivity seeming to decrease by a factor of four. However, during the next three days of testing, the sensitivity remained acceptably constant; the substandard check was 0.35, 0.36, 0.39 inches of deflection for 16 amps lamp current. After this, the radiometer was recalibrated with the black-body, and since its calibration had changed, all equipment was again moved back to the test cell for a check on the substandard. On this test, a deflection of 0.39 inch at 16 amperes lamp current was recorded. Although the cause of the lack of stability was never ascertained, because it occurred early in the testing and was followed by a week of stable performance and because the useful data were taken on only the last day after which a primary standard calibration and good substandard checks were performed, confidence is high that the radiometer was performing well during the important tests.

The amplified signal from the radiometer was found to be linear in steradiancy. The thermocouple is designed for use in a dual beam system where a constant check on its sensitivity is provided by use of a reference signal and ratio recording. In the present case, the preamplifier tube filaments and plates were supplied by external power supplies which could be a source of lack of repeatability. The geometry of the optical bench did not allow the use of a blackbody calibration in situ as would have been desirable. For these reasons, it is estimated that the accuracy of the measurement was of the order of  $\pm 5$  percent.

#### A.5 COMPARISON OF TOTAL RADIATION RESULTS WITH SPECTRAL ANALYSIS RESULTS

With the knowledge that the particle emission cross section is independent of wavelength and hence the particles emit as grey bodies, it is possible to reduce the data of total radiation tests, (obtained by Dobbins and reported in the third quarterly report), to spectral emission cross section. The results of this reduction indicate an emission cross section for the particles used in the latter tests (Davel  $5\mu$ ) on the order of  $10^{-2}$ . It is not possible to refine this estimate of particle emission cross section because the total radiation test is not sensitive when significant amounts of water vapor are present. The main conclusion from the total radiation is that the particle radiation was small compared to the gas ( $H_2O$ ) radiation in the simulator firing. The magnitude of this result is, however, in agreement with the results of the spectral emission tests of Carlson.

A number of improvements can be made in order to give more accurate measurements of both total and spectral emissivity tests of oxide particles. Both types of measurements would be improved by using a propellant formulation that eliminated the background radiation due to  $H_2O$ . This can be done by selecting a propellant-diluent combination that produces atomic species. Spectral measurements will be improved by using a spectrometer on several monochrometers that make observations at fixed wavelengths. The sensitivity can then be improved. Transmission tests can be made in order to deduce particle size and scattering cross section. This information can then be used to predict emission cross section as function of particle size.

## A.6 REFERENCES

- A.1 Milligan, R. A., "Measurement of Particle and Gas Temperatures in a Slightly Luminous Premixed Flame," J.O.S.A. 51, 535, (1961).
- A.2 Stull, V. R. and Plass, G. N., "On Emissivity of Carbon Flames," J.O.S.A. 50, 121 (1961).
- A.3 Heller, W. and Tabibian, R. M., J. Colloid Science 12, 25 (1957).
- A.4 Penner, S. S., Quantitative Molecular Spectroscopy and Gas Emissivities," Addison Wesley, Reading, Massachusetts, p. 322 (1959).